ARTICLE IN PRESS

Physics Reports xxx (xxxx) xxx

Contents lists available at ScienceDirect

Physics Reports

journal homepage: www.elsevier.com/locate/physrep

Matter manipulation with extreme terahertz light: Progress in the enabling THz technology

Peter Salén [a], Martina Basini [b], Stefano Bonetti [b,c], János Hebling [d,e], Mikhail Krasilnikov [f], Alexey Y. Nikitin [g,h], Georgii Shamuilov [a], Zoltán Tibai [d], Vitali Zhaunerchyk [i], Vitaliy Goryashko [a,*]

[a] Department of Physics and Astronomy, Uppsala University, Uppsala, Sweden
[b] Department of Physics, Stockholm University, Stockholm, Sweden
[c] Department of Molecular Sciences and Nanosystems, Ca' Foscari University of Venice, Venice, Italy
[d] University of Pécs, Pécs, Hungary
[e] MTA-PTE High-Field Terahertz Research Group, Institute of Physics, Pécs, Hungary
[f] Deutsches Elektronen-Synchrotron, Zeuthen site, Zeuthen, Germany
[g] Donostia International Physics Center (DIPC), Donostia-San Sebastian, Spain
[h] IKERBASQUE, Basque Foundation for Science, Bilbao, Spain
[i] Department of Physics, University of Gothenburg, Gothenburg, Sweden

ARTICLE INFO

Article history:
Received 11 February 2019
Received in revised form 3 September 2019
Accepted 4 September 2019
Available online xxxx
Editor: F. Parmigiani

Keywords:
Dynamics of charge carriers
Phonons and spins
Dirac materials and graphene
Alignment of molecules and action spectroscopy
THz acceleration and streaking
THz technology
Optical rectification and THz generation in plasma
Transition and synchrotron radiation
Free-electron lasers and electron beams
Transportation
Focusing and diagnostics of THz light

ABSTRACT

Terahertz (THz) light has proven to be a fine tool to probe and control quasi-particles and collective excitations in solids, to drive phase transitions and associated changes in material properties, and to study rotations and vibrations in molecular systems. In contrast to visible light, which usually carries excessive photon energy for collective excitations in condensed matter systems, THz light allows for direct coupling to low-energy (meV scale) excitations of interest. The development of light sources of strong-field few-cycle THz pulses in the 2000s opened the door to controlled manipulation of reactions and processes. Such THz pulses can drive new dynamic states of matter, in which materials exhibit properties entirely different from that of the equilibrium. In this review, we first systematically analyze known studies on matter manipulation with strong-field few-cycle THz light and outline some anticipated new results. We focus on how properties of materials can be manipulated by driving the dynamics of different excitations and how molecules and particles can be controlled in useful ways by extreme THz light. Around 200 studies are examined, most of which were done during the last five years. Secondly, we discuss available and proposed sources of strong-field few-cycle THz pulses and their state-of-the-art operation parameters. Finally, we review current approaches to guiding, focusing, reshaping and diagnostics of THz pulses.

© 2019 The Author(s). Published by Elsevier B.V. This is an open access article under the CC BY-NC-ND license (http://creativecommons.org/licenses/by-nc-nd/4.0/).

Contents

* Corresponding author.
E-mail address: vitaliy.goryashko@physics.uu.se (V. Goryashko).

https://doi.org/10.1016/j.physrep.2019.09.002
0370-1573/© 2019 The Author(s). Published by Elsevier B.V. This is an open access article under the CC BY-NC-ND license (http://creativecommons.org/licenses/by-nc-nd/4.0/).

Please cite this article as: P. Salén, M. Basini, S. Bonetti et al., Matter manipulation with extreme terahertz light: Progress in the enabling THz technology, Physics Reports (2019), https://doi.org/10.1016/j.physrep.2019.09.002.

1. Introduction

Terahertz (THz) radiation is all around us. For example, this page emits blackbody radiation mainly in the THz region (defined here from 0.3 THz to 30 THz). However, this THz radiation or THz radiation from traditional microwave sources is usually too weak to have any measurable impact on the properties of the materials that are studied with it. The situation drastically changed at the beginning of the 2000s: the technique of optical rectification with phase matching in crystals lacking inversion symmetry such as lithium niobate was developed [1,2]. This technological breakthrough enabled the development of table-top sources of single-cycle THz pulses with field strengths exceeding 1 MV/cm. Such a field strength is comparable with the intrinsic field strength in a wide range of strongly correlated materials and, therefore, it became possible to engineer new dynamic states of materials by modifying their intrinsic fields, see Section 2. Prominent examples include a THz field-induced ferroelectric phase in paraelectric materials, THz excitation of a transient Josephson plasma wave in a superconducting cuprate at a temperature significantly above the critical temperature of the sample, nonlinear harmonic generation in graphene to mention a few.

Please cite this article as: P. Salén, M. Basini, S. Bonetti et al., Matter manipulation with extreme terahertz light: Progress in the enabling THz technology, Physics Reports (2019), https://doi.org/10.1016/j.physrep.2019.09.002.

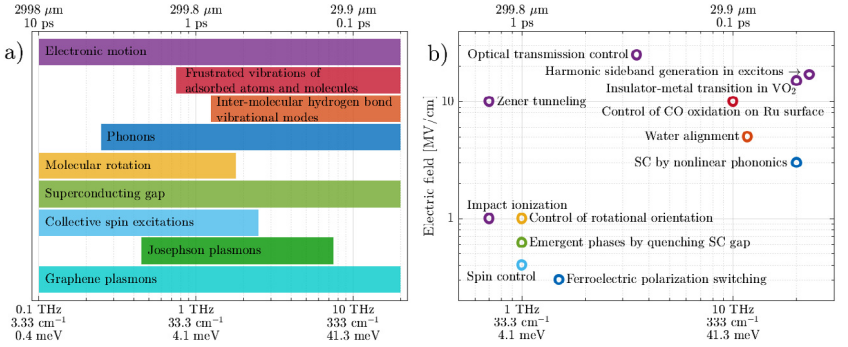

Fig. 1. (a) Fundamental excitations in solids and molecular systems in the THz region. (b) Examples of applications of strong-field THz light. Specific data points are taken from the following references: electronic motion (purple) [4–8], phonons (blue) [9,10], superconducting gap (SC, light green) [11], molecular rotation (yellow) [12], intermolecular H-bond (orange) [13], frustrated vibrations (red) [14], collective spin excitations (light blue) [15].

The aim of this review is threefold: (i) to survey recent studies dealing with the transformation, control and engineering of the properties of various materials with strong-field few-cycle THz light, Section 2; (ii) to introduce the operation principles for sources of strong-field few-cycle THz light and to survey the state-of-the-art performance of such sources, Section 3; (iii) to outline techniques for guiding, diagnosing and recomposing THz pulses, Section 4.

We have reviewed around 200 studies on the interaction of *strong-field* THz pulses with various materials. Most of the reviewed studies have been performed during the last 5 years. Clearly the field is very dynamic and the previous excellent review [3] does not reflect the diversity of new research directions. This has motivated the current review.

In general, THz radiation is an efficient tool to investigate a multitude of low-energy excitations existing in the THz region. Important examples are resonances of phonons, plasmons, spins, intersubband transitions, excitons, macromolecular vibrations and molecular rotations. Here: (i) phonons and plasmons are collective lattice and electron vibrations, respectively; (ii) subbands are electronic energy bands formed in quantum wells, in which the electrons are confined in two directions; and (iii) excitons are bound electron–hole pairs. THz radiation is also a fine tool: the energy of THz photons matches the fine energy structure of the mentioned resonances. This is highly advantageous in comparison with optical photons, which often contain excessive energy relative to the type of low-energy resonances given above and, therefore, provides a blunt tool. The extra energy from the optical photons is, for example, distributed as phonon excitations or hot electron distributions, which result in less control and unwanted temperature increase. THz radiation, on the other hand, allows one to specifically target the excitation of interest and thus opens the door to controlled manipulation of reactions and processes, as well as properties of matter.

Resonant excitation of the phonon modes using strong-field THz pulses can lead to a distortion of the lattice structure. This provides the possibility for control of the lattice geometry, which changes the material properties, such as the magnetic order, the superconductive character or the ferroelectric polarization, as discussed in Section 2.1. Moreover, collective spin excitations are created and manipulated with the strong magnetic fields of intense single-cycle THz waves, see Section 2.3, which will have important implications for the development of, *e.g.*, new data storage and processing devices based on spin orientation. Collective electron motions driven by strong THz fields can influence atoms and molecules adsorbed to surfaces to a degree where the control of catalytic processes is possible. These THz waves are also useful for the direct manipulation of atomic and molecular systems that lead to rotational and vibrational control, Section 2.4.

In addition to the collective excitations described above, several other systems can be driven by strong-field few-cycle THz pulses. The characteristic energy regions of various THz excitations and related examples of strong-field THz applications are presented in Fig. 1a and 1b, respectively. In some cases the control is exerted non-resonantly by the strong THz field, which is commonly exploited in charge-carrier dynamics research, Section 2.2. For example, the acceleration by THz electric fields promotes valence electrons to the conduction band, so-called impact-ionization, which leads to increased conductivity in semi-conductors. At sufficiently high fields the electrons may even be driven from the valence band to the conduction band on a neighboring site in a tunneling process. Moreover, the THz field has been demonstrated to ionize excitons by dragging the electron from the hole, and even to generate harmonic frequencies of radiation by recolliding the exciton-electron with the hole. THz radiation also strongly interacts with Dirac electrons in graphene leading to a variety of nonlinear effects useful for practical applications.

The dynamics of THz excitations typically occurs on the picosecond (ps) timescale and can efficiently be studied using THz pump–probe schemes. These measurements require intense pulses short enough to provide sufficient temporal resolution and consequently strong-field single-cycle THz waves are suitable. Such THz pulses may be used both as the pump to drive the system, and as the probe, or in combination with, *e.g.*, optical pulses. Moreover, the broad bandwidth of the single-cycle transient (∼100%) is beneficial for probing as it allows monitoring the pump-induced effects in a large spectral region.

Please cite this article as: P. Salén, M. Basini, S. Bonetti et al., Matter manipulation with extreme terahertz light: Progress in the enabling THz technology, Physics Reports (2019), https://doi.org/10.1016/j.physrep.2019.09.002.

High-brightness electron beams are an essential ingredient of state-of-the-art X-ray free-electron lasers and ultrafast electron diffractometers. Recently, it has been shown that the required high-brightness beams can be generated and accelerated by compact THz-driven electron guns and linear accelerators. Currently, the charge of beams produced with THz technology is low but photonic electron guns and accelerators have a large potential and are an active area of research, Section 2.5. In addition, strong-field THz pulses allow the temporal characterization of femtosecond (fs) and attosecond pulses from free-electron lasers and high-harmonic generation sources.

Nonlinear THz experiments performed in recent years have been made possible by strong fields available with modern THz technology. Since the technology is still under development, Section 3 of the review is devoted to sources of strong-field THz pulses. The main class of such sources makes use of optical rectification of intense laser pulses in nonlinear media, see Section 3.1.1. In this method, an optical pulse with sub-100 fs duration illuminates a crystal lacking inversion symmetry that favors the accumulation of non-zero nonlinear net polarization. This polarization propagates at the speed of the driving laser pulse and is a source of Cherenkov radiation at lower frequencies lying below the infrared lattice vibrations [16,17]. However, since the driving laser pulse propagates faster than the generated THz pulse, a phase mismatch occurs. This mismatch limits efficient interaction to distances over which the acquired phase shift is less than 2π. By tilting the wavefront of the driving laser, the phase velocity of the generated pulse is made equal to that of the driving pulse [1]. The interaction region then extends across the whole crystal thus enabling a huge increase in the generated field [2].

Generation of intense THz pulses in gaseous and solid media based on femtosecond-laser-induced plasma formation, discussed in Section 3.2, is a new, very promising approach. The THz pulse energy of several hundreds of μJ has experimentally been demonstrated in solid foils using the mechanism of sheath radiation. In this approach, upon the illumination of a thin metal foil by an intense femtosecond laser pulse, hot electrons are "blown" away from the foil leaving behind a strong electrostatic potential. This potential ionizes atoms and the dynamics of an induced plasma leads to strong THz transients. Theoretical modeling shows that the field strength of 100 MV/cm (V/Å) is within reach.

Another class of THz sources that has demonstrated record high fields of several tens of MV/cm is based on transition radiation from relativistic electron bunches passing through a metallic foil, Section 3.3.1 (*throughout the text, we use the term "bunch" to emphasize beams of short duration whereas the "beam" is used as a generic term for the particle distribution*). As the bunch approaches and impinges on the foil, its field re-organizes from the Coulomb field in free-space to the field in the foil, which is compatible with the properties of that medium and the induced polarization. During this process of re-organization some field is shaken off in the form of a single-cycle electromagnetic wave. The cutoff frequency of the emitted field is usually limited by the inverse bunch duration. The emitted energy scales logarithmically with the bunch's kinetic energy so that GeV electron bunches are needed to produce 10 MV/cm THz pulses. Therefore, the availability of ultrahigh-field THz sources based on transition radiation is very limited. Only a few national laboratories in the world operate such sources, see Fig. 2. The situation may, however, change with the development of multifoil radiators of coherent transition radiation [18], see Section 3.3.2. Moreover, by using transition radiation from plasmonic surfaces, it is possible to create wavefronts with any desired shape and topological charge [19].

Electron bunches provided by an accelerator can radiate in an external magnetic field (synchrotron radiation, Section 3.4). If the electron bunch follows a sinusoidal path in a periodic magnetic device (*undulator*), the emitted power increases as the number of periods, but the number of oscillation cycles increases as well [20]. In Fig. 2, the small bandwidth of the undulator source is due to multiple undulator periods (nine), so the pulse is multi-cycle.

A new class of strong-field *single-cycle* sources based on undulator radiation from specially prepared trains of electron bunches has recently been proposed and studied theoretically [21–23]. The key idea is to enable constructive interference between broadband light waveforms emitted by different bunches only at one position of the resulting wavepacket. A prepared train of bunches introduces a phase-locking condition, so that the emitted pulse shortens in a way similar to mode locking in cavity lasers (Sections 3.4 and 3.5).

An efficient use of THz pulses in experiments requires adequate THz transportation and diagnostics, which is discussed in Sections 4.1 and 4.2, respectively. Moreover, the control and guiding of THz fields in two-dimensional materials has received considerable attention in the field of plasmonics as a new path towards constructing small-scale photonic devices. The interaction of THz transients with collective electrons on the surface or in thin layers of a metal can form surface plasmon polaritons, which exhibit a reduced wavelength compared with the exciting light and can be confined to nano-scale dimensions. In Section 4.3 we emphasize graphene, which possesses exotic electronic and mechanical properties. It supports graphene plasmon polaritons (GPs) that can be confined to extremely small dimensions and can be controlled by electrostatic fields. Hence, the manipulation of GPs holds great potential for future THz applications.

2. Science applications of strong-field THz light

2.1. Coherent phonon dynamics

Coherent lattice excitation by short light pulses is a promising route towards ultrafast control of phase transitions and associated changes in material properties. In this section we will describe the concepts and potential of nonlinear THz lattice excitations. Applications of the obtained lattice control are discussed with emphasis on effects emergent in superconducting materials in the presence of strong-field THz radiation and polarization switching in ferroelectric materials.

Please cite this article as: P. Salén, M. Basini, S. Bonetti et al., Matter manipulation with extreme terahertz light: Progress in the enabling THz technology, Physics Reports (2019), https://doi.org/10.1016/j.physrep.2019.09.002.

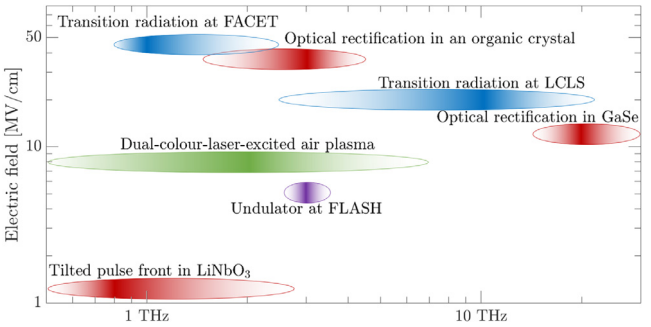

Fig. 2. Sources of strong-field THz radiation. The demonstrated record parameters in the parameter space of field strength vs. frequency are shown by ellipses. The maximum hue shows the central frequency of the source, while the FWHM bandwidth is given by the width of the corresponding ellipse. Note that the central frequency is not necessarily at the center of the characteristic source bandwidth. The inverse bandwidth determines the minimum possible pulse duration. The height of the ellipses has no special meaning. Data points are taken from the following Refs.: dual-color-laser-excited air plasma [24], tilted pulse front [25], optical rectification in GaSe [26], in an organic crystal [27,28], transition radiation at LCLS [29], at FACET [30], undulator at FLASH [31–33]. Although the latter is not a single-cycle source, it provides strong THz fields and gives a hint about future undulator-based single-cycle sources (see Section 3.4 and [20]).

2.1.1. Nonlinear lattice excitations

The control of coherent lattice vibrations (*i.e.*, phonons) is crucial to promote and tune several properties of matter. As will be shown later, the control of phonon frequencies and amplitudes allows the tuning of structural distortions, the switching of ferroelectric and ferroelastic properties and in some cases, of a local magnetic field. Traditionally, coherent lattice excitation by short light pulses has been obtained by optical femtosecond pulses in Raman scattering techniques [34–36], where the coherent phonon modes are excited by scattering of the radiation via an intermediate electronic energy level. Such experiments are, however, associated with uncontrolled excitation of additional channels, *e.g.*, electronic level excitation above the energy gap, that interfere with the measurement and may lead to sample damage. Moreover, the Raman tensor (R) weights the scattering efficiency so that only modes with appreciable R value (*i.e.*, even symmetry) can be excited. On the other hand, infrared (IR)-active phonons (*i.e.*, odd symmetry) can be excited directly by means of a resonant THz field. Note that historically, the low-frequency phonon modes are referred to as the IR modes whereas the actual frequency of the mode is often in the THz region.

Up to now, Raman scattering and THz absorption of photons by the crystal lattice have been considered complementary techniques to excite all the vibrational symmetries. At the same time, with the higher THz fields of 1 MV/cm accessible today, new attractive excitation mechanisms (sum-frequency [37] and non-linear modes coupling [38,39]) have been exploited in order to drive even symmetry modes. In this sense, strong THz radiation is nowadays able to drive phonon modes of odd and even symmetries. In the first direct comparison between the impulsive stimulated Raman scattering (ISRS) and THz absorption approaches, it was suggested that the issues related to the nonlinear processes induced by high optical fluences in the Raman experiments can efficiently be avoided using resonant THz excitation of the lattice [40]. A comparison with linear lattice excitations and molecular systems is given in a recent perspective article [41]. Moreover, it has recently been calculated [42] that the THz efficiency in exciting Raman active modes is up to one order of magnitude higher with respect to the well-known scattering process.

In the light of the experimental evidences in the last five years, three ways exist to efficiently drive a Raman-active mode by means of a strong THz field, two of them including nonlinear lattice excitations. First, the *THz sum-frequency excitation* (THz-SFE) mechanism is able to drive lattice vibrations with an efficiency proportional to the square of the field intensity. This is a two-photon absorption mechanism for which two frequencies, within a broad THz pulse, sum up to transfer the combined energy of the photons to one Raman active vibrational state. The THz-SFE was experimentally demonstrated in 2017 in a diamond crystal [37], where an intense THz pulse with a central frequency of 20 THz is found to coherently drive the Raman-active F_{2g} mode at a frequency of 40 THz.

Second, a THz-resonant IR-active mode can be driven to the *anharmonic regime* and, consequently, be non-linearly coupled to higher frequency modes. This anharmonic process is able to transfer vibrational energy from a lower frequency IR mode to a higher frequency IR, Raman-active or silent coherent vibration. For example, THz-driven phonon upconversion was demonstrated in the prototypical transition metal oxide strontium titanate [43]. In this case, the lowest optical soft phonon mode, tunable between 1.5 and 2.5 THz by varying the sample temperature, was excited by a single-cycle pulse centered at 0.75 THz and with its spectrum extending to 2.5 THz. The transformation of the excited phonon mode into higher frequency modes at 5.15 and 7.6 THz (silent) was observed by monitoring the atomic displacements using X-ray diffraction with femtosecond resolution. The model is that of a driven anharmonic oscillator with coordinate Q_{IR}, frequency ω_{IR} and damping γ_{IR} which couples to another, higher frequency oscillator with coordinate Q, frequency ω and damping γ. The equations of motion read

$$\ddot{Q}_{IR} + 2\gamma_{IR}\dot{Q}_{IR} + (\omega_{IR}^2 + k_1 Q_{IR}^2)Q_{IR} = Z_{IR}^* E_{THz}, \tag{1}$$

$$\ddot{Q} + \gamma\dot{Q} + \omega^2 Q = Z_2^* E_{THz} - a_{21} Q_{IR}^3. \tag{2}$$

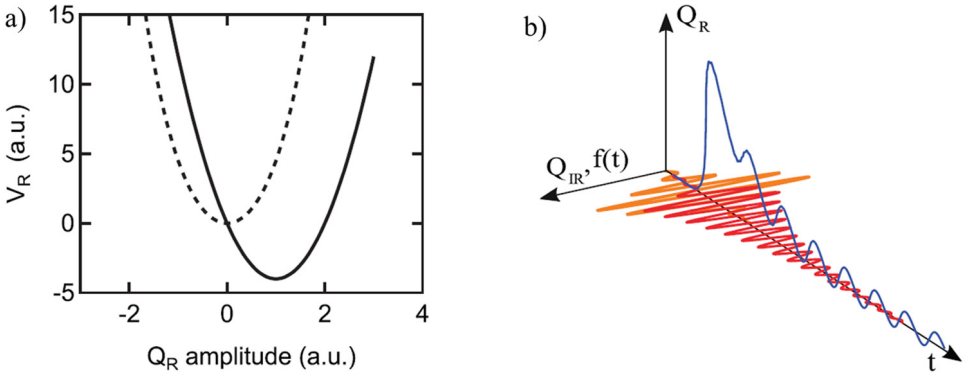

Fig. 3. (a) Nonlinear phononics enables a transient displacement of the crystal potential-energy minimum along a Raman-mode coordinate Q_R via anharmonic coupling to the driven IR-active mode, Q_{IR}. (b) Illustrates the displacement of Q_R (blue) induced by the THz electric field $f(t)$ (orange) that drives the IR-active mode (red).
Source: Adopted from Ref. [38].

Here E_{THz} is the driving THz field, Z^* is the mode effective charge (equals zero for Raman active) and k_1 and a_{12} are the anharmonic phonon contribution and the phonon–phonon coupling constant, respectively. Eq. (1) describes the motion of a driven oscillator with a frequency that increases with the square of the mode amplitude. Eq. (2) describes the motion of a harmonic oscillator with two driving forces (*i.e.*, the THz electric field and the IR phonon mode). The key point is the term containing the third power of Q_{IR}, which effectively extends the bandwidth of the driving THz field to overlap with the higher frequency Q mode, thus resulting in a more efficient energy transfer.

Third, the *ionic Raman scattering* (IRS), proposed in Refs. [44–46], uses an excited IR-active phononic state as an intermediate scattering level, instead of an electronic state as in conventional Raman scattering. The lattice potential including the anharmonic coupling to the Raman normal mode with coordinate Q_R can, to the lowest order, be expressed as [38,39]

$$\frac{1}{2}\omega_{IR}^2 Q_{IR}^2 + \frac{1}{2}\omega_R^2 Q_R^2 - a_{12} Q_{IR} Q_R^2 - a_{21} Q_{IR}^2 Q_R, \tag{3}$$

where a_{ij} are the anharmonic coupling constants. For a centrosymmetric crystal a_{12} is zero and a_{21} is nonzero for Raman-active modes. The equations of motion for the IR and Raman modes then become

$$\ddot{Q}_{IR} + 2\gamma_{IR}\dot{Q}_R + (\omega_{IR}^2 a_{21} Q_R) Q_{IR} = Z_{IR}^* E_{THz}, \tag{4}$$

$$\ddot{Q}_R + 2\gamma_R \dot{Q}_R + \omega_R^2 Q_R = a_{21} Q_{IR}^2, \tag{5}$$

where E_{THz} describes the driving THz field and γ_{IR} and γ_R are the damping constants of the IR and Raman modes, respectively. The $a_{21}Q_{IR}^2$ term represents a constant force on the Raman mode that displaces the potential energy curve along Q_R and thus invokes a changed lattice structure that survives within the duration of the IR-mode as shown in Fig. 3. The IRS mechanism was experimentally demonstrated on $La_{0.7}Sr_{0.3}MnO_3$ by Först et al. in 2011, who labeled it nonlinear phononics [47].

The transient modification of the lattice structure by nonlinear phononics can be exploited for material control in several ways [38], *e.g.*, by driving insulator–metal transitions [48–50], melting of magnetic [51] and orbital order [51,52], inducing superconductive characteristics [39]. Ultimately, a recent study [53–55] demonstrated that intense THz fields may enable control of ferroelectric polarizability by driving the lattice configuration energy state over the ferroelectric potential barrier (see Section 2.1.3).

Additional control via nonlinear phononics has been reported in a theoretical study [56] by simultaneous excitation of two IR-active modes with coordinates Q_{IR_1} and Q_{IR_2}. This excitation scheme introduces the cubic coupling term of the form $Q_{IR_1} Q_{IR_2} Q_R$ in the potential energy surface, which anharmonically couples the two IR modes to the Raman mode. This way one may obtain control over the direction of the transient distortion by changing the orientation of the light polarization, as was demonstrated using the $ErFeO_3$ model system.

The ionic Raman scattering process exploited for nonlinear phononics as described above activates a lower frequency Raman mode via difference-frequency components of the phonon fields of the excited higher-frequency IR mode. These schemes can, analogous to traditional photonic Raman scattering, be extended to sum-frequency generation, which allows for the coherent excitation of higher frequency Raman modes via the cubic $Q_{IR}^2 Q_R$-type coupling term [42]. Such a process was recently experimentally observed in Bi_2Se_3 [57], where the Raman mode at the second harmonic of the resonantly driven dipole active mode at 2.05 THz was coherently excited. Moreover, Melnikov et al. interpreted the coherent Raman oscillations at 1 THz and 2.25 THz as activated by four-phonon interactions via the quartic $Q_{IR}^2 Q_{R_1} Q_{R_2}$ and $Q_{IR}^2 Q_{R_2}^2$-type coupling terms, respectively.

Please cite this article as: P. Salén, M. Basini, S. Bonetti et al., Matter manipulation with extreme terahertz light: Progress in the enabling THz technology, Physics Reports (2019), https://doi.org/10.1016/j.physrep.2019.09.002.

The excitation of coherent Raman modes via quartic anharmonic coupling terms is expected to be useful for lattice control since it permits coupling to Raman modes that are forbidden by cubic coupling. It has also been suggested to drive dynamical symmetry breaking in specific crystal structures [50]. Driving an IR-active phonon mode with frequency ω_{IR} to sufficiently high amplitude is important for excitation of otherwise inaccessible Raman modes. In addition, it provides access to the higher order harmonic contribution and thus enables detailed investigation of the anharmonic shape of the lattice potential energy surface. The slice of the lattice potential energy surface along the excited Q_{IR} coordinate can be written as

$$\frac{1}{2}\omega_{IR}^2 Q_{IR}^2 + a_3 Q_{IR}^3 + a_4 Q_{IR}^4 \ldots \tag{6}$$

In this expression the first term represents the potential energy of the harmonic oscillator with frequency ω_{IR} and the remaining terms are the higher order harmonic components, where a_i are material-specific constants. The couplings to other modes have been neglected here. The availability of field strengths near 1 MV/cm has enabled the exploitation of the lowest order phonon nonlinearities [47] corresponding to the cubic terms. Recently, an order of magnitude higher field (20 MV/cm at 17.5 THz) was used to excite up to the 5th harmonic of the A_1 mode in the ferroelectric lithium niobate ($LiNbO_3$) [58]. Such studies allow the reconstruction of the potential energy surface of specific phonon modes and provide a benchmark for computational studies.

Phonon modes play one of the key roles in the collective structural transformation both in classical and in quantum phase transitions. By means of direct excitation of collective lattice oscillations (*i.e.*, soft phonons) in the nonlinear regime and their coupling to additional other modes, it is possible to change the equilibrium symmetries in the system. In June 2019 two similar studies [59,60] experimentally demonstrated a THz field-induced ferroelectric (FE) phase in the well-known quantum paraelectric strontium titanate. The idea of Nelson et al. [59] and Nova et al. [60] was to induce strong lattice deformations by means of strong mid-infrared optical pulses resonant with a FE lattice vibration. With a strong enough electric field, the excited vibration enters into a nonlinear regime which overcomes the quantum fluctuation, thus resulting in a metastable FE phase. These are important and rare examples of light-induced phase transition above the transition temperature, *i.e.*, in the presence of fluctuating order.

We note that the coupling of the excited lattice mode and the electronic structure has been suggested as an alternative path towards nonlinear phonon control of materials [61]. The experimentally observed charge-order melting in the doped manganite $Pr_{0.5}Ca_{0.5}MnO_3$ induced by 17.5 THz pulses displayed a nonlinear fluence dependence, inconsistent with nonlinear-phononics type anharmonic coupling to Raman modes. Instead, the calculations identified a highly nonlinear coupling between the driven IR mode and the electronic degrees of freedom that modified the electronic structure.

Nonlinear phononics can also be applied to drive coherent oscillations of the macroscopic magnetic moment in a magnetic material. An important example is given by the experimental study in [62], where the nonlinear mixing of simultaneously excited perpendicular lattice modes drives rotation as well as displacements of the atoms in the lattice. This induced lattice rotation creates an effective local magnetic field up to 36 mT resulting in the excitation of a spin precession in the orthoferrite $ErFeO_3$.

Finally, we briefly review topological materials as new quantum materials in which only topology is responsible for unusual transport properties. Topological insulators are insulating in the bulk and conducting at the surface, topological semimetals are semimetal in the bulk and the valence and conduction bands touch near the Fermi level. Depending on whether the bands are doubly degenerate or nondegenerate, a topological material is called a topological Dirac semimetal or a topological Weyl semimetal [63]. The latter displays extremely high magnetoresistance and mobility of massless charge carriers, which is indicative of the Weyl fermion properties. The topological properties of topological semimetals can be manipulated through atomic-scale lattice distortions. The generation of interlayer strain by means of THz light excitation of lattice displacements alters considerably the electronic structure, but leads to less lattice damage than uniaxial straining. A THz field-driven charge-current mechanism in a Weyl semimetal (*i.e.*, tungsten ditelluride) has recently been proposed [64] to explain the experimental evidence of an orthorhombic-to-monoclinic and centrosymmetric phase induced by strong THz pulses. It is worth to note that the possibility of an ultrafast manipulation of the topological properties of such materials opens the possibility to develop a topological switch in the THz frequency range.

2.1.2. Towards THz-induced superconductivity

Conventional superconductors

Conventional superconductors (SCs) are described by the BCS theory (Bardeen–Cooper–Schrieffer), which suggests that an attraction between electrons mediated by electron–phonon coupling overcomes the electron–electron repulsion and forms Cooper pairs. These opposite-spin electron pairs avoid interaction with the lattice and are thus allowed to move through the material without energy losses. The density of Cooper pairs is proportional to the magnitude of a gap in the electron energy spectrum, characteristic of the superconducting state, the so-called superconducting gap, Δ_{SC}. The gap is a measure of the binding strength between the paired electrons. At sufficiently low temperatures the Cooper pairs can be sustained due to a low risk of thermally induced pair-breaking and consequently a superconducting state can emerge.

The recent availability of intense THz sources has triggered investigations of the superconducting order-parameter dynamics in conventional SCs. Such collective modes can be created from a broken phase symmetry in the SC, spontaneously, or induced by an external stimuli. In particular, the Higgs mode, which represents the amplitude contribution

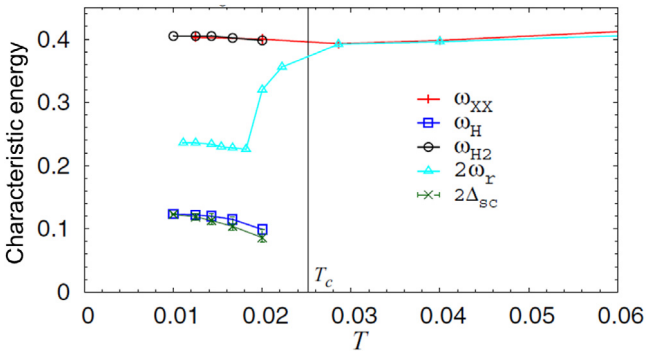

Fig. 4. Characteristic energies of collective excitations in a model system of an unconventional SC with strong electron–phonon coupling. ω_H is the frequency of the Higgs mode, which equals $2\Delta_{SC}$ as predicted in the absence of any interaction to other modes. ω_{XX} is the frequency of a coherent oscillation in response to phonon displacement. For a pure coherent phonon mode $\omega_{XX} = 2\omega_r$ is expected, where ω_r is the renormalized phonon frequency. However, below T_c, $\omega_{XX} > 2\omega_r$, indicating that ω_{XX} is not a pure phonon mode. Moreover, $\omega_{XX} = \omega_{H2}$, which suggests that the new mode with frequency ω_{H2} emerging from the calculations is a new collective mode that is intertwined with the coherent phonon mode.
Source: Adopted from Ref. [71].

to the complex order parameter in condensed matter physics, was quite recently observed experimentally in a BCS superconductor using intense THz pulses in a THz-pump THz-probe scheme [65,66]. The single-cycle THz pulse enabled an excitation, resonant with the superconducting gap, sufficiently short compared to the response time of the BCS state, which is proportional to the inverse of the gap. At the same time, the thermal excitation of the lattice that leads to Cooper-pair breaking using optical pulses could be reduced. Consequently, it was possible to induce a coherent correlation between different quasi-particle states that generated oscillations of the superconducting order parameter indicative of the Higgs mode.

The superconducting order-parameter dynamics has been studied theoretically by purely electronic models [65,67–69] and by including a strong electron–phonon coupling [70,71]. Specifically, it is desired to investigate the interplay between the phonon dynamics and the Higgs mode, and what types of collective excitations can exist in systems characterized by strong electron–phonon coupling. By including nonequilibrium phonon dynamics in their simulations, Murakami et al. showed that the Higgs mode excitation involved another amplitude mode, denoted as H_2, associated with coherent phonon motions intertwined with the SC order parameter. The frequency dependence as a function of temperature of this H_2 amplitude mode is shown in Fig. 4. The H_2 mode originates from a two phonon mode (simultaneous excitation of two phonons) and it couples to the Higgs mode in the strong electron–phonon coupling regime. The coupling between the Higgs mode and the H_2 mode pushes the energy of the Higgs mode slightly below the quasi-particle continuum, making the Higgs mode longer lived. The experimental study of the predicted coherent phonon dynamics and its effect on the superconducting parameters require intense laser pulses in the THz spectral region that trigger these collective excitations. Lattice-deformation created by nonlinear phononics is a suitable tool for initiating this dynamics. Moreover, it has been demonstrated theoretically that the energy relaxation provided by the strong electron–phonon coupling permits a fast enhancement of superconductivity that is reachable with pump–probe experiments initiated by the THz lattice distortions [70]. Thus, the path is open towards ultrafast THz-enhanced superconductivity.

Cuprates

In some high-temperature superconducting cuprates, a connection between one-dimensional modulations of charge and spin, and superconductivity exists [72–74]. At specific doping levels where these stripe orders appear, a significant reduction of the superconducting transition temperature, T_c, is observed. By applying intense 20 THz pulses to striped materials, superconducting-like signatures were first demonstrated in 2011 [75] at a temperature of 10 K, just above the T_c. The radiation was made resonant with Cu–O vibrations of $La_{1.675}Eu_{0.2}Sr_{0.125}CuO_4$ ($LESCO_{1/8}$), which perturbed the lattice structure that supported the stripe structure. Fig. 5a displays the measurement of the reflectance spectrum (normalized to the spectrum before the pump pulse) at a time delay of 5 ps after the pump pulse. The appearance of a plasma edge, the drop in reflectivity at $\sim$60 cm^{-1} (1.8 THz), is related to the formation of a Josephson plasma resonance along the c-axis. Fig. 5b shows that the temporal evolution of the imaginary conductivity σ_2 increases rapidly at low frequency. It has been suggested that these evidences may be consistent with a superconductive phase, however further experiments are needed to support this claim.

Recently, superconducting-like features were also demonstrated far above T_c for the bilayer cuprate $YBa_2Cu_3O_{6.5+x}$ [76,77]. In this case, the 20 THz pulses were tuned to the coherent excitation of apical oxygen distortions. By comparing parameters such as the THz reflectance and complex conductivity, strong similarities between the light-generated and the equilibrium (below-T_c) properties were found. For example, a photo-induced plasma-edge very close to the equilibrium Josephson plasma resonance and a photo-induced change in imaginary conductivity, $\sigma_2(\omega)$, was observed, which corresponded to that generated from a decrease of temperature below T_c. The Josephson resonance signature could

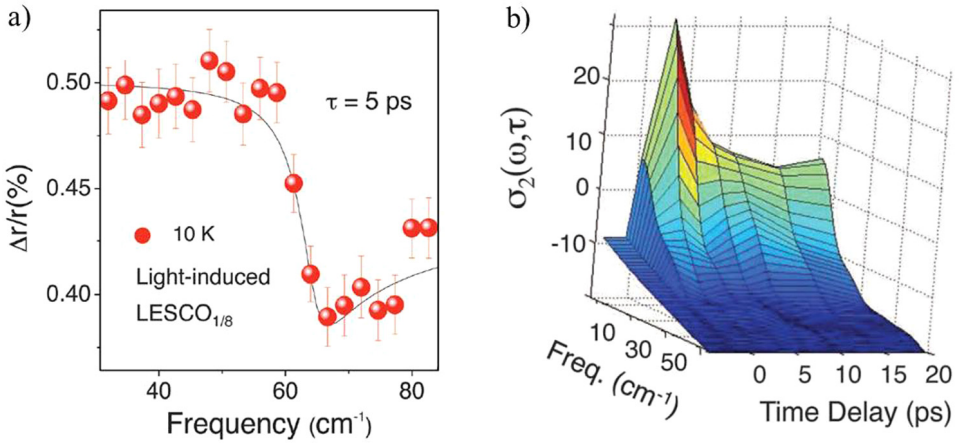

Fig. 5. (a) Transient reflectance of the stripe-ordered cuprate $LESCO_{1/8}$. The drop of reflectivity at $\sim$60 cm $^{-1}$ reveals the appearance of a Josephson plasma resonance in the c-axis THz optical properties upon 20 THz excitation. (b) Temporal evolution of the imaginary conductivity σ_2 as a function of frequency. A $1/\omega$ frequency dependence appears on a $<$2 ps timescale. Both these characteristics are also found in cuprate SCs.
Source: Adopted from Ref. [75].

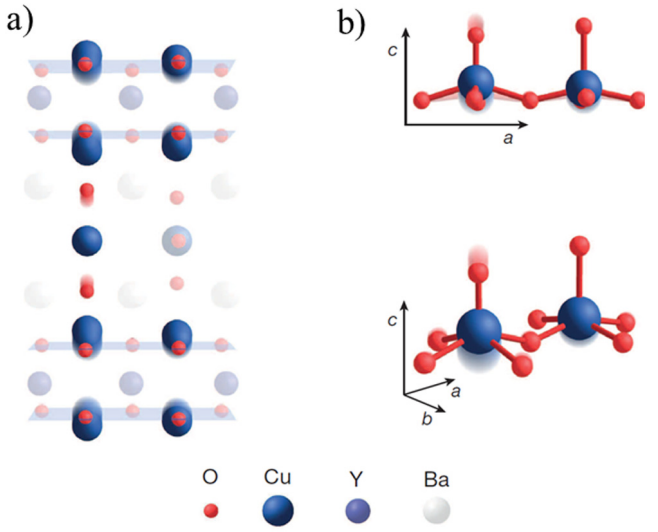

Fig. 6. Transient lattice structure of $YBa_2Cu_3O_{6.5}$ upon 20 THz excitation resonant with apical oxygen (oxygen between the bi-layers) distortions at above T_c. (a) shows the simultaneous increase and decrease of the intra-bilayer and inter-bilayer distances, respectively. (b) illustrates the increase in Cu–O buckling.
Source: Adopted from Ref. [9].

be detected at temperatures up to 300 K. Other signatures of superconductivity, besides the Josephsons plasma, have yet to be observed in the ultrafast regime, but they are being attempted. Using femtosecond X-ray diffraction, the behavior of the lattice structure was investigated for this exotic state. These studies revealed that the nonlinear excitation of the crystal lattice structure creates a displaced lattice geometry (Fig. 6) which cause drastic changes in the electronic structure that may favor superconductivity [9]. The destabilization of the charge-density wave order was also proposed to be a possible contributing factor.

It has been suggested that strong THz pulses are experimental probes for otherwise silent electronic order due to the power of nonlinear response of revealing silent symmetries (silent to the linear response). This is important for clarifying the role of various types of electronic order for unconventional superconductivity in the cuprates. The hypothesis that superfluid stripes exist in the superconductive phase is an example of such electronic order. This is not easy to validate experimentally because the stripe alignment causes interlayer superconducting tunneling to vanish on average, thus showing no signature in the linear optical response. However, with the high THz field accessible today, one can potentially observe such signatures in the nonlinear optical response in which the average assumes a non-zero value. In a recent work,

a giant Terahertz third harmonic, characteristic of nonlinear Josephson tunneling, was observed in $La_{1.885}Ba_{0.115}CuO_{6.5}$ [78]. This result underlines the power of nonlinear terahertz optics for further understanding of unconventional SCs.

Organic systems

The study of photo-induced superconductivity has also been extended to non-cuprate materials, where in contrast to cuprates, any enhancement of superconductivity is not related to melting of an ordered state. Experiments on the intercalated fullerene superconductor K_3C_{60} using 20–50 THz pulses with fields of 1.5 MV/cm [79] at a temperature up to 100 K, revealed a gapped real conductivity and a divergent imaginary conductivity appearing 1 ps after the excitation pulse. These studies were later complemented by investigations of the pressure dependence of these features [80]. It was suggested that the coherent excitation of the lattice may enhance superconductivity far above T_c and, thus, it may promote superconductivity in a more general way than previously assumed. In particular, specific nonlinear phonon modes excited in this study lead to stronger electron–phonon coupling that could favor superconductivity. A recent theoretical study [81] of nonequilibrium superconductivity in light-driven electron–phonon systems with lattice nonlinearities also reported significantly enhanced electron–phonon coupling. Another theoretical study [82] of the light-induced nonequilibrium state of phonons in strongly driven electron–phonon systems demonstrated signatures of superconductivity that appeared at higher temperatures compared with equilibrium.

An alternative mechanism leading to the detected optical response in alkali-fullerides A_3C_{60}, different from that based on phonon excitation as discussed above, has been proposed recently [83]. It is motivated by the observed overlap of the pumping frequencies that induce such a response, with the previously unexplained 100 meV wide mid-infrared absorption peak in alkali fullerides. In Ref. [83] this absorption peak is argued to represent triplet exciton creation. By exciting quasiparticles (*i.e.*, not Cooper-paired electrons) into these long-lived exciton states, the laser pulse cools down the quasiparticles system to a reduced effective temperature, which permits the superconducting-like optical response to exist above T_c.

Finally, we emphasize that the observed features induced by intense THz excitation in fullerenes and cuprates are not necessarily signatures of a superconducting phase. For example, it has been suggested [84] that the THz pulse may induce collective oscillations of entropy and electric charge that strongly couple with the probe radiation, leading to the same behavior of the reflectivity curves as the one observed experimentally in [79].

2.1.3. Ultrafast control of ferroelectric polarization

Ferroelectric materials exhibit permanent electric dipole moments that can be reversed by an electric field, thus allowing control of the electric polarization. The strong research interest in ferroelectrics is connected with their electromechanical and electro-optic applications in a broad range of devices such as transducers, actuators, motors, sensors, and non-volatile memories [85–91]. Manipulation of the ferroelectric polarization on a sub-nanosecond timescale has been demonstrated using short electric-field pulses [92]. However, higher switching speeds reaching the sub-picosecond temporal domain would have a tremendous impact on the development of, *e.g.*, non-volatile memory devices.

In order to enable sub-picosecond switching of the ferroelectric polarization, lattice excitation by short light pulses has been investigated. Such studies have been carried out using optical pulses that excite lattice vibrations via impulsive stimulated Raman scattering [36,40,93] or using strong THz fields that directly drive the lattice [40,94]. Although no direct evidence of polarization switching was reported from these experiments, Chen et al. [94] observed signs of large amplitude polarization rotation, while Dastrup et al. [40] demonstrated driving $LiNbO_3$ lattice vibrations into the anharmonic regime using THz fields on the order of 1 MV/cm, which is a promising step towards the goal of polarization switching.

In a theoretical study, Qi et al. [53] reported the possibility of controlled polarization switching by inducing large-amplitude coherent lattice vibrations in the $PbTiO_3$ using a series of temporally shaped THz fields. Ferroelectric polarization switching in perovskite materials is associated with the excitation of the so-called soft phonon mode shown in Fig. 7a, which was recently confirmed to be driven by single-cycle THz pulses in experiments on $SrTiO_3$ [95]. In the simulations by Qi et al. polarization reversal was achieved within 15 ps by driving these soft modes using seven half-cycle THz waves (blue dashed line in Fig. 7c) with a lobe of 150 fs, 3 MV/cm peak field strength and polarized in the z-direction. In order to suppress further polarization switching back to the original orientation, an out-of-phase wave was added that trapped the system in the desired polarization state. The polarization dynamics is shown as the green solid line in Fig. 7c. Moreover, Qi et al. further demonstrated that a more efficient polarization control could be accomplished with x-polarized pulses that allow passing through or near saddle points on the potential energy surface (see Fig. 7b). The polarization dynamics using four x-polarized pulses of 1 MV/cm peak field strength is shown in Fig. 7d.

The required polarization-switching field of the ferroelectric $PbZn_{0.4}Ti_{0.6}O_3$ thin film has been calculated to be 0.2 MV/cm [96]. The timescale for the polarization rotation is limited by the nucleation time, during which an oppositely polarized domain is formed that initiates the switching in the ferroelectric material. Minimum nucleation times are typically on the order of 0.1 ps [97] and for the $PbZn_{0.4}Ti_{0.6}O_3$ it was predicted to be 0.47 ps [96]. Using a single-cycle THz pulse with a peak field strength of 0.3 MV/cm and with a frequency between roughly 1 and 2 THz matching a range of phonon excitations, ultrafast polarization control was recently investigated in a $PbZn_{0.4}Ti_{0.6}O_3$ thin film [10]. The induced polarization change was probed by recording the second-harmonic-generation (SHG) signal of a time-delayed optical pulse sensitive to the polarization rotation. Fig. 8 shows the THz pump waveform (Fig. 8a) and the SHG signal induced in the $PbZn_{0.4}Ti_{0.6}O_3$ film (Fig. 8b), and in two centrosymmetric materials [Fig. 8b, $SrTiO_3$ (red) and Si (blue)] for reference, which display a two-orders-of-magnitude lower response. The strong modulation of the SHG signal is interpreted as

Please cite this article as: P. Salén, M. Basini, S. Bonetti et al., Matter manipulation with extreme terahertz light: Progress in the enabling THz technology, Physics Reports (2019), https://doi.org/10.1016/j.physrep.2019.09.002.

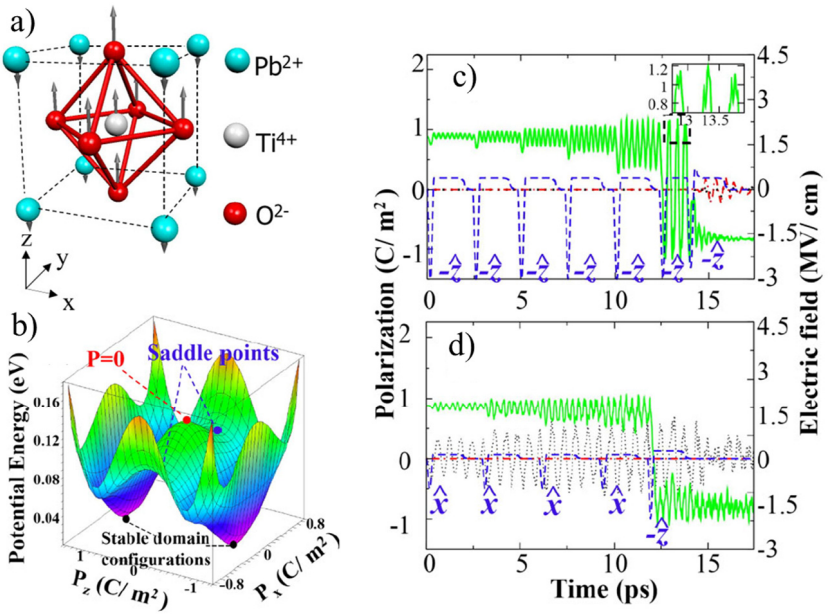

Fig. 7. (a) The soft phonon mode of $PbTiO_3$, indicated by the arrows, is driven by several half-cycle THz fields between two stable polarization configurations (b). The polarization reversal can be obtained either by a sequence of *z*-polarized or *x*-polarized THz pulses (blue dashed lines in (c) and (d), respectively). The green line is the *z*-polarization.
Source: Adopted from Ref. [53].

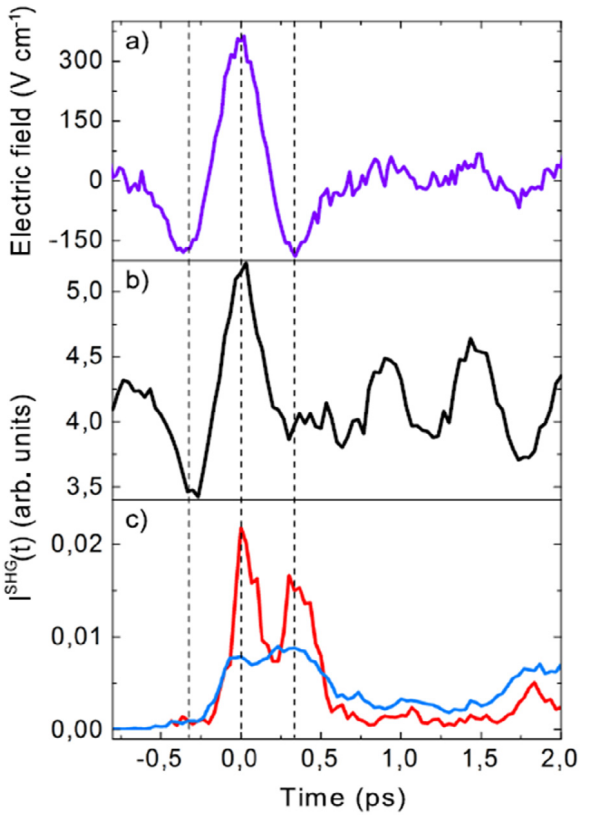

Fig. 8. (a) Time-trace of the electric field of the single-cycle THz pump pulse. The transient SHG signal reflecting a THz-induced polarization change in a $PbZn_{0.4}Ti_{0.6}O_3$ thin film (b) and in $SrTiO_3$ (red line) and Si (blue line) (c).
Source: Adopted from Ref. [10].

switching of the out-of-plane polarization into the plane, in parts of the film. The observed switching occurred on a similar (sub-picosecond) timescale and field as predicted by theory [96].

In the above examples, ferroelectric polarization switching was obtained using strong THz fields that directly drive the crystal vibrations. An alternative route towards ferroelectric polarization switching is provided by the excitation of higher frequency modes that activate the low-frequency modes via anharmonic coupling as described in Section 2.1.1. This method was proposed by A. Subedi in 2015 [54], who suggested that this could be a general technique for ultrafast switching of the polarization in perovskite transition-metal oxide ferroelectrics. Later, this approach was applied to $LiNbO_3$, where ultrafast transient polarization reversal was demonstrated using ∼20 THz pulses [55]. Insufficient fluence (95 mJ/cm) was explained as a likely cause of the partial, 40%, polarization change. Moreover, the polarization was only maintained during ∼200 fs before returning to the initial state. A possible remedy discussed in the paper [55] was the use of additional pulses that excite supplementary modes in order to provide further relaxation channels that could lead to stabilization of the polarization state.

2.2. Charge-carrier dynamics

Charge-carrier dynamics is central to high-speed electronics, optoelectronics, and fundamental solid-state physics. Using intense single-cycle THz pulses, it is possible to drive nonlinear responses of materials, and to study them with sub-picosecond temporal resolution, which allows for a deeper understanding of charge-carrier dynamics and enables new technological solutions. In particular, by obtaining control of the charge carriers via the strong electric field of the THz pulse, the conductivity and optical properties of materials can be manipulated. Semiconductors have been immensely important for the development of electronics and optoelectronics and significant further progress is expected by nonlinear THz studies. More recently, the field of Mottronics, which exploits electronic phase transitions in a class of correlated-electron materials called Mott insulators, has emerged as a promising path towards faster and more efficient electronics. Furthermore, various two-dimensional (2D) structures, in particular graphene, which displays exotic electronic properties, has been increasingly used in research on THz applications. In this section these types of materials will be discussed with respect to the control of charge-carrier dynamics induced by strong THz fields.

2.2.1. Semiconductors

Low-dimensional structures

One strong reason for the usefulness of semiconductors is that specific resonances between energy levels can be designed, thanks to the ability to engineer semiconductor quantum wells, wires and dots, where the particles are confined to two, one or zero dimensions, respectively. In these structures, energy-level splittings are often in the THz range. The high degree of control over the energy levels, by structure design or external stimuli, make such semiconductor nanostructures suitable for experiments that can lead to advanced applications of quantum optics, coherent control and high-field physics. We start by briefly discussing a few examples of how the special characteristics inherent to semiconductor confinement in different dimensions are exploited in research aiming for control of charge carriers and their dynamics using strong THz fields.

Quantum confinement of semiconductors permits highly tunable control of its optical properties by light, which is attractive for optoelectronic applications. The quantum dot represents the ultimate confinement in zero dimensions. Tunability can be achieved by the Stark shift created with a strong electric field that modulates the energy levels of the quantum dot's electrons and holes. For example, instantaneous control of the optical absorption in semiconductor quantum dots has been achieved with THz peak-fields of 220 kV/cm [98]. More recently the field dependent frequency shift of exciton luminescence was demonstrated by a significant modulation of the semiconductor quantum-dot band-gap, induced by a THz single-cycle wave of MV/cm-scale peak field [99], (Fig. 9a). Pein et al. also found indications of charge-carrier transport between quantum dots. A field driven transfer of valence band electrons to the conduction band of a neighboring quantum dot was observed as illustrated in Fig. 9b, thus enabling the generation of bound electron–hole pairs (excitons) even in the absence of an external charge source.

Semiconducting carbon nanotubes present exciting opportunities for fundamental physics studies and for applications in THz devices as they can be used to generate, modulate, polarize and detect THz radiation [100]. The one-dimensional structure creates a strong Coulomb interaction between electrons. In single-walled carbon nanotubes (SWNT) this interaction leads to a large exciton binding energy of hundreds of meV, which makes SWNTs stable at room temperature. Consequently, they are suitable for investigating, *e.g.*, the nonlinear THz response associated with exciton ionization dynamics [101].

Engineered semiconductor quantum wells can be utilized for the construction of THz and far-infrared optoelectronic devices such as detectors [102] and lasers [103] based on intersubband transitions (transitions between states created by the confinement of the quantum wells). Using single-cycle THz pulses with a peak field of 20 kV/cm, efficient electron transfer between subbands has been demonstrated [104]. Such controlled preparation of a system in a specific state is essential in quantum optics and can be exploited for *e.g.*, THz amplification or Q-switching. The 2D-confinement of electrons and holes also enhances the Coulomb interaction and the formation of excitons. Thus, semiconductor quantum wells, and lower-dimensional structures, are often used in dynamical studies of exciton systems, which is described next.

Please cite this article as: P. Salén, M. Basini, S. Bonetti et al., Matter manipulation with extreme terahertz light: Progress in the enabling THz technology, Physics Reports (2019), https://doi.org/10.1016/j.physrep.2019.09.002.

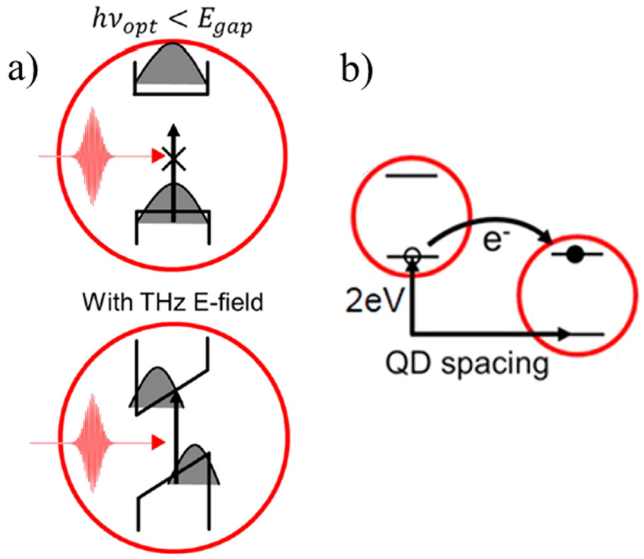

Fig. 9. (a) Illustration of band-gap reduction in a semiconductor quantum dot by a THz pulse, which permits the absorption of an optical photon. (b) shows the THz-field induced voltage drop between the quantum dots that can lead to electron transfer from the valence band to the conduction band of a neighboring quantum dot and thus exciton formation.
Source: Adopted from Ref. [99].

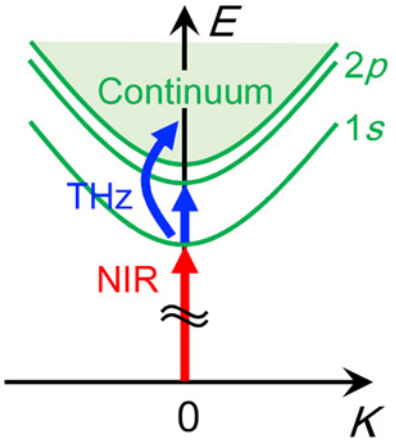

Fig. 10. Schematic of exciton energy levels and associated excitations. The red arrow represents exciton formation by IR excitation, the blue straight and curved arrows illustrate resonant excitation between exciton levels and field ionization to the continuum, respectively.
Source: Adopted from Ref. [113].

Excitons

Many THz studies of charge-carrier processes in semiconductors involve the exciton [6,99,101,105–113]. Excitons can be formed by optical excitation of an electron from the highest filled valence band to the empty conduction band, separated by a band-gap of approximately 1 eV. The Coulomb attraction between the created excited electron and the depleted state, the hole, may result in a bound hydrogen-like state. These excitons have an energy structure similar to the hydrogen atom, although the binding energy is scaled down by a factor of 1000 and lies in the THz spectral range, see Fig. 10. Hence, similar interactions with intense light pulses as for the atom, and their effects, can be explored.

High-order-sideband generation (HSG) has been observed from recollisions between exciton electrons and holes [109]. The mechanism is similar to high-order harmonic generation in which an intense field removes an electron from the atom or molecule and induces large-amplitude oscillations where the repeated collisions with the charged core result in emission of high-harmonic radiation. The highest-order harmonic is determined by the maximum energy gained by the electron, $E_{\max} \approx I_P + 3.2U_P$, where I_P is the ionization potential and $U_P = e^2F^2/16\pi^2 m_e f^2$ is the ponderomotive energy. The latter is the average classical kinetic quiver energy of the electron (mass m_e, elementary charge e) induced by the electric field with field strength F and frequency f. Thus, by using low frequency (THz) fields to drive the excitons and

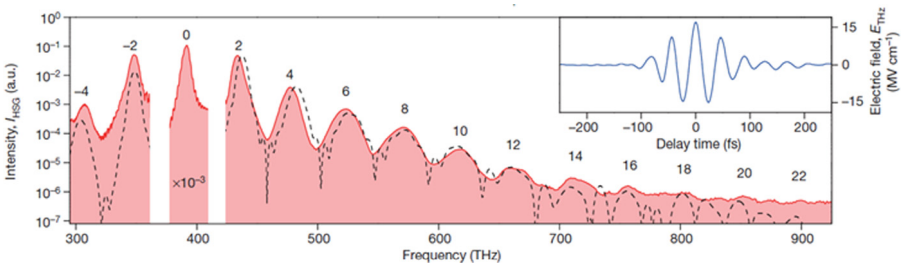

Fig. 11. Measured intensity spectrum (red) of high-order sidebands from WSe_2 driven by a phase-locked THz transient featuring a center frequency of 23 THz and an external peak field strength of $E_{THz} = 17$ MVcm^{-1} (see inset) under resonant optical excitation at a frequency of 392 THz (labeled by 0, 0th order has been multiplied by a factor of 10^{-3}; other numerals denote the order of sidebands). The black dashed curve shows the calculated intensity spectrum in arbitrary units.
Source: Adopted from Ref. [6].

cause recollisions between optically excited electron–hole pairs, it was predicted that HSG could be achieved at much lower field strengths (kV/cm to MV/cm) compared with the corresponding high-order harmonic generation in atoms and molecules [114,115]. This was experimentally confirmed by observing sidebands of a near-infrared laser, which was used to create the excitons that were driven by the THz field, up to the eighteenth order [109]. It shows that recollisions in excitons can be studied at intensities well below the damage threshold of the semiconductor while using quasi-continuous wave sources. HSG may provide a new nonlinear spectroscopy tool for investigating the structure of optical excitations in condensed matter. Furthermore, the new mechanism for ultrafast wavelength conversion has potential applications in terabit-rate optical communications. More recently, HSG has been generated with fields in the 10–100 MV/cm region and with driving frequencies in the 20–30 THz range [6,116]. Radiation that covers the full THz-to-visible spectral range was produced (Fig. 11), which promises a new route towards creating sub-femtosecond light pulses.

Strong THz fields have been employed to demonstrate many other phenomena in exciton systems. THz fields on the 10 kV/cm scale have been shown to shift excitonic absorption resonances by the Stark effect [117], or by the dynamical Franz–Keldysh effect [105,112], which modifies the spectrum through induced motions of the electrons and holes. Moreover, CEP-stable THz pulses have been employed to create sub-cycle modulations in optical absorption [111]. Fields in the 10 kV/cm range are also sufficient to ionize excitons and THz-pump optical-probe experiments using single-cycle THz pulses at such field strengths have demonstrated the exciton-ionization features in the optical spectra [108]. Recently the THz-induced motion of the exciton associated with its internal transitions and tunnel ionization were revealed by observing the time-resolved emission from the perturbed interband polarization [113]. At THz peak fields in the MV/cm range exciton generation through Zener tunneling (ZT) and impact ionization (IMI) can be studied [107], which is discussed more in the next section.

Carrier multiplication

The understanding of photo-induced carrier concentrations in semiconductors, and their dynamics, is essential for technological advances such as the design of new solar cells [118,119], photon detectors [120] and electroluminescent emitters [121,122]. The strong fields exceeding 1 MV/cm available with present THz light sources open new research possibilities in this area. A key process in this context is the generation of multiple electron–hole pairs, so-called carrier multiplication (CM) [123], which has been addressed in several studies using such intense THz pulses. Strong electric fields have been suggested to drive CM by two main nonlinear mechanisms mentioned earlier, ZT and IMI. In ZT, the energy band levels are shifted on atomic length scales by the field, which enables interband tunneling from a valence band to an energetically degenerate conduction band on a next-neighboring unit cell [124], similarly as illustrated in Fig. 9b. IMI entails promotion of valence band electrons to the conduction band by collisions with energetic electrons. Such energetic electrons may be obtained by acceleration in strong THz fields. While ZT and IMI are examples of interband scattering processes, there may be additional contributions to the conductivity changes from intraband processes that do not influence the carrier concentration. One prominent example is intervalley scattering (IVS) [125,126], in which the scattering of conduction band electrons into side valleys in k-space, where the carrier mobility is different, influences the conductivity.

Field-induced nonlinear behavior in semiconductors is often studied using metamaterials that enhance the incoming THz field. The nonlinear response of GaAs in the 0.2–1.6 THz range was demonstrated by Fan et al. [4] using split ring resonators (SRRs), see Fig. 12d inset. Moreover, Fan et al. observed IVS in n-doped GaAs for the weaker incident fields below 160 kV/cm, while at higher incident fields, corresponding to approximately 0.64–1.6 MV/cm in the SRR-gap, an increased conductivity was observed and interpreted as carrier generation by IMI. Fig. 12 shows the drop in transmission (a) with increasing fields, associated with the drop in mobility (c), caused by IVS. The increasing transmission and conductivity with field strengths at higher incident fields, associated with IMI, is demonstrated in Fig. 12b and d. Measurements were also performed on semi-insulating GaAs, which has a significantly lower carrier concentration, that suppresses intraband processes and makes IMI more difficult. Also, an increased conductivity was observed at

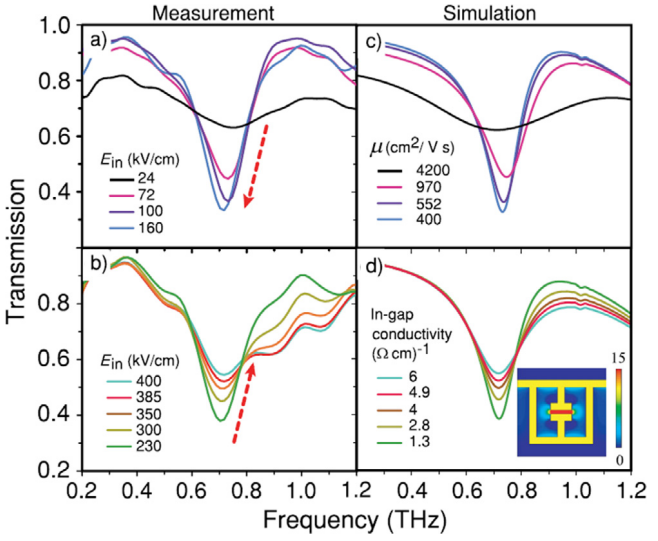

Fig. 12. (a) and (b) Experimental electric field transmission as a function of frequency for various incident peak electric fields. (c) Simulated transmission of the SRR array on doped GaAs film for different electron mobilities at a constant carrier density of 1×10^{16} cm^3. In these simulations the mobility of the carriers throughout the film is changed. μ is the electron mobility. (d) Simulated transmission on doped GaAs for various in-gap conductivities. In these simulations the mobility is constant and the carrier density is modified according to IMI simulations. The inset in (d) shows the simulated on-resonance field enhancement, highlighting that the largest enhancement occurs within the SRR gaps.
Source: Adopted from Ref. [4].

incident fields above 160 kV/cm, which was attributed to IMI. At the maximum in-gap field of 2.8 MV/cm an increase in carrier concentration by ten orders of magnitude was demonstrated. Although IMI was considered the main contribution, calculations suggested that the increase in carrier concentration by ZT is only one order of magnitude lower and may also play a role. Similar experimental studies on undoped GaAs have proposed both IMI [127] and ZT [5] as the dominant mechanism using maximum THz fields exceeding 10 MV/cm. However, measurements carried out with sub-1 MV/cm THz fields [25] ruled out ZT as a contributing factor due to the small amount of electron–hole pairs created by such low fields.

In addition to studies of charge-carrier dynamics using metamaterials to obtain strong E-fields, recent experiments [8] have been carried out using THz single-cycle waves with 25 MV/cm peak field produced by optical rectification in Diethylaminosulfur trifluoride (DAST) [128–130]. These studies explored the highly nonlinear optical responses appearing above 10 MV/cm fields in the electro-optic crystal GaP. Spectral broadening reaching 500% of a 50 fs near infrared pulse, as well as optical transmission change and conductivity increase caused by ZT and IMI were observed. This experimental scheme offers the advantage compared with investigations using THz metamaterials, which are characterized by a resonant temporal response, that it more directly measures the optical and electronic dynamics.

Access to short, intense THz pulses have provided new ways to address IMI dynamics in a larger range of initial carrier concentrations and with electric fields in the MV/cm region. Previous investigations have been limited to sub-MV/cm field strengths and high initial carrier concentrations to avoid excessive heating of the sample and electron avalanches that may damage the sample [131]. Using single-cycle THz pulses the heating effects can be reduced while permitting a high field and thus low initial carrier concentrations. In a recent pump–probe experiment, a 400-nm pre-pump induced a controlled initial carrier concentration in silicon and an 800-nm probe pulse monitored the IMI dynamics initiated by the single-cycle THz pump pulse. The THz wave was enhanced by antennas to a maximum peak field of 3.6 MV/cm [132]. It showed that a single electron can generate over 10^8 electrons by CM processes.

In order to further develop THz electronics it is crucial to understand the frequency dependence of the semiconductor response to an electric field [133]. In this respect it is important to determine the critical electric field at which CM leads to a strongly enhanced conductivity [134] as a function of THz frequency. Such an investigation was recently performed on semi-insulating GaAs [135] and revealed an increase in the critical field from 0.4 to 2.3 MV/cm by increasing the frequency from 0.7 to 1.5 THz.

2.2.2. Mott insulators

An alternative path towards controlling the conductivity, different from the direct manipulation of charge in semiconductors, is provided by correlated-electron materials. In these systems the interaction between electrons is non-negligible and may severely influence the character of the material. This makes them sensitive to phase transitions triggered by external stimuli, such as light, pressure, temperature, mechanical strain, electric or magnetic fields [136–138].

Mott insulators are a special class of correlated-electron materials that can be exploited for efficient switching between the insulating and conducting phase. It has the conventional band structure of a conductor when electron correlations

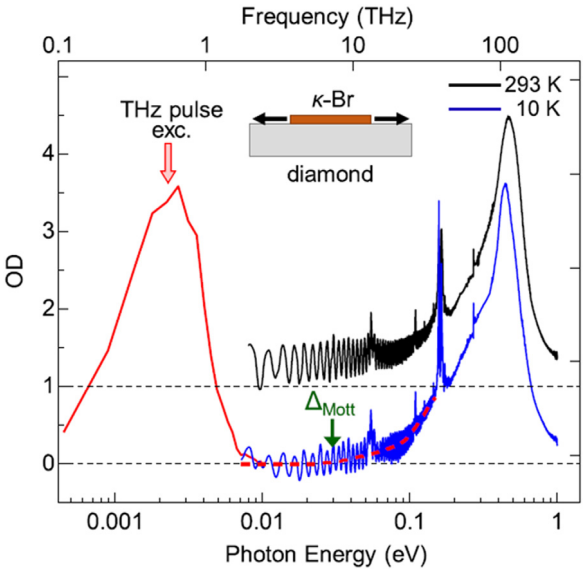

Fig. 13. Optical density (*OD*) spectrum of a thin κ-Br crystal on a diamond substrate at 10 K (blue solid line) and 293 K (black solid line). The red line shows the Fourier power spectrum of the electric-field waveform of the THz pulse used for excitation in the THz-induced experiments. The complete transparency to the THz pulse makes the material a suitable choice for electric-field-induced carrier generation by ZT. The inset shows a schematic of κ-Br on a diamond substrate.
Source: Adopted from Ref. [144].

are neglected, but the strong Coulomb repulsion between electrons impedes their flow by fixing them to one crystal site, which opens up an insulating gap, the Mott gap. Transitions between the insulating and conducting phase in these systems, Mott transitions, are dominantly driven by electron-correlation effects, as opposed to, *e.g.*, large energy-dissipative structural changes. Such transitions are central in the new field of Mottronics that promises the development of new so-called Mott transistors where the ON/OFF switching is based on Mott transitions [139]. This opens the door to higher switching speeds and downsized electronic devices compared with existing semiconductor based electronics [140,141].

Mott transitions have been intensely studied in correlated-electron systems based on organic compounds [142–144] and transition-metal oxides [139,145–152]. Mott transitions in organic correlated-electron systems driven by strong THz fields were highlighted in a recent review by Miyamoto et al. [144]. We will give a brief summary of their work in the next section and then we will focus on the extensively studied but heavily debated transition-metal oxide VO_2.

Organic Mott insulators

Organic molecular compounds display rich physics caused by electron correlations and has been used as a playground for many-body physics. Miyamoto et al. [144] discussed the THz-induced Mott transition studies performed on the organic molecular compound κ-type ET-salt, κ-$(ET)_2X$. When this crystal is placed on a diamond substrate and cooled down to 10 K it becomes a Mott insulator, which has been verified by THz optical density (*OD*) measurements. The *OD*-spectra display $OD = 0$ below 30 meV at 10 K (blue line in Fig. 13) while it is positive at 293 K (black line in Fig. 13), revealing that a Mott gap of 30 meV is open at 10 K. The Mott transition depends on the temperature decrease and the strain created by the diamond substrate on the κ-$(ET)_2X$ crystal with decreasing temperature. By preparing the κ-$(ET)_2X$ crystal on diamond in the insulating state at 10 K, Miyamoto et al. showed that the THz-induced absorption changes ΔOD_{THz} using 180 kV/cm peak THz-fields corresponded to the differential absorption spectrum between the metal phase and the Mott insulator phase in the 0.1–0.8 eV spectral region. This demonstrated that a Mott transition can be induced by the THz field. The mechanism for the transition was suggested to be field-induced quantum tunneling from the lower to the higher Hubbard bands, which are separated by the Mott gap, *i.e.*, a similar process to the ZT observed in band insulators. This creates holon and doublon pairs, which means that the electrons go from being distributed on one site each to populating sites with zero (holons) or two (doublons) electrons. Hence, localized electrons become mobile and the material becomes metallic.

Time-resolved THz studies were performed in order to explore the dynamical aspects of charge-carrier generation in the THz-induced Mott transition. The measured dynamics, which is shown in Fig. 14 together with the profile of the THz pulse, revealed a slower rise time of the induced absorption change $\Delta OD_{THz}(t)$ for lower compared with higher THz excitation fields. The absorption change is an indication of increased metallization. Hence, it was interpreted as a manifestation of the delay in the collapse of the Mott band-gap, *i.e.*, when the produced amount of carriers is enough to melt the electron localization, for the lower fields. The characteristic time for the band-gap collapse obtained from

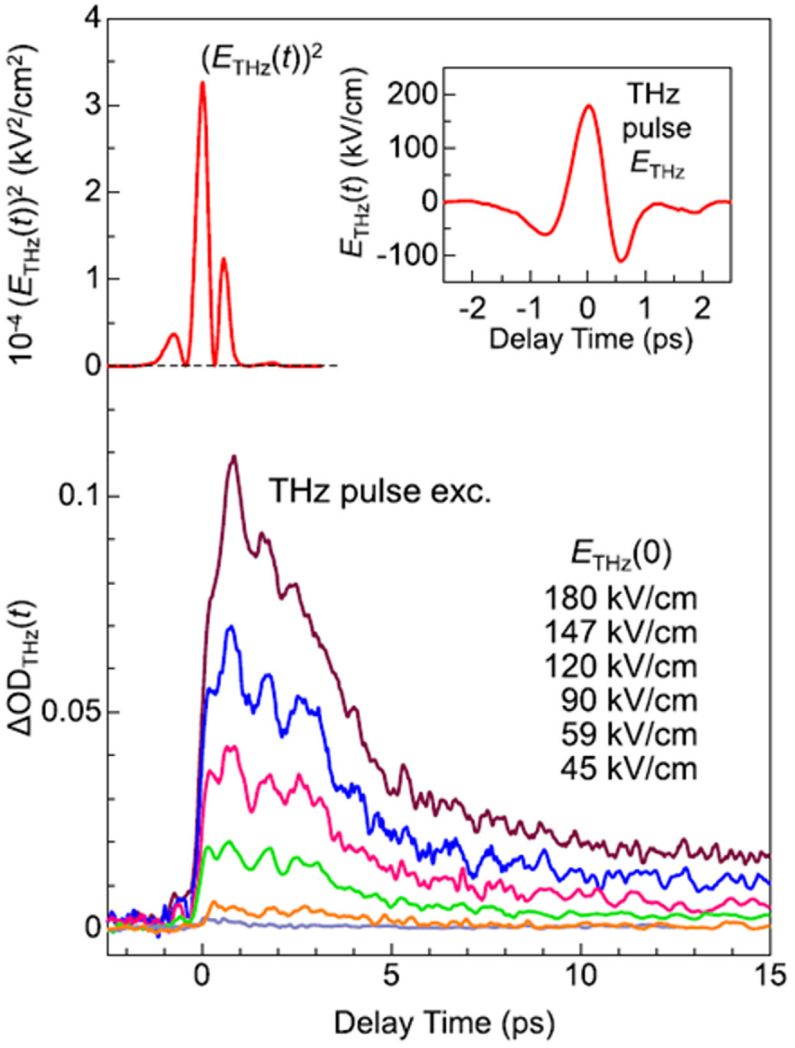

Fig. 14. Time-evolution (bottom) of the absorption change $\Delta OD_{THz}(t)$ measured at 0.124 eV induced by a THz pulse with the profile shown at the top of the figure. The dynamics reveals a fast initial rise, which can be interpreted as increased metallization. The rise time is slower for weaker peak fields of the THz pulse, indicative of a delay in the collapse of the Mott band-gap. At longer timescales the $\Delta OD_{THz}(t)$ signals decrease with a fast decay up to 5 ps and slower decay up to 100 ps.
Source: Adopted from Ref. [144].

the low-field (45 kV/cm) data was 0.13 ps. The time-resolved measurements also revealed an oscillatory structure in the $\Delta OD_{THz}(t)$ signal that was attributed to coherent molecular motions. Hence, electron-lattice interactions cannot be neglected in κ-type ET compounds.

Vanadium dioxide — VO_2

Correlated-oxides have been extensively studied with the aim of understanding the insulator–metal-transition (IMT) mechanism in these materials [146]. VO_2 is a prototypical system for correlated-electron IMT which was the first to be investigated using a THz field to trigger the phase transition [148]. It has the unique property that the insulator–metal phase transition occurs close to room temperature (340 K) and is interesting from a technological perspective, because it displays a five-orders-of-magnitude conductivity-jump (in single-crystals) between the two phases [146] and can be tuned via epitaxial strain (in thin films) [153]. However, the exact mechanism for the IMT in VO_2 is under debate. It is understood that the phase transition involves both electron–electron and electron-lattice interactions but the question is which drives the other. Experiments using strong single-cycle THz fields up to 3.3 MV/cm have shown that the IMT is associated with acceleration of electrons by the field that heats the lattice through electron-lattice interactions and thus increases the temperature above the critical temperature for the IMT to occur [148]. Using higher fields from multi-cycle THz pulses reaching 15 MV/cm and centered at approximately 20 THz, Mayer et al. demonstrated that carriers were

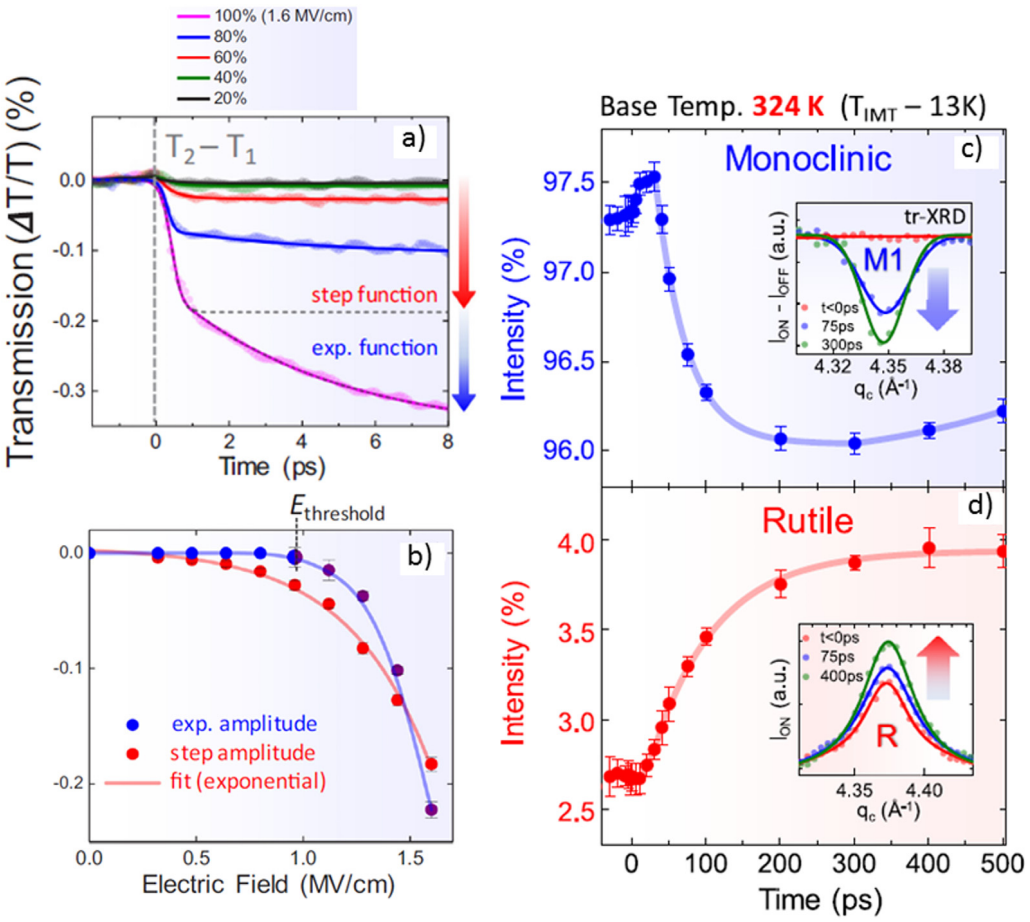

Fig. 15. (a) Electronic dynamics in a VO_2 thin film undergoing an IMT induced by an ultrafast THz pulse with different field strengths. It shows the difference between the transmission spectra recorded 13 and 37 degrees below T_{IMT}, thus highlighting the processes triggered by electron tunneling, which are most efficient at temperatures closer to T_{IMT}. The step-like drop in transmission observed in (a) is attributed to electron tunneling, and the subsequent exponential decay is attributed to slower metallization dynamics. (b) demonstrates the distinct field-strength dependence of the electron-tunneling process (red) and the metallization dynamics (blue) by plotting the amplitude of their respective features. The latter reveals a threshold onset at 1 MV/cm associated with an absorbed energy density sufficient to initiate lattice dynamics. (c) and (d) show the structural dynamics of the VO_2 crystal film undergoing an IMT induced by the ultrafast THz electric-field pulse with 1 MV/cm peak electric field. The longterm structural changes begin at ∼30 ps.
Source: Adopted from Ref. [152].

generated by field-induced tunneling and that the IMT proceeded non-thermally [7]. Complementary studies with single-cycle THz waves at similar field strength would be beneficial in order to clarify any effects associated with the employed multi-cycle excitation.

Although there is still some controversy regarding the exact mechanism for the VO_2 IMT, there has been several, both theoretical and experimental studies, demonstrating that the metallic phase can be produced without large structural changes, *i.e.*, through a Mott transition [150–152]. For example, a recent theoretical study [150] considered the purely electronic component of the IMT in VO_2 by keeping the lattice fixed. Najera et al. were able to explain several experimental features within their model and to conclude that the Mott mechanism dominates the temperature driven IMT. Moreover, experimental attempts to separate the electronic and structural processes in the IMT of VO_2 has revealed that a purely electronic phase transition precedes the thermally driven IMT [149]. Furthermore, VO_2 thin films in heterostructures containing oxygen-deficient VO_2 layers were shown to exhibit isostructural IMT [154].

In particular, experiments using THz fields exceeding 1 MV/cm to trigger IMT have demonstrated that the electronic phase transition occurs simultaneously with the exciting THz pulse, induced by Zener-type electron tunneling, and are accompanied by a slower structural change [152]. Fig. 15a shows the initial electronic dynamics as the difference between the transmission spectra at the temperatures ($T_{IMT} - 13$) and ($T_{IMT} - 37$), where T_{IMT} is the phase-transition temperature. This highlights the processes triggered by electron tunneling since they are more efficient at temperatures closer to T_{IMT}. The electron tunneling process that initiates the IMT is assisted by Wannier–Stark-like band renormalization that is less temperature sensitive and the spectral subtraction removes this contribution. The rapid drop in transmission is a signature

of an ultrafast nonthermal field-induced tunneling and is followed by the slower metallization dynamics characterized by an exponential decay. The distinct field-dependence of the amplitudes shown in Fig. 15b demonstrates the different origin of the two processes. While the electron tunneling displays an exponential behavior starting at low field strengths, the exponential-decay amplitude shows a threshold behavior at 1 MV/cm. At this threshold a sufficiently efficient tunneling process is initiated that leads to band-gap collapse and increased temperature as the field-accelerated electrons collide with the lattice. The increased temperature then initiates the lattice transformation from the monoclinic to the rutile phase. The lattice dynamics associated with this transition is shown in Fig. 15c and d. The first ∼30 ps display a constant X-ray diffraction signal for the rutile peak, while the monoclinic peak increases, thus suggesting the temporary formation of a new monoclinic phase with a higher structure factor. After that, the expected simultaneous decay of the monoclinic phase and growth of the rutile phase is observed.

Further studies are needed that target in particular the initial few-picosecond structural dynamics. However, results in Ref. [152] show that intense THz pulses can drive IMT in VO_2 by efficient electron tunneling and that the electronic and structural dynamics can occur on different timescales. It opens the door to efficient conductivity switching in correlated-electron systems.

2.2.3. 2D materials

Emerging 2D materials ranging from insulators and semiconductors to semimetals have recently shown a strong potential in photonic technologies, particularly in the THz frequency range [155]. 2D materials arise from layered van der Waals (vdW) crystals, where atoms are strongly bonded within the single crystal plane and weakly interact (due to vdW forces) with those from the planes above and below. The weak vdW forces enable the extraction of single or a few layers of atoms and allow transferring these 2D layers to the top of bulk (3D) media (exfoliation). Moreover, the individual atomic layers of different crystal lattices can also be glued together ("lego concept") [156] opening up exciting opportunities for designing various physical properties of the resulting vertical heterostructures on demand. Additionally, 2D materials and their heterostructures possess high confinement of the electronic states out of plane. This superior confinement leads to unique quantum effects not accessible with their original 3D counterparts (such as photoluminescence [157], quantum Hall effect [158] or superconductivity [159], to mention a few). Most importantly, 2D materials support a variety of polaritons, electromagnetic fields coupled to oscillating dipole-carrying excitations, and, thus, can strongly interact with light in a wide range of the electromagnetic spectrum, including THz [160,161].

A well-known example of 2D materials, which has found a significant use for THz applications, is graphene, presenting a single atomic layer of graphite with a thickness of 0.34 nm (see Fig. 16a). Graphene is formed by a honeycomb lattice of carbon atoms in which electrons have a linear dispersion, and behave as massless Dirac fermions, obeying the relativistic Dirac equation [162]. Unlike metals, having abundance of free charges, graphene is a semimetal and allows controlling its carrier concentration via chemical doping, gating, or *THz radiation* [163–166]. The latter makes possible tuning of graphene's optical response on a picosecond timescale.

Graphene and 2D materials show a strong nonlinear response to an incident electromagnetic wave [167,168]. This response can be attributed to the nonlinear optical susceptibility, χ_{eff}, which is usually represented as a series in powers of the electric field with the coefficients $\chi_{\text{eff}}^{(n)}$. Importantly, for 2D materials with the centrosymmetry of their crystal lattice (such as graphene) in a symmetric dielectric surrounding (*e.g.*, for free-standing monolayers, see Fig. 16a) the even powers of the electric field ($n = 2, 4, \ldots$) do not appear in this series, so that related nonlinear effects are forbidden. In this case only the odd powers of the electric field ($n = 1, 3, \ldots$) play a role. Particularly, the dominating third-order susceptibility, $\chi_{\text{eff}}^{(3)}$, enables third-harmonic generation (THG), four-wave mixing (FWM), optical Kerr effect and saturable absorption. As an example, Fig. 17 shows the nonlinear transmittance of THz radiation as a function of THz fluence for different Fermi levels. As observed in earlier works [169,170], the THz-induced transparency occurs on a sub-picosecond timescale. It is explained by the formation of a nonequilibrium distribution of carriers that has an increased momentum scattering rate and a correspondingly decreased carrier mobility.

To realize even-order nonlinear effects in graphene, a centrosymmetry breaking is required. To this end, a graphene monolayer can be placed on a substrate [171] (see Fig. 16b). Alternatively, the symmetry can be broken by the edges of the 2D layers, by natural curvature fluctuations and by the application of static electric fields [172]. Any of the above symmetry-breaking realizations can enable the even-order nonlinear effects. The latter are typically dominated by the second-order susceptibility, $\chi_{\text{eff}}^{(2)}$, and thus include second harmonic generation (SHG), sum and difference frequency generation (SFG and DFG, respectively), optical rectification, and the Pockels effect. Importantly, in the DFG process one of the incoming signals can be amplified, potentially enabling realization of 2D optical parametric oscillators for producing broad THz wavelength-tunable coherent light sources.

Nonlinear effects in graphene, governed by the hot Dirac fermion dynamics, have attracted a considerable interest. Graphene in the nonlinear regime can enable novel compact and ultrathin THz technologies, allowing for active tuning via the applied voltage [174,175]. Among the most remarkable nonlinear phenomena demonstrated in graphene, we would like to mention: high-harmonic generation [176] (in particular, up to the seventh order at room temperature [177]), dynamic Hall effect [178], all-optical wide-band nonlinear modulator [179], second-order nonlinear photon-drag currents [180,181], DFG (generation of a broadband gate-tunable THz plasmonic signal from pump and probe signals in telecom range) [182] and SHG [183]. We would also like to highlight that the light intensity required for nonlinear THz effects in graphene can be reached by exploiting localized plasmon polaritons in doped graphene nanostructures [184,185].

Please cite this article as: P. Salén, M. Basini, S. Bonetti et al., Matter manipulation with extreme terahertz light: Progress in the enabling THz technology, Physics Reports (2019), https://doi.org/10.1016/j.physrep.2019.09.002.

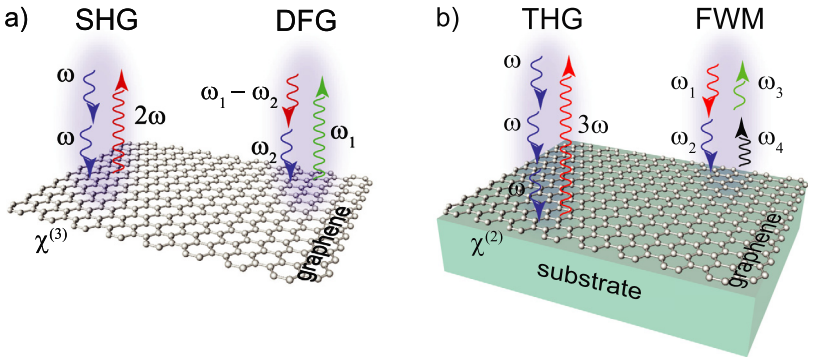

Fig. 16. Schematic illustration of nonlinear optical effects in graphene. (a) A sheet of free-standing graphene possesses centrosymmetry which prohibits even-order nonlinear effects. (b) The substrate breaks the 2D centrosymmetry of graphene so that even-order nonlinear effects become allowed.

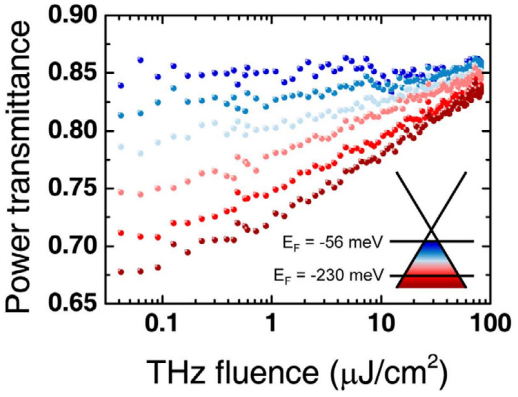

Fig. 17. Experimental measurements of the power transmittance of strong-field THz radiation vs. THz fluence for different Fermi levels of graphene. The fluence of 100 J/cm^2 corresponds to a peak electric field of around 300 kV/cm. The range of the variation of the Fermi energy and the corresponding color coding are depicted in the inset.
Source: Adopted from Ref. [173].

Moreover, since plasmons in graphene can provide strong and inhomogeneous (varying along graphene) electromagnetic fields, their excitation can enable contributions analogous to those due to the magnetic dipole and electric quadrupole effects in centrosymmetric atoms or molecules, allowing for the second order nonlinearities (impeded for graphene in a symmetric dielectric environment, as detailed above), according to the theory [186,187].

Nonlinear harmonic generation in graphene is worth an additional discussion in view of very large values of graphene's nonlinear susceptibility in the THz region [177,188]. For any material to demonstrate an appreciable nonlinear response, the driving field must be comparable to the intrinsic field of that material. For conventional 3D materials, the intrinsic field is usually determined by the energy of the chemical bond and typically on the order of V/Å (100 MV/cm). In contrast, for graphene in the THz region the characteristic field that determines the onset of nonlinear effects is given by $E_i = (h\omega/e)\sqrt{\pi n_c}$ and is on the order of 10 kV/cm [189]. Here, ω is the frequency of interest and n_c is the density of charge carriers. The physical origin of the strongly nonlinear response of graphene to the THz field is the nonlinear intraband THz conductivity of graphene electrons. Though efficient harmonic generation in graphene at THz frequencies was predicted more than a decade ago [189], the experimental demonstration was reported only recently [177]. Fig. 18 shows the generation of terahertz harmonics up to the seventh order in single-layer graphene under normal ambient conditions. The nonlinear susceptibility of graphene is shown to exceed that of typical solids by many orders of magnitude (*e.g.*, six orders of magnitude for $\chi^{(3)}_{\text{eff}}$). Hefez et al. explained such a strong nonlinear optical response by the collective thermal response of graphene's background Dirac electrons to the driving terahertz field.

Another set of interesting optical effects in the THz frequency range takes place under the application of a perpendicular static magnetic field to graphene. Due to the cyclotron resonance in the classical regime and the inter-Landau-level transitions in the quantum regime, graphene can show giant Faraday rotation (up to several degrees) [190] and the magnetic circular dichroism. Moreover, in graphene both the Faraday rotation and the magnetic circular dichroism can be modulated in intensity, tuned in frequency and, importantly, inverted by the electrostatic doping (at a fixed magnetic

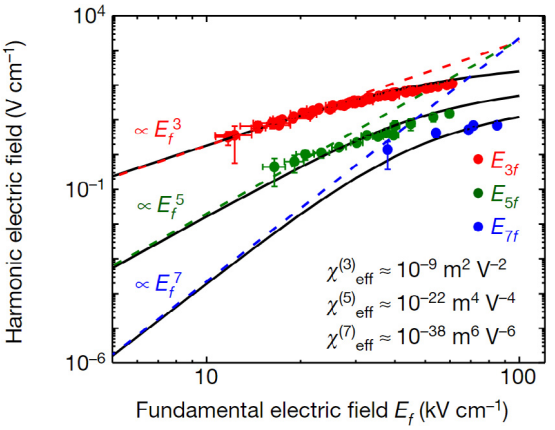

Fig. 18. The amplitude of high-order harmonics vs. the driving THz field strength. For the third (red), fifth (green) and seventh (blue) harmonics, the fundamental field frequency was 0.68 THz, 0.37 THz, and 0.3 THz, respectively. The dots stand for experimental data whereas the solid lines represented theoretical results. The dashes lines are low-field asymptotes in the form of power functions of corresponding odd orders.
Source: Adopted from Ref. [177].

field) [191]. In addition, in a patterned array of graphene (*e.g.*, arrays of disks or antidots), strong magneto-plasmonic resonances can emerge [191,192], potentially allowing one to exploit graphene for magneto-optical THz applications.

2.3. Spin dynamics

Intense THz pulses permit control of the spin dynamics, and thus the transient magnetic properties, of certain materials. Such control is crucial for the development of, e.g., magnetic storage and data processing devices. In this section, different interactions between intense THz pulses and various magnetically ordered materials are discussed, as well as their scientific applications.

2.3.1. THz interactions with magnetically ordered materials

The interaction between magnetically ordered materials and intense broadband THz pulses can involve different mechanisms, leading to net effects on the material that can result in complex spin dynamics. However, this complex dynamics can often be analyzed and modeled based on a few fundamental interactions, which in turn can be singled out by their symmetry or by their relative magnitude and relevance in different classes of materials. Those fundamental interactions can be broadly classified in three main types. First, the direct action of the THz magnetic field on the magnetic moments in the material. Second, the direct coupling of the THz electric field to the electronic or lattice structure, which in turn affects the spin order. Third, the indirect coupling of the electromagnetic radiation in the form of heat deposited in the material. We will look at them in some details in the following paragraphs.

The first fundamental interaction to be considered is the direct coupling between the spins in the samples and the magnetic field component of the broadband THz pulse. This interaction is described by the Landau–Lifshitz–Gilbert (LLG) equation [193,194]

$$\frac{d\mathbf{M}}{dt} = \gamma \mathbf{M} \times \mathbf{H}_{\text{eff}} - \frac{\alpha}{M_s} \mathbf{M} \times \frac{d\mathbf{M}}{dt}, \tag{7}$$

where γ is the gyromagnetic ratio, $\mathbf{M}$ is the magnetization of the sample with saturation magnetization M_s, $\mathbf{H}_{\text{eff}}$ is the effective magnetic field acting on the magnetization (including the magnetic component of the THz pulse), and α the dimensionless Gilbert damping parameter. This equation correctly describes both resonant as well as non-resonant dynamics in the THz range, provided the sample thickness is much smaller than the wavelength of the THz radiation. Otherwise, one has to solve Eq. (7) together with the Maxwell equations to account for the propagation of the radiation in the material. The former is typically the case of antiferromagnets, and the LLG describes the motion of the net magnetization $\mathbf{M} = \mathbf{S}_1 + \mathbf{S}_2$ emerging due to the canting of neighboring spins $\mathbf{S}_1$ and $\mathbf{S}_2$ during precession. The latter is commonly observed in ferromagnets, whose magnetic resonances are in the gigahertz range. We will discuss some of these cases in detail below. In the case of resonant dynamics at THz frequencies, collective spin excitations may also couple with the light, forming hybrid polariton modes. In this case, the phenomenon requires a more complex description [195], beyond the scope of this review.

The second mechanism with which THz radiation can interact with magnetically ordered samples is the coupling of the spins to the electric field of the radiation, via indirect interaction with an excitation which is electric-dipole active. The details of this indirect interaction can be quite complex and include several different effects, but the basic

idea is that the THz electric fields affect either the electronic or the lattice structures, coupled to the magnetic order. A notable case is the one of multiferroics, *i.e.*, materials where both ferroelectric and magnetic orders coexist, and where so-called "electromagnons", *i.e.*, spin excitations that are electric-dipole active, can be found. In all these different cases, the requirement for the electric field to be of importance is the sample being an insulator. In the case of a conductor, the electric field is efficiently screened at the surface of the sample, hence it has no importance for the spin dynamics. This is strictly correct for typical electric field magnitudes achievable on table-top sources ($\sim$100 MV/m), which are still small perturbations compared to the typical interatomic fields ($\sim$1 V/Å or 10 GV/m). When THz electric field strengths comparable to the interatomic fields are generated at linear accelerators, changes to the magnetic anisotropy can be observed even in metallic samples [196].

While the two mechanisms just described are proportional to the magnetic or electric fields magnitude, the third and last type of interaction discussed here is proportional to the square of the magnetic field, *i.e.*, to the intensity of the radiation deposited in the material. This interaction is particularly prominent in metallic samples, even at moderate THz field strengths. As stated in the previous paragraph, the electric field is effectively screened at the surface of a conductor, within one atomic layer and on a timescales of femtoseconds, dictated by the Fermi velocities ($\sim$ 1 nm/fs) [197]. The magnetic field, however, penetrates the material up to a distance given by the skin depth $\delta = \sqrt{2\rho/\mu_0\omega}$, where ρ is the resistivity of the material.[1] In a typical conductor, the skin depth is on the order of 100 nm–1 μm at 1 THz. We assumed here $\mu_r = 1$, which in the THz range is a realistic estimate, even for magnetic materials. For thin film samples, this is equivalent to a transient, but constant in magnitude magnetic field present in the material. The effect of such a transient magnetic field is to generate screening eddy currents. These currents can reach densities of 10^{10}–10^{11} A/m^2 in thin films, and in magnetic materials they are necessarily spin-polarized. As we will discuss below, the generation of such large spin-polarized currents can affect magnetic order as well.

2.3.2. Resonant coherent spin control with magnetic fields

One of the very first experiments combining intense THz radiation and magnetism was the study of the 1 THz magnon in NiO [15]. This material is a natural occurring antiferromagnet with a Néel temperature of approximately 500 K, where the superexchange interaction promotes antiparallel alignment of the Ni spins along different crystal planes. In Ref. [15], a single-cycle THz field with amplitude of 0.3 MV/cm (0.1 T) was sent through a 45 μm thick NiO single crystal and the spin dynamics was probed with the time-resolved Faraday effect at near-infrared wavelengths. The measured dynamics is shown in Fig. 19, with the temporal curves of the pump field and the Faraday rotation of the polarization in the main plot, and the corresponding frequency spectra in the inset. The energy of the spin system can be modeled with the Hamiltonian

$$\mathcal{H} = -J\mathbf{S}_1 \cdot \mathbf{S}_2 + \mathbf{D} \cdot \left(\mathbf{S}_1^2 + \mathbf{S}_2^2\right) + \gamma \mathbf{H}_{\mathrm{THz}}(t) \cdot (\mathbf{S}_1 + \mathbf{S}_2), \tag{8}$$

where $J < 0$ is the exchange constant, $\mathbf{D}$ includes the magnitude and the direction of the magnetic anisotropy with respect to the lattice structure, and $\mathbf{H}_{\mathrm{THz}}(t)$ is the time-varying THz magnetic field. The first term of Eq. (8) describes the exchange interaction between nearest-neighboring spins; the second term is proportional to the strength and direction of the spin–orbit coupling; finally, the last term measures the strength of the Zeeman interaction.

This Hamiltonian allows one to compute the effective field as $\mathbf{H}_{\mathrm{eff}} = -\delta\mathcal{H}/\delta\mathbf{M}$, which is then used to calculate the magnetization dynamics with Eq. (7). The last term of Eq. (8) suggests that coherent control of the spin-order is possible with THz magnetic fields, where amplification or suppression of the spin excitation is realized depending on the relative phase of the THz magnetic field, as directly demonstrated in Ref. [15]. Another signature of the magnetic nature of the excitation was recently found measuring the frequency dependence of the resonance on magnetic fields up to 10 T, driven with multi-cycle intense THz fields [198,199].

By increasing the THz magnetic field amplitude, the second harmonic of the frequency of the 1-THz magnon was also observed [200]. This effect arises from quadratic, rather than linear, coupling of the spin precession to the magneto-optic probe (*i.e.*, magnetic linear birefringence rather than Faraday effect).

Similar coherent magnetization dynamics occurs in the ferrimagnetic orthoferrite $DyFeO_3$, where both ferromagnetic-like and antiferromagnetic-like excitations at around 0.5 THz have been observed [201]. The same types of excitations are present also in ferrimagnetic $YFeO_3$, where two-dimensional magnetic resonance spectroscopy has recently been implemented [202], and high-order magnon modes clearly detected.

Very recently, control of the antiferromagnetic vector using THz pulses has been demonstrated also in CuMnAs thin films [203]. While obtaining time-resolved data in thin antiferromagnetic films is still challenging, there is clearly an opportunity for intense THz fields to realize ultrafast control of magnetic state in antiferromagnets [204,205].

2.3.3. Resonant coherent spin control with electric fields

Coherent control of the spin order is also possible using the electric field component of THz radiation. This has been achieved in three ways: (a) via the control of the electronic band structure, by modulation of the exchange and spin–orbit

[1] See Jackson, chapter 8 [197]. Some unclear and incorrect statements are still found in the literature, which we hope this review will help clear out. The simplest argument on why only a small fraction of the electric field can penetrate into the sample is the conservation of energy: $\epsilon_0|E_0|^2 = \epsilon_r\epsilon_0|E_c|^2$, where E_0 is the electric field in vacuum and E_c is the electric field in the conductor with relative permittivity ϵ_r being 10^4–10^5 in a conductor.

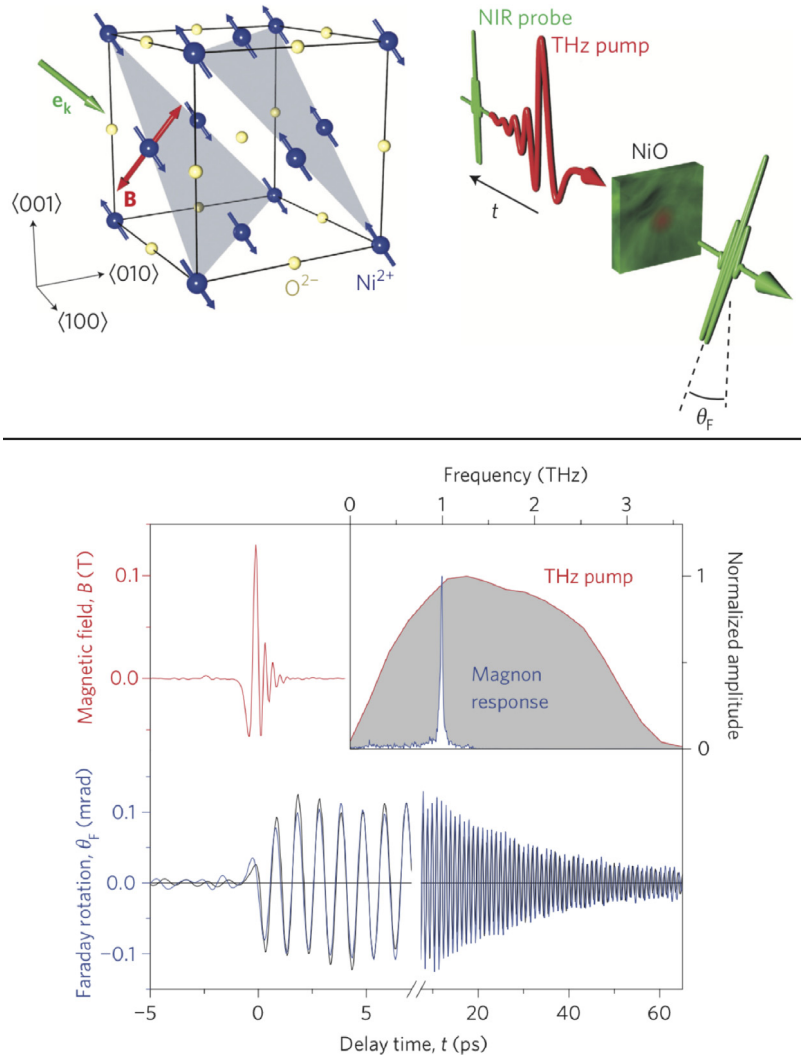

Fig. 19. Top panel: Schematic of the lattice and spin structure of NiO, and of the experimental geometry used to detect the Faraday rotation angle θ_F. Bottom panel: Temporal profile of the THz magnetic field; (bottom) Faraday rotation proportional to the amplitude of the 1 THz magnon excited in NiO. Inset: Fourier transform of the traces in the main panel.
Source: Adapted from Ref. [15].

interactions; (b) by direct coupling to magnetic excitations which are electrically-dipole active, so-called electromagnons; (c) by resonant excitation of phonons which can modulate the exchange interaction. In all these three cases, the materials are insulating.

Control of the electronic band structure was recently demonstrated in the antiferromagnet $TmFeO_3$, where intense THz electric fields were used to control the magnetic anisotropy of the Fe ions by resonantly pumping an electronic orbital transition [206]. It was shown that this mechanism triggers coherent spin dynamics of much larger amplitude than the one which can be excited by direct coupling with the magnetic field component of the THz radiation.

During the preparation of this review, a new paper on the resonant control of spins using electric fields was published [207]. The authors used custom-made antennas to enhance the terahertz electric field in the near-field to modify the magnetic anisotropy in the antiferromagnetic orthoferrite $TmFeO_3$. In turn, the sudden change of anisotropy induces a spin motion of ballistic character which switches the magnetic order on a picosecond timescale.

The coupling to resonant magnetic excitations was instead demonstrated in $TbMnO_3$ [208], a system with cycloidal spin order with an associated electromagnon at around 1.5 THz. When resonantly pumped with an intense THz pulse, this electromagnon caused the spin cycloid to twist by a few degrees, demonstrating direct control of the magnetic order via electric fields. In order to probe such an effect, femtosecond resonant magnetic scattering techniques at free-electron lasers were used.

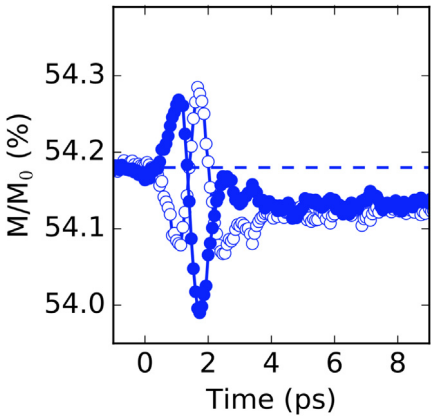

Fig. 20. Dynamics of the magnetization in a metallic CoFeB thin film following excitation with a single-cycle THz field. While the THz pulse is present in the sample, the response reverses its sign upon reversal of the THz magnetic field direction (filled and empty symbols). When the THz pulse leaves the sample, the material is demagnetized, independently of the THz magnetic field direction.
Source: Adapted from Ref. [211].

In addition to driving magnons, THz radiation can also resonantly excite optical phonons, as discussed in Section 2.1. In combination with a magneto-optical probe pulse, one can therefore study the coupling between crystal lattice and spins. Using this approach, two experiments have recently been performed. In one case, the excitation of two phonon modes with orthogonal polarizations, results in a circularly polarized ionic motion [62]. The induced rotating charge creates an effective magnetic field which drive the spins in the rare-earth orthoferrite $ErFeO_3$. This magnetic field couples then efficiently with the magnon excitation at around 0.75 THz, also present in this material.

In a second work, the equilibration of lattice and spins in yttrium iron garnet $Y_3Fe_5O_{12}$ (YIG) was probed [209]. Then, it was found that magnetic order reduces on distinct timescales of 1 ps and 100 ns. On the 1-ps scale, spins and phonons reach quasi-equilibrium in terms of energy through phonon-modulated exchange interaction, resulting in a novel constrained state of increased temperature yet unchanged total magnetization. Only on the much slower 100-ns scale, the excess of spin angular momentum is released to the crystal lattice, leading to full equilibrium between spins and lattice.

2.3.4. Resonant and non-resonant spin dynamics in conducting ferromagnets

In metallic systems, THz induced magnetization dynamics is a rather new approach to understand and explore new aspects of ultrafast magnetism. In addition to a $\mathbf{M} \times \mathbf{H}_{\mathrm{THz}}$ torque acting coherently on the magnetization [210], there are also conduction electrons that are set in motion generating the current necessary to screen the THz magnetic field. This current is spin-polarized due to the different scattering probability for spin-up and spin-down electrons in a ferromagnet. For large enough THz fields, the induced current density can reach levels comparable to those necessary to observe spin torque dynamics, *i.e.*, $10^{10} - 10^{11}$ A/m^2. In this regime, the spin-dependent electronic scattering causes enough spin-flips to lead to an effective demagnetization in the material on the same timescales of the electron–electron scattering, *i.e.*, few tens of femtoseconds [211]. This is much faster than the typical timescales (hundreds of femtoseconds) of ultrafast demagnetization induced not with THz but with near-infrared radiation. The signature of such fast timescales is in the temporal shape of the THz field imprinted in the demagnetization response. The reason for this effect is believed to be due to the enhanced Eliot–Yafet mechanism at lattice defects.

Originally observed in Ref. [211] and shown in Fig. 20, this combination of coherent and dissipative response has now been reproduced in different studies [212–214]. It has also been shown that for a given THz field amplitude, materials with perpendicular magnetic anisotropy seem to demagnetize to a much greater extent [213]. It was noted that this could be consistent with the mechanism of defect-driven spin-polarized scattering, where the many interfaces in the multilayer films, typically used to induce strong magnetic anisotropy, act as extended defects, where spin-flips are occurring with high probability.

Finally, it is worth mentioning that the first experiments involving strong THz fields to control metallic ferromagnetic samples were performed several years ago and described in Refs. [196,215,216]. In those studies, the THz magnetic fields were generated via coherent transition radiation (CTR) from a $\sim$30 GeV electron bunch and on the order of 1–10 T, causing the magnetization to fully reverse. This is believed to be the fastest possible mechanism (about 1 ps) to achieve magnetization reversal, but it is lacking direct experimental confirmation, as the CTR experiments did not allow for the implementation of time-resolved capabilities. A pioneering study using photo-conductive switches and the time-resolved Kerr effect was able to observe the dynamic in Fe microstructures under a 0.6 T sub-terahertz field [217]. The development of table-top THz-generation techniques, together with the use of metamaterials, is expected to lead to the realization of THz magnetic fields comparable to those achieved by CTR. This would in turn open up for pump–probe experiments where the reversal time can be measured directly [213,218].

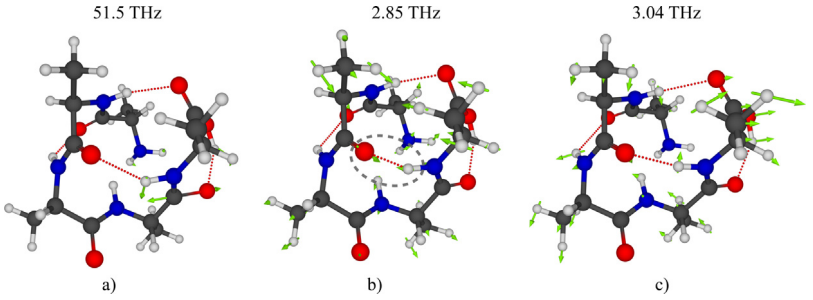

Fig. 21. One of the lowest energy conformers that can be assumed for penta-alanine in the gas phase. The red dotted lines depict intramolecular hydrogen bonds involved in stabilization of the folded penta-Ala structure. The green arrows in plots (a), (b), and (c) show the displacement of atoms associated with excitation of normal modes at 51.5 THz, 2.85 THz, and 3.04 THz, respectively. The molecular structure as well as harmonic normal modes have been obtained with density functional theory calculations. The gray ellipse in plot (b) shows the hydrogen bond participating in the formation of the intramolecular C_{10} ring.

2.4. Controlling molecular dynamics with short intense THz pulses

In this section the control of the rotational and vibrational dynamics of molecular ensembles and individual molecules by short intense THz pulses is discussed. Such control enables more efficient interrogation of molecules, *e.g.*, by rotational alignment in the gas phase, and ultimately steering of chemistry in liquids and on surfaces.

2.4.1. THz interaction with molecules

Molecules can respond to the THz radiation in different ways. For molecules in the gas phase, rotational degrees of freedom can be excited upon absorbing THz photons [219,220]. For molecules in liquids, however, molecular rotations are limited by the surrounding species resulting in librational motions. In relatively large molecules, THz photons excite delocalized vibrational modes and, in what follows, this is elaborated in more detail. Generally, the number of vibrational modes in a nonlinear molecule is given as $3N$-6, where N is the number of atoms, *i.e.*, the number of modes grows with complexity of the molecule. Vibrational modes with relatively large frequencies ($\approx$40–120 THz, the so called mid-infrared (mid-IR) modes) are local and are associated with stretching of chemical bonds. For example, mid-IR spectroscopy of peptides and proteins typically explore characteristic vibrational modes of peptide links, –CO-NH-. One of these modes is amide I and it corresponds to stretching of the C=O bond located on –CO-NH-. Fig. 21a exemplifies the amide I vibration for penta-alanine (Ala–Ala–Ala–Ala–Ala). In contrast to the mid-IR modes, the THz vibrational modes are delocalized, implying that they spread over large parts or an entire molecule (Fig. 21b and c). In addition to delocalized intramolecular vibrations, THz photons can also resonantly excite nuclear motions of weak intermolecular and intramolecular bonds such as hydrogen bonding. Such non-covalent bonds play a significant role in, *e.g.*, stabilization of folded structures of proteins, bonding of two DNA strands, interaction of macromolecules with ambient molecules *etc.* As an example, Fig. 21b presents 2.85 THz vibrational mode of penta-alanine associated with stretching of the hydrogen bond emphasized in the figure with the gray dashed oval. This hydrogen bond forms the intramolecular ring comprising 10 atoms (C_{10}), which is commonly present in β-turns of proteins [221].

2.4.2. Testing Fröhlich hypothesis

THz vibrations are inherently involved in functioning of biological systems. This is rationalized by the fact that THz modes are readily excited at the room temperature. Pump (THz)-probe spectroscopy with short intense THz pulses provides a mean to study evolution of these modes in time as well as to investigate how they dissipate through interconversion to other modes. Also, short intense THz pulses can potentially be used to test Fröhlich hypothesis as was proposed by Weightman [222]. Half a century ago Fröhlich speculated that there are extended THz vibrational modes in biological systems such that the energy supplied to the system through the excitation of these modes is not completely thermalized [223]. Although this hypothesis still remains controversial, some supportive experimental evidences have already been reported [224].

2.4.3. THz Kerr effect

The Kerr optical effect implies that the material becomes birefringent upon irradiation with intense optical pulses. This effect is nonlinear and its magnitude (*i.e.*, the difference in indices of refraction in parallel and perpendicular directions with respect to the light polarization) scales with the square of the electric field of the optical pulse. The THz Kerr effect was demonstrated for the first time by Hoffmann et al. in 2009 [225] using an EOS setup as described in Section 4.2. Their experimental studies were performed in a pump–probe fashion, in which a single-cycle THz pulse induced birefringence in several different liquid samples. The birefringence was probed by 800 nm light pulses with 100 fs duration. The time-dependent signals associated with the THz Kerr effect were observed to have a fast and slow component which

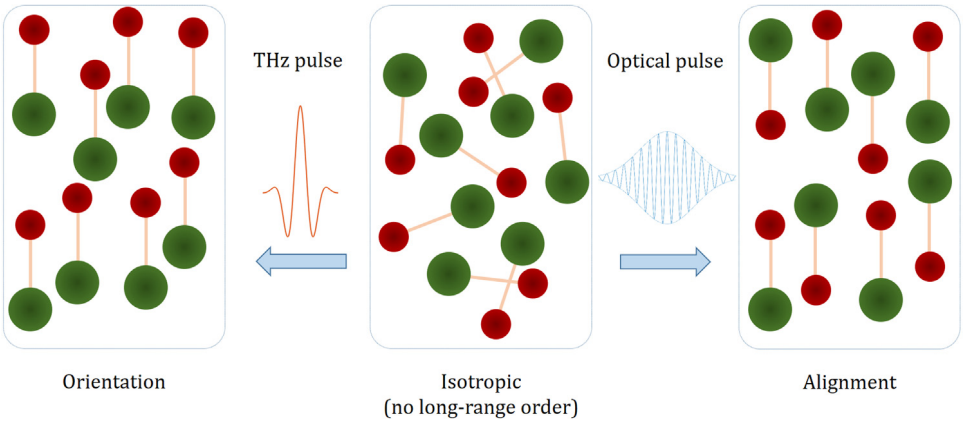

Fig. 22. Illustration of the molecular alignment, induced by an optical pulse, and orientation, produced by a THz pulse. In the latter case the molecules have the same up/down direction.
Source: Adapted from Ref. [238].

corresponded to an electronic and nuclear response, respectively. The slow component was observed for polar molecules and was attributed to the molecular orientation dynamics. This observation implies that short intense THz pulses can be used to control molecular orientation which was employed in subsequent studies both in the liquid [13,225–227] and gas phases [219,220,228].

2.4.4. Rotational alignment and orientation

The random orientation of molecules, such as in a gas-phase sample, leads to unwanted averaging of experimental signals over all molecular orientations. However, intense laser pulses permit alignment of molecules (Fig. 22) using the fact that the interaction between the electric field and the molecule depends on their relative angle. The angular preparation of the molecules can be exploited in several types of experiments including high-harmonic generation [229–232], photoelectron angular distribution measurements [233,234], ultrafast X-ray diffraction [235,236] and strong-field ionization angular dependence studies [237].

For molecular studies it is essential to generate alignment in a field-free environment, *i.e.*, after the duration of the laser pulse. This can be accomplished by creating periodic occurrences of aligned molecules via the formation of coherent rotational motions, *i.e.*, rotational wavepackets. The rotational wavepackets can be created by coupling different rotational states using short intense laser pulses. Such, so-called impulsive, or nonadiabatic, alignment, has been successfully employed with optical lasers via Raman excitation of molecules [239–241].

Molecular orientation presents another degree of control, in which, contrary to alignment, the molecules have the same up/down direction, as illustrated in Fig. 22. Such molecular orientation has been achieved using DC fields and intense optical pulses but is associated with challenges due to the non field-free environment using static fields, and low degree of orientation as well as undesired excitations, of the target molecule using optical pulses.

Intense short THz pulses offer a promising opportunity for enhanced control of the orientation and alignment through the strong electric field that, in a classical description, creates a torque on the molecules, which induces coherent rotational motion. In a quantum mechanical description, the adjacent rotational states are coupled by the THz field and with a broad-band single-cycle pulse coherences can be created at many rotational frequencies.

Gas phase

The first experimental demonstration of rotational alignment in the gas phase was performed in a carbonyl sulfide (OCS) sample using moderate field strengths of tens of kV/cm [219]. Both rotational orientation and alignment was achieved as shown in Fig. 23a and b, respectively. Fig. 23a displays the emission produced when the coherently rotating molecules radiate in phase, which is associated with a net orientation, while Fig. 23b shows the measured birefringence in the gas sample that results from the alignment. The periodic signal is pronounced already in this experiment and a significantly increased effect could be expected using higher fields above 1 MV/cm [219]. Moreover, the use of two time-delayed single-cycle THz pulses has been shown to induce larger rotational coherences as well as further control of their magnitudes and relative phases [220]. An important difference compared with optical excitation is that THz induced orientation and alignment is phase sensitive as shown in Fig. 23c and d.

Simulations applied to hydrogen bromide (HBr) have suggested that high degrees of molecular orientation can be achieved using single-cycle THz pulses of 1 MV/cm electric field strength combined with femtosecond optical pulses [12]. The ensemble average of $\cos\theta$, where θ is the angle between the laboratory-fixed and the molecular axes, was estimated to be $\langle\cos\theta\rangle \sim 0.84$, compared with a value of 0.74 previously obtained in non field-free conditions [242]. There is a

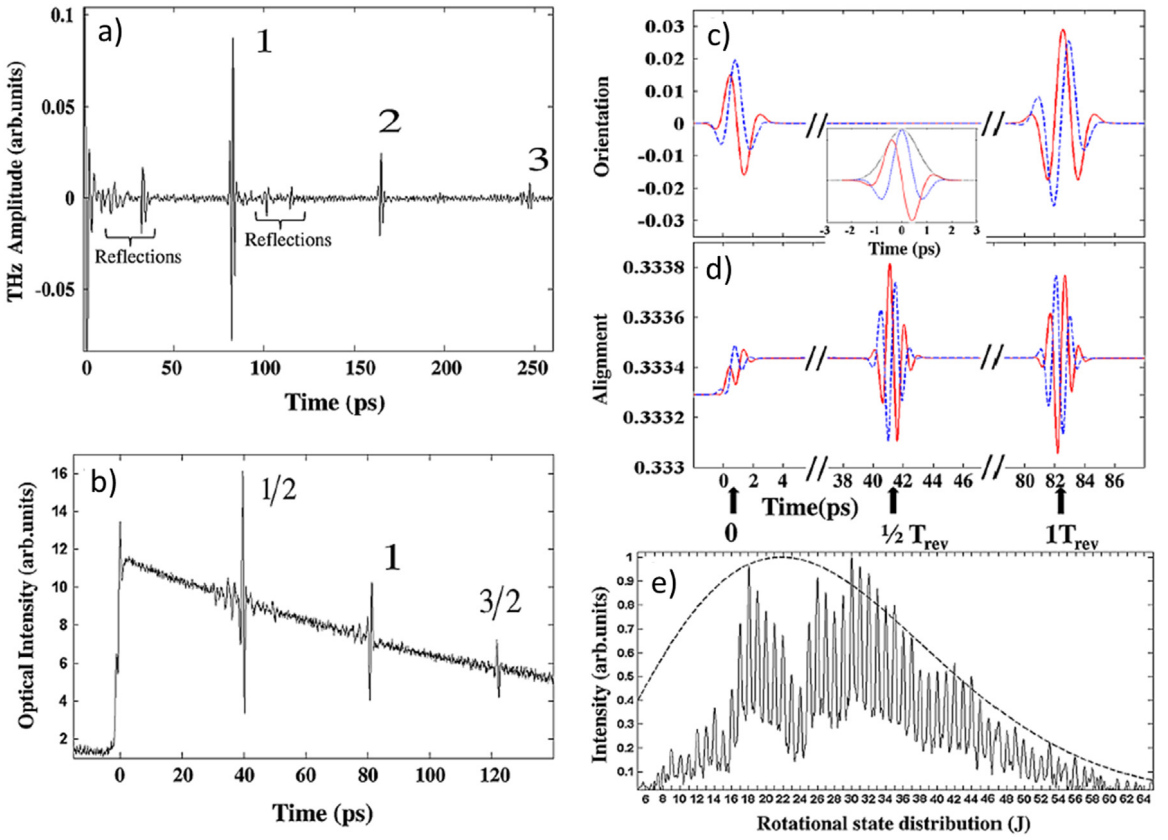

Fig. 23. The time-resolved orientation of OCS molecules is probed by the THz induced free-induction-decay emission (a) measured by EOS. The alignment is probed by the induced birefringence (b) monitored by a variably delayed optical probe pulse. (c) Simulations showing the orientation $\langle \cos\theta \rangle$, where θ is the angle between the laboratory-fixed and the molecular axes, and the alignment $\langle \cos^2\theta \rangle$ (d). The inset shows the THz pulse envelope (black dotted curve) and the field phase shifted by 90 deg (blue dashed and red solid curves), which results in phase shifted orientation and alignment profiles. (e) Normalized rotational level contribution to the coherent signal in (b) which was measured at 300 K. The calculated thermal rotational distribution is depicted by the dashed curve.
Source: Adopted from Ref. [219].

demand for intense half-cycle THz pulses for further development in this research area as they have been proposed to be very useful for creating rotational orientation [243–248].

The progress in THz rotational control and insight into the nonlinear THz interactions associated with molecular orientation [219,220,249] has driven the development of 2D THz rotational spectroscopy [250]. Lu et al. [250] have demonstrated ultrafast 2D THz spectroscopy applied to a gas-phase sample using two single-cycle THz pulses delayed by t_1. The generated signal was detected via EOS (Section 4.2) using an optical pulse delayed by t_2 with respect to the second THz pulse. A 2D frequency plot could be obtained by Fourier transforming t_1 and t_2, in which the off-diagonal peaks provide information about the coupling between states. Such 2D THz experiments are powerful tools for the study of rotational dynamics as they permit control of the rotational motions via the two time-delayed pump pulses and have the capacity to elucidate rotational coherence dynamics with subpicosecond temporal resolution.

The extension of the successfully used 2D IR spectroscopy [251], which permits studies of, *e.g.*, coupled molecular motions in biological systems [252], into the THz spectral region has been difficult because of the many existing degrees of freedom, including gas rotational modes, and the demand for intense THz pulses. The 2D IR experiments typically employ three IR input pulses that are delayed with respect to each other. Hybrid schemes, such as the one used in Ref. [250] have also been developed that employ both THz and optical pulses. However, by including a third THz pulse delayed with respect to the others in the experiments reported in Ref. [250], it would be possible to extract more information, such as rotational energy transfer and relaxation pathways. However, the restricted intensity of THz pulses has limited such experiments to solids [253].

Liquid phase

The rotational dynamics in liquids is influenced by the intermolecular interactions that lead to, *e.g.*, hindered molecular rotations, so-called librations, and reorientational motions of the molecules as they adjust to the new environment created by excitations. Such dynamics proceeds on the timescale corresponding to THz frequencies and can strongly influence

chemical reactions. Recent advances in developing intense THz sources have now enabled the study of nonlinear rotational effects in liquids [13,225–227].

In a recent study [226] Kerr-effect measurements were conducted in order to investigate the transient birefringence induced in different liquids by optical vs. THz excitation. These experiments demonstrated that the transient birefringence is enhanced by more than an order of magnitude using THz excitation, compared with optical one, in highly polar liquids. In addition a resonant effect was observed for the THz pulses. These effects were explained by efficient coupling of the intense THz pulses to the librational modes, which led to reorientational motion. The observations suggest that efficient alignment in liquids and even coherent control of reactions are within reach.

Molecular alignment has also been achieved using multiple THz pulses [254]. By varying the timing between two THz transients, the orientational alignment of the molecules in the liquid could be controlled. These measurements were performed with 2D THz–THz–Raman (TTR) spectroscopy in which two carrier-envelope-phase stable THz pump pulses are used in combination with a weak NIR Raman probe pulse. This method is sensitive to the birefringence of the liquid and also to the couplings between different molecular vibrational modes.

Recently, orientation of liquid water molecules was demonstrated using single-cycle THz pulses (0.25 THz) of 510 kV/cm electric field strength and was probed by the optical Kerr effect. Though, the observed dynamics could not fully be reproduced by the modeling of the dynamics [227]. Water is a unique liquid of fundamental importance for, *e.g.*, biological systems. Useful parameters required for accurate simulations of water dynamics, such as the polarizability of water molecules, are not known, but could be obtained with THz experiments [228]. However, alignment of water molecules in the liquid phase is difficult because of rigid hydrogen-bonded structure and the fast energy dissipation into the water network. Efficient alignment requires exciting hindered librational motions of the water molecules in the hydrogen-bonded network that move on timescales that match the reorientations of the surrounding water. In a recent experiment, water alignment was demonstrated by resonant excitation of librational modes using THz-pump THz-probe experiments at 11.7 THz and 7.8 THz [13]. The rotational dynamics revealed a significantly enhanced water molecular alignment compared with the above described measurements using single-cycle pulses [227]. Specifically, the strong-field THz excitation generated significant alignment at 11.7 THz excitation but not at 7.8 THz. It was explained by the matching of the 11.7 THz driving field with the natural system fluctuations that resulted in efficient water alignment. This experimental result agreed well with simulations that showed a significant pump frequency dependence displaying a signal peak at around 12 THz using a THz field of 5 MV/cm.

2.4.5. Excitation of molecular vibrations

Single molecules

Scanning tunneling microscopy (STM) employs quantum tunneling to investigate surfaces at the atomic resolution. In this method, a tip biased with a DC voltage scans the surface. Cocker et al. [255] have developed the THz-STM approach in which a short THz pulse substituted the DC bias. The authors investigated single pentacene molecules absorbed on NaCl monolayer. In particular they observed a sharper contrast of the highest occupied molecular orbital (HOMO) lobes in THz-STM images compared to those acquired using the DC bias. Introducing a second THz pulse with a certain delay with respect to the first one made it possible to investigate ultrafast dynamics of individual pentacene molecules on the scale of a single molecular orbital. It was observed that upon removing an electron from the HOMO orbital by the first THz pulse, an oscillatory motion of a pentacene molecule was excited, which was probed by the second pulse. This oscillatory motion was attributed to the van der Waals interaction between the molecule and substrate. The introduction of the THz-STM technique opens the door to a new class of ultrafast dynamics experiments in which molecular motion is probed on the femtosecond timescale at the level of a single electronic orbital.

A complementary approach for single-molecule THz spectroscopy was demonstrated for C_{60} by using the single molecular transistor geometry, in which an investigated molecule is captured in a sub-nanometer gap between a source and a drain of the transistor [256]. Upon irradiation with a THz single-cycle pulse, center-of-mass oscillations of the C_{60} molecule are excited. Such oscillations facilitate tunneling (THz-induced vibron-assisted tunneling) between the source and the molecule, and subsequently between the molecule and the drain. THz spectra are obtained from interferograms of photocurrent induced by two THz pulses delayed in time with respect to each other.

Liquid phase

Thermally activated motions in liquids include intermolecular and intramolecular vibrations. Recently the first coherent excitation of intramolecular vibrational modes via nonlinear THz interaction in a liquid was reported [257]. The coherent excitation was accomplished using a two-photon interaction of one THz pulse and a Raman interaction from a continuously delayed 800 nm pulse. Similarly to the studies by Hoffmann et al. in Ref. [225], the measurements using THz Kerr effect spectroscopy revealed rotational dynamics, but also intramolecular vibrations could be observed as oscillations superimposed on the rotational signal. Although this was not a 2D experiment, because the signal was only measured with respect to the delay between the THz pump and the 800 nm probe, it opened the door to multidimensional THz spectroscopy of vibrational motions in the condensed phase. Since then 2D TTR spectroscopy has been exploited to measure the anharmonic coupling between vibrational states, revealed by off-diagonal peaks in the 2D spectra, for various liquids [254,258]. This type of 2D THz experiments opens the possibility to control vibrational populations as well as coherences between the vibrational states. Hence, it provides the first step towards control of liquid phase chemistry

Please cite this article as: P. Salén, M. Basini, S. Bonetti et al., Matter manipulation with extreme terahertz light: Progress in the enabling THz technology, Physics Reports (2019), https://doi.org/10.1016/j.physrep.2019.09.002.

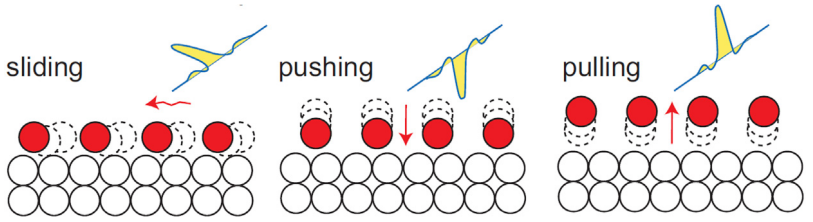

Fig. 24. Illustration of the manipulation of atoms on a surface using different orientations of the polarization of a half-cycle THz pulse. *Source:* Adopted from Ref. [261].

with light. Furthermore, 2D THz spectroscopy may reveal couplings between intermolecular modes and permit separation of the homogeneous and inhomogeneous line broadening, which would enhance the spectral resolution of the typically blurred 1D THz spectra. The possibilities offered by vibrational 2D THz spectroscopy applied to liquids are elaborated in more detail in a recent perspective article [259].

2.4.6. Adsorbed molecules

Surface chemistry and catalytic reactions are suitable targets for THz studies because many surface vibrations exist at these frequencies, such as phonons, collective electron motions and frustrated vibrations of molecules bound to the surface. The high-field quasi-half-cycle (quasi-unipolar) THz pulses with electric fields on the order of 10 MV/cm, corresponding to the Coulomb force between the electron and nuclei, provide a handle to manipulate adsorbed atoms and molecules by initiating a coherent motion. Calculations have shown that electric field strengths in the 10 MV/cm range can displace a water-molecule layer on Au by 0.5 Å [260]. Moreover, by using quasi-half-cycle pulses with field strengths comparable to the internal molecular electric field and with duration comparable to the vibrational period, it is possible to drag the nuclei along a desired direction by orienting the polarization of the THz pulse as illustrated in Fig. 24. This has been suggested as a path towards efficient reaction control at surfaces [261]. The direct coupling to the vibrations of the adsorbed molecules by the THz pulse provides a crucial advantage compared with previous attempts at controlling femtochemistry on metal surfaces using ultrashort optical pulses. The latter method relies on indirect coupling to the molecules via excitation of phonons and hot electrons, and thus allows little control of the reaction pathway. In contrast, the use of THz pulses permits targeting specifically the motion of the adsorbed molecules.

THz-induced control of CO oxidation on Ru(0001) has been demonstrated [14] using the strong quasi-half-cycle fields of THz transients generated by coherent transition radiation (CTR) from an ultrashort relativistic electron bunch at the Linac Coherent Light Source (see Section 3.3.1 for CTR principles). The experiments were carried out using THz pulses with 10 MV/cm peak field centered at 10 THz. The CTR-produced THz pulses are radially polarized and have both longitudinal and transversal electric field components at the focus. The electric-field components perpendicular to the surface move the surface conduction electrons closer to, or away from, the adsorbed atoms and molecules, which provides a handle to control the adsorbates. In the Ref. [14] it was suggested that the THz-induced CO oxidation was driven by Ru–O vibrational excitation caused by the transfer of electrons to the non-bonding Ru–O orbitals when the electron density is polarized to the surface. This increases the translational energy of the O atoms and enhances the probability to react with CO and form CO_2.

2.5. THz manipulation of electron beams

Charged particle accelerators have found wide applications in industry and research. They are used for driving photon sources such as free-electron lasers (FEL) and synchrotrons, for proton and ion treatment of cancer, for food sterilization and quality control in industry. Conventional accelerator technology uses radio frequency (RF) fields to accelerate charged particles. In linear electron accelerators, conventional 2.856 GHz accelerating structures are limited to the maximum accelerating field of about 50 MV/m. This results in km-long accelerators for the production of multi-GeV beams needed for, for example, X-ray sources. At the same time, by employing electromagnetic fields of higher frequencies the breakdown threshold of accelerating structures can be increased [262]. An increase in the accelerating field correspondingly implies a more compact accelerator. Acceleration, formation and diagnostics of electron beams with strong-field THz transients is a dynamic and very promising field of research started in the late 2000s. In this section, we summarize key achievements in this field.

In the linear accelerator, the bunch of electrons gains energy from an external electromagnetic wave in a accelerating structure maintaining synchronism (constant phase relation) between the bunch and the wave. It is an attractive option to use optical laser fields and dielectric accelerating structures to reach accelerating fields of hundreds of MV/m [263]. However, to obtain high-quality beams, all particles in the bunch must experience almost the same phase and amplitude of the accelerating field. With an optical or IR laser, this means a femtosecond-scale time bucket to be populated with particles. Such a short bunch duration strongly limits the bunch charge because of Coulomb repulsion. Therefore, in

dielectric laser accelerators the bunch charge that can properly be accelerated does not exceed 1 pC [263]. For competitive FEL operation tens of pC of charge in the driving bunch are needed. In addition, a sub-femtosecond scale synchronization is needed for acceleration by IR fields. In contrast to optical or IR fields, acceleration by THz fields is a viable option. Recent studies on the bunch formation show that with RF technology it is possible to generate and compress several MeV, 30–50 pC bunches down to the 50 fs level [264,265]. Then, such bunches can further be accelerated, for example, within one bucket of a 1-THz field.

For acceleration, strong-field high-pulse-energy THz radiation is needed: (i) the stronger the field, the higher the electron energy gain; (ii) the higher the THz pulse energy, the longer interaction is sustained before the THz pulse is depleted. Since only one cycle of the field is used for acceleration, a few-cycle THz wave is more suitable for acceleration than a multi-cycle wave having the same pulse energy.

For efficient acceleration, the beam and the accelerating field must be synchronized to preserve a constant phase shift between the two. The synchronization can be achieved by using: (i) a waveguiding structure which slows down the wave [266,267], (ii) a slow ponderomotive wave produced by a THz wave and an undulator field [268], or (iii) a longitudinally polarized photon beam propagating at a subluminal velocity in free space [269].

In the Ref. [266], a THz pulse from a laser-based source is first converted into a radially polarized one (using a segmented waveplate), which is further focused into an accelerating structure (3 mm long). The latter is a dielectric capillary with a metal outer boundary serving as a circular THz waveguide. The dielectric allows for matching of the group and phase velocity of the THz pulse with the injected particle bunch. With a 10 μJ initial THz pulse, the on-axis electric field within the structure turned out to be 10 MV/m. The injected electron bunch experienced an accelerating gradient of about 2.3 MeV/m. Although modest at the proof-of-principle stage, this acceleration method is scalable and flexible. In contrast with laser-driven plasma wakefield acceleration, it preserves the high brightness of the particle beam provided by a photoinjector. Moreover, it paves the way towards all-optical acceleration and manipulation of particle beams.

Direct manipulation of electron beams with THz pulses was also demonstrated through the inverse free-electron laser mechanism [268,270]. To this end, electrons are overlapped with a THz field within an undulator. The THz field and a static, periodic (along the interaction direction) magnetic field of the undulator form a slow ponderomotive wave synchronous with the beam. To counteract the diffraction of the THz field along the undulator and preserve an efficient energy transfer from the THz field to the beam, a waveguide is inserted (curved parallel plates). Changing the separation between these plates allows one to control the resonant electron energy within the undulator. The direction of the energy transfer between the THz wave and the beam depends on the relative phase between the two. By changing the relative phase, the compression and decompression of short (compared to THz period) 4–9 MeV electron bunch were demonstrated experimentally Ref. [268]. The 150-keV energy modulation of long bunches was also achieved. Thanks to the waveguide, the inverse free-electron laser interaction was sustained for up to 30 cm. In the same manner, bunch acceleration can be performed. With a modest 1 μJ THz pulse, the gradient reached 0.25 MeV/m. With state-of-the-art THz sources, see Section 3, this value can clearly be increased.

While the approaches demonstrated in [266,268] use well-known methods in accelerator physics adapted to the THz range, a new type of the accelerating structure was introduced in [267]. It can both accelerate and streak electrons depending on the phasing of driving THz fields. Two THz pulses are injected from the sides to an accelerating structure, see Fig. 25. Depending on the relative phase between the pulses, two regimes are possible: (i) the acceleration and compression regime by the combined electric field (magnetic fields cancel each other), and (ii) the deflection and streaking regime by the combined magnetic field (electric fields are mutually cancelled). In the streaking regime, the electrons of the beam acquire different transverse momenta depending on the arrival time to the THz-wave-beam interaction region. Then, the electron distribution projected, for example, onto a yttrium aluminium garnet (YAG) screen gives the information about the temporal profile of the electron beam. The demonstrated accelerating field is 70 MV/m whereas the streaking resolution is 10 fs. It is interesting to note that a very similar setup was proposed in [18], see Section 3.3.2, but for THz generation by electron beams instead of THz acceleration.

The production of high-quality electron bunches for ultrafast applications with single-cycle THz fields is a new pivotal direction of research in accelerator technology. The Ref. [271] reports a THz-driven electron gun, shown in Fig. 26, with an accelerating gradient of over 300 MV/m in a micrometer-scale waveguide. This accelerating gradient is record high compared to state-of-the-art RF guns, which achieve 200 MV/m gradient [265]. The demonstrated bunch charge of 32 fC is too low for driving light sources but sufficient for ultrafast electron diffraction [272–274]. In the experiment, a THz pulse with a pulse energy of 35 μJ and a center frequency of 0.5 THz is focused into a waveguide. Thanks to focusing, the accelerating field reaches 350 MV/m in the gun. However, the final beam energy (around 0.4 keV) is low because of a short interaction region. The absolute energy spread of the electrons in the THz gun is comparable with that of state-of-the-art conventional RF guns.

2.6. Conclusions

Research exploiting the recently developed THz technology, producing ultrashort THz pulses with field strengths exceeding 1 MV/cm, shows a tremendous impact on a variety of scientific areas.

The strong-field THz transients now available have enabled the investigation and control of nonlinear lattice responses that influence the material properties. For example, using field strengths of ∼1 MV/cm, IR active modes can be driven

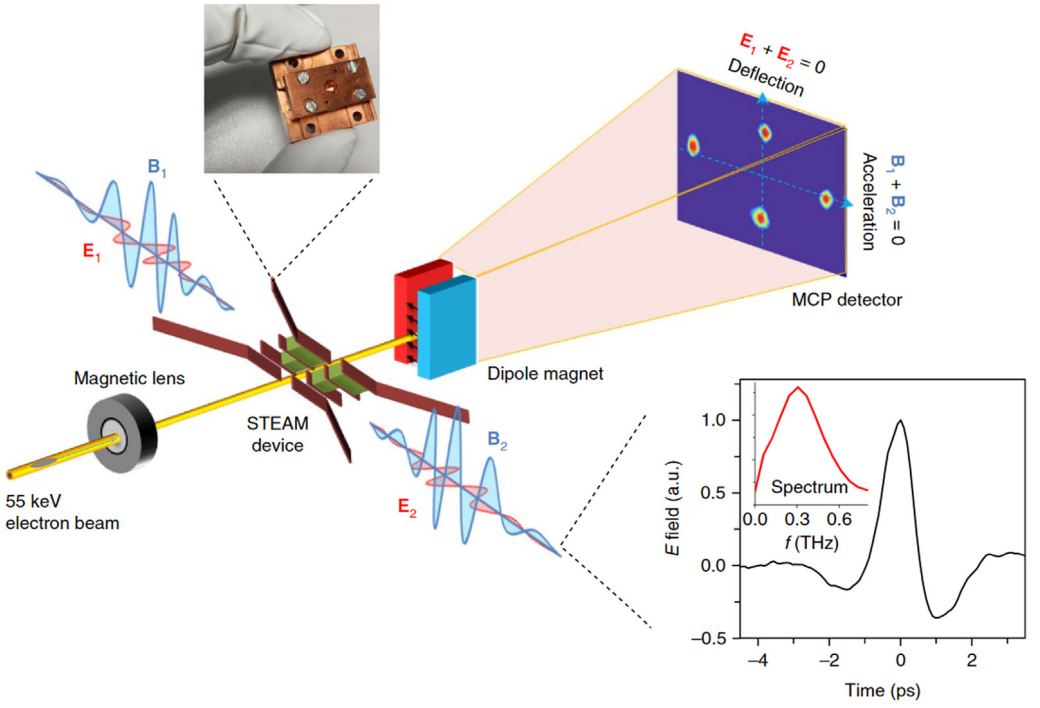

Fig. 25. A pre-accelerated, 55 keV electron beam traverses a set of parallel-plate waveguides stacked together. The waveguides form a three-cell accelerating structure with a π phase shift between the cells such that the beam experiences the same accelerating phase as it propagates through the structure. The structure is powered symmetrically from the sides by two THz pulses and depending on the phase between the pulses, the resulting field is completely dominated by either an electric or a magnetic component.
Source: Adopted from [267].

into the anharmonic regime, which permits coherent excitation of Raman active modes via anharmonic coupling. The associated nonlinear coupling terms result in a displaced potential energy curve and a transient lattice structure modification that can be exploited for material control. Such nonlinear lattice excitations have produced signatures that may indicate induced transient superconductivity in cuprates and organic systems, which could provide further clues to the underlying mechanisms behind the transition to this important state. Nonlinear lattice excitations have also enabled initial demonstrations of sub-picosecond polarization switching in ferroelectric materials with applications in, *e.g.*, non-volatile memory device technology.

The strong THz electric fields also enable control of the material properties by direct manipulation of charges in semiconductors, or by influencing the interactions between electrons in correlated electron systems, such as Mott insulators. For example, electric fields in the 1 MV/cm range have improved our understanding of carrier multiplication (CM) leading to increased conductivity in semiconductors, which is a key process in many technological applications, including solar cells. In particular, such THz fields have enabled experiments that shed more light on the impact ionization (IMI) and Zener tunneling (ZT) contribution to CM and provided new ways to study their dynamics at a larger range of initial carrier concentrations. Furthermore, extreme spectral broadening of optical pulses and semiconductor optical transmission modifications has been achieved via IMI and ZT induced by THz pulses with 25 MV/cm electric field strength.

The mechanism of THz-induced insulator–metal transitions (IMT) driven by electron correlation effects, so-called Mott transitions, has been clarified using THz fields exceeding 1 MV/cm. The importance of field-induced tunneling for generating carriers that initiate the process has been demonstrated. The IMT mechanism of VO_2 has been heavily debated but recent experiments using strong-field THz pulses suggest that the phase transition is driven by electron tunneling and that the electronic dynamics can occur on a faster timescale than the lattice dynamics.

THz-driven nonlinear effects in graphene have recently attracted much attention in view of very large values of graphene's nonlinear susceptibility in the THz region. In contrast to conventional 3D materials, graphene manifests a nonlinear behavior in the THz range already for moderate fields on the order of 10 kV/cm. A variety of THz-driven nonlinear effects in graphene have been demonstrated: high-harmonic generation, dynamic Hall effect, all-optical wide-band nonlinear modulation, second-order nonlinear photon-drag currents.

Coherent magnetization dynamics has been triggered by intense THz pulses, both via the magnetic and electric fields. Using single-cycle THz pulses the control of magnons in antiferromagnetic NiO has been achieved via interaction of the 0.1 T (300 kV/cm) magnetic field with the spins. Even stronger fields of 1–10 T generated by coherent transition radiation

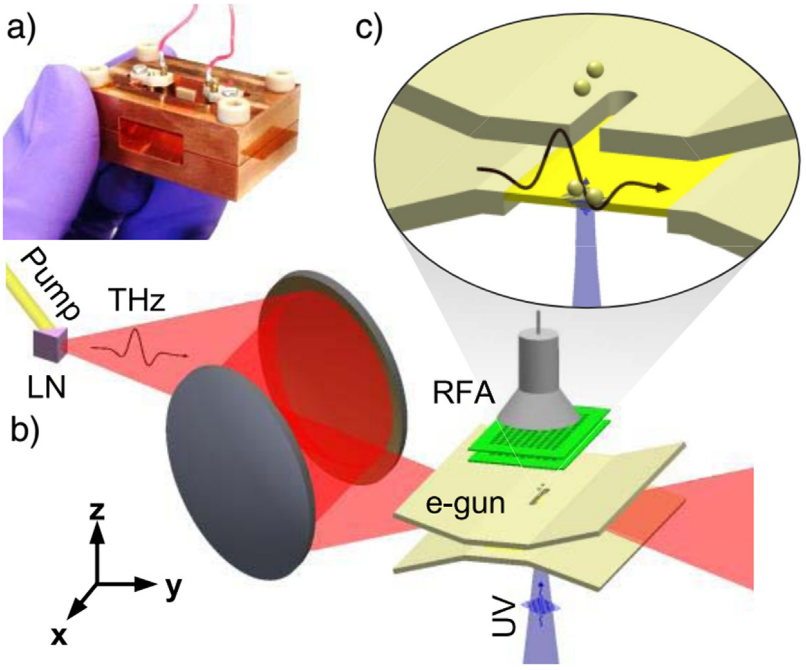

Fig. 26. All-optical THz gun (a). Figure (b) shows the concept of the gun. A single-cycle THz pulse is first produced via optical rectification in a lithium niobate crystal, and then focused into a parallel-plate waveguide with tapered input. The waveguide supports dispersion-free TEM modes and focuses the THz pulse. The inset (c) presents a schematic of the acceleration region. An external UV pulse illuminates a thin copper foil that is used as a cathode for photo-emission of electrons. The illumination is from the back side. The emitted electrons are accelerated by the THz pulse and extracted through a narrow slit in the waveguide wall.
Source: Adopted from [271].

(CTR) from a 30 GeV electron bunch have shown magnetization reversal on an ultrafast timescale, estimated as 1 ps, in metallic ferromagnetic samples. Time resolved studies are, however, required to confirm the exact switching time. Intense THz pulses have also provided essential knowledge about demagnetization dynamics in metallic ferromagnets.

Field-free molecular alignment and orientation is desirable in a broad class of experiments including ultrafast X-ray diffraction and has been demonstrated for gas-phase molecules using single-cycle THz transients with moderate field strengths of ∼50 kV/cm at the sample. Further control of such periodic orientation is expected with schemes involving a combination of 1 MV/cm THz waves and femtosecond optical pulses. In addition, alignment, as well as vibrational control of molecules in the liquid phase has been obtained, which opens the possibility of steering chemical reactions in solution. Moreover, by exciting the Ru–O vibrations on a Ru surface using single-cycle THz pulses with a 10 MV/cm peak field centered at 10 THz, CO oxidation has been achieved. Such pulses were generated via CTR at the high-energy linac at LCLS. The high electric field of the THz pulse offers the possibility of manipulation and high-gradient acceleration of electron bunches, with implications for the development of compact linear accelerators and ultrafast electron diffractometers. In particular, an all-optical THz-driven electron gun with an accelerating gradient of over 300 MV/m has been reported. This development is a decisive step towards the realization of single-shot electron diffraction on a 10-fs scale needed for studying the dynamics of strongly correlated materials.

In addition to the manipulation of matter by strong THz fields, many studies require picosecond, or sub-picosecond, time resolution in order to follow the fast dynamics initiated by the intense THz pulse. Such studies benefit from the short pulse duration offered by single-cycle or few-cycle THz transients. Several recent experiments have exploited the short and intense THz pulses in nonlinear pump–probe measurements. Pump–probe experiments carried out with a single-cycle THz pump pulse combined with either THz or optical probe pulses have addressed the dynamics of, *e.g.*, exciton ionization, carrier multiplication, superconductive-order-parameter oscillations, ferroelectric polarization switching, magnon excitations, and molecular alignment and orientation. Moreover, X-ray pulses have been useful for resolving the structural dynamics initiated by the THz pulse. This has, for example, enabled the separation of the timescales associated with lattice and electronic dynamics in Mott insulators and has provided insight into the mechanism of phase transitions into superconducting-like states.

Desired THz pulse properties for future applications will be discussed in Section 5.

Please cite this article as: P. Salén, M. Basini, S. Bonetti et al., Matter manipulation with extreme terahertz light: Progress in the enabling THz technology, Physics Reports (2019), https://doi.org/10.1016/j.physrep.2019.09.002.

3. Generation of strong-field THz light

3.1. Optical rectification

Though optical rectification was predicted in 1962, the generation of single-cycle THz pulses was demonstrated only in 1985. Then, it took another two decades to develop THz sources delivering single-cycle pulses with MV/cm field strength. Nowadays, THz generation through optical rectification is an established technology and contemporary research efforts are mainly focused on extending the frequency range and increasing the conversion efficiency of rectification.

3.1.1. Basics of optical rectification and phase matching

Optical rectification (OR) is a nonlinear optical phenomenon. If an electromagnetic field with high electric field strength interacts with matter, the response of the matter (its electric polarization **P**) is usually not proportional to the electric field **E**, instead the polarization vector can be described as

$$\mathbf{P} = \epsilon_0(\chi^{(1)}\mathbf{E} + \chi^{(2)}\mathbf{EE} + \chi^{(3)}\mathbf{EEE} + \chi^{(4)}\mathbf{EEE} + \cdots). \tag{9}$$

Here ϵ_0 is the vacuum permittivity, and $\chi^{(n)}$ is the nth-order susceptibility tensor of the material. The first term in Eq. (9) is responsible for the difference of the light velocity inside the matter from that in vacuum. The second term can be the source of radiation having a different frequency from that of the driving electric field. If the driving field contains at least two frequency components, sum-frequency and difference-frequency generation can occur.

For the special case of illumination of a nonlinear crystal with a high-intensity, ultrashort pump laser pulse having a *broad spectrum*, the frequency components matching the difference between the frequency components of the ultrashort pulse are generated. If the frequency dependence of $\chi^{(2)}$ is negligible, these new frequency components result in a single-cycle electromagnetic pulse with a temporal shape equal to the derivative of the temporal shape of the pump laser pulse intensity [275]. This is the OR process. If the duration of the pump laser pulse is in the range of hundred femtoseconds, the oscillation period of the produced single-cycle pulse is also in the sub-picosecond range. Correspondingly, its spectrum has a maximum in the THz frequency range, and the width of the spectrum is larger than the mean frequency. To sum up, OR of (typically near-infrared (NIR)) ultrashort laser pulses in a nonlinear optical crystal can result in single-cycle THz pulses.

OR, as every nonlinear optical frequency conversion process, can be effective only if the phase-matching condition is fulfilled. This means that the THz wavelets generated at different points of the nonlinear crystal along the propagation path must arrive to the exit surface of the crystal with the same phase, thus yielding constructive interference among the wavelets. For OR the phase-matching condition can be expressed as a velocity-matching condition according to [276]

$$v_{\mathrm{NIR}}^{\mathrm{gr}} = v_{\mathrm{THz}}, \tag{10}$$

where v_{NIR} is the group velocity of the NIR laser pulse and v_{THz} is the phase velocity of the THz pulse.

Let us assume that the velocity matching condition is fulfilled and the absorption coefficient both in the NIR and THz range is small compared to L^{-1}, where L is the length of a nonlinear crystal illuminated by NIR laser pulses of intensity I. Then the intensity conversion efficiency (from the NIR pulse to the THz one) of the OR process can be approximated by a formula describing the difference frequency generation process [277]:

$$\eta_{\mathrm{THz}} = \frac{2\omega^2 d_{\mathrm{eff}}^2 L^2 I}{\epsilon_0 n_{\mathrm{NIR}}^2 n_{\mathrm{THz}} c^3} \tag{11}$$

Here ω is the (main) angular frequency of the generated THz pulse, d_{eff} is the effective nonlinear optical coefficient, c is the velocity of light in vacuum, and n_{NIR} and n_{THz} are the indices of refraction in the NIR and THz range, respectively. The effective nonlinear coefficient, d_{eff}, depends on the polarization of both the NIR laser pulse and the generated THz radiation, and can be calculated from the nonlinear optical tensor, d, having half the values of the corresponding elements of the 2nd order susceptibility tensor [278]. From Eq. (11), the relation for the peak electric field of the generated THz pulse follows:

$$E_{\mathrm{THz}} \sim \omega d_{\mathrm{eff}} L I. \tag{12}$$

According to Eq. (11), the THz generation efficiency of OR is proportional to the square of both the frequency of the generated THz radiation and the nonlinear optical coefficient, and is proportional to the intensity of the laser pulse. Since the frequency of the THz radiation is small (about two orders of magnitude smaller than the frequency of the visible or NIR light), it is indispensable to use nonlinear optical crystals having high d_{eff}, and to apply a high laser intensity, for obtaining efficient OR. The applicable laser intensity is usually limited by multiphoton absorption.

Note that, because of the phonon resonances between the NIR and THz ranges, the value of d_{eff} for THz OR is not equal to the value for sum-frequency generation of NIR pulses, when all involved frequencies are above the phonon resonances. For semiconductors d_{eff} is somewhat smaller in the THz range than in the NIR range whereas for ferroelectric crystals (lithium niobate $LiNbO_3$ (LN), lithium titanate $LiTiO_3$ (LT)) the situation is opposite. The d_{ij} elements of the nonlinear

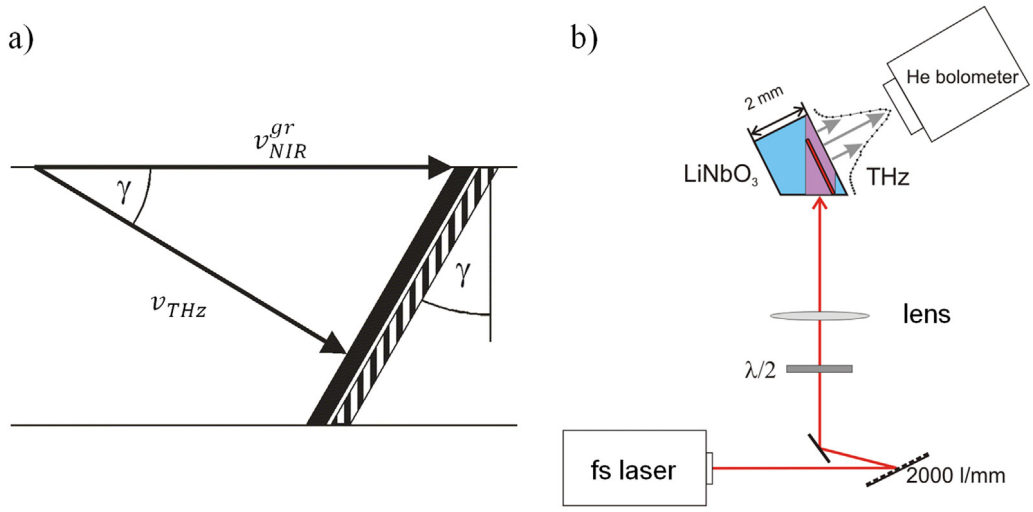

Fig. 27. The working principle (a), and the typical setup of a TPFP LN THz source (b).
Source: Adopted from Ref. [1].

optical tensor, or the $\chi_{ij}^{(2)}$ elements of the 2nd order susceptibility tensor (both applicable to the OR process) can be calculated from the corresponding elements of the (clamped) r electro-optic tensor according to [277,279]

$$d_{ij} = \chi_{ij}^{(2)}/2 = -\frac{n^4 r_{ji}}{4}. \tag{13}$$

It is also important to notice that for some materials (*e.g.*, for ferroelectric crystals), the α_{THz} absorption coefficient in the THz range can be a few times larger than 10 cm^{-1}, limiting the usable crystal length L, see Eqs. (11) and (12). In this case, another expression has to be applied instead of Eq. (11), [277].

In what follows, typical setups for OR and the results obtained with them will be presented separately for three different types of nonlinear crystals: ferroelectric crystals, semiconductors, and organic crystals.

3.1.2. Optical rectification in ferroelectric crystals

Since the nonlinear susceptibility of the ferroelectric crystals (*e.g.*, $LiNbO_3$ (LN), $LiTiO_3$ (LT)) has a large contribution from phonon resonances at about 10 THz, it is much higher for the OR process than for other frequency conversion processes (*e.g.*, the second harmonic generation) involving photons only in the visible or near infrared range. Because of this large nonlinearity (see Table 1), ferroelectric crystals are very promising for OR. At the same time, since their linear susceptibility also has large contribution from the phonon resonances, their index of refraction in the THz range is much higher than their group index in the visible or NIR range. Hence, velocity matching using birefringence or dispersion in the visible or NIR range is not possible for ferroelectric crystals.

In 2002, the so-called tilted-pulse-front-pumping (TPFP) technique was suggested to achieve velocity matching [1]. Its working principle is the following (see Fig. 27a): when a plane intensity front of the pump laser pulse generates THz radiation, this radiation propagates perpendicularly to the intensity front. If the intensity front is tilted (compared to the phase front), meaning it is not perpendicular to the propagation direction of the pump pulse, then the velocity matching condition is

$$v_{\mathrm{NIR}}^{\mathrm{gr}} = v_{\mathrm{THz}} \cos(\gamma) \tag{14}$$

instead of Eq. (10), where γ is the tilt angle of the intensity front. By choosing γ appropriately, velocity matching can be achieved for

$$v_{\mathrm{THz}} > v_{\mathrm{NIR}}^{\mathrm{gr}}. \tag{15}$$

A typical setup for OR using TPFP is shown in Fig. 27b. It consists of a femtosecond laser, an optical grating for introducing the tilting, a nonlinear crystal (typically LN), and an imaging optics to image the pump pulse spot on the grating into the nonlinear crystal. In order to enable both the perpendicular entrance of the pump into the LN crystal and the perpendicular exit of the THz pulse from the crystal, the LN has a wedge angle equal to the γ tilt angle.

It has been proved only recently that TPFP in LN crystals is a very efficient single-cycle THz source in the 0.2–2 THz range. Pumping with only a few mJ Ti:sapphire laser pulses resulted in THz pulses with an energy exceeding 2 μJ [277]. Using an off-axis paraboloidal mirror pair for focusing, a peak electric field strength of more than 1.2 MV/cm was achieved [25]. The THz pulse energy and field strength achieved were sufficient to induce nonlinear effects when being

Table 1
Relevant parameters of a few nonlinear crystals most frequently used for OR. r is the electro-optic coefficient, d_{eff} is the effective nonlinear optical coefficient, $n_{\text{NIR}}^{\text{gr}}$ is the group index of refraction at the pumping wavelength λ given in the curly brackets, n_{THz} is the phase index of refraction on the THz range, α_{THz} is the absorption coefficient in the THz range, β, γ, and δ are the two-, three- and four photon absorption coefficients at the pumping wavelength, respectively.

	r (pm/V)	d_{eff} (pm/V)	$n_{\text{NIR}}^{\text{gr}}$ (λ)	n_{THz}	α_{THz} (1/cm)	β (cm/ GW)	γ (cm^3/ GW^2)	$10^6 \times \delta$ (cm^5/ GW^3)
ZnTe	4.04	68.5	3.24 (800)	3.17	1.3	4.2		30
			2.98 (1030)					
			2.79 (1700)					
GaAs	1.43	65.6	3.99 (800)	3.59	0.5			
			3.5 (1800)					
			3.43 (2300)					
GaP	0.93	24.8	3.56 (800)	3.34	0.2		0.04	30
			3.32 (1030)					
			3.12 (1700)					
GaSe	1.7	86			0.5			
sLN	30.9	168	2.25 (800)	4.96	17			0.01
sLN (100 K)	30.9	168	2.25 (800)	4.76	4.8			
sLT (100 K)			2.22 (800)	5.7				
DAST	77	615	3.39	2.58		0.7		
DSTMS		214		2.22				

applied to different materials in pump–probe experiments [3]. Higher pump energies of the driving laser produced a THz pulse energy of 0.43 mJ [280] and by cooling the LN crystal more than 3% energy conversion efficiency was achieved [281]. The highest reported electric field achieved with this technique is 4 MV/cm at 0.3 THz frequency [282].

Despite these impressive results it became evident that the large required tilt angle severely limits, in a few different ways, further increase of the THz pulse energy and electric field in the TPFP LN THz source. The main limitations are the following: (1) Every beam with a tilted intensity front contains an angular dispersion, [283]:

$$\tan\gamma = \lambda \frac{d\theta}{d\lambda}. \tag{16}$$

Furthermore, group velocity dispersion, proportional to the square of the angular dispersion, appears. Because of group velocity dispersion, the pulse duration of an ultrashort pulse having a large tilted intensity front evolves very fast during propagation. This results in a short effective THz generation length, limiting the efficiency. (2) The angular dispersion together with imaging errors creates significantly different pulse durations at the edges of the pump spot in the image plane compared with the pulse duration at the center. This pulse duration discrepancy results in reduced efficiency and low quality of the THz beam. (3) The large wedge angle leads to a large path length difference for the pump and THz pulses on the face opposite to the face, through which the crystal is pumped. Consequently, the THz pulse shape generated is strongly dependent on the transversal position with respect to the propagation axis, thus resulting in decreased efficiency and low THz beam quality.

The 1st type of limitation can be mitigated in two different ways: (i) using pump pulses with narrower spectrum (shorter Fourier-transform-limited pulses) [284], and (ii) using nonlinear crystals, which need smaller tilt angles [285,286].

Both the 2nd and 3rd types of the tilted front limitation could be eliminated by using a contact grating on the input face of a plane-parallel nonlinear crystal for tilting the intensity front, instead of using the external grating imaging system [287]. Although such a LN THz source was realized, its efficiency was low because of technical reasons originating from the large required tilt angle/groove density [288,289]. At the same time, the contact grating technique was very

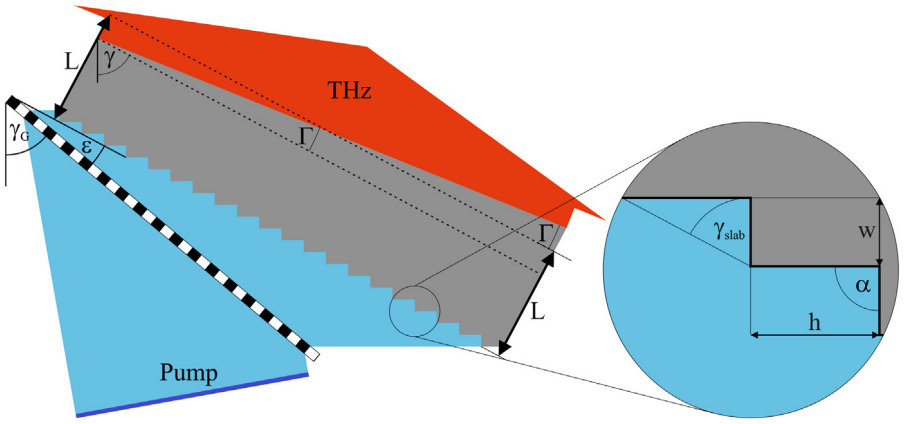

Fig. 28. Hybrid TPFP LN setup consisting of a transmission grating (wide black dashed line) for creating a pre-tilt of the pump intensity front and a plane-parallel LN slab (marked in gray) with an echelon structure on its input face. The solid dark blue line shows the intensity front of the pump pulse whereas the resulting THz pulse is shown in red. The whole interaction region of length L is effectively used for coherent THz generation.. *Source:* Adopted from Ref. [293].

effective for a semiconductor nonlinear optical material [286]. Hopefully, by improving the technique of producing high groove density relief gratings on the surface of LN, the contact grating technique will be made effective for LN and LT materials too.

Decreasing the required groove density is possible using the so-called hybrid TPFP LN setup [290], in which the necessary tilt of the intensity front is created in two steps. First, about half of the tilt angle is generated by a conventional grating-imaging optics setup. Second, the remaining part of the required tilt is introduced via diffraction of the pump beam on the (reduced groove density) contact grating created on the input face of the LN crystal. Thanks to the smaller tilt angle introduced in the first step, the 2nd type of the tilted front limitation is also very much relaxed compared to the conventional setup. Although in this setup a LN prism has to be used, its wedge angle is only about 30 °, thus relaxing also the 3rd type of the limitation significantly.

Very recently another type of the hybrid TPFP LN setup has been suggested [291]. It uses a plane-parallel LN slab with an echelon grating structure on its input face, see Fig. 28 (note that in this setup the position and purpose of the echelon grating is different from the one used in the work of Ofori-Okai [292]). Here a pre-tilt angle (γ_0 in air) equal to the required final tilt angle inside the LN crystal ($\gamma = 63\,^\circ$) is introduced via diffraction of the pump beam on a transmission grating. When the pump laser pulse enters the crystal through the echelon grating structure, the (average) tilt angle of the intensity front turns out to be equal to the required tilt angle inside the LN crystal.

Note that contrary to the original suggestion [291], a single transmission grating is enough to introduce the necessary pre-tilt and thus any imaging can be omitted [294]. Hence, the setup avoids imaging errors, and the pump beam spot size as well as the generated THz energy are scalable.

3.1.3. Optical rectification in semiconductor crystals

Semiconductors were among the first crystals used for THz pulse generation by OR [295]. Although many semiconductors are suitable for efficient THz generation, ZnTe became the most frequently used one for high-energy THz pulse generation thanks to its rather large nonlinear optical coefficient (see Table 1). What is even more important, for this material the velocity matching condition (Eq. (10)) is fulfilled for the wavelength (≈810 nm) of the widely-used Ti:sapphire ultrashort-pulse laser. The upscaling of the generated THz energy up to 1.5 μJ was possible just by increasing the pump pulse energy and the pump spot size [296,297]. Focusing of the THz beam (around 30 mm FWHM diameter) from a large-aperture ZnTe single crystal wafer resulted in more than 200 kV/cm field strength [297]. However, the energy conversion efficiency from the pump laser pulse to the THz one was only 3×10^{-5}. It was recognized that two-photon absorption (2PA) and the THz absorption of the free carriers generated by the 2PA limit the efficiency.

2PA can be eliminated by using longer wavelength pump sources [298]. Pumping of GaAs with 1.8 μm pump pulses resulted in 5×10^{-4} efficiency [299]. The investigation of the generated THz pulse energy as a function of the pump intensity by pumping ZnTe, GaP and LN crystals with 1.03 μm wavelength pulses of an Yb laser clearly demonstrated (see Fig. 29) the efficiency limiting effect of not only the 2PA, but also the three-photon absorption (3PA), (even four-photon absorption (4PA) in the case of LN) [300]. Table 1 shows some 2PA, 3PA, and 4PA coefficients.

Of course, not only 2PA, but also 3PA and 4PA, can be eliminated by using long enough pump wavelengths. However, for longer wavelengths the index of refraction is smaller, and typically a longer wavelength results in a higher pump pulse velocity than the THz phase velocity such that Eq. (10) is not fulfilled. In such a situation the TPFP velocity matching technique can be used. This technique was applied in setups using GaAs [299], and very recently, using ZnTe [285] for OR.

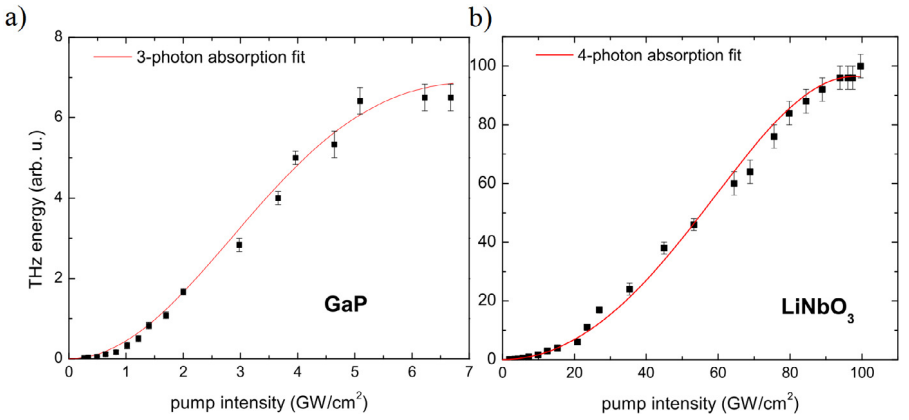

Fig. 29. Measured (squares) saturation of THz pulse generation by OR in GaP (a) and LN (b). The fitting curves were obtained by taking into account 2PA and 3PA for GaP and 2PA, 3PA, and 4PA for LN.
Source: Adopted from Ref. [300].

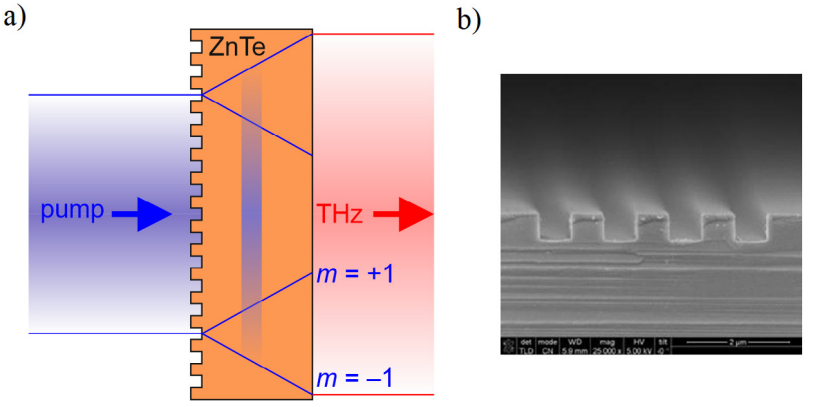

Fig. 30. Scheme of the contact grating ZnTe TPFP THz source.
Source: Adopted from Ref. [285].

In the latter case, 1.7 μm pump pulses were used in order to eliminate both 2PA and 3PA, and as high as 0.7% conversion efficiency was achieved.

The TPFP technique applied to long wavelength pumping of semiconductors in order to achieve velocity matching, requires only 30 degrees or less tilting angle [285]. This moderate tilting can be realized using the so-called contact grating technique (see previous subsection) [287]. The experimental setup in this case is very simple (see Fig. 30): the pump beam enters perpendicularly to the surface of the plane-parallel ZnTe crystal, and the generated THz pulse leaves the crystal collinearly with the pump beam [286]. In this setup the diffraction of the pump beam into the $+/-1$ order creates the tilt of the pump intensity fronts in the diffracted beams with opposite signs, merging the two pulse fronts into a single strip parallel to the output surface of the crystal (see Fig. 30a) [301]. (The intensity fronts are parallel to the surfaces of the crystal for both orders.) Even with an imperfect contact grating structure, this setup resulted in 0.3% conversion efficiency [286], and further increase of the efficiency is predicted for optimized conditions (crystal thickness, pump pulse duration) [302].

Among different semiconductors having nonlinear optical response, GaSe is the one that allowed the generation of near single-cycle THz pulses with the highest focused electric field [26]. The reported peak field strength was 12 MV/cm, that is 60 times larger than that obtained using ZnTe [297]. In the case of GaSe, optical parametric amplification (OPA) was actually used instead of OR for THz generation. However, neither the different frequency conversion processes, nor the different nonlinear optical materials used explain this huge contrast in the achieved peak electric field. Instead, the separation in frequency between the generated THz pulses (<2 THz for ZnTe and 22 THz for GaSe) is the main reason. According to Eq. (12), for the same nonlinear optical coefficients (ZnTe and GaSe have similar d_{eff} values, see Table 1) and the same pump intensities, the peak field strength at the output surface on the nonlinear crystal will be proportional to the central frequency of the generated THz pulse. Using focusing optics with the same numerical aperture a further increase, proportional to the frequency ratio is expected for the focused field.

3.1.4. Optical rectification in organic crystals

Using 10 nJ pump pulses from a Ti:sapphire laser, THz pulse generation by OR from an organic nonlinear optical crystal DAST was demonstrated as early as 1992 [303], but the detected focused THz field was only 2 V/cm. Using 50 μJ energy pump pulses at 1.5 μm resulted in a 20 kV/cm focused THz field [304]. In that paper some important properties of DAST were reported, such as nonlinear coefficients for different polarizations, THz absorption resonances and 2PA coefficients at 1.3 μm. This value is advantageously small: $\beta = 0.7$ cm/GW.

It was also demonstrated that other organic crystals such as OH1 and DSTMS are excellent materials for THz generation by OR. For example, by pumping OH1 at a 1.35 μm wavelength an almost linear increase in conversion efficiency up to 1.75% was achieved for pump peak intensities up to 110 GW/cm^2 [305]. Using pulses of up to 35 mJ energy from a Cr:forsterite laser working at 1.25 μm wavelength, more than 1%, 2%, and 3% conversion efficiency was demonstrated for DSTMS, DAST and OH1 nonlinear crystals, respectively [130]. Focusing the generated THz pulses, peak electric fields between 6 and 18 MV/cm were achieved. The corresponding magnetic field reached 5 T.

The process of growing of the mentioned organic nonlinear crystals limits their size to about 1 cm × 1 cm × 1 mm. At the same time, the small thickness is compensated by the huge nonlinear optical coefficient of these crystals (see Table 1). The limitation on the usable pump spot size from the small transversal size of the crystals can be eliminated by using partitioned crystals [306] assembled as a mosaic of crystal pieces on the surface of a substrate. Using this technique, THz pulse energies as high as 0.9 mJ were generated [27]. This is the highest THz pulse energy generated up to now.

Organic crystals are also suitable for generating ultra-broadband THz pulses. Pumping DSTMS with 25-fs-long Ti:sapphire laser pulses, THz pulses with 22 THz FWHM spectral width were generated. The temporal shape of the THz pulses consists of the dominant (energy wise) part that is approximately one and a half cycles long and contains a leading peak having an amplitude of 0.8 MV/cm and 40 fs duration, followed by a ringing for a few picoseconds.

3.2. Plasma-based THz generation

A promising alternative for THz pulse generation is based on femtosecond-laser-induced plasma formation in a gaseous medium. THz generation in plasmas has the advantage that the applicable pump intensity is not limited by damage threshold and high frequency generation is not limited by phonon resonances.

3.2.1. THz generation in air-plasma

Intense THz pulses have been generated in photo-induced plasma using femtosecond laser pulses with intensities exceeding the ionization threshold of gas molecules. In the first experiment, demonstrated by Hamster et al. [307], TW 120 fs optical pulses were focused both on gas and solid targets. For the former, the ponderomotive force of the laser pulses, originating from the gradient of the laser intensity, led to strong separation of electrons and ions. When the laser pulse duration was close to the inverse plasma frequency, the ponderomotive charge separation resonantly excited plasma waves. Correspondingly, the resulting plasma density oscillations were accompanied by strong broadband THz radiation. Moreover, at the highest plasma densities an additional peak in the radiation spectrum with the frequency completely different from the bulk plasma frequency was observed. The proposed explanation was the nonlinear current at the frequencies corresponding to the sum and difference of the carrier frequency and bandwidth of the laser pulses.

Using external DC bias in the focal point of the intense laser pulse, the energy of the THz pulse can be increased by one order of magnitude. The bias creates a transversal polarization and accelerates the electrons, which enhances the THz field. The first demonstration of the DC-bias method was carried out by Löffler et al. [308].

To increase THz pulse energy further, the nonlinear interaction of the fundamental (ω) and the second harmonic (2ω) in a laser generated plasma was proposed by Cook et al. [309] in 2000. In the setup, a thin β-barium borate (BBO) crystal was placed after the focusing lens in the path of the Ti:Sapphire (800 nm) fundamental beam to generate the second harmonic. The ω and 2ω waves combined created a plasma at the focus. The process of THz generation was described by four-wave-mixing (FWM) (a third-order nonlinear process), where the polarization in the THz range is as follows [310]:

$$\mathbf{P}(\omega_{\mathrm{THz}}) = \epsilon_0 \chi^{(3)}(\omega_{\mathrm{THz}}, 2\omega - \omega_{\mathrm{THz}}, -\omega, -\omega)\mathbf{E}(2\omega - \omega_{\mathrm{THz}})\mathbf{E}^*(\omega)\mathbf{E}^*(\omega). \tag{17}$$

However, the third-order nonlinearity resulting from either bound electrons or free electrons in the plasma turned out to be too small to explain the observed THz field strength [311]. Kim et al. [311] developed a transient photocurrent model to explain the third-order nonlinearity, where the motion of the electrons produced a DC electron current. The resulting electric field of the fundamental and the second harmonic can be expressed as:

$$E_{\omega+2\omega} = E_\omega \cos(\omega t + \phi) + E_{2\omega} \cos[(\omega t + \phi) + \theta], \tag{18}$$

where E_ω and $E_{2\omega}$ are the corresponding amplitudes, and θ is the relative phase between the fields [311]. Fig. 31a shows the electric fields and the drift velocity of the electrons for $\theta = 0$ (even function symmetry) and for $\theta = \pi/2$. The ionization occurs near the peak of the laser field and, in the case of $\theta = 0$, the velocity of the electrons is cancelled for the electrons, which are born at the opposite laser field slopes (Fig. 31a dashed area) [311]. For $\theta = \pi/2$, a time-varying electron current density is created, which produces THz radiation [311]. The generated transient current is given by the superposition of elementary currents produced by the electrons born at different times t':

$$J_\perp(t) = \int_{t_0}^{t} q_e v_e(t, t') N_e(t') dt', \tag{19}$$

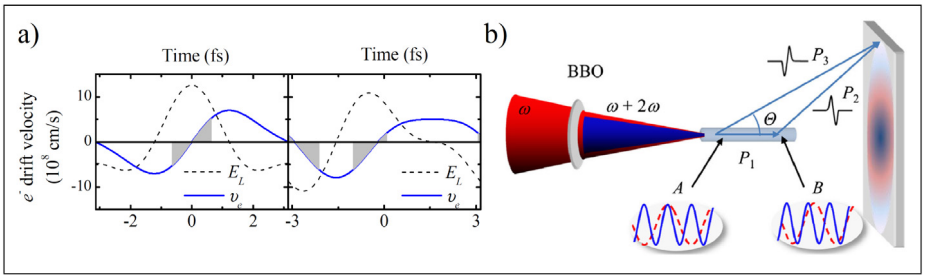

Fig. 31. (a) Drift electron velocity (solid line) vs. ϕ in the laser field (dashed line) for $\theta = 0$ and $\theta = \pi/2$ in the photocurrent model [311]. (b) Setup for THz generation using a long two-color filament in the off-axis phase matching method. The cone-shaped THz radiation is produced by interference between the waves emitted from the local sources along the filament [314].
Source: Adopted from Refs. [311,314].

where $v_e(t, t')$ is the electron's velocity and $N_e(t')$ is the electron density. The power of the produced THz pulse is proportional to dJ/dt [311]. Many later experiments showed that the photocurrent and the amplitude of the THz pulses are very sensitive to the relative phase θ (the plasma interaction length is typically limited to 10 mm). In 2008, by using this technique, Kim et al. [312] demonstrated a coherent broadband THz source with 5 μJ energy and more than 10^{-4} conversion efficiency.

Further improvement of the THz pulse generation is possible with longitudinal extension of the plasma. Filamentation appears spontaneously when an intense laser pulse is focused on, and launched through, a transparent medium with a critical power higher than $P_{cr} = 3.72\lambda^2/8\pi n_0 n_2$, where n_0 and n_2 are the index of refraction and optical Kerr constant at the laser frequency (for air $P_{cr} \approx 5$ GW), respectively. Long scale plasma filaments can occur due to the balancing between self-focusing caused by modification of the index of refraction by the Kerr effect and the ionization-induced defocusing. The intensity of the self-guided pulse is increased adequately in the paraxial region and maintained for a long distance of some cm. The first single-color (more than 10 cm long) filament experiment on THz generation was demonstrated in air with femtosecond pulses by D'Amice et al. [313] in 2007. The THz radiation is emitted in a very narrow cone in the forward direction and the angle of the most intense radiation can be described with $\theta_{max} = \sqrt{\lambda/L}$, where λ is the radiation wavelength and L is the length of the medium.

In the case of two-color filaments, the relative phase (θ) between the fundamental and the second harmonic wave varies along the plasma interaction region. Therefore, the amplitude and the polarity of the THz radiation generated at different points also change, which is predicted to create negligible THz energy gain in the longitudinal direction. At the same time, phase matching can be satisfied in the off-axis instead of the on-axis direction, which was explained by the interference effect (see Fig. 31b). You et al. [314] carried out experiments using the off-axis phase matching method for short filaments (<7 cm) and Oh et al. [315] extended the study for longer filaments and TW-level lasers, for which efficient broadband THz pulse generation is possible.

The relative phase between the fundamental and the second harmonics can be described as $\theta = \omega(n_\omega - n_{2\omega})l/c + \theta_0$, where n_ω and $n_{2\omega}$ are the indices of refraction of the plasma filament at ω and 2ω, respectively, l is the filament length and θ_0 is the relative phase at the beginning of the filament. Because of plasma dispersion, θ changes along the filament from 0 to π over a dephasing length $l_d = (\lambda/2)(n_\omega - n_{2\omega})^{-1}$, where $\lambda = 2\pi c/\omega$ is the wavelength. For instance, using a Ti:sapphire laser and $\sim 10^{19}$ cm^{-3} electron density air, the dephasing length is just $l_d \approx 22$ mm, which limits the filament length to a few cm. However, You et al. [314] showed that efficient THz generation by constructive interference can be possible in the off-axis direction when $\cos(\theta) = 1 - \lambda_{THz}/2l_d$ (see Fig. 31b). The far-field THz radiation has a conical shape due to the off-axis interference. The total THz electric field can be estimated as the sum of contributions from the local, nonlinear polarization along the filament. Using a 2 TW Ti:sapphire laser and a ~15 cm long filament, a THz pulse energy of ~7 μJ was measured [315]. THz emission from two-color laser-induced plasma was also studied using the noble gases neon, argon, krypton and xenon [316]. The dependence of the spectrum and the energy of the THz pulses were measured as a function of gas type, gas pressure and the input pulse energy up to 6 mJ using a Ti:sapphire laser [316].

Gorodetsky et al. [317] extended the theoretical model of THz radiation from two-color laser-induced plasma filaments. The model uses relativistic plasma densities and includes broadband THz pulses. According to their calculations, the THz far-field has a donut like shape, which shows very good agreement with the experiments. Their result shows that the angle of the emission decreases with a reduced electron density and increases with the filament length [317]. The THz radiation can be increased with the extension of the filament length.

Recent studies showed that increasing the pump wavelength can enhance the THz pulse energy and the conversion efficiency for single-cycle THz field generation by two-color laser induced ionization. In 2013 Clerici et al. [318] experimentally investigated the dependence of the THz field on the wavelength of the fundamental laser (λ), where the wavelength was varied from 800 nm to 2020 nm. The experimental setup is shown in Fig. 32a in which the wavelength-tuneable pulses from the optical parametric amplifier are focused together with the second harmonic. The generated THz pulses are collected by parabolic mirrors and focused to the air-biased-coherent-detection (ABCD) setup [318]. Instead of

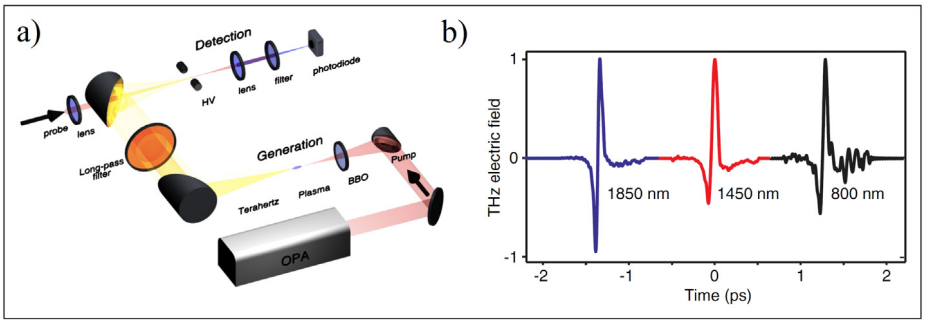

Fig. 32. The scheme of the experimental setup using a two-color laser induced plasma source (a). The normalized THz electric field distributions acquired by the ABCD detection scheme at 1850, 1450, and 800 nm pump wavelengths (b).
Source: Adopted from Ref. [318].

the λ^2 theoretical and numerical prediction, the THz pulse energy turned out to be proportional to $\lambda^{4.6}$ in the investigated region. It was also demonstrated that one order of magnitude higher conversion efficiency can be achieved with a 1800 nm pump pulse compared with a 800 nm pump pulse. The peak electric field of the observed THz pulses exceeded 4.4 MV/cm, as calculated from the energy (630 nJ), beam profile (∼85 μm) and temporal electric field distribution of the THz pulse. The normalized electric field distributions of measured THz pulses at 1850 nm, 1450 nm and 800 nm are shown in Fig. 32b.

Recently, THz generation was studied numerically by Fedorov et al. [319] using the two-color filamentation technique with mid-infrared 3.9 μm laser pulses in air. It was predicted that the conversion efficiency could be two orders of magnitude higher than in the case of 800 nm and could exceed the one percent level. Furthermore, the energy of the THz pulses could reach the mJ level and the electric field strength could go beyond the GV/cm level [319].

Also recently, through numerical simulations the investigation of the two-color filamentation by femtosecond pulses in air was extended from 800 nm to 10.6 μm by Nguyen et al. [320] using a three-dimensional unidirectional solver. In their calculation, the effects of the ambient conditions (temperature and humidity) and the influence of the many-body Coulomb ionization were outlined. It turned out that two-color CO_2 laser filaments can produce a THz conversion efficiency exceeding the one percent level at moderate laser intensities ($<10^{15}$ W/cm^2) and the THz pulses can reach the mJ energy scale [320].

3.2.2. THz generation in solid foils

THz pulse generation is also possible in plasmas, which are produced at the surface of solids by high-power lasers with intensities exceeding 10^{18} W/cm^2. Such a process induced by laser pulse interaction with a metal foil (5 μm thick titanium) target was observed by Sagisaka et al. [321] in 2008. An antenna mechanism model was proposed, where the THz radiation is generated at the front surface of the metal foil by electrons moving along the target surface and producing a time-dependent electric current [321]. According to their calculations, the total energy of the THz pulse can be estimated as

$$E_{\mathrm{THz}} = \frac{B^2}{4\pi}\frac{4\pi r^3}{3},$$

where B is the generated magnetic field and r is the electron displacement. Li et al. [322] has reported THz pulses with 50 μJ energy from the front surface of a solid target in 2011.

THz pulse generation was also observed in the vicinity of the *rear side* of the metal foil and the first intense THz pulse generation was demonstrated by Gopal et al. in 2013. For sub-joule incident laser pulse energies from a Ti–Sapphire laser, 460 μJ [323] and 700 μJ [324] THz pulse energies were measured.

A recent publication by Herzer et al. [325] has extended the investigation of the THz generation at the rear side of the metal foil. The dependence of the THz pulse energy on the pump pulse duration, energy, target material and thickness was examined. In general, upon illumination of the foil by intense laser pulses, two processes can lead to coherent THz radiation: transition radiation and sheath radiation [325]. First, transition radiation is generated due to the hot electrons, which exit the rear surface (see Section 3.3.1 for more details on transition radiation). Then, sheath radiation is generated due to the transient dynamics of the plasma sheath [325]. The physical picture of sheath radiation in some more detail is as follows: due to the interaction of laser pulses with the metal foil, hot electrons are first generated and accelerated. Then, they propagate through the foil and leave the rear surface [325]. This process creates a strong quasi-static electric field (referred to as the sheath field) due to the charge separation. Furthermore, the sheath field ionizes neutral atoms on the rear surface, and accelerates them in the forward direction. The ion acceleration process (knows as sheath acceleration) leads to the emission of very broadband transient THz radiation. The coherence, energy and the spectra of the generated radiation depend on the dynamics and the temporal characteristics of the ion bunch [325].

The schematic view of the experiment, where both processes were measured, is shown in Fig. 33a [325]. The two different radiation processes occur at different radiation angles (in Fig. 33a transition radiation, displayed in red, has

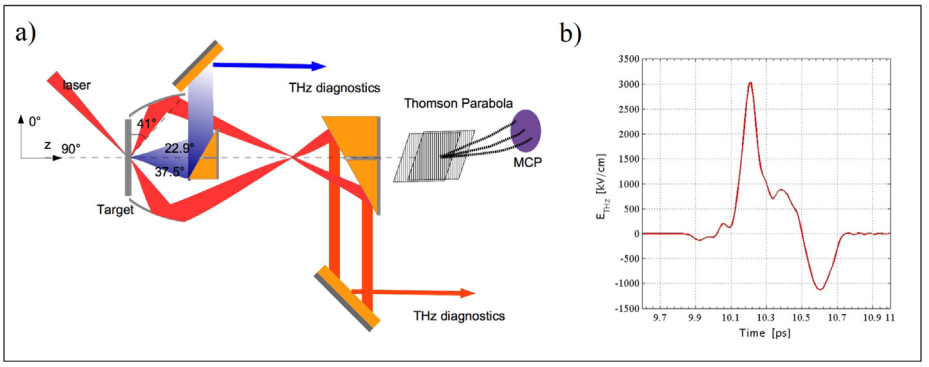

Fig. 33. (a) Schematic of the experimental setup for THz generation in a solid foil. Red and blue lines indicate the sheath radiation and transition radiation paths. (b) EO measurements of the THz radiation generated by sheath are shown.
Source: Adopted from Ref. [325].

a 41 ° radiation angle while that of sheath radiation, displayed in blue, is defined between $90 - 22.9\,°$ and $90 + 37.5\,°$) and the radiation is radially polarized in both cases. Using a 30 fs, 1 J pump laser pulse, 712 μJ and 40 μJ pulse energies were measured for the sheath and transition radiation cases, respectively. The temporal shape of the electric field of sheath is shown in Fig. 33b and it demonstrates the peak electric field exceeding 3 MV/cm. According to the theoretical prediction, it could go beyond 100 MV/cm [325].

3.3. Radiation from charged particles passing through discontinuities

THz light sources based on transition radiation from ultrarelativistic electron bunches have demonstrated the highest field strength (around 50 MV/cm) compared to any other THz technology with the cutoff frequency up to 30 THz. In Section 3.3.1, we consider the underlying physical principles of such sources and some recent experimental results. Novel ideas on how to improve the efficiency and control the emission pattern of transition radiation-based sources are presented in Section 3.3.2.

3.3.1. Transition radiation

A charged particle moving with a constant velocity along a straight line in free space does not radiate. The situation, however, changes if the moving charge traverses an interface, for example, between free space and a medium while continuing its uniform motion. The electromagnetic fields of the charge in free space and the medium are different due to the presence of polarization in the medium. Therefore, the Coulomb field of the charge in vacuum has to reorganize its structure as the charge passes through the interface. During this reorganization process some part of the Coulomb field bounded to the charge is released in the form of radiation known as *transition radiation* [326]. In this picture, the charge is assumed to be in subluminal uniform motion in the medium and, therefore, no Cherenkov radiation is present.

The simplest and widely used configuration for the production of transition radiation is that of a uniformly moving charge crossing an interface between vacuum and a metal. This situation is schematically depicted in Fig. 34a. The charge moves at speed v in the free half-space ($z < 0$) perpendicularly towards the metal occupying another half of the half-space ($z > 0$). It induces an image charge on the metal surface. For a perfect metal, the field distribution is equivalent to that of the original charge, plus the field distribution of an oppositely charged image source on the other side of the interface, Fig. 34a.

The configuration of the moving charge and its image can be thought of as an electric dipole with a moment $p = 2evt\,U(z - vt)$, where U is the Heaviside unit-step function. At the time $t = 0$, the moving charge impinges on the metal surface at $z = 0$ and abruptly disappears as its field becomes screened. This abrupt change results in a non-zero value of the second time derivate of the dipole momentum: $\ddot{p} = 2ev\,\delta(z - vt)$ giving rise to a spherical wave diverging from the point where the electron disappeared (recall that for *dipole radiation* $\mathbf{E} \propto \ddot{\mathbf{p}}$):

$$E_\theta = B_\phi = \frac{e}{2\pi\varepsilon_0 c^2}\,\delta\left(t - \frac{r}{c}\right)\frac{\beta\sin\theta}{r}. \tag{20}$$

Here, r, θ and ϕ are the spherical coordinates and $\theta = 0$ corresponds to the positive direction along the z-axis. For convenience, the particle velocity v is normalized to the speed of light c, $\beta = v/c$. Qualitatively, the field distribution can be understood by considering the fields produced by the charge as it instantly stops. This situation is depicted in Fig. 34b, which shows a snapshot of the electric field distribution. In the vicinity of the charge, the electric field is a Coulomb field of the charge at rest. In the far zone, the electric field is a Coulomb field of the uniformly moving charge. An abrupt change in the charge velocity requires the electric field lines to reorganize. As a result, an azimuthal component of the electric field appears. It decays as $1/r$ corresponding to a propagating wave [327].

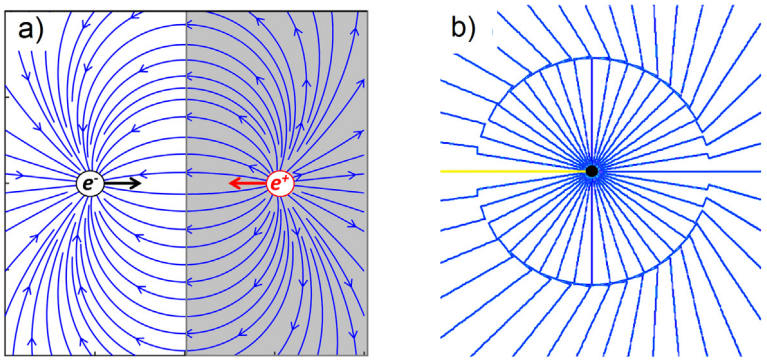

Fig. 34. (a) Electric field lines (blue) of a uniformly moving (from left to right) charge and its image in the metal (shaded rectangle). (b) Electric field lines (blue) of the charge (black) that was in a uniform motion along the straight line (yellow) at 30% of the speed of light and, then, abruptly stopped. An instant change in the velocity gave rise to a spherical wave with the electric field lines being orthogonal to the Coulomb field lines of the charge at rest..

The Fourier component $E_\theta(\omega)$ of Eq. (20) propagates in the radial direction and has an amplitude proportional to $\exp(i\omega r/c)$. In this model of transition radiation, the white spectrum reflects the assumption of a perfect conductor and, correspondingly, of instantaneous screening of the charge (delta function factor in Eq. (20)) as it impinges on the metal surface. This assumption is a good approximation for most of the metals in the THz frequency range and up to the visible spectral region. At shorter wavelengths, for instance ultraviolet and soft X-ray regions, metals become transparent to electromagnetic radiation. Hence, the upper boundary of the spectral range of transition radiation extends to roughly the plasma frequency. The *relativistic* correction factor modifies the Fourier component $E_\theta(\omega)$ to read

$$E_\theta(\omega) = \frac{e}{4\pi^2\varepsilon_0 c}\frac{\beta\sin\theta}{1-\beta^2\cos^2\theta}\frac{e^{i(\omega/c)r}}{r}. \tag{21}$$

Already from the elementary picture of transition radiation, Eqs. (20)–(21), we can draw a few conclusions: (i) the electric field distribution has a donut shape and vanishes on the axis of the effective dipole, (ii) the spectral bandwidth of the emitted field depends on how quickly the charge becomes screened in the medium, (iii) the field strength depends on the charge velocity, and (iv) for relativistic motion, the donut shape field distribution becomes skewed towards the direction of charge motion, resembling a butterfly.

The *spectral energy* emitted per unit solid angle and per electron is given by the Ginzburg–Frank formula

$$\frac{\mathrm{d}^2 W_{\mathrm{GF}}}{\mathrm{d}\omega\mathrm{d}\Omega} = \frac{e}{4\pi^2\varepsilon_0 c}\frac{\beta^2\sin\theta^2}{(1-\beta^2\cos^2\theta)^2} \tag{22}$$

This formula holds in the far-field zone for normal incidence of the charge and an infinitely large screen. The angular distribution has its maximum at the angle $\theta \approx 1/\gamma$. Integration over the solid angle gives the spectral energy per electron

$$\frac{\mathrm{d}W_{\mathrm{GF}}}{\mathrm{d}\omega} = \frac{e^2}{4\pi^2\varepsilon_0 c}\left(\frac{1+\beta^2}{2\beta}\ln\frac{1+\beta}{1-\beta}-1\right) \tag{23}$$

and for relativistic motion $\gamma = (1-\beta^2)^{-1/2} \gg 1$ it takes on the limiting form

$$\frac{\mathrm{d}W_{\mathrm{GF}}}{\mathrm{d}\omega} \approx \frac{e^2}{2\pi^2\varepsilon_0 c}\ln\gamma. \tag{24}$$

Alternatively, the efficiency of the generation of transition radiation per electron can conveniently be written in terms of the number of emitted photons. Consider a frequency band from ω to $\omega + \mathrm{d}\omega$ and introduce the number of emitted photons in the band n_ω. By definition, the spectral energy density is $\mathrm{d}W/\mathrm{d}\omega = n_\omega\hbar$. Then, Eq. (24) yields

$$n_\omega = \frac{2\alpha}{\pi}\ln\gamma, \tag{25}$$

where $\alpha = e^2/(4\pi\varepsilon_0\hbar c) \approx 1/137$ is the fine constant. For mid-relativistic beams with, for example, $\gamma \sim 10$, one photon in the frequency band from ω to $\omega + \mathrm{d}\omega$ is emitted per approximately one hundred counts of the charge impingement on the interface. For an electron bunch composed of N electrons, $\mathrm{d}W/\mathrm{d}\omega$ and correspondingly n_ω must additionally be multiplied by N^2. This is the *regime of coherent transition radiation* (CTR).

The physical mechanism of transition radiation is based on the acceleration of charges in a medium in response to the Coulomb field of the uniformly moving charge. Hence, there is no appreciable radiation from the moving charge unless it

is sufficiently close to the medium and its field is in phase with the excited field. The length needed to form the emission is known as the *formation length* [328]. The phase of the driving field is simply determined by the phase of the moving Coulomb field, *i.e.*, $(\omega/v)z$. The phase of the on-axis transition radiation is $(\omega/c)z$. The formation length is defined by the condition that the interference term between the two fields becomes small, $\omega(1/v - 1/c)z \gg 2\pi$, *i.e.*, two fields become uncorrelated. The minus sign corresponds to the co-propagating fields, *i.e.*, the charge and transition radiation move in the same direction. The *formation length* L_f is defined as the phase difference of 2π, which yields

$$L_f = \frac{\lambda}{1-\beta} \approx 2\gamma^2\lambda. \tag{26}$$

This can also be interpreted as the distance over which the radiation field slips ahead of the electron by one radiation wavelength. For a charged particle with an energy of a few GeV, the formation length of THz radiation in the forward direction is huge: on the order of 100 m. Therefore, the backward transition radiation is used in practical setups. In this case, $L_f \approx \lambda$ and a detector or focusing mirror can be placed closely to the emitting area.

In the transverse direction, the Coulomb field of the moving charge extends to distances in the order of $\gamma v/\omega$ [328]. This scale, $\gamma v/\omega$, is known as the *transverse coherence length* $L_\perp$. For ultra-relativistic particles, $L_\perp$ is some tens of centimeters at THz frequencies. The physical meaning of $L_\perp$ is the minimum radius of the emitting screen required to provide efficient scattering of the incident Coulomb field of the moving charge off the screen in order to produce appreciable transition radiation at frequency ω. If the screen radius a is smaller than $\gamma\lambda$, then the spectral energy per unit solid angle (22) is reduced and takes on the form [329]

$$\frac{\mathrm{d}^2W_{\mathrm{disk}}}{\mathrm{d}\omega\mathrm{d}\Omega} = \frac{\mathrm{d}^2W_{\mathrm{GF}}}{\mathrm{d}\omega\mathrm{d}\Omega}\left[1 - J_1\left(\frac{2\pi a \sin\theta}{\lambda}\right)\right]^2. \tag{27}$$

For an electron bunch of *finite duration*, the waves emitted by individual electrons are phase shifted with respect to each other. The phase shift depends on the electron position in the bunch and, correspondingly, the time instant the electron impinges on the screen. In order for the coherent superposition of the waves to occur, the rms phase shift should be much smaller than the wavelength. The effect of the finite bunch duration is taken into account by the *form-factor* $F(\omega) = (1/e)\int I(s)\exp(-i\omega s/v)ds$, where $I(s)$ is the electron current profile with s being the coordinate along the bunch. Then, the spectral energy $\mathrm{d}W_{\mathrm{GF}}/\mathrm{d}\omega$ renormalizes by the factor $N^2|F(\omega)|^2$ giving the relative reduction compared to the case of a point-like source containing N electrons. For relativistic bunches, the impact of finite transverse extent of the bunch can be disregarded because of a large transverse coherence length.

The record-high THz field of 44 MV/cm (0.44 V/Å) was achieved in a coherent transition radiation source using 14 GeV electron bunches from the Linac Coherent Light Source (LCLS) at Standford [29]. The corresponding magnetic field is around 14 T. The electric, and correspondingly magnetic, field has a clear dominant peak that is useful for symmetry breaking in experiments or for studying nonlinear processes having a threshold. The schematic of the radiation source is depicted in Fig. 35. It uses electron bunches impinging on a 10-μm-thick Be foil at 45 degrees. Fig. 36a shows the temporal profile of the electric field reconstructed from autocorrelation measurement results using the Kramers–Kronig relation. The electron bunches are as short as 70 fs FWHM and carry the charge up to 350 pC. The total energy emitted in the forward direction reaches 1 mJ and the spectral energy spans a wide spectrum from 3 to 30 THz peaking at 10 THz. The dependence of the emitted energy vs. the bunch duration for different bunch charges is presented in Fig. 36b. Similar, though slightly less outstanding, parameters of THz sources based on coherent transition radiation have been demonstrated at the Facility for Advanced Accelerator Experimental Tests also located at Standford [29] and at the free-electron laser Freie-Elektronen-Laser in Hamburg (FLASH). Another Ref. [330] reports a compact THz source with a field strength of 10 kV/cm employing 3 MeV, 1 ps, 60 pC electron bunches. Using a train of electron bunches with 100 pC charge at 120 MeV beam energy, a narrowband (less than 10%) CTR signal with a peak field up to 1 MV/cm was observed in Ref. [331].

EOS applied at FLASH allowed for direct determination of the temporal profile of the THz electric field below 10 THz, Fig. 37. Note that for experiments requiring frequency resolution, a bandpass filter can be applied as demonstrated also in Fig. 37. In EOS measurements, a femtosecond laser is synchronized to the electron bunch with a synchronization accuracy of better than 100 fs. The THz field induces birefringence in a crystal used for sampling. This birefringence, linear with the applied field, is probed via a change in the optical polarization of the femtosecond laser pulse. The delay between the THz pump pulse and the femtosecond laser pulse probe is changed in steps of 33 fs. The measurement reveals the fine structure of the THz pulse: the central dominant peak is accompanied by two peaks with the amplitudes being approximately half of the maximum. This profile is a typical manifestation of the dispersion effect of spatially confined light in free space [332]. Because of transverse confinement the longitudinal wavenumber is a nonlinear function of frequency. Hence, a transversely-confined pulse exhibits dispersion even in free space and corresponding temporal reshaping, see a related demonstration of the reshaping in Fig. 4 of Ref. [333].

3.3.2. Diffraction radiation

In general, transition radiation occurs each time a charge in uniform motion passes through an *inhomogeneous medium* or next to any discontinuity in the medium. The interface between two semi-infinite homogeneous media discussed in Section 3.3.1 is a particular case of the discontinuity between the two media. Another simple example is transition

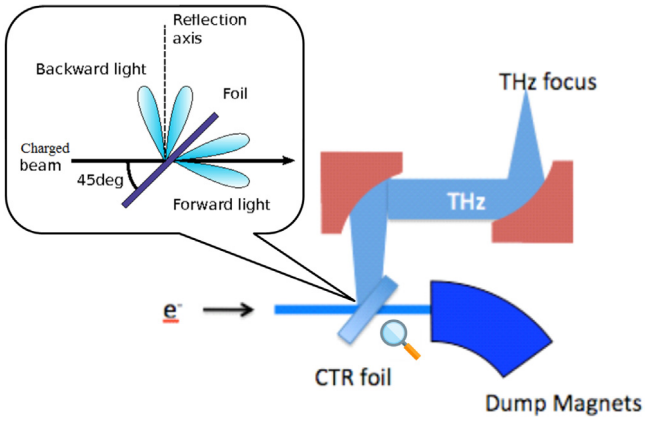

Fig. 35. Schematic of a setup used for the generation, guiding and focusing of coherent transition radiation. The inset shows schematically the emission pattern from an electron bunch impinging at 45 deg. on a thin metal foil. Two off-axis parabolic mirrors are used to transport and focus the radiation.
Source: Adapted from [29].

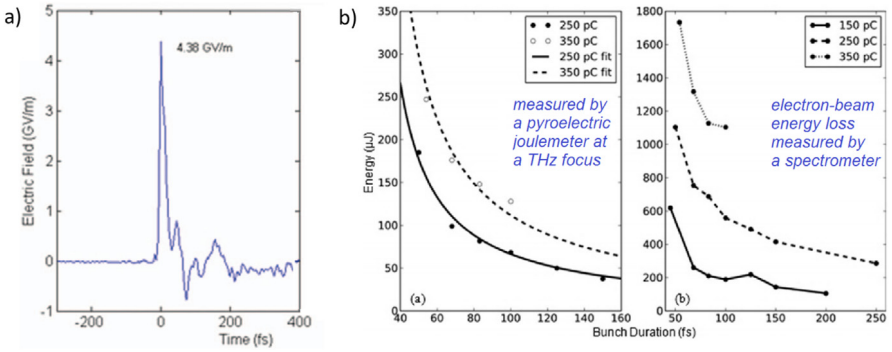

Fig. 36. (a) Reconstructed THz field profile at the focus. (b) Emitted energy of the THz pulse measured at the focus (left) and estimated through the electron-beam energy loss (right).
Source: Adopted from Ref. [29].

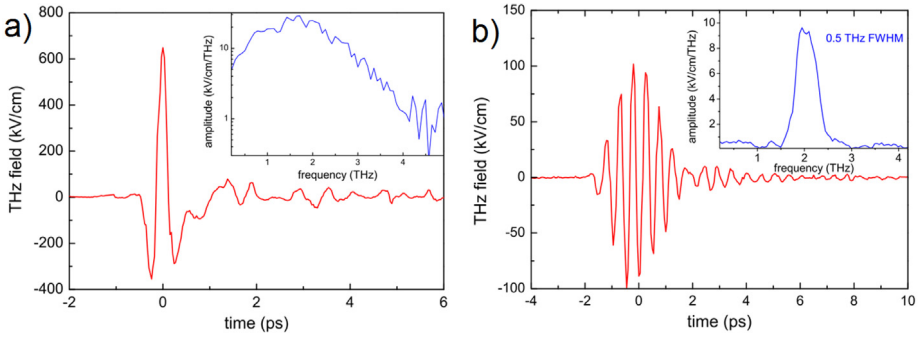

Fig. 37. Experimental results on single-cycle coherent THz transition radiation demonstrated at the free-electron laser Freie-Elektronen-Laser in Hamburg (FLASH). THz pulses with energies up to 100 μJ are generated from 500 MeV electron bunches. Adopted from Ref. [334]. (a) Field strength of the single-cycle pulse in the time domain and the corresponding spectral amplitude depicted in the inset. (b): Generation of multicycle THz pulses from the single-cycle transition radiation by using a bandpass filter with a center frequency at 2 THz and 0.5 THz bandwidth.

radiation due to a charge passing through a round aperture in a flat screen. In this case, diffraction plays a role and the produced radiation is referred to as diffraction radiation [335,336]. By employing specially designed finite-size discontinuities such as apertures, zone-plates and gratings, it is possible to *control the angular distribution and the spectrum* of produced diffraction radiation [337].

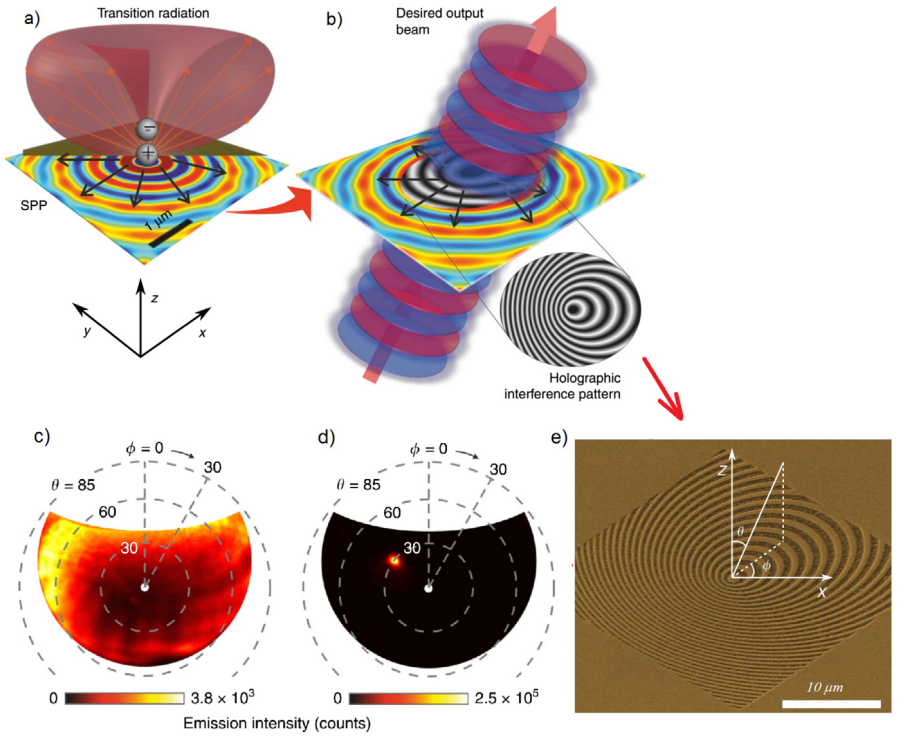

Fig. 38. Concept and measurement results of a holographic electron-driven light source, adopted from Ref. [19]. (a) An electron normally incident on a planar metallic interface produces donut-shaped transition radiation diverging in the radial direction from the impingement point, see Eq. (20). This radiation originates from the induced polarization in the metal, which at optical frequencies is represented by SPPs, see Section 4.3. SPPs are schematically depicted by colored circles on the interface. The red and blue colors correspond to peaks and troughs of the electric field distribution. (b) By controlling the excitation of SPPs and, hence, controlling the polarization in the metal, a collimated oblique plane wave is generated as the electron impinges on the interface. This is realized by using the holographic principle: in simulations, the field of a desired output wavefront is superimposed with the field of SPPs shown in (a) to produce a holographic interference pattern. Then, this pattern is created on the metallic surface by ion beam milling on an optically thick gold film, (e). (c) and (d) Experimental measurements of the radiation intensity from a non-structured and structured film. (e) The image of the nanostructured film obtained with electron scanning microscopy.

Li et al. [19] have introduced a flexible method of generating light beams with potentially any *desired wavefront shape and topological charge* using diffraction radiation from a holographic plasmonic metasurface, Fig. 38. Though this method was experimentally demonstrated in the optical region, it can potentially be extended to the THz region by using suitable materials supporting *THz surface plasmon polaritons* (SPPs) such as graphene (for SPPs see Section 4.3). The field strength delivered by such a source can be high for high-charge ultrarelativistic bunches.

Though THz sources based on coherent transition radiation have demonstrated the world record-high peak fields, there is a deficiency that limit their wide use: the emitted energy depends logarithmically on the electron energy and multi-GeV bunches are needed to produce sub-mJ pulses. In order to overcome this limitation, a *multifoil radiator* was proposed [18]. The radiator comprises a stack of thin conducting disks with successively decreasing radii, forming a truncated cone along the z-axis, Fig. 39. A short electron bunch passes through the radiator along the symmetry axis. In each gap between two adjacent disks, the electron bunch generates a wave propagating radially outwards with the field distribution in the form of a ring. The superposition of waves from different gaps yields a wave with the conical wavefront and the resulting field distribution resembles the wide part of the funnel. For a cylindrical electron bunch, the thickness of this "funnel" is determined by the bunch duration. The emitted field is essentially quasi-half-cycle as in the case of traditional transition radiation. For certain angles of the cone forming the radiator, the waves are emitted to free space with little reflection.

The total radiated energy is estimated as

$$W \approx M \frac{gQ^2}{8\pi\varepsilon_0 d^2}, \tag{28}$$

where M is the number of gaps, g is the gap length, Q is the bunch charge, $d = \sqrt{l^2 + a^2 + g^2/12}$ with l and a being the electron bunch length and radius, respectively. The average electric field is $E_z \approx Q/(8\pi\varepsilon_0 d^2)$. For a mid-relativistic bunch of, for example, 10 MeV, with a charge of 0.5 nC and with a moderate emittance of 0.5 mm mrad, the field strength and emitted energy can reach about 1 MV/cm and 1 mJ, respectively [18].

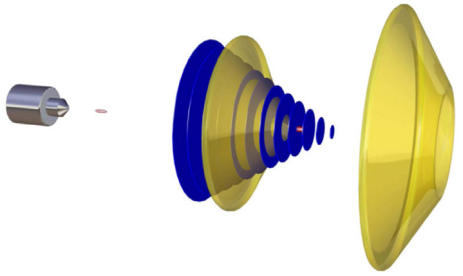

Fig. 39. A cylindrical electron bunch (red) passes through a set of thin disks (blue) and generates a wave with the cylindrical wavefront (yellow).

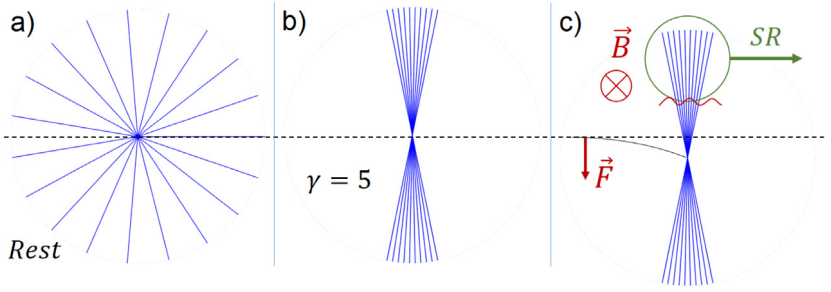

Fig. 40. The origin of synchrotron radiation. (a) A resting particle (electron) with electric field lines. (b) The same particle moves along the dashed line with a relativistic factor γ. (c) The particle enters a transverse magnetic field **B** to be deflected. The resulting electric field distortion causes emission of SR photons.

The first experimental results on a multifoil radiator [338] demonstrated more than an order of magnitude enhancement in emitted energy compared to the single disk case. Moreover, a multifoil radiator with a linear field polarization has been designed and tested experimentally. This development opens the door for a compact and efficient THz source that can be used at many accelerator laboratories. In addition, a multifoil THz radiator can be combined with an intrinsically synchronized X-ray source based on bremsstrahlung for THz pump/X-ray probe experiments as proposed in [339].

In passing, we note that several THz sources making use of electron bunches passing through discontinuities are available for user operation [31]. For instance, the user facility TeraFERMI, producing *strong-field* CTR, has recently became operational [340]. A THz source using edge radiation (form of synchrotron radiation from a short magnet) is also available for user operation at FLASH [341]. A diffraction radiation THz source is open for users at the Terahertz facility at ELBE (TELBE) [33].

3.4. Synchrotron and free-electron laser radiation

3.4.1. Coherent synchrotron radiation

Synchrotron radiation (SR) is the type of radiation emitted by relativistic charged particles in an external magnetic field. The origin of SR lies in classical electrodynamics: whenever a charged particle is accelerated, the surrounding electric field distribution is distorted. Then, a fraction of the field detaches from the particle and constitutes a waveform of separate photons (see Fig. 40). SR was first observed in 1947 in the first synchrotron built by General Electric (a circular accelerator with phase-stabilized radio-frequency accelerating field, where electrons at relativistic energies are steered into a circle by external magnetic fields). At that time, it was named “Schwinger radiation", but by the 1970s the term “synchrotron radiation” became dominant [342]. An example of natural occurrence of SR is the Crab Nebula [343], the first astronomical object identified with a historical supernova explosion, which was noted by Chinese astronomers in 1054. SR has proven to be the most intense and flexible mechanism of light generation, giving access to virtually any wavelength of electromagnetic radiation. At THz frequencies, SR is especially important, since it is difficult to cover this region of the spectrum with laser-based sources.

Consider a charged particle with the Lorentz factor γ (operating machines are usually driven by electron beams). The particle’s propagation axis introduces a preferential direction. In the instantaneous rest frame of the particle, the Coulomb field is spherically symmetric. However, in the laboratory frame, the electric field along the propagation axis is suppressed by a factor of γ^2, whereas the transverse electric field is multiplied by γ. The electric field lines are then concentrated in the plane perpendicular to the propagation direction with an opening angle proportional to $1/\gamma$ (see Fig. 40). Thus, the electric field of a charge moving with a relativistic velocity has a disk-like shape. When the particle enters an external magnetic field B, it is deflected due to the Lorentz force and drags its electric field to follow. To catch up, a fraction of this

disk-like field at some distance R outwards from the particle trajectory has to move *faster than the speed of light*. Since such superluminal motion is forbidden, this field fraction simply detaches and propagates along the instantaneous axis. Another way to qualitatively describe SR is to think of it as of the inelastic scattering of charged particles on the magnetic field photons. The quantitative description of SR is formulated in terms of Liénard–Wiechert potentials and is presented in numerous textbooks [328,344].

Physical properties of synchrotron radiation include [345]:

- Narrowly focused radiation pattern. The light emanates forward from the source particle into a cone with an opening angle $\propto 1/\gamma$. In a uniform magnetic field, the radiation cone is directed along the instantaneous axis at the moment of emission. In a periodic magnetic field (a wiggler or an undulator), it coincides with the non-deflected beam path.
- Widely tunable spectral distribution. Uniform magnetic fields and wigglers produce smooth continuous spectra characterized by a critical wavelength $\lambda_c \propto 1/(\gamma^2 B)$. In an undulator, there is constructive interference between photons emitted at different positions of the source particle. Therefore, the emitted spectrum consists of quasi-monochromatic peaks at

$$\lambda = \frac{\lambda_u}{2n\gamma^2}\left(1 + \frac{\mathcal{K}^2}{2} + \gamma^2\theta^2\right), \quad \mathcal{K} = \frac{eB_0\lambda_u}{2\pi mc}, \tag{29}$$

  where λ_u is the undulator period and $\mathcal{K}$ is the undulator parameter (or deflection parameter) with e and m being the charge and mass of the particle respectively, B_0 being the amplitude of the magnetic field and c being the speed of light. The harmonic number is given by n and θ stands for the angle between the undulator axis and the direction to the observer.
- High photon flux. The energy loss experienced by the emitting particle is proportional to $\gamma^3 B$. If the magnetic field is periodic, the proportionality is $\gamma^2 \overline{B^2} L$, where $\overline{B^2}$ is the square-average field and L is the length of the wiggler or the undulator. Thus, particles with higher energy in a stronger magnetic field emit more light. Photon flux is the number of photons emitted per second into a solid angle element within 0.1% of the bandwidth. Using an undulator additionally increases the flux due to coherence and smaller bandwidth. A coherent SR-based light source attains the highest X-ray photon flux in the observable universe [346].
- Polarization control. SR polarization follows the oscillation plane of source particles. If the magnetic field is uniform, the emitted light is linearly polarized and has ellipticity out of the particle trajectory plane. In periodic fields, ellipticities cancel out, giving linear polarization in the desired plane. If the source particles follow a helical trajectory, their oscillation plane rotates and gives rise to circular polarization components. Using helical magnetic field arrangements (*e.g.*, APPLE-II/III and Delta undulators) allows for producing linear, circular or elliptical polarization [347–349].
- Tunable time structure. In a uniform field, source particles emit a "sweeping searchlight" pattern. Thus, at a fixed point, an observer would see a flash of light as long as it takes for the particle bunch to pass by the aperture for SR extraction (typically, sub-nanosecond to picosecond duration). A wiggler produces longer pulses. As a side note, in an undulator, it is possible to arrange interference in such a way that the emitted pulse duration would decrease significantly, down to attoseconds (1 as $= 10^{-18}$ s) in proposed free-electron lasers [20].

Coherent synchrotron radiation from a bending magnet is a simple and robust way of generating quasi-half-cycle THz radiation, see Fig. 41a. Temporal coherence takes place if the particle bunch length is much smaller than the radiation wavelength, which is attainable for THz frequencies (see Fig. 46). Then, the whole bunch radiates like a single particle. Many existing linear electron accelerators produce picosecond or sub-picosecond electron bunches that are efficient sources of THz SR. One of the first clear experimental demonstrations of coherent SR in the sub-THz region was performed in 1989 with the Tohoku 300 MeV linear accelerator (Japan) [350]. In 2002, at the Jefferson lab (US) a dedicated high-intensity SR-based THz source was built using 500-fs electron bunches from the energy recovery linac [351]. The central frequency in the experiment was 0.6 THz with a FWHM bandwidth of about 0.5 THz. Field strength measurements were not available but an order-of-magnitude estimate is about 0.1 MV/cm. Another early example was shown in the BESSY II storage ring (Germany) [352,353] with comparable parameters. Nowadays, THz beamlines making use of coherent synchrotron radiation are available for users at several synchrotron facilities [354–356], see also the review [31] and the references therein.

3.4.2. Coherent undulator radiation and free-electron lasers

In order to increase the pulse energy of SR, an electron bunch is usually steered through a periodic magnetic field which causes periodic deflections of the bunch trajectory. The emitted energy becomes N times larger compared to that from a bending magnet, where N is the number of oscillations performed by the bunch. See an example of the electric field distribution from an oscillating and moving forward electron in Fig. 41b. A simple but rigorous description of coherent undulator radiation can be found in Ref. [20]. Note that the electron bunch duration must be much smaller than the period of the radiation field for coherence to take place. Such coherent undulator radiation is often referred to as super-radiant radiation. For short bunches and a periodic undulator, the emitted pulse energy reads as [20]:

$$\mathcal{E}_r \approx \frac{Q_b^2 \lambda_u N}{4\varepsilon_0 S_b} \frac{\mathcal{K}^2/2}{1 + \mathcal{K}^2/2}. \tag{30}$$

Please cite this article as: P. Salén, M. Basini, S. Bonetti et al., Matter manipulation with extreme terahertz light: Progress in the enabling THz technology, Physics Reports (2019), https://doi.org/10.1016/j.physrep.2019.09.002.

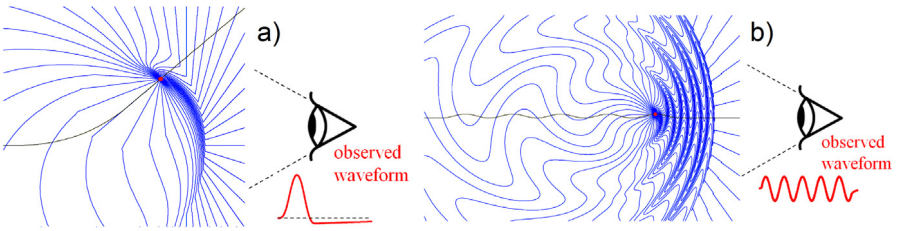

Fig. 41. (a) Electric field lines (blue) from an electron (red dot) moving along a curved path (black) in a bending magnet. The generated waveform shown next to the observer eye is quasi-half-cycle. Note that the field integral is zero [357], *i.e.*, $\int E(t)\mathrm{d}t = 0$. (b) The electric field lines and waveform (sinusoidal) for harmonic oscillations in an undulator.

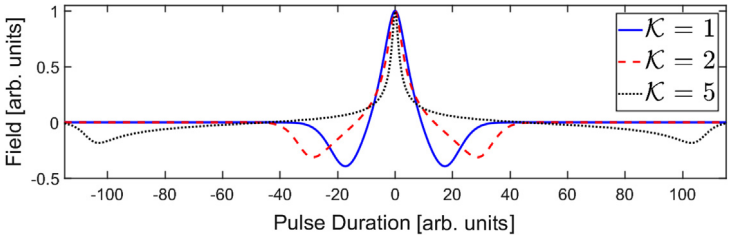

Fig. 42. Dependence of the waveform generated in a single-period undulator on the undulator parameter. The normalized vector potential of the undulator field is $A = (z/\sigma_u)\exp[-z^2/2\sigma_u^2]$ with σ_u being the characteristic space scale.
Source: Adopted from [333].

Here, Q_b is the bunch charge, λ_u and $\mathcal{K}$ are the undulator period and undulator parameter, respectively, $S_b = \pi r_b^2$ is the transverse bunch area with r_b being the bunch radius. The maximum $\mathcal{E}_r$ is obtained when $\mathcal{K} \gg 1$.

Electron bunches used for X-ray free-electron lasers are well suited for the production of strong-field THz pulses by means of coherent undulator radiation. At the FLASH facility in Germany, 1 GeV sub-100 fs electron bunches generate THz pulses with a field strength of around 5 MV/cm in a dedicated undulator, see Fig. 2 and Refs. [31–33]. One limitation of this type of sources for certain applications is the narrow bandwidth of THz pulses because they contain multiple cycles, typically around 10. Recall that the relative bandwidth is inversely proportional to the number of undulator periods, *i.e.*, $1/N$. In addition, the field changes sinusoidally and thus has no preferential direction, which is needed for surface chemistry applications, Section 2.4.

Preparing an electron bunch shorter than the radiation wavelength is a technical challenge, and many undulator-based THz sources use long electron bunches and rely on the FEL lasing. The process starts from incoherent spontaneous undulator radiation. Then, the light emitted by the tail of the particle bunch propagates through the bunch (photons travel faster than electrons) and affects the particles ahead of the tail. This impact is known as the ponderomotive force. This force gradually organizes particles of the bunch into disk-shaped *microbunches* separated by the resonant undulator wavelength, see Eq. (29). Hence, different parts of the source bunch become phase locked and radiate coherently. Coherent light gives stronger ponderomotive effect, thus increasing microbunching further and forming a feedback loop, which results in exponential power growth. This process is usually referred to as *free-electron laser* (FEL) amplification [358,359]. To enhance the FEL process further, mirrors are used to form the FEL-oscillator.

Several dedicated user facilities based on THz FEL-oscillators are currently operational: FLARE [360] at Radboud University, the Netherlands; CLIO [361] at University of Paris, France; FELBE [362] at Helmholtz-Zentrum Dresden-Rossendorf (HZDR), Germany. A super-radiant THz undulator source is available at HZDR [31,33]. In addition, more than a dozen of research THz and IR FELs are operated worldwide.

The generation of single-cycle or even quasi-half-cycle pulses with undulators has recently become an active field of research, see the recent review [20] and references therein. The simplest approach makes use of a short electron bunch and a single-period undulator, which naturally gives a radiation pulse composed of one oscillation cycle of the field [363]. The shape of the generated waveform can be controlled by the undulator field profile and undulator parameter [333], see an example in Fig. 42. The emitted pulse energy in this approach is, however, low and the field is correspondingly weak.

In order to generate strong-field single-cycle pulses, a scheme has been proposed that uses a prebunched beam and a tapered undulator [21–23]. In a tapered undulator, the undulator magnetic field profile is position-dependent, *i.e.*, $\mathcal{K} = f(z)$ is a function of z. Hence, the radiation wavelength, see Eq. (29), also changes along the undulator, and the emitted waveform is intrinsically chirped. From signal theory, it is known that if the bandwidth of a chirped signal equals that of the desired single-cycle or quasi-half-cycle signal, then the chirped signal can be converted to the desired one by adjusting the phase between the harmonics. Fig. 43 shows a chirped multicycle waveform and quasi-half-cycle one having exactly the same spectral bandwidth but different phase relations between the Fourier components.

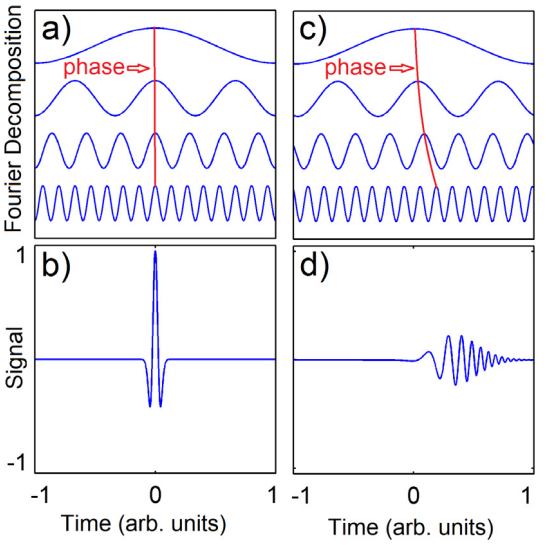

Fig. 43. Schematic illustration of the Fourier decompositions (a) and (c) of the quasi-half-cycle (b) and frequency-chirped (d) pulses, respectively. The quasi-half-cycle pulse is formed by the superposition of in-phase sinusoidal components, whereas the frequency-chirped pulse is composed of the sinusoidals with a nonlinear phase shift in between them. The Fourier amplitudes are not to scale.
Source: Adopted from [23].

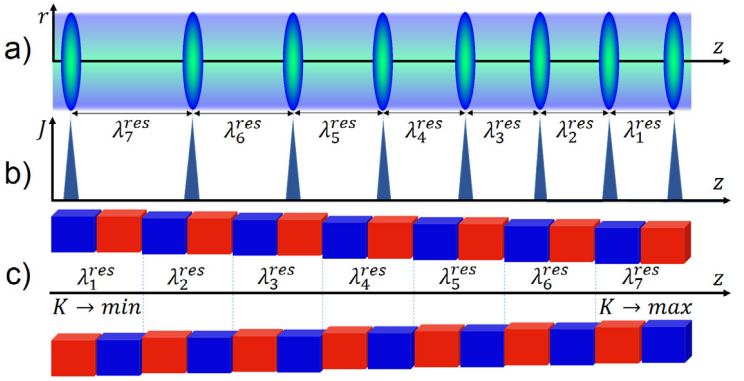

Fig. 44. Matching of the current pattern (b) with chirped undulator radiation. The undulator (c) with a constant period λ_u has a strong inverse taper ($\mathcal{K}$ increases with z). The instantaneous radiation wavelength λ_1 given by Eq. (29) changes along the undulator giving rise to a chirped undulator waveform. The radiation wavelength is the shortest (within the emitted waveform) at the undulator entrance and the longest at its exit. Each microbunch of the beam (a) as it passes through the radiator generates a chirped waveform containing a spectrum of resonant wavelengths and their harmonics. If one injects a sequence of microbunches (a) separated by these wavelengths, the phase locking condition between different modes is fulfilled. Then, the interference between the radiation from different microbunches forms an isolated single-cycle pulse.

In order to satisfy the phase lock condition for coherence, the injected sequence of microbunches must follow a specific pattern that matches the tapering profile of the undulator. As derived in Refs. [21,23], this pattern consists of thin microbunches along the z-axis separated by the instantaneous (local) resonant wavelength Eq. (29) for each period of the undulator (Fig. 44). The whole process can be viewed as FEL amplification with a chirp of the electron beam. In a sense, it is similar to the chirped pulse amplification (CPA) technique [364], which was awarded the Nobel Prize in 2018.

Fig. 45, panels a and b, shows the electric field distribution in the frequency-space and time-space domains produced by a *single short bunch* in a tapered undulator. The same type of distributions for the field produced by a *prebunched beam* are depicted in the panels c and d. Note that the spectra produced by the single bunch and prebunched beam are approximately the same. Some differences in the spectra are unavoidable because an infinite number of the bunches in the prebunched beam are needed to completely "synchronize" the infinite number of the Fourier components. The simulations [23] show that quasi-half-cycle THz pulses from tapered undulators can reach a field strength of around 10 MV/cm with focusing. At the same time, the technology of prebunched beam generation is still developed insufficiently. In the next section, we discuss the current status of the generation of electron bunches for THz light sources.

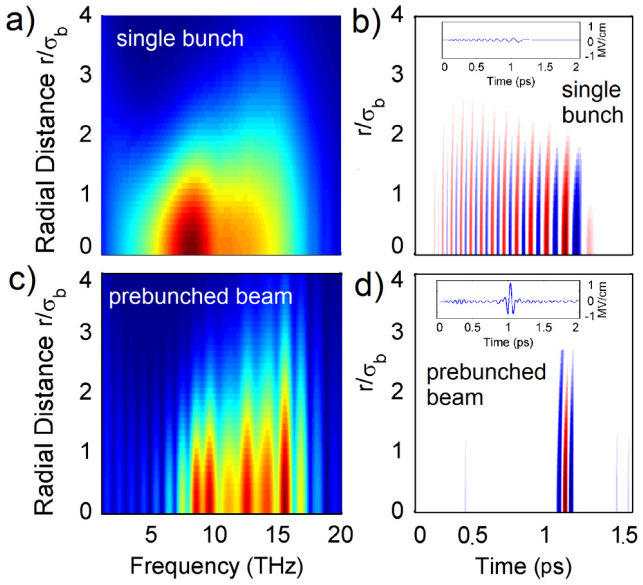

Fig. 45. (a) Density plot of the electric field generated by a single bunch as a function of frequency and normalized radial distance; (b) the same field but as a function of *time* and radial distance; (c) total electric field generated by a prebunched beam as a function of frequency and normalized radial distance; (d) the same field but as a function of *time* and radial distance. The insets show the on-axis electric fields for the single bunch and the prebunched beam.

3.5. Formation of electron beams for THz light sources

3.5.1. Requirements on beam quality

When considering an electron beam as a radiation source, the cornerstone notion is the *beam brightness*. It can broadly be defined as the number of particles per unit volume of the total *phase space* [365]. Thus, there are two ways to achieve high brightness: either have more electrons or a smaller phase space volume. Let us focus on the latter. The total phase space of a beam is six-dimensional and accounts for positions and momenta of each particle, namely, (x, x', y, y', z, z'). Correspondingly, the phase volume is the integral that envelops all particles which are considered to be part of the beam. To simplify the picture, the total phase space is usually split into transverse (x, x', y, y') and longitudinal (z, z') parts because the beam propagation axis gives a preferential direction. In circular accelerators, the revolution plane allows for splitting the transverse phase space further, into horizontal and vertical. The chosen phase space volume (divided by π) is typically referred to as the *emittance*.

The transverse emittance mainly defines transverse characteristics of the emitted light wave, such as the initial waist and divergence. For having *spatially coherent* radiation from the beam, the transverse beam emittance must be smaller than the diffraction limit, $\epsilon < \lambda/(4\pi)$, where λ is the wavelength, at which the radiation is observed. On the other hand, the longitudinal emittance (and, consequently, brightness) is the key parameter for attaining *longitudinally coherent* emission. The more "coherent" electrons the beam contains, the higher the intensity of emitted light. Let us focus on the longitudinal motion further.

The longitudinal emittance is composed of the electron bunch duration and energy spread. The first condition on coherence demands the bunch duration to be much smaller than the characteristic period of radiation, $\sigma_t \ll T$. For example, a Gaussian bunch of rms duration σ_t has a form-factor $|F(\omega)|^2 = e^{-\omega^2\sigma_t^2}$, $\omega = 2\pi/T$, which decreases rapidly with increasing frequency. This implies a dramatic decrease in radiated intensity once the condition is violated and coherence is lost, as illustrated in Fig. 46. When the condition is met, the entire bunch emits light coherently, as a single particle (also known as super-radiance).

The second component of the longitudinal emittance is the energy spread, which governs the gradual elongation of an electron bunch as it propagates. The corresponding condition for attaining coherence reads $\sigma_\delta/\gamma^2 \ll \lambda/L$, where σ_δ is the *relative* energy spread, γ is the Lorentz-factor of the electron bunch, and L is the radiation formation length. For transition radiation, $L \approx \lambda$ (Section 3.3.1), while for synchrotron radiation, $L \propto r_0/\gamma$, with r_0 being the trajectory curvature radius. For undulator radiation, the formation length can be taken as the physical undulator length, *i.e.*, on the order of one meter for a THz undulator. This results in stringent demands on the beam energy spread for a THz source based on coherent undulator radiation.

Energy spread is often classified as correlated or uncorrelated. The former implies that some spread was deliberately introduced at an earlier stage to manipulate the beam. There are methods to mitigate the correlated energy spread, *e.g.*, Ref. [367]. On the contrary, uncorrelated energy spread originates from the very source of particles and depends on the method of extraction. A non-zero uncorrelated energy spread can also be understood as a finite temperature of the beam.

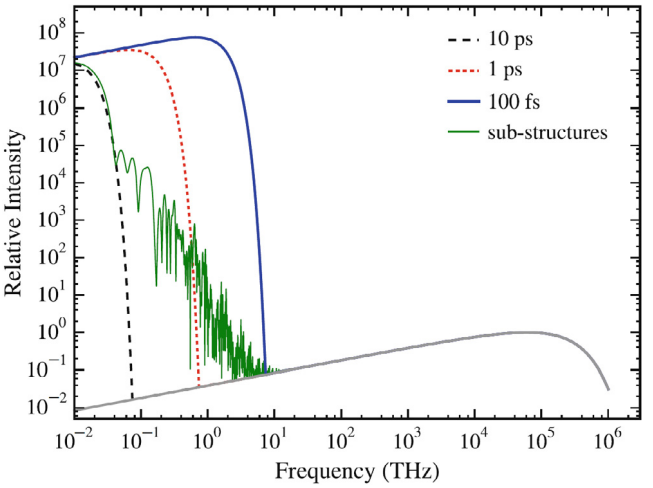

Fig. 46. Calculated spectra of coherent synchrotron radiation emitted by Gaussian bunches of 10, 1 and 0.1 ps rms duration. For shorter durations, the cut-off frequency extends further towards higher values. The green curve corresponds to a bunch with a sub-picosecond sub-structure (envelope rms duration of 8.4 ps). Fractions of this sub-structured bunch emit coherently as long as the sub-structure (*e.g.*, a spike of a comb beam) is much shorter than the period. According to the Ref. [366], for all cases, the bunch charge was 418 pC and the spectra were normalized to the maximum of incoherent radiation.
Source: Figure adopted from [366].

3.5.2. Generation of bunches and comb beams

There are three main types of electron emission implemented in particle accelerators: field emission, thermionic emission and photoemission. High-field emitters are essentially diodes, where the cathode is razor- or needle-shaped to enhance the local electric field. While field emitters used in electron microscopes have demonstrated record low emittance for low-charge beams, control of the temporal beam profile is complicated and such emitters are not used in precision light sources. Thermionic emission is assisted by heating the cathode, so that the electrons inside can have energies above the Fermi level. Photoemission relies on photoeffect: photons of the driving laser beam provide the energy required for electrons to leave the cathode material. The photoinjector is the main source of high-brightness beams for free-electron lasers.

Regardless of the emission type, extracted electrons are to be accelerated immediately after they leave the cathode. Otherwise, the nonrelativistic beam is subject to space-charge forces, which cause degradation of emittance. For that reason, electron sources are usually integrated into an RF gun with a final energy of about 5 MeV. It is worth mentioning laser-driven plasma wakefield accelerators as an alternative, such as the self-injecting "bubble" regime [368], although the energy spread remains a challenge yet.

Let us focus on photoinjectors. Being the state-of-the-art sources, they are associated with high accelerating gradients (100-MV/m scale), high bunch charge (nC scale), small bunch duration (picosecond scale), low transverse emittance ($\lesssim$1 mm mrad), small energy spread ($\lesssim$0.1% relative) and high repetition rates (MHz scale) [33]. A photoinjector typically consists of a photocathode gun and a booster cavity. The photocathode is the key component, and the choice of material for it is crucial, see Ref. [369] and references therein. Periphery includes RF power supply, emittance compensation coils, vacuum system and the driving laser. The latter is usually ultraviolet (frequency-tripled Ti:sapphire), so that the photons carry energy above the work function of the cathode's material.

In simple terms, a photoinjector is a device for conversion of high-precision laser pulses into high-precision electron bunches. One important feature of this conversion is that the current profile of an electron bunch emerging from the cathode to some extent reproduces the intensity profile of the driving laser pulse (Fig. 47). Thus, by shaping the laser pulse, one can create a specific distribution of electrons. For THz light generation, *comb beams* are most appropriate since the space-charge effect is mitigated. A comb laser pulse can be created by time delay and recombination [331], or with birefringent crystals [370,371]. Then, a comb electron beam emerges. Comb beams with a separation between current spikes on the order of the THz period are already used to emit THz light through coherent transition radiation (Section 3.3) [331,371,372] and are proposed for undulators [373,374]. To generate a chirped comb beam, such as the current pattern in Fig. 44, it is required to make a comb laser pulse with uneven separations. The general approach is the same as for evenly spaced beams. Particularly, it is demonstrated using three α-BBO birefringent crystals with an output of eight bunches within the chirped comb electron beam [374].

One of imperfections in the photons-to-electrons conversion process is space-charge fields present between the electrons of the extracted bunch. Usually, these fields distort the phase space portrait of the bunch as it propagates and increase the emittance. However, it turns out that in this case, space-charge forces can recover the comb structure after 1/2 of the plasma oscillation period [370].

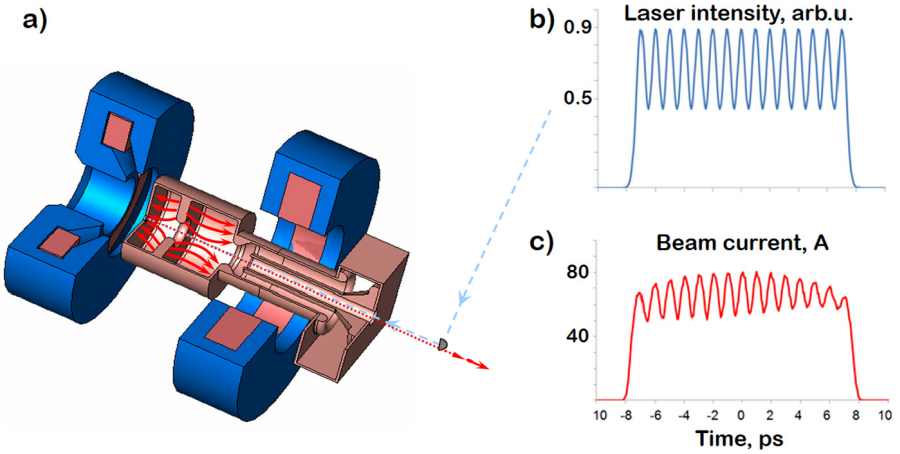

Fig. 47. (a) Geometry of a photoinjector. The photocathode is located in the 1.6-cell S-band (2.856 GHz) accelerating structure. The electric field distribution within the structure is shown by red arrows. In the fractional cell, the RF field distribution on the cathode is optimal for maximum brightness. The following full-size cell accelerates the extracted electrons to a relativistic energy to prevent the emittance degradation. Magnets of the emittance compensation line are shown in blue. (b) Temporal profile of the driving laser pulse, incident on the cathode. (c) Corresponding simulated temporal profile of the extracted electron bunch (comb beam).

3.5.3. Acceleration and compression of beams

Downstream, the high-brightness electron bunch is to be accelerated. For undulator-based THz light sources, typical required electron energies lie in the range of 10–40 MeV. These energies can be reached with well-developed RF technology within a rather moderate size of the machine (10–20 meters long). For ultraintense transition radiation, GeV-scale beams are needed, and the accelerators are correspondingly longer. Acceleration of particles with RF fields is formulated in numerous textbooks, *e.g.*, [345]. The general principle of operation is almost identical to modulation, which is described below, except that the electron bunch gains energy as the whole.

For coherent radiation, the electron bunch must be kept well compressed over the radiation formation length. The compression process, also known as *bunching*, can be done in a drift space (ballistic bunching), within a dedicated accelerating section (velocity bunching) or with a deflective chicane (magnetic bunching), that gives additional tunability [375].

Consider the longitudinal phase space of the electron bunch (z, E). To start the compression, the electron bunch must acquire a negative energy chirp. In other words, particles in the tail have to move faster than the equilibrium particle (Fig. 48a, shaded area, higher energy), whereas particles in the head have to move slower (non-shaded area, lower energy). To apply the chirp, or to *modulate* the bunch, it is overlapped with an external electric field provided by an RF bunching cavity or modulating laser (orange diagonal line in Fig. 48a). The overlap means that the reference particle experiences zero electric field and remains unperturbed (as opposed to acceleration, when it gains energy). Particles in the head (non-shadowed area, dashed curve in Fig. 48a) are out of phase with the external field and lose energy. On the contrary, particles in the tail gain energy. Thus, the phase space portrait of the bunch during the energy modulation transits from the dashed curve to the solid red curve filled with particles in Fig. 48a. In general, the modulation depends on the applied electric field and is characterized by induced energy spread (also called the modulation depth).

After the modulation, the electron bunch propagates in the bunching section. Its phase space portrait rotates clockwise, which results in a gradual increase of the instantaneous current (Fig. 48). The bunch is said to be fully compressed when its phase space portrait is closest to the example in Fig. 48c and the current is maximized. In such a state, the bunch is ideal for coherent emission. In practice, nonlinearity of the longitudinal phase space limits the achievable compression. To improve the focus, one can use a higher-harmonic field cavity [376] or other methods, *e.g.*, in Ref. [377]. The particles, however, still have the energy chirp from modulation. As they propagate further, the compression degrades, the current decreases and the bunch is said to be overcompressed. Thus, the compression is to be matched with the radiation formation length.

For a sequence of bunches, such as the comb beam (Fig. 47c), the modulated phase space portrait is sinusoidal (zoomed-out Fig. 48a). Each peak of the comb corresponds to a compressed bunch current (Fig. 48f), formed at crests of linear parts of the sine function. Similarly, for a chirped comb beam, such as the one needed for the scheme in Fig. 44, the modulated phase space portrait is a chirped sine function. A simple example of such curve is given in Fig. 49. A linear chirp implies a linear dependence of frequency on a longitudinal coordinate. Thus, bunches at different positions experience different slopes of the modulating field. At the same time, crest positions, where bunching occurs, vary inversely, following wavelengths, as required to match the undulator in Fig. 44. As mentioned above, such phase space portraits can be created in the photoinjector [374] with the comb recovered after a drift [370].

In some cases, *e.g.*, for transition radiation (Section 3.3.1), the electron beam must be accelerated to higher energies. Standard acceleration methods do not preserve the sophisticated comb structure, and it has to be imprinted afterwards, to the full-energy beam. The same applies, if, for any reason, modulation at the cathode is not an option. To create the chirped

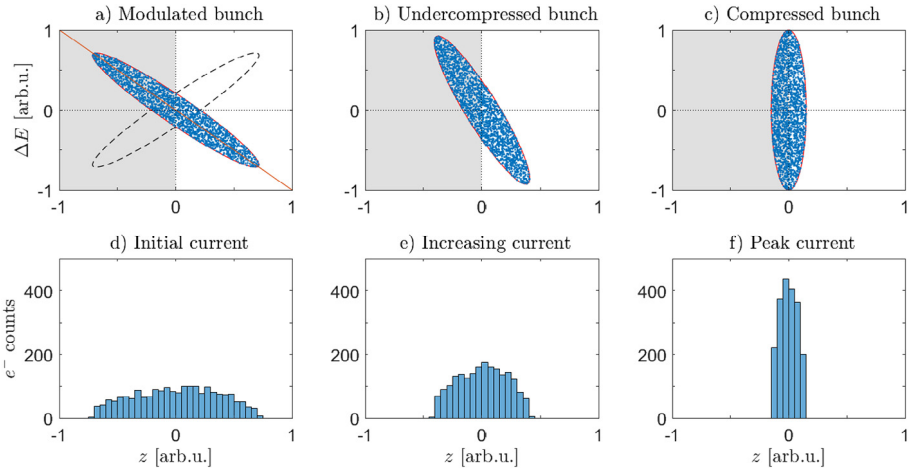

Fig. 48. A simplified example of bunch compression (2000 particles). (a)–(c) Phase space portraits of (a) the bunch entering the compression drift after interaction with the modulating electric field (orange line), the dashed curve corresponds to non-modulated, original phase portrait, (b) the modulated bunch in an intermediate position, (c) the fully compressed bunch, suitable for super-radiant emission. Particles in shaded regions move faster than the non-perturbed reference particle in the center. Particles in non-shaded regions move slower than the reference particle. (d)–(f) Corresponding histograms, which are proportional to the instantaneous electric current of the bunch.

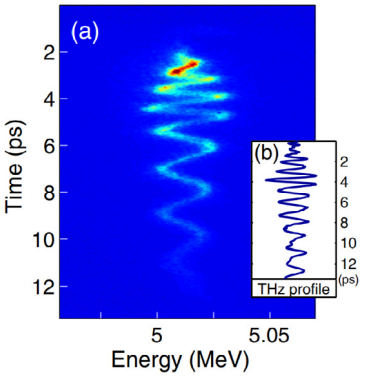

Fig. 49. (a) An example of a chirped longitudinal phase space (measurement results). The inset (b) shows the waveform of the THz pulse used for broadband modulation via inverse FEL process.
Source: Adopted from Ref. [268].

comb bunch pattern shown in Fig. 44 from an arbitrary bunch, one can use the inverse free-electron laser mechanism. The initial bunch with no features in the phase space portrait (dashed ellipse in Fig. 48a) is injected for modulation into a tapered undulator. Inside, it interacts with the modulating field of a co-propagating broadband THz laser pulse. Each period of the undulator–modulator enables resonant interaction of the light pulse with electrons only at specified wavelengths [Eq. (29)]. As the resonant wavelength monotonically changes along the trajectory, the electrons interact with different spectral components of the light pulse, thus undergoing *broadband modulation*. The result of this process is a chirped phase space portrait, *e.g.*, in Fig. 49.

At THz frequencies, broadband modulation implies additional challenges, such as insufficient modulation depth even with a rather complex laser setup. Another limitation may arise from significant diffraction of the modulating pulse over the interaction region. Both effects can be mitigated with a waveguide inside the undulator–modulator, *e.g.*, curved parallel-plate wave guide (CPPWG) [268]. It increases the effective interaction region to a meter-scale and provides the required modulation depth.

To sum up, there is a variety of mature techniques for preparation of electron beams for super-radiant THz sources. At the same time, new methods of beam formation are being developed in order to improve the beam quality, acceleration efficiency, and accelerator compactness.

3.5.4. THz diagnostics of beams

Few-cycle THz pulses can serve not only for electron beam formation but also for diagnostics of ultrashort beams [267, 378,379]. Particularly, such THz pulses can be used to determine the arrival time and temporal profile of the electron

beam. A conventional tool for this purpose is a transversely deflecting RF cavity [380,381], whose electric field imprints a transverse momentum onto the beam. Because of the relative phase between the field and the electrons, the momentum changes along the beam such that the beam rotates in the phase space upon its further propagation. Then, an image of an energy dispersed beam on a YAG screen gives the information about the longitudinal phase-space of the beam. However, it is not always possible to use the conventional transversely deflecting RF cavity for various reasons, including space and cost limitations. A THz pulse, having a higher frequency than the RF field, provides a sharper deflection, as required for ultrashort electron beams.

In free space, the interaction of a laser pulse and a beam is inefficient because the magnetic force counteracts the electric one. Hence, for having enhanced beam deflection, the THz pulse and electrons are overlapped in a resonator [378] or a waveguiding structure [379]. For instance, in Ref. [378], the interaction region is inside of a narrow slit made in a metallic foil. The slit enhances the near electric field of the pulse and makes it dominant over the magnetic field in the resulting deflection. A measurement of the beam arrival time with 1.5 fs (rms) accuracy was demonstrated. However, only low-charge beams can be characterized because of the narrow gap of the slit. In their next work [379], Zhao et al. developed a streaking device based on the extended beam-THz field interaction in a dielectric waveguide. A large dynamic range of streaking was achieved while keeping high temporal resolution: as the beam underwent a nearly 50-fold compression, the beam profile was captured with a resolution of a few tens of femtoseconds and 3 fs rms arrival time accuracy. In Ref. [267], as discussed earlier, 10 fs streaking resolution was reached using the magnetic field instead of the electric one.

Beams of femtosecond-scale duration are used as a probe in ultrafast electron diffraction (UED) experiments [272,382–385]. The common approach to bunch compression is to use strong RF bunching [386]. There is, however, a payback: RF-buncher phase jitter introduces electron beam energy jitter, which results in the jitter of the arrival time. To account for it, a THz-based deflector is a fine tool. Refs. [387,388] report femtosecond precision for the bunch duration and sub-femtosecond precision for arrival time. As shown in Ref. [379], controlling the THz pulse polarization significantly increases the dynamic range of such measurements while keeping high resolution. Although the THz field strength implemented so far is modest (sub-MV/cm), scaling it up would only provide better resolution. With such precision, the UED technology becomes even more attractive for applications.

As a side point, UED experiments often rely on electron beams with kinetic energy of several MeVs (mega-electron-volts, mildly relativistic beam). Characterizing electron bunches of few-MeV energy in the time domain with femtosecond resolution is an achievement by itself, because it is not straightforward to implement well-developed techniques for non-relativistic (keV) or ultra-relativistic (GeV) beams to the intermediate energy range [378].

These methods of electron beam diagnostics are essentially variants of the technique known as streaking, which is used to indirectly characterize ultrashort particle and light beams in the time domain. Depending on the object studied, the timescale varies from few picoseconds [389] down to the attosecond regime (1 as $= 10^{-18}$ s) [390,391]. For light beams, an intermediate stage of conversion into photoelectron wavepacket is required, which is usually done with a gas target.

Using a THz pulse as the streaking field, one can characterize a femtosecond-scale light pulse [392,393], such as the output of currently operating X-ray free-electron lasers (FELs) [394–398]. Today's X-ray FELs typically operate in the regime of self-amplified spontaneous emission (SASE) [399]. SASE starts from a stochastic process, which results in jitter of the arrival time of the generated X-ray pulse. It is of utmost importance for user stations to analyze the temporal structure of each arriving pulse and correlate it with an optical pump laser or another reference. This problem is very similar to the arrival time jitter of a UED beamline, and it can be solved in a similar manner by THz streaking. Within a THz pulse, the time window for overlap is as long as 100 fs, which is enough to cover the arrival time jitter. The required THz pulse can be generated in a dedicated undulator, as at FLASH [395,400] (see Section 3.4), or via optical rectification, as, for example, at SACLA [398,401] (see Section 3.1.1). The latter was reported to have few-femtosecond resolution in good agreement with the values measured through X-ray-induced transient reflectivity (or transmission) change of a membrane [402–406]. Thus, THz streaking may be used as a complement in order to improve the temporal resolution of pump–probe experiments at X-ray FELs. Demonstrated setups utilize THz pulses with field strength on the order of 100 kV/cm. Delivering fields above 1 MV/cm would significantly increase streaking efficiency and the resolution.

Finally, THz streaking can be employed to directly probe electron dynamics in molecules. In attosecond streaking [390,391], the key role is played by photoelectrons born through single-photon absorption. However, once a molecule is pumped by an XUV/X-ray pulse into a highly excited state, there are other ways for it to relax on a longer timescale. One prominent example is the study of autoionization dynamics of molecular oxygen [407–409]. After single-photon absorption, there is still extra energy in the molecule, which may be released through emission of a secondary electron by autoionization. Recording the spectrum of secondary electrons requires a longer period of the streaking field, namely, in the infrared or THz frequency range. The spectrum of autoionization electrons allows one to calculate the lifetime of the corresponding highly excited energy state of the molecule.

In passing, THz-based techniques for acceleration, manipulation and diagnostics of electron beams, although still in infancy and demanding further studies, are promising.

3.6. THz spintronic emitters

It is worth mentioning that very recently, a novel method to generate broadband terahertz radiation has been discovered, and implemented in the so-called THz spintronic emitters [410–415]. The fundamental mechanism is a spin-

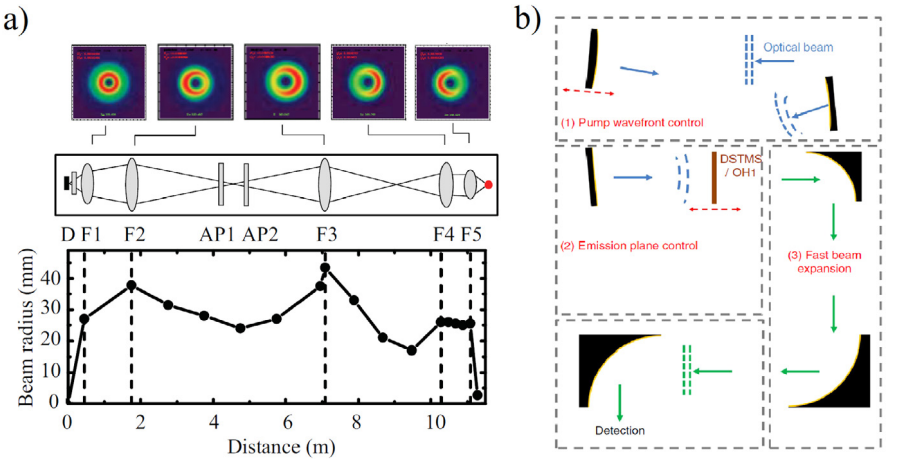

Fig. 50. The layout of the beam line optics of a CTR THz pulse source at PAL [416]. Top: Intensity distributions (0.5 THz) at the positions of the F1-F5 mirrors. Middle: Locations of the optics through the system. Bottom: Beam radii estimated along the beam propagation (a). Schematic layout of the λ^3 focusing of the THz pulses of an organic crystal OR source.
Source: Adopted from Ref. [129].

to-charge conversion due to different microscopic effects (*e.g.*, spin Hall, Rashba), all localized either to the interface or within a few nm thick active material. Since these emitters rely on charge transport in metallic samples, they can emit terahertz radiation of much broader bandwidth (up to 30 THz), as they are not affected by the typical phonon absorption problems in nonlinear bulk crystals.

Since the nanometer-confinement of charge transport is fundamental for the spintronic emitters to function, and since THz radiation would also be absorbed by thick metallic layers, the scaling of the emitters has only be attempted in the lateral directions. In a recent work, an emitter of 7.5 cm in diameter was pumped with an amplified laser system, and terahertz fields of up to 0.3 MV/cm were successfully generated [414]. These fields are large enough to start being of interest for the study of nonlinear dynamics, and it is reasonable to expect that future works will use the spintronic emitters to this purpose. The challenge and opportunity are in the unique combination of low-pulse energy (5 nJ) and high bandwidth (30 THz), which allows for much tighter focusing of the radiation compared to conventional emitters. The low-pulse energy could be an advantage in minimizing thermal effects and increase the relative weight of the coherent response.

Since no work has been published yet which uses the spintronic emitters for driving nonlinear dynamics, which is the focus of this Review, we will not discuss them in greater detail. However, it is possible that these emitters will become a complementary source to the ones described here in a near future.

4. Control, guiding and diagnostics of THz light

4.1. Transportation and focusing

Similarly to optical setups, lenses and mirrors can be used in order to control the propagation and the waist of the THz beam. A careful planning of the THz transport lines is especially important when the THz source and the experimental area are separated by a long distance (over 10 m) or when the practical application (*e.g.*, electron manipulation) is sensitive to the beam waist.

Femtosecond THz pulse transportation over a long distance was demonstrated experimentally at the Pohang Accelerator Laboratory (PAL), where the spectral range of the radiation was varied from 0.2 to 3 THz [416]. The THz pulses were generated by CTR (Section 3.3.1). Minimal intensity loss requires careful examination with respect to the potentially large diffraction associated with the long wavelength of the THz radiation [416]. The calculation of the transportation was carried out using the THz Transport code developed by B. Schmidt (DESY) and the result of the simulation is shown in Fig. 50a. The radius of the radiation is 1 mm at the source and the variation of the radii along the beam propagation is shown in Fig. 50a, bottom panel. Five off-axis elliptic or parabolic mirrors (F1-F5, see Fig. 50a, middle panel) were used to collimate or focus the beam (the radius of the optical elements are 50 mm or 75 mm). The last mirror (F5) was used to tightly focus the beam to the experimental area. The transmittance of the transport depends on the THz frequency: at frequencies above 1 THz the transmittance is 80% and at 0.2 THz it is just 20% due to the diffraction loss on the finite size optical elements [416]. The result suggests that the energy of the THz pulse is $\sim$10 μJ at the experimental area, *i.e.*, 11 m from the THz source.

Recently, Hauri et al. [129] reported on the ultimate confinement of THz pulses generated by OR in organic crystals (DSTMS and OH1) in a λ^3 volume. The schematic view of the setup is shown in Fig. 50b. The THz pulses were generated

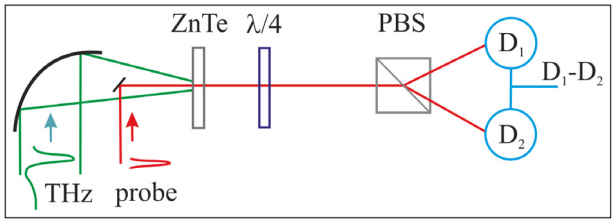

Fig. 51. A typical EOS setup. *Source:* Adopted from Ref. [420].

in the DSTMS/OH1 crystal, which was adjusted along with the first optics stage for optimum focusing. The unavoidable distortion of the generated THz wavefront was pre-compensated by controlling the pump-pulse wavefront using a reflective telescope. In the third stage, the process is combined with fast expansion of the THz beam in order to smear out the high-frequency intensity modulations and minimize the effect of the natural divergence [129].

The results showed the spot size to be four times smaller using the λ^3 focusing regime than what was previously achieved and that using this method, diffraction limited focusing is feasible. The method leads to extremely intense THz radiation of 11 GW/cm^2 and a field strength of 83 MV/cm [129].

4.2. Diagnostics

For matter manipulation, typical levels of THz pulse energy and average power are μJ and mW, respectively. Convenient commercial devices exist for energy measurements of such pulses, for example pyroelectric detectors. For measuring the spatial intensity distribution in the THz range, there are commercially available pyroelectric and micro-bolometric cameras. In this short subsection, we will deal only with waveform measurement techniques for THz pulses. It is important, since the direct measurement of the electric field of a THz pulse is simple, in contrast with visible or NIR light, and gives more information than measuring the temporal intensity profile.

The most important THz waveform detection techniques are sampling by unbiased photoconductive switches [417], EOS [418], and THz air breakdown coherent detection (THz-ABCD) [419]. These techniques are based on inverse processes of the ones used for THz generation in biased photoconductive switches, in OR sources, and in two-color-laser-pumped plasma, respectively. Among these, EOS is used most often, especially in pump–probe experiments and dynamic matter manipulation.

A typical EOS setup is shown in Fig. 51. The driving ultrashort laser pulse is divided into two parts. The stronger part is used for THz pulse generation. The strong-field THz pulse, after the interaction with the investigated or controlled matter, arrives into the electro-optic crystal (ZnTe in the figure). After traversing a delay line (not shown in the figure), linearly polarized weaker part of the laser pulse (the probe) also arrives into the electro-optic crystal. In the presence of the THz field, index of refraction of the nonlinear crystal is temporarily different for two induced polarizations of the material. Consequently, polarization components of the probe pulse acquire different phase shifts while passing through the electro-optic crystal. Using the $\lambda/4$-plate, and setting the polarizer beam splitter (PBS) and the detector-pair appropriately, the difference signal of the detector-pair will be zero in the case of zero THz field (balanced detection), and will be proportional to the THz field. The $\lambda/4$-plate ensures a linear relation between the intensity difference δI measured by the detector-pair and the electric field E_{THz} of the THz pulse. Assuming a zincblende-type electro-optic crystal, same THz and probe polarizations and same THz phase velocity and probe group velocity, the relation reads [420]

$$\delta I = I_p \omega n^3 E_{\mathrm{THz}} r_{41} L/c. \tag{31}$$

Here I_p is the intensity of the probe, ω is the angular frequency of the probe, n is the index of refraction, r_{41} is the electro-optic coefficient, L is the length of the crystal and c is the speed of light. Changing the delay between the THz and the probe pulse, the temporal shape of the THz electric field can be measured. Using 1 kHz, or a higher repetition-rate laser, a signal-to-noise-ratio (SNR) exceeding 10^4 can be achieved with this EOS method. Note that Eq. (31) can be applied only if the THz pulse phase velocity is equal to the pump group velocity and dispersion of the electro-optic coefficient together with THz absorption can be neglected.

EOS measurements can also be used for characterizing ultra-broadband THz pulses that have significant spectral content at higher frequencies than the phonon resonance of electro-optic crystals (*e.g.*, 5.3 THz for ZnTe). In this case, frequency dependence of the electro-optic coefficient cannot be neglected. However, the THz waveform can be found from the measured EOS signal using the response function of the EOS setup [421,422], which can be calculated from properties of the electro-optic material.

Potential and accuracy of the EOS technique are exemplified by direct sampling of the electric-field vacuum fluctuations [423]. Moreover, EOS can be used for THz time-domain spectroscopic imaging [424]. Finally, different setups, based on EOS can be used for single-shot measurements of the THz wave shape, although at significantly reduced SNR [425–427].

Please cite this article as: P. Salén, M. Basini, S. Bonetti et al., Matter manipulation with extreme terahertz light: Progress in the enabling THz technology, Physics Reports (2019), https://doi.org/10.1016/j.physrep.2019.09.002.

4.3. Controllable guiding and nanoscale confinement with graphene plasmons

Guiding and manipulation of THz waves with conventional materials (such as, *e.g.*, dielectric lenses or metallic waveguides, discussed above) do not allow for active control of fields (tuning of the wavelength, confinement length etc.). Conventional materials neither provide an appreciable reduction in the wavelength, so that THz waves cannot be compressed to small (sub-diffraction) volumes, and thus cannot provide substantial field enhancement. Graphene has recently emerged as a promising alternative to metals and dielectrics. Charge carriers in graphene have high mobility, which together with its flexibility, environmental stability and a sensitivity to electrostatic fields makes graphene very appealing for photonics and optoelectronics (*e.g.*, solar cells, light-emitting devices, high-speed THz broad-band room-temperature photodetectors and ultrafast lasers) [428,429]. Some of the particularly interesting THz graphene applications (*e.g.*, "flatland optics": atomically-thick waveguides, resonators or modulators) are related to the intrinsic graphene plasmon polaritons [430,431]. The latter are also very attractive for fundamental studies of light–matter interaction in 2D materials, such as non-equilibrium photo-induced plasmons (with femtosecond activation) [432] or probing of nonlocal optical conductivity [433] among others.

In this section, we exemplify the fundamentals of THz optics with graphene. In particular, we discuss in detail the dispersion relation and extreme field confinement of THz graphene plasmon polaritons (GPs).

GPs are confined electromagnetic fields coupled to charge-carrier (Dirac electrons or holes) oscillations in graphene. GPs exist in the energy range of 0.4–250 meV, thus covering the frequency range from the mid-IR to THz, see also Fig. 1. GPs have extremely short wavelengths, λ_p (down to two orders of magnitude smaller than the wavelength of light in free space, $\lambda_p \ll \lambda_0$), and therefore large confinement of their electromagnetic fields. Most importantly, the wavelength of GPs is tunable via changing the chemical potential, E_F, by external gate voltage, see Fig. 52c.

The dispersion of GPs in graphene on dielectric substrates (as well as free-standing graphene, see Fig. 52a) presents a square-root dependency of frequency ω upon wavevector k as $\omega \propto \sqrt{k}$, analogously to plasmon polaritons in 2D electron gases. The dispersion of GPs (red curves in Fig. 52d) is well separated from the line representing light, $\omega = kc$ (not shown, since it is virtually indistinguishable from the vertical axis), so that GPs have photon momenta significantly larger than those corresponding to the free-space photons.

The GPs can be described within classical electromagnetic theory. In this case graphene is assumed to be an infinitesimally thin conducting sheet with 2D complex-valued conductivity σ, which fully dictates the properties of the GPs. In the THz frequency range, the electronic contribution to the graphene conductivity is dominated by the intraband electron–photon scattering processes, so that σ has the classical Drude form (neglecting the temperature contribution) [431,434]

$$\sigma = \frac{ie^2|E_F|}{\pi\hbar^2(\omega + i\tau^{-1})}, \tag{32}$$

with E_F and τ being the chemical potential (proportional to the square root of the concentration of the Dirac charge carriers) and relaxation time of the charge carriers (proportional to the transport mobility), respectively. While the real part of the complex conductivity, $\mathrm{Re}(\sigma)$, characterizes the energy loss in the system, its imaginary part, $\mathrm{Im}(\sigma)$, characterizes the phase shift between the electric field and the induced current ("inertness" of the charge carriers to respond to changing electric field).

The dependence of GPs wavevector k_p upon frequency ω reads as [435]

$$k_p(\omega) = \frac{\omega}{c}\sqrt{1 - \left(\frac{c}{2\pi\sigma}\right)^2}. \tag{33}$$

For large values of k_p, according to the Drude model given by Eq. (32), the dispersion relation of GPs becomes

$$k_p(\omega) = \frac{\hbar}{2e^2}\,\frac{\hbar\omega(\omega + i/\tau)}{|E_F|}. \tag{34}$$

Thus, the real part of the GP momentum decreases with E_F and is quadratic in ω, *i.e.*, $\mathrm{Re}(k_p) \propto \omega^2/|E_F|$. The dispersion curves of GPs in free-standing graphene are shown in Fig. 52d by the red curves, for two different chemical potentials. The strong dependency of the GP wavelengths upon the chemical potential gives high tunability of GPs, which is important in many THz opto-electronic applications (such as photodetection, sensing and signal processing for communications) requiring an active control over the THz electromagnetic fields on the subwavelength scale [430,431,436]. The large momenta (short wavelengths) of GPs, as well as their strong confinement to the graphene sheet, can be seen in Fig. 52e, where the GP electric field snapshot is shown together with the wavelength in free space at a frequency of 5 THz. Notice that the strong confinement of the electromagnetic field to graphene gives the enhancement of the field strength and can lead to appreciable nonlinearities [182,188,437,438].

The intensity of blue and red fringes in the electric field snapshot (Fig. 52e) decreases from left to right due to the finite amplitude propagation length of GPs, $L_p = 1/\mathrm{Im}(k_p)$. The propagation length L_p and the figure of merit ($\mathrm{FOM} = L_p/\lambda_p$) of GPs is particularly important for the applications requiring the THz transport along graphene (*e.g.*, photonic circuits or communication technologies). Due to the small wavelength of the GPs, the absolute values of L_p are not large, being

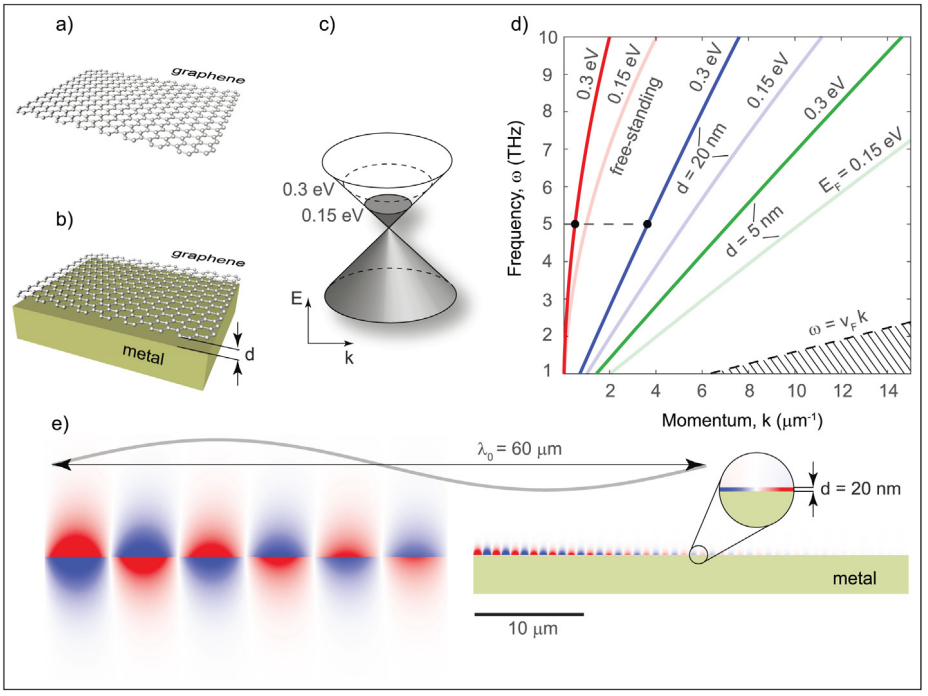

Fig. 52. Conventional and acoustic GPs. (a, b) Schematics of the free-standing graphene and graphene on top of metal gate, respectively. (c) Schematics of the electron dispersion near the Dirac point. The gray color represents the filling of the Dirac cone with the charge carriers at two doping levels. (d) Dispersion relation of conventional GPs (red curves) and AGPs (blue and green curves) for two values of the Fermi level. The dispersion of the AGPs is shown for two spacers, d = 20 nm (blue curves) and d = 5 nm (green curves). The dashed black curve represents the slope given by the Fermi velocity in graphene. The hatched region corresponds to Landau damping (due to the intraband electronic excitations). In (d, e) the relaxation time is assumed to be $\tau = 0.5$ ps.

substantially limited by the transport mobility. In contrast, the FOM can potentially reach large values, so that GPs can propagate along the distance of many GP wavelengths. For instance, for the transport mobility on the order of 10000 $cm^2((V{\cdot}s))$, typical for graphene grown by chemical vapor deposition (CVD), FOM reaches the values on the order of 10. In the graphene encapsulated between h-BN layers, the mobility can be an order of magnitude larger and so the values of FOM [439].

A completely different regime of GPs can be found in graphene separated from a metal pad by a thin spacer, d (Fig. 52b). Such a configuration is typical in the graphene samples with gating. Being virtually perfectly conducting at THz frequencies, the metal acts as a "mirror" for the GPs and the latter strongly hybridize into the screened acoustic-like mode [440], analogous to the acoustic GPs in double-layer graphene [182,441,442]. The dispersion of acoustic GPs (AGPs) for the graphene above the metal in free space, in neglect of the absorption, reads

$$k_p(\omega) = \frac{\omega}{c}\sqrt{\frac{\hbar^2 c^2}{4de^2 E_F}}. \tag{35}$$

It is radically different from that of conventional GPs (given by Eq. (34)), as the momentum scales linearly with the frequency, $k_p(\omega) \propto \omega$. Additionally, apart from the different dependence upon the chemical potential (the momenta of GP and AGPs differ by a factor of $\sqrt{E_F}$), k_p of AGPs increases with decreasing d. This is illustrated in Fig. 52d by the dispersion curves for AGPs for two chemical potentials and two graphene-metal separations (blue and green curves). As the result of the increasing k_p, the closer graphene is placed to the metal, the higher is the AGP confinement. The immense confinement of the AGPs is shown in Fig. 52e for $d = 20$ nm. Particularly, zooming in the gap region, one can see that the THz field is completely squeezed and channeled inside the nanometric gap. Such enormous compression of the electromagnetic waves can lead to strong quantum nonlocalities [433], including nonlocal response of the metal below graphene [443]. Strikingly, with the decrease of both d and E_F, the dispersion curves of AGPs approach the region of the Landau damping (shown in Fig. 52d by the hatched area), restricted by the condition $k = \omega v_F$ (black dashed line). In this regime the THz AGPs are slowed down to the Fermi velocity of electrons, v_F, giving rise to various many-body electronic effects [433].

Importantly, thanks to this very strong spatial confinement, THz plasmon polaritons in graphene (as well as in other 2D materials) can produce ultrahigh fields. The field enhancement can be estimated from the energy conservation as $E_0^2\lambda_0^2 \sim E_p^2\lambda_p d$, where E_0 and λ_0 are the field amplitude and wavelength in free space, respectively, and E_p and λ_p are

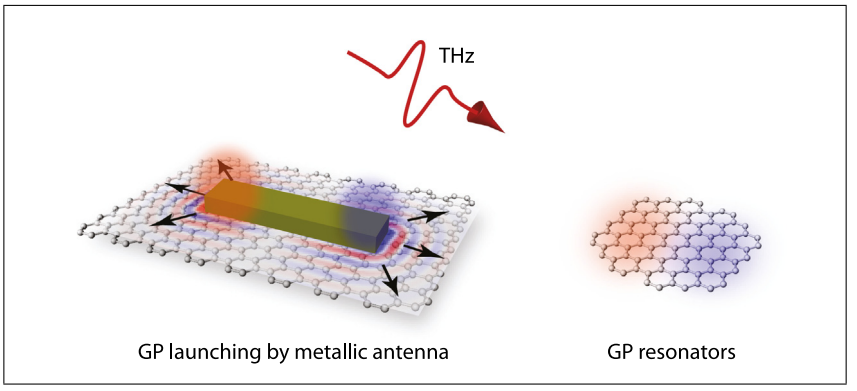

Fig. 53. Excitation of GPs by an incident THz wave. (a) Launching of propagating GPs via metallic dipolar rod antenna. (b) Excitation of GPs Fabry–Perot modes in a nanoresonator (with the size matching a half-wavelength of GPs).

the corresponding quantities for GP. For the parameters in Fig. 52e, the field enhancement factor is around 400 so that moderate amplitude (kV/cm) THz fields can be brought to the MV/cm scale. This immediately suggests an interesting direction of future research: the *coherent local* control of spins in oxides Section 2.3.3 with strong fields of GPs. Such an approach is an attractive way towards nanoscale ultrafast magnetic switches driven by strong-field few-cycle THz pulses.

At the same time, due to the high confinement of both AGPs and conventional GPs, and as a consequence, the momentum mismatch with the free-space photons, their optical excitation via far-field radiation suffers severe complications. The momentum mismatch can be overcome by the use of metallic optical antennas [444] (see Fig. 53a), gratings [445], resonators [446] (for instance, ribbons or disks supporting "bright" Fabry–Perot-like modes, as shown in Fig. 53b), tips of the near-field microscopes [439,440] or free electrons [447]. Optical antennas are particularly interesting for the excitation of the propagating GPs. Apart of being straightforwardly integrable with graphene samples and providing high GP launching efficiency, they allow for the controllable shaping of the GPs wavefronts [444]. In contrast, in graphene resonators the excited GP modes present highly-localized standing waves. Graphene resonators can potentially be used for studying nonlocal effects in materials using strong-field THz radiation.

5. Summary and outlook

The recent availability of intense THz pulses with electric field strength above 1 MV/cm has opened the door to previously inaccessible nonlinear studies. These new possibilities have enabled a better understanding of several physical and chemical processes in solids, liquids and molecules as well as the manipulation of their properties. In this review, we have described studies using the latest THz technology with respect to a broad range of research topics.

Looking to the future, it is clear that further development of THz light sources will have a strong impact by providing the tool that enables presently unfeasible experiments. One important parameter is the THz field strength. For example, the studies of coherent control of spin order via the electric field have been restricted to insulating materials because of the efficient screening of the electric field at the surface of a conductor. However, with THz electric fields comparable to the typical interatomic field strength of 100 MV/cm, it will be possible to extend such studies to conductors. THz field enhancement with graphene plasmon polaritons is a promising method for reaching high fields, though no experimental demonstration has been done yet. Furthermore, the availability of ultrashort THz transients with strong magnetic fields in the 1–10 T (3–30 MV/cm) range is demanded in order to initiate magnetization reversal in metallic ferromagnetic samples, and to measure the timescale of this process via pump–probe experiments.

It is also necessary to produce strong-field THz waves in the entire THz spectral region. As illustrated in Fig. 1a, there are important THz excitations across the whole frequency range. For example, a multitude of phonon modes can be excited nonlinearly by intense THz pulses with varying spectral content, which will be useful for the control of ferroelectric polarization and superconductive phase transitions. A strong effort towards the realization of half-cycle THz pulses with high fields is required. Such pulses have been predicted to facilitate efficient control of molecules adsorbed to surfaces, ferroelectric polarization and molecular orientation. Moreover, for this type of pulses it will be essential to access a large spectral range.

A highly beneficial feature of novel THz light sources will be the ability to reach the 5–15 THz spectral region. In this frequency range, present laser-based THz sources, relying on optical rectification, normally do not operate because of absorption in crystals, while the broad bandwidth of THz pulses generated in plasma results in a limited field amplitude per frequency unit. Although methods using the difference frequency generation can achieve electric fields in the 1 MV/cm range with frequencies between 4 and 18 THz, the generated pulse energy of 2 μJ has been restricted to a 1 kHz repetition rate [448]. Moreover, ultrashort few-cycle transients cannot be produced, only narrowband, multi-cycle, pulses. At the

same time, conventional designs of accelerator-based sources struggle with the need for unrealistically short electron bunches necessary for super-radiant amplification at frequencies above 5 THz. Note that the two examples of experiments performed using strong THz fields in the 5–15 THz range presented in Fig. 1b, were carried out using accelerator-based THz sources. However, one of them used the large scale accelerator at LCLS for generating CTR and the other one employed the oscillator-based FEL at FELIX, which produces multi-cycle THz pulses. Also note that the transition radiation sources at FACET and LCLS, see Fig. 2, are closed down. Access to intense few-cycle or half-cycle pulses in the 5–15 THz frequency window creates the opportunity to investigate unexplored processes by new excitation and probing possibilities. However, the development of corresponding THz sources is clearly needed.

A general limitation of laser-based THz sources is the repetition rate, which typically does not exceed 10 kHz. This factor will limit, for example, the efficiency of THz pump/X-ray probe experiments at MHz-repetition rate FELs driven by superconducting accelerators. Moreover, the variable repetition rate is essential for matching the requirements of different types of studies. For example, pump–probe measurements typically request repetition rates of 1–10 kHz and a reduced repetition frequency is sometimes desired in condensed phase experiments in order to limit the temperature increase. In contrast, the large average power that can be generated with a high repetition rate is specifically required in gas-phase experiments because of the low concentration of particles. Although experiments in condensed phase environments sometimes demand a limited average power of the THz radiation, there are ways to overcome this problem, such as using rotating samples, liquid jets, and cooling of the sample. The high average power made available by a superconducting linear accelerator will, thus, be a general asset in many experiments because of the significantly reduced measurement time.

While the technology of THz detection is well established for strong-field (high-power) THz radiation, the development of high-sensitivity THz detectors will be beneficial for studies of nonlinear THz effects characterized by weak intensities. One can mention graphene as one of several very promising materials for new THz detectors [429]. Apart from graphene's broadband absorption spectrum and unique optoelectronic characteristics, THz graphene-based photodetectors have demonstrated high sensitivity (with a noise-equivalent power of a few tens of $pW/\sqrt{Hz}$ at room temperature), appreciable response time (below 30 ns) and a high dynamic range [449,450]. On top of that, graphene possesses complementary metal-oxide-semiconductor (CMOS) integrability and therefore is compatible with the silicon-based platform for electronics and photonics.

To summarize, fundamental THz research will benefit from the further development of the technology for THz light generation. Such advances are desired with respect to both laser- and accelerator-based sources since they are complementary. While the compactness of laser-based sources is highly attractive, the accelerator-based THz sources have the advantage of being more flexible concerning wavelength tunability and repetition rate, and can achieve higher average powers.

Acknowledgments

The authors are grateful to Prof. Philipp Werner (University of Fribourg) and Dr. Yuta Murakami (Tokyo Institute of Technology) for explaining some aspects of their work [71].

Funding information

The authors acknowledge the support of the funding agencies: A.Y.N. — the Spanish Ministry of Science, Innovation and Universities (national project MAT2017-88358-C3-3-R) and Basque Government (Grant No. IT1164-19); J.H. and Z.T. — the Hungarian Scientific Research Fund (OTKA) (Grant No. 125808 and 129134); V.G. — the Swedish Research Council (VR Starting Grant 2016-04593 "Generation of giant half-cycle pulses of THz light"); P.S. and V.G. — the Stockholm-Uppsala Centre for Free-Electron Laser Research (SUFEL); S.B. — the European Research Council (ERC Starting Grant 715452 "Magnetic speed limit").

References

[1] J. Hebling, G. Almasi, I. Kozma, J. Kuhl, Velocity matching by pulse front tilting for large area THz-pulse generation, Opt. Express 10 (21) (2002) 1161, http://dx.doi.org/10.1364/oe.10.001161.
[2] K.-L. Yeh, M.C. Hoffmann, J. Hebling, K.A. Nelson, Generation of 10μj ultrashort terahertz pulses by optical rectification, Appl. Phys. Lett. 90 (17) (2007) 171121, http://dx.doi.org/10.1063/1.2734374.
[3] T. Kampfrath, K. Tanaka, K.A. Nelson, Resonant and nonresonant control over matter and light by intense terahertz transients, Nat. Photonics 7 (9) (2013) 680–690, http://dx.doi.org/10.1038/nphoton.2013.184.
[4] K. Fan, H.Y. Hwang, M. Liu, A.C. Strikwerda, A. Sternbach, J. Zhang, X. Zhao, X. Zhang, K.A. Nelson, R.D. Averitt, Nonlinear terahertz metamaterials via field-enhanced carrier dynamics in GaAs, Phys. Rev. Lett. 110 (2013) 217404, http://dx.doi.org/10.1103/PhysRevLett.110.217404.
[5] C. Lange, T. Maag, M. Hohenleutner, S. Baierl, O. Schubert, E.R.J. Edwards, D. Bougeard, G. Woltersdorf, R. Huber, Extremely nonperturbative nonlinearities in GaAs driven by atomically strong terahertz fields in gold metamaterials, Phys. Rev. Lett. 113 (2014) 227401, http://dx.doi.org/10.1103/PhysRevLett.113.227401.
[6] F. Langer, M. Hohenleutner, C.P. Schmid, C. Poellmann, P. Nagler, T. Korn, C. Schüller, M.S. Sherwin, U. Huttner, J.T. Steiner, S.W. Koch, M. Kira, R. Huber, Lightwave-driven quasiparticle collisions on a subcycle timescale, Nature 533 (2016) 225, http://dx.doi.org/10.1038/nature17958.
[7] B. Mayer, C. Schmidt, A. Grupp, J. Bühler, J. Oelmann, R.E. Marvel, R.F. Haglund, T. Oka, D. Brida, A. Leitenstorfer, A. Pashkin, Tunneling breakdown of a strongly correlated insulating state in VO_2 induced by intense multiterahertz excitation, Phys. Rev. B 91 (2015) 235113.

[8] C. Vicario, M. Shalaby, C.P. Hauri, Subcycle extreme nonlinearities in gap induced by an ultrastrong terahertz field, Phys. Rev. Lett. 118 (2017) 083901, http://dx.doi.org/10.1103/PhysRevLett.118.083901.
[9] R. Mankowsky, A. Subedi, M. Först, S.O. Mariager, M. Chollet, H.T. Lemke, J.S. Robinson, J.M. Glownia, M.P. Minitti, A. Frano, M. Fechner, N.A. Spaldin, T. Loew, B. Keimer, A. Georges, A. Cavalleri, Nonlinear lattice dynamics as a basis for enhanced superconductivity in YBa2cu3o6.5, Nature 516 (7529) (2014) 71–73, http://dx.doi.org/10.1038/nature13875.
[10] K.A. Grishunin, N.A. Ilyin, N.E. Sherstyuk, E.D. Mishina, A. Kimel, V.M. Mukhortov, A.V. Ovchinnikov, O.V. Chefonov, M.B. Agranat, THz electric field-induced second harmonic generation in inorganic ferroelectric, Sci. Rep. 7 (1) (2017) http://dx.doi.org/10.1038/s41598-017-00704-9.
[11] X. Yang, C. Vaswani, C. Sundahl, M. Mootz, P. Gagel, L. Luo, J.H. Kang, P.P. Orth, I.E. Perakis, C.B. Eom, J. Wang, Terahertz-light quantum tuning of a metastable emergent phase hidden by superconductivity, Nature Mater. 17 (7) (2018) 586–591, http://dx.doi.org/10.1038/s41563-018-0096-3.
[12] K. Kitano, N. Ishii, J. Itatani, High degree of molecular orientation by a combination of THz and femtosecond laser pulses, Phys. Rev. A 84 (2011) 053408, http://dx.doi.org/10.1103/PhysRevA.84.053408.
[13] F. Novelli, F. Sebastiani, C. Hoberg, L.R. Pestana, K.C. Bennett, N. Stavrias, L.V.D. Meer, G. Schwaab, T. Head-Gordon, M. Havenith, Molecular alignment of bulk water: Observing a giant THz Kerr effect upon librational excitation, 2018, arXiv:1809.04261.
[14] J.L. LaRue, T. Katayama, A. Lindenberg, A.S. Fisher, H. Öström, A. Nilsson, H. Ogasawara, THz-pulse-induced selective catalytic CO oxidation on Ru, Phys. Rev. Lett. 115 (2015) 036103, http://dx.doi.org/10.1103/PhysRevLett.115.036103.
[15] T. Kampfrath, A. Sell, G. Klatt, A. Pashkin, S. Mährlein, T. Dekorsy, M. Wolf, M. Fiebig, A. Leitenstorfer, R. Huber, Coherent terahertz control of antiferromagnetic spin waves, Nat. Photonics 5 (1) (2011) 31.
[16] G.A. Askar'yan, Cherenkov and transition radiation from electromagnetic waves, Sov. Phy. J. Exp. Theor. Phys. 15 (1962) 943.
[17] D.H. Auston, K.P. Cheung, J.A. Valdmanis, D.A. Kleinman, Cherenkov radiation from femtosecond optical pulses in electro-optic media, Phys. Rev. Lett. 53 (1984) 1555–1558, http://dx.doi.org/10.1103/PhysRevLett.53.1555.
[18] N.A. Vinokurov, Y.U. Jeong, Generating high-power short terahertz electromagnetic pulses with a multifoil radiator, Phys. Rev. Lett. 110 (6) (2013) 064805, http://dx.doi.org/10.1103/physrevlett.110.064805.
[19] G. Li, B.P. Clarke, J.-K. So, K.F. MacDonald, N.I. Zheludev, Holographic free-electron light source, Nature Commun. 7 (1) (2016) http://dx.doi.org/10.1038/ncomms13705.
[20] A. Mak, G. Shamuilov, P. Salén, D. Dunning, J. Hebling, Y. Kida, R. Kinjo, B.W.J. McNeil, T. Tanaka, N. Thompson, Z. Tibai, G. Tóth, V. Goryashko, Attosecond single-cycle undulator light: a review, Rep. Progr. Phys. 82 (2) (2019) 025901, http://dx.doi.org/10.1088/1361-6633/aafa35.
[21] T. Tanaka, Proposal to generate an isolated monocycle x-ray pulse by counteracting the slippage effect in free-electron lasers, Phys. Rev. Lett. 114 (4) (2015) 044801, http://dx.doi.org/10.1103/physrevlett.114.044801.
[22] Y. Kida, R. Kinjo, T. Tanaka, Synthesizing high-order harmonics to generate a sub-cycle pulse in free-electron lasers, Appl. Phys. Lett. 109 (15) (2016) 151107, http://dx.doi.org/10.1063/1.4964643.
[23] V.A. Goryashko, Quasi-half-cycle pulses of light from a tapered undulator, Phys. Rev. Accel. Beams 20 (8) (2017) 080703, http://dx.doi.org/10.1103/physrevaccelbeams.20.080703.
[24] T.I. Oh, Y.J. Yoo, Y.S. You, K.Y. Kim, Generation of strong terahertz fields exceeding 8 MV/cm at 1 kHz and real-time beam profiling, Appl. Phys. Lett. 105 (4) (2014) 041103, http://dx.doi.org/10.1063/1.4891678.
[25] H. Hirori, K. Shinokita, M. Shirai, S. Tani, Y. Kadoya, K. Tanaka, Extraordinary carrier multiplication gated by a picosecond electric field pulse, Nature Commun. 2 (2011) 594, http://dx.doi.org/10.1038/ncomms1598.
[26] F. Junginger, A. Sell, O. Schubert, B. Mayer, D. Brida, M. Marangoni, G. Cerullo, A. Leitenstorfer, R. Huber, Single-cycle multiterahertz transients with peak fields above 10 MV/cm, Opt. Lett. 35 (15) (2010) 2645, http://dx.doi.org/10.1364/ol.35.002645.
[27] C. Vicario, B. Monoszlai, C.P. Hauri, GV/msingle-cycle terahertz fields from a laser-driven large-size partitioned organic crystal, Phys. Rev. Lett. 112 (21) (2014) 213901, http://dx.doi.org/10.1103/physrevlett.112.213901.
[28] C. Vicario, B. Monoszlai, C.P. Hauri, Erratum: GV/m single-cycle terahertz fields from a laser-driven large-size partitioned organic crystal [phys. rev. lett. 112, 213901 (2014)], Phys. Rev. Lett. 121 (25) (2018) 259901, http://dx.doi.org/10.1103/physrevlett.121.259901.
[29] Z. Wu, A.S. Fisher, J. Goodfellow, M. Fuchs, D. Daranciang, M. Hogan, H. Loos, A. Lindenberg, Intense terahertz pulses from SLAC electron beams using coherent transition radiation, Rev. Sci. Instrum. 84 (2) (2013) 022701, http://dx.doi.org/10.1063/1.4790427.
[30] D. Daranciang, J. Goodfellow, M. Fuchs, H. Wen, S. Ghimire, D.A. Reis, H. Loos, A.S. Fisher, A.M. Lindenberg, Single-cycle terahertz pulses with $>$ 0.2 V/Å field amplitudes via coherent transition radiation, Appl. Phys. Lett. 99 (14) (2011) 141117, http://dx.doi.org/10.1063/1.3646399.
[31] M. Gensch, Super-radiant linac-based THz sources in 2013, in: Proceedings of FEL2013, JACoW, 2013, pp. 474–476.
[32] M. Gensch, L. Bittner, A. Chesnov, H. Delsim-Hashemi, M. Drescher, B. Faatz, J. Feldhaus, U. Fruehling, G. Geloni, C. Gerth, O. Grimm, U. Hahn, M. Hesse, S. Kapitzki, V. Kocharyan, O. Kozlov, E. Matyushevsky, N. Morozov, D. Petrov, E. Ploenjes, M. Roehling, J. Rossbach, E. Saldin, B. Schmidt, P. Schmueser, E. Schneidmiller, E. Syresin, A. Willner, M. Yurkov, New infrared undulator beamline at FLASH, Infrared Phys. Technol. 51 (5) (2008) 423–425, http://dx.doi.org/10.1016/j.infrared.2007.12.032.
[33] B. Green, S. Kovalev, V. Asgekar, G. Geloni, U. Lehnert, T. Golz, M. Kuntzsch, C. Bauer, J. Hauser, J. Voigtlaender, B. Wustmann, I. Koesterke, M. Schwarz, M. Freitag, A. Arnold, J. Teichert, M. Justus, W. Seidel, C. Ilgner, N. Awari, D. Nicoletti, S. Kaiser, Y. Laplace, S. Rajasekaran, L. Zhang, S. Winnerl, H. Schneider, G. Schay, I. Lorincz, A.A. Rauscher, I. Radu, S. Mährlein, T.H. Kim, J.S. Lee, T. Kampfrath, S. Wall, J. Heberle, A. Malnasi-Csizmadia, A. Steiger, A.S. Müller, M. Helm, U. Schramm, T. Cowan, P. Michel, A. Cavalleri, A.S. Fisher, N. Stojanovic, M. Gensch, High-field high-repetition-rate sources for the coherent THz control of matter, Sci. Rep. 6 (1) (2016) 22256, http://dx.doi.org/10.1038/srep22256.
[34] H.J. Zeiger, J. Vidal, T.K. Cheng, E.P. Ippen, G. Dresselhaus, M.S. Dresselhaus, Theory for displacive excitation of coherent phonons, Phys. Rev. B 45 (1992) 768–778, http://dx.doi.org/10.1103/PhysRevB.45.768.
[35] R. Merlin, Generating coherent THz phonons with light pulses, Solid State Commun. 102 (2–3) (1997) 207–220, http://dx.doi.org/10.1016/s0038-1098(96)00721-1.
[36] Y.-X. Yan, E.B. Gamble, K.A. Nelson, Impulsive stimulated scattering: General importance in femtosecond laser pulse interactions with matter, and spectroscopic applications, J. Chem. Phys. 83 (11) (1985) 5391–5399, http://dx.doi.org/10.1063/1.449708.
[37] S. Maehrlein, A. Paarmann, M. Wolf, T. Kampfrath, THz sum-frequency excitation of a Raman-active phonon, Phys. Rev. Lett. 119 (12) (2017) 127402, http://dx.doi.org/10.1103/PhysRevLett.119.127402.
[38] R. Mankowsky, M. Först, A. Cavalleri, Non-equilibrium control of complex solids by nonlinear phononics, Rep. Progr. Phys. 79 (6) (2016) 064503, http://dx.doi.org/10.1088/0034-4885/79/6/064503.
[39] A. Cavalleri, Photo-induced superconductivity, Contemp. Phys. 59 (1) (2017) 31–46, http://dx.doi.org/10.1080/00107514.2017.1406623.
[40] B.S. Dastrup, J.R. Hall, J.A. Johnson, Experimental determination of the interatomic potential in LiNbO3 via ultrafast lattice control, Appl. Phys. Lett. 110 (16) (2017) 162901, http://dx.doi.org/10.1063/1.4980112.
[41] P. Hamm, M. Meuwly, S.L. Johnson, P. Beaud, U. Staub, Perspective: THz-driven nuclear dynamics from solids to molecules, Struct. Dyn. 4 (6) (2017) 061601, http://dx.doi.org/10.1063/1.4992050.
[42] D.M. Juraschek, S.F. Maehrlein, Sum-frequency ionic Raman scattering, Phys. Rev. B 97 (17) (2018) 174302, http://dx.doi.org/10.1103/physrevb.97.174302.
[43] M. Kozina, M. Fechner, P. Marsik, T. van Driel, J.M. Glownia, C. Bernhard, M. Radovic, D. Zhu, S. Bonetti, U. Staub, M.C. Hoffmann, Terahertz-driven phonon upconversion in SrTiO3, Nat. Phys. (2019) http://dx.doi.org/10.1038/s41567-018-0408-1.

[44] A.A. Maradudin, R.F. Wallis, Ionic Raman effect. Scattering by localized vibration modes, Phys. Rev. B 2 (10) (1970) 4294–4299, http://dx.doi.org/10.1103/physrevb.2.4294.
[45] R.F. Wallis, A.A. Maradudin, Ionic Raman effect. II. The first-order ionic Raman effect, Phys. Rev. B 3 (6) (1971) 2063–2075, http://dx.doi.org/10.1103/physrevb.3.2063.
[46] T.P. Martin, L. Genzel, Ionic Raman scattering and ionic frequency mixing, Phys. Status Solidi B 61 (2) (1974) 493–502, http://dx.doi.org/10.1002/pssb.2220610214.
[47] M. Först, C. Manzoni, S. Kaiser, Y. Tomioka, Y. Tokura, R. Merlin, A. Cavalleri, Nonlinear phononics as an ultrafast route to lattice control, Nat. Phys. 7 (11) (2011) 854–856, http://dx.doi.org/10.1038/nphys2055.
[48] A.D. Caviglia, R. Scherwitzl, P. Popovich, W. Hu, H. Bromberger, R. Singla, M. Mitrano, M.C. Hoffmann, S. Kaiser, P. Zubko, S. Gariglio, J.-M. Triscone, M. Först, A. Cavalleri, Ultrafast strain engineering in complex oxide heterostructures, Phys. Rev. Lett. 108 (13) (2012) 136801, http://dx.doi.org/10.1103/physrevlett.108.136801.
[49] M. Rini, R. Tobey, N. Dean, J. Itatani, Y. Tomioka, Y. Tokura, R.W. Schoenlein, A. Cavalleri, Control of the electronic phase of a manganite by mode-selective vibrational excitation, Nature 449 (7158) (2007) 72–74, http://dx.doi.org/10.1038/nature06119.
[50] A. Subedi, A. Cavalleri, A. Georges, Theory of nonlinear phononics for coherent light control of solids, Phys. Rev. B 89 (22) (2014) 220301, http://dx.doi.org/10.1103/physrevb.89.220301.
[51] M. Först, R.I. Tobey, S. Wall, H. Bromberger, V. Khanna, A.L. Cavalieri, Y.-D. Chuang, W.S. Lee, R. Moore, W.F. Schlotter, J.J. Turner, O. Krupin, M. Trigo, H. Zheng, J.F. Mitchell, S.S. Dhesi, J.P. Hill, A. Cavalleri, Driving magnetic order in a manganite by ultrafast lattice excitation, Phys. Rev. B 84 (24) (2011) 241104, http://dx.doi.org/10.1103/physrevb.84.241104.
[52] R.I. Tobey, D. Prabhakaran, A.T. Boothroyd, A. Cavalleri, Ultrafast electronic phase transition in La1/2Sr3/2MnO4 by coherent vibrational excitation: Evidence for nonthermal melting of orbital order, Phys. Rev. Lett. 101 (19) (2008) 197404, http://dx.doi.org/10.1103/physrevlett.101.197404.
[53] T. Qi, Y.-H. Shin, K.-L. Yeh, K.A. Nelson, A.M. Rappe, Collective coherent control: Synchronization of polarization in ferroelectric PbTiO3 by shaped THz fields, Phys. Rev. Lett. 102 (24) (2009) 247603, http://dx.doi.org/10.1103/physrevlett.102.247603.
[54] A. Subedi, Proposal for ultrafast switching of ferroelectrics using midinfrared pulses, Phys. Rev. B 92 (21) (2015) 214303, http://dx.doi.org/10.1103/physrevb.92.214303.
[55] R. Mankowsky, A. von Hoegen, M. Först, A. Cavalleri, Ultrafast reversal of the ferroelectric polarization, Phys. Rev. Lett. 118 (19) (2017) 197601, http://dx.doi.org/10.1103/physrevlett.118.197601.
[56] D.M. Juraschek, M. Fechner, N.A. Spaldin, Ultrafast structure switching through nonlinear phononics, Phys. Rev. Lett. 118 (5) (2017) 054101, http://dx.doi.org/10.1103/physrevlett.118.054101.
[57] A.A. Melnikov, K.N. Boldyrev, Y.G. Selivanov, V.P. Martovitskii, S.V. Chekalin, E.A. Ryabov, Coherent phonons in a Bi2Se3 film generated by an intense single-cycle THz pulse, Phys. Rev. B 97 (21) (2018) 214304, http://dx.doi.org/10.1103/physrevb.97.214304.
[58] A. von Hoegen, R. Mankowsky, M. Fechner, M. Först, A. Cavalleri, Probing the interatomic potential of solids with strong-field nonlinear phononics, Nature 555 (7694) (2018) 79–82, http://dx.doi.org/10.1038/nature25484.
[59] X. Li, T. Qju, J. Zhang, E. Baldini, J. Lu, A. Rappe, K. Nelson, Terahertz field-induced ferroelectricity in quantum paraelectric SrTiO3, Science 364 (2019) 1079–1082, http://dx.doi.org/10.1126/science.aaw4913, URL https://science.sciencemag.org/content/364/6445/1079.
[60] T. Nova, A. Disa, M. Frechner, A. Cavalleri, Metastable ferroelectricity in optically strained SrTiO3, Science 364 (2019) 1075–1079, http://dx.doi.org/10.1126/science.aaw4911, URL https://science.sciencemag.org/content/364/6445/1075.
[61] V. Esposito, M. Fechner, R. Mankowsky, H. Lemke, M. Chollet, J.M. Glownia, M. Nakamura, M. Kawasaki, Y. Tokura, U. Staub, P. Beaud, M. Först, Nonlinear electron-phonon coupling in doped manganites, Phys. Rev. Lett. 118 (24) (2017) 247601, http://dx.doi.org/10.1103/physrevlett.118.247601.
[62] T. Nova, A. Cartella, A. Cantaluppi, M. Först, D. Bossini, a.K. R.V. Mikhaylovskiy, R. Merlin, A. Cavalleri, An effective magnetic field from optically driven phonons, Nat. Phys. 13 (2017) 132–136, http://dx.doi.org/10.1038/nphys3925.
[63] B. Yan, C. Felser, Topological materials: Weyl semimetals, Annu. Rev. Condensed Matter Phys. 8 (2017) 337–354, http://dx.doi.org/10.1146/annurev-conmatphys-031016-025458.
[64] E.J. Sie, C.M. Nyby, C.D. Pemmaraju, X.S. Su Ji Park, M.C.H. J. Yang, B.K. Ofori-Okai, R. Li, A.H. Reid, S. Weathersby, E. Mannebach, N. Finney, D. Rhodes, D. Chenet, A. Antony, L. Balicas, J. Hone, T. Devereaux, X.W. T.F. Heinz, A.M. Lindenberg, An ultrafast symmetry switch in a Weyl semimetal, Nature 565 (2019) 61–66, http://dx.doi.org/10.1038/s41586-018-0809-4.
[65] R. Matsunaga, N. Tsuji, H. Fujita, A. Sugioka, K. Makise, Y. Uzawa, H. Terai, Z. Wang, H. Aoki, R. Shimano, Light-induced collective pseudospin precession resonating with higgs mode in a superconductor, Science 345 (6201) (2014) 1145–1149, http://dx.doi.org/10.1126/science.1254697.
[66] R. Matsunaga, Y.I. Hamada, K. Makise, Y. Uzawa, H. Terai, Z. Wang, R. Shimano, Higgs amplitude mode in the BCS superconductors Nb1-xtixn induced by terahertz pulse excitation, Phys. Rev. Lett. 111 (5) (2013) 057002, http://dx.doi.org/10.1103/physrevlett.111.057002.
[67] R.A. Barankov, L.S. Levitov, B.Z. Spivak, Collective rabi oscillations and solitons in a time-dependent BCS pairing problem, Phys. Rev. Lett. 93 (16) (2004) 160401, http://dx.doi.org/10.1103/physrevlett.93.160401.
[68] R.A. Barankov, L.S. Levitov, Synchronization in the BCS pairing dynamics as a critical phenomenon, Phys. Rev. Lett. 96 (23) (2006) 230403, http://dx.doi.org/10.1103/physrevlett.96.230403.
[69] F. Peronaci, M. Schiró, M. Capone, Transient dynamics of d-wave superconductors after a sudden excitation, Phys. Rev. Lett. 115 (25) (2015) 257001, http://dx.doi.org/10.1103/physrevlett.115.257001.
[70] M.A. Sentef, A.F. Kemper, A. Georges, C. Kollath, Theory of light-enhanced phonon-mediated superconductivity, Phys. Rev. B 93 (14) (2016) 144506, http://dx.doi.org/10.1103/physrevb.93.144506.
[71] Y. Murakami, P. Werner, N. Tsuji, H. Aoki, Multiple amplitude modes in strongly coupled phonon-mediated superconductors, Phys. Rev. B 93 (9) (2016) 094509, http://dx.doi.org/10.1103/physrevb.93.094509.
[72] J.M. Tranquada, B.J. Sternlieb, J.D. Axe, Y. Nakamura, S. Uchida, Evidence for stripe correlations of spins and holes in copper oxide superconductors, Nature 375 (6532) (1995) 561–563, http://dx.doi.org/10.1038/375561a0.
[73] Y. Nakamura, S. Uchida, Anisotropic transport properties of single-crystal La2-x-yNdySrxCuO4: Effect of the structural phase transition, Phys. Rev. B 46 (9) (1992) 5841–5844, http://dx.doi.org/10.1103/physrevb.46.5841.
[74] J. Fink, E. Schierle, E. Weschke, J. Geck, D. Hawthorn, V. Soltwisch, H. Wadati, H.-H. Wu, H.A. Dürr, N. Wizent, B. Büchner, G.A. Sawatzky, Charge ordering in La1.8-xEu0.2srxCuO4 studied by resonant soft x-ray diffraction, Phys. Rev. B 79 (10) (2009) 100502, http://dx.doi.org/10.1103/physrevb.79.100502.
[75] D. Fausti, R.I. Tobey, N. Dean, S. Kaiser, A. Dienst, M.C. Hoffmann, S. Pyon, T. Takayama, H. Takagi, A. Cavalleri, Light-induced superconductivity in a stripe-ordered cuprate, Science 331 (6014) (2011) 189–191, http://dx.doi.org/10.1126/science.1197294.
[76] S. Kaiser, C.R. Hunt, D. Nicoletti, W. Hu, I. Gierz, H.Y. Liu, M.L. Tacon, T. Loew, D. Haug, B. Keimer, A. Cavalleri, Optically induced coherent transport far above Tc in underdoped YBa2Cu3O6+x, Phys. Rev. B 89 (18) (2014) 184516, http://dx.doi.org/10.1103/physrevb.89.184516.
[77] W. Hu, S. Kaiser, D. Nicoletti, C.R. Hunt, I. Gierz, M.C. Hoffmann, M.L. Tacon, T. Loew, B. Keimer, A. Cavalleri, Optically enhanced coherent transport in YBa2Cuo6.5 by ultrafast redistribution of interlayer coupling, Nature Mater. 13 (7) (2014) 705–711, http://dx.doi.org/10.1038/nmat3963.

Please cite this article as: P. Salén, M. Basini, S. Bonetti et al., Matter manipulation with extreme terahertz light: Progress in the enabling THz technology, Physics Reports (2019), https://doi.org/10.1016/j.physrep.2019.09.002.

[78] S. Rajasekaran, J. Okamoto, L. Mathey, M. Fechner, V. Thampy, G.D. Gu, A. Cavalleri, Probing optically silent superfluid stripes in cuprates, Science 359 (6375) (2018) 575–579, http://dx.doi.org/10.1126/science.aan3438.
[79] M. Mitrano, A. Cantaluppi, D. Nicoletti, S. Kaiser, A. Perucchi, S. Lupi, P.D. Pietro, D. Pontiroli, M. Riccò, S.R. Clark, D. Jaksch, A. Cavalleri, Possible light-induced superconductivity in K3C60 at high temperature, Nature 530 (7591) (2016) 461–464, http://dx.doi.org/10.1038/nature16522.
[80] A. Cantaluppi, M. Buzzi, G. Jotzu, D. Nicoletti, M. Mitrano, D. Pontiroli, M. Riccò, A. Perucchi, P.D. Pietro, A. Cavalleri, Pressure tuning of light-induced superconductivity in K3C60, Nat. Phys. 14 (8) (2018) 837–841, http://dx.doi.org/10.1038/s41567-018-0134-8.
[81] M. Babadi, M. Knap, I. Martin, G. Refael, E. Demler, Theory of parametrically amplified electron-phonon superconductivity, Phys. Rev. B 96 (1) (2017) http://dx.doi.org/10.1103/physrevb.96.014512.
[82] M. Knap, M. Babadi, G. Refael, I. Martin, E. Demler, Dynamical cooper pairing in nonequilibrium electron-phonon systems, Phys. Rev. B 94 (21) (2016) http://dx.doi.org/10.1103/physrevb.94.214504.
[83] A. Nava, C. Giannetti, A. Georges, E. Tosatti, M. Fabrizio, Cooling quasiparticles in A3C60 fullerides by excitonic mid-infrared absorption, Nat. Phys. 14 (2) (2017) 154–159, http://dx.doi.org/10.1038/nphys4288.
[84] G. Chiriacò, A.J. Millis, I.L. Aleiner, Transient superconductivity without superconductivity, Phys. Rev. B 98 (22) (2018) http://dx.doi.org/10.1103/physrevb.98.220510.
[85] N. Setter, D. Damjanovic, L. Eng, G. Fox, S. Gevorgian, S. Hong, A. Kingon, H. Kohlstedt, N.Y. Park, G.B. Stephenson, I. Stolitchnov, A.K. Taganstev, D.V. Taylor, T. Yamada, S. Streiffer, Ferroelectric thin films: Review of materials, properties, and applications, J. Appl. Phys. 100 (5) (2006) 051606, http://dx.doi.org/10.1063/1.2336999.
[86] J.F. Scott, Applications of modern ferroelectrics, Science 315 (5814) (2007) 954–959, http://dx.doi.org/10.1126/science.1129564.
[87] O. Auciello, J.F. Scott, R. Ramesh, The physics of ferroelectric memories, Phys. Today 51 (7) (1998) 22–27, http://dx.doi.org/10.1063/1.882324.
[88] G. Catalan, J.F. Scott, Physics and applications of bismuth ferrite, Adv. Mater. 21 (24) (2009) 2463–2485, http://dx.doi.org/10.1002/adma.200802849.
[89] T.M. Shaw, S. Trolier-McKinstry, P.C. McIntyre, The properties of ferroelectric films at small dimensions, Annu. Rev. Mater. Sci. 30 (1) (2000) 263–298, http://dx.doi.org/10.1146/annurev.matsci.30.1.263.
[90] R.K. Vasudevan, N. Balke, P. Maksymovych, S. Jesse, S.V. Kalinin, Ferroelectric or non-ferroelectric: Why so many materials exhibit "ferroelectricity" on the nanoscale, Appl. Phys. Rev. 4 (2) (2017) 021302, http://dx.doi.org/10.1063/1.4979015.
[91] A. Zenkevich, Y. Matveyev, K. Maksimova, R. Gaynutdinov, A. Tolstikhina, V. Fridkin, Giant bulk photovoltaic effect in thin ferroelectric BaTiO3 films, Phys. Rev. B 90 (16) (2014) 161409, http://dx.doi.org/10.1103/physrevb.90.161409.
[92] A. Grigoriev, D.-H. Do, D.M. Kim, C.-B. Eom, B. Adams, E.M. Dufresne, P.G. Evans, Nanosecond domain wall dynamics in ferroelectric Pb(Zr, Ti)O3 thin films, Phys. Rev. Lett. 96 (18) (2006) 187601, http://dx.doi.org/10.1103/physrevlett.96.187601.
[93] S. Fahy, R. Merlin, Reversal of ferroelectric domains by ultrashort optical pulses, Phys. Rev. Lett. 73 (8) (1994) 1122–1125, http://dx.doi.org/10.1103/physrevlett.73.1122.
[94] F. Chen, Y. Zhu, S. Liu, Y. Qi, H.Y. Hwang, N.C. Brandt, J. Lu, F. Quirin, H. Enquist, P. Zalden, T. Hu, J. Goodfellow, M.-J. Sher, M.C. Hoffmann, D. Zhu, H. Lemke, J. Glownia, M. Chollet, A.R. Damodaran, J. Park, Z. Cai, I.W. Jung, M.J. Highland, D.A. Walko, J.W. Freeland, P.G. Evans, A. Vailionis, J. Larsson, K.A. Nelson, A.M. Rappe, K. Sokolowski-Tinten, L.W. Martin, H. Wen, A.M. Lindenberg, Ultrafast terahertz-field-driven ionic response in ferroelectric BaTiO3, Phys. Rev. B 94 (18) (2016) 180104, http://dx.doi.org/10.1103/physrevb.94.180104.
[95] M. Kozina, M. Pancaldi, C. Bernhard, T. van Driel, J.M. Glownia, P. Marsik, M. Radovic, C.A.F. Vaz, D. Zhu, S. Bonetti, U. Staub, M.C. Hoffmann, Local terahertz field enhancement for time-resolved x-ray diffraction, Appl. Phys. Lett. 110 (8) (2017) 081106, http://dx.doi.org/10.1063/1.4977088.
[96] A.Q. Jiang, H.J. Lee, C.S. Hwang, J.F. Scott, Sub-picosecond processes of ferroelectric domain switching from field and temperature experiments, Adv. Funct. Mater. 22 (1) (2011) 192–199, http://dx.doi.org/10.1002/adfm.201101521.
[97] S. Jesse, B.J. Rodriguez, S. Choudhury, A.P. Baddorf, I. Vrejoiu, D. Hesse, M. Alexe, E.A. Eliseev, A.N. Morozovska, J. Zhang, L.-Q. Chen, S.V. Kalinin, Direct imaging of the spatial and energy distribution of nucleation centres in ferroelectric materials, Nature Mater. 7 (3) (2008) 209–215, http://dx.doi.org/10.1038/nmat2114.
[98] M.C. Hoffmann, B.S. Monozon, D. Livshits, E.U. Rafailov, D. Turchinovich, Terahertz electro-absorption effect enabling femtosecond all-optical switching in semiconductor quantum dots, Appl. Phys. Lett. 97 (23) (2010) 231108, http://dx.doi.org/10.1063/1.3515909.
[99] B.C. Pein, W. Chang, H.Y. Hwang, J. Scherer, I. Coropceanu, X. Zhao, X. Zhang, V. Bulović, M. Bawendi, K.A. Nelson, Terahertz-driven luminescence and colossal stark effect in CdSe–CdS colloidal quantum dots, Nano Lett. 17 (9) (2017) 5375–5380, PMID: 28786683, http://dx.doi.org/10.1021/acs.nanolett.7b01837.
[100] R. Wang, L. Xie, S. Hameed, C. Wang, Y. Ying, Mechanisms and applications of carbon nanotubes in terahertz devices: A review, Carbon 132 (2018) 42–58, http://dx.doi.org/10.1016/j.carbon.2018.02.005, URL http://www.sciencedirect.com/science/article/pii/S0008622318301209.
[101] R. Shimano, S. Watanabe, R. Matsunaga, Intense terahertz pulse-induced nonlinear responses in carbon nanotubes, J. Infrared Millim. Terahertz Waves 33 (8) (2012) 861–869, http://dx.doi.org/10.1007/s10762-012-9914-x.
[102] F.F. Sudradjat, W. Zhang, J. Woodward, H. Durmaz, T.D. Moustakas, R. Paiella, Far-infrared intersubband photodetectors based on double-step III-nitride quantum wells, Appl. Phys. Lett. 100 (24) (2012) 241113, http://dx.doi.org/10.1063/1.4729470.
[103] P. Sookchoo, F.F. Sudradjat, A.M. Kiefer, H. Durmaz, R. Paiella, M.G. Lagally, Strain engineered sige multiple-quantum-well nanomembranes for far-infrared intersubband device applications, ACS Nano 7 (3) (2013) 2326–2334, PMID: 23402572, http://dx.doi.org/10.1021/nn305528t.
[104] D. Dietze, J. Darmo, K. Unterrainer, Efficient population transfer in modulation doped single quantum wells by intense few-cycle terahertz pulses, New J. Phys. 15 (6) (2013) 065014, URL http://stacks.iop.org/1367-2630/15/i=6/a=065014.
[105] K.B. Nordstrom, K. Johnsen, S.J. Allen, A.-P. Jauho, B. Birnir, J. Kono, T. Noda, H. Akiyama, H. Sakaki, Excitonic dynamical Franz-Keldysh effect, Phys. Rev. Lett. 81 (1998) 457–460, http://dx.doi.org/10.1103/PhysRevLett.81.457.
[106] J.R. Danielson, Y.-S. Lee, J.P. Prineas, J.T. Steiner, M. Kira, S.W. Koch, Interaction of strong single-cycle terahertz pulses with semiconductor quantum wells, Phys. Rev. Lett. 99 (2007) 237401, http://dx.doi.org/10.1103/PhysRevLett.99.237401.
[107] S. Watanabe, N. Minami, R. Shimano, Intense terahertz pulse induced exciton generation in carbon nanotubes, Opt. Express 19 (2) (2011) 1528–1538, http://dx.doi.org/10.1364/OE.19.001528, URL http://www.opticsexpress.org/abstract.cfm?URI=oe-19-2-1528.
[108] B. Ewers, N.S. Köster, R. Woscholski, M. Koch, S. Chatterjee, G. Khitrova, H.M. Gibbs, A.C. Klettke, M. Kira, S.W. Koch, Ionization of coherent excitons by strong terahertz fields, Phys. Rev. B 85 (2012) 075307, http://dx.doi.org/10.1103/PhysRevB.85.075307.
[109] B. Zaks, R. Liu, M. Sherwin, Experimental observation of electron–hole recollisions, Nature 483 (2012) 580, http://dx.doi.org/10.1038/nature10864, URL https://www.nature.com/articles/nature10864{#}supplementary-information.
[110] N.S. Köster, A.C. Klettke, B. Ewers, R. Woscholski, S. Cecchi, D. Chrastina, G. Isella, M. Kira, S.W. Koch, S. Chatterjee, Controlling the polarization dynamics by strong THz fields in photoexcited germanium quantum wells, New J. Phys. 15 (7) (2013) 075004, URL http://stacks.iop.org/1367-2630/15/i=7/a=075004.
[111] K. Uchida, T. Otobe, T. Mochizuki, C. Kim, M. Yoshita, H. Akiyama, L.N. Pfeiffer, K.W. West, K. Tanaka, H. Hirori, Subcycle optical response caused by a terahertz dressed state with phase-locked wave functions, Phys. Rev. Lett. 117 (2016) 277402, http://dx.doi.org/10.1103/PhysRevLett.117.277402.

[112] B. Pietka, N. Bobrovska, D. Stephan, M. Teich, M. Król, S. Winnerl, A. Pashkin, R. Mirek, K. Lekenta, F. Morier-Genoud, H. Schneider, B. Deveaud, M. Helm, M. Matuszewski, J. Szczytko, Doubly dressed bosons: Exciton polaritons in a strong terahertz field, Phys. Rev. Lett. 119 (2017) 077403, http://dx.doi.org/10.1103/PhysRevLett.119.077403.
[113] Y. Murotani, M. Takayama, F. Sekiguchi, C. Kim, H. Akiyama, R. Shimano, Terahertz field-induced ionization and perturbed free induction decay of excitons in bulk GaAs, J. Phys. D: Appl. Phys. 51 (11) (2018) 114001, URL http://stacks.iop.org/0022-3727/51/i=11/a=114001.
[114] R. Liu, B. Zhu, High-order THz-sideband generation in semiconductors, AIP Conf. Proc. 893 (1) (2007) 1455–1456, http://dx.doi.org/10.1063/1.2730455, URL https://aip.scitation.org/doi/abs/10.1063/1.2730455.
[115] J.-Y. Yan, Theory of excitonic high-order sideband generation in semiconductors under a strong terahertz field, Phys. Rev. B 78 (2008) 075204, http://dx.doi.org/10.1103/PhysRevB.78.075204.
[116] O. Schubert, M. Hohenleutner, F. Langer, B. Urbanek, C. Lange, U. Huttner, D. Golde, T. Meier, M. Kira, S.W. Koch, R. Huber, Sub-cycle control of terahertz high-harmonic generation by dynamical bloch oscillations, Nat. Photonics 8 (2014) 119, http://dx.doi.org/10.1038/nphoton.2013.349, URL https://www.nature.com/articles/nphoton.2013.349{#}supplementary-information.
[117] H. Hirori, M. Nagai, K. Tanaka, Excitonic interactions with intense terahertz pulses in ZnSe/ZnMgSSe multiple quantum wells, Phys. Rev. B 81 (2010) 081305, http://dx.doi.org/10.1103/PhysRevB.81.081305.
[118] R.D. Schaller, V.I. Klimov, High efficiency Carrier multiplication in PbSe nanocrystals: Implications for solar energy conversion, Phys. Rev. Lett. 92 (2004) 186601, http://dx.doi.org/10.1103/PhysRevLett.92.186601.
[119] N.M. Gabor, Z. Zhong, K. Bosnick, J. Park, P.L. McEuen, Extremely efficient multiple electron-hole pair generation in carbon nanotube photodiodes, Science 325 (5946) (2009) 1367–1371, http://dx.doi.org/10.1126/science.1176112, URL http://science.sciencemag.org/content/325/5946/1367.
[120] R.H. Hadfield, Single-photon detectors for optical quantum information applications, Nat. Photonics 3 (2009) 696, http://dx.doi.org/10.1038/nphoton.2009.230.
[121] J.A. Misewich, R. Martel, P. Avouris, J.C. Tsang, S. Heinze, J. Tersoff, Electrically induced optical emission from a carbon nanotube FET, Science 300 (5620) (2003) 783–786, http://dx.doi.org/10.1126/science.1081294, URL http://science.sciencemag.org/content/300/5620/783.
[122] J. Chen, V. Perebeinos, M. Freitag, J. Tsang, Q. Fu, J. Liu, P. Avouris, Bright infrared emission from electrically induced excitons in carbon nanotubes, Science 310 (5751) (2005) 1171–1174, http://dx.doi.org/10.1126/science.1119177, URL http://science.sciencemag.org/content/310/5751/1171.
[123] P.A. Wolff, Theory of electron multiplication in silicon and germanium, Phys. Rev. 95 (1954) 1415–1420, http://dx.doi.org/10.1103/PhysRev.95.1415.
[124] C. Zener, R.H. Fowler, A theory of the electrical breakdown of solid dielectrics, Proc. R. Soc. Lond. Ser. A Math. Phys. Eng. Sci. 145 (855) (1934) 523–529, http://dx.doi.org/10.1098/rspa.1934.0116, URL http://rspa.royalsocietypublishing.org/content/145/855/523.
[125] J. Hebling, M.C. Hoffmann, H.Y. Hwang, K.-L. Yeh, K.A. Nelson, Observation of nonequilibrium carrier distribution in Ge, Si, and GaAs by terahertz pump–terahertz probe measurements, Phys. Rev. B 81 (2010) 035201, http://dx.doi.org/10.1103/PhysRevB.81.035201.
[126] D. Turchinovich, J.M. Hvam, M.C. Hoffmann, Self-phase modulation of a single-cycle terahertz pulse by nonlinear free-carrier response in a semiconductor, Phys. Rev. B 85 (2012) 201304, http://dx.doi.org/10.1103/PhysRevB.85.201304.
[127] Y.-G. Jeong, M.J. Paul, S.-H. Kim, K.-J. Yee, D.-S. Kim, Y.-S. Lee, Large enhancement of nonlinear terahertz absorption in intrinsic GaAs by plasmonic nano antennas, Appl. Phys. Lett. 103 (17) (2013) 171109, http://dx.doi.org/10.1063/1.4826272.
[128] C. Vicario, B. Monoszlai, C.P. Hauri, GV/m single-cycle terahertz fields from a laser-driven large-size partitioned organic crystal, Phys. Rev. Lett. 112 (2014) 213901, http://dx.doi.org/10.1103/PhysRevLett.112.213901.
[129] M. Shalaby, C.P. Hauri, Demonstration of a low-frequency three-dimensional terahertz bullet with extreme brightness, Nature Commun. 6 (1) (2015) 5976, http://dx.doi.org/10.1038/ncomms6976.
[130] C. Vicario, M. Jazbinsek, A.V. Ovchinnikov, O.V. Chefonov, S.I. Ashitkov, M.B. Agranat, C.P. Hauri, High efficiency THz generation in DSTMS, DAST and OH1 pumped by Cr:forsterite laser, Opt. Express 23 (4) (2015) 4573, http://dx.doi.org/10.1364/oe.23.004573.
[131] S. Trumm, M. Betz, F. Sotier, A. Leitenstorfer, A. Schwanhäußer, M. Eckardt, O. Schmidt, S. Malzer, G.H. Döhler, M. Hanson, D. Driscoll, A.C. Gossard, Ultrafast spectroscopy of impact ionization and avalanche multiplication in GaAs, Appl. Phys. Lett. 88 (13) (2006) 132113, http://dx.doi.org/10.1063/1.2191880.
[132] A.T. Tarekegne, H. Hirori, K. Tanaka, K. Iwaszczuk, P.U. Jepsen, Impact ionization dynamics in silicon by MV/cm THz fields, New J. Phys. 19 (12) (2017) 123018, URL http://stacks.iop.org/1367-2630/19/i=12/a=123018.
[133] B.J. Baliga, Power semiconductor device figure of merit for high-frequency applications, IEEE Electron Device Lett. 10 (10) (1989) 455–457, http://dx.doi.org/10.1109/55.43098.
[134] M. Sparks, D.L. Mills, R. Warren, T. Holstein, A.A. Maradudin, L.J. Sham, E. Loh, D.F. King, Theory of electron-avalanche breakdown in solids, Phys. Rev. B 24 (1981) 3519–3536, http://dx.doi.org/10.1103/PhysRevB.24.3519.
[135] P.D. Salmans, Semiconductor Terahertz Electronics and Novel High-Speed Single-Shot Measurements (Ph.D. thesis), Brigham Young University, US, 2017.
[136] P. Limelette, A. Georges, D. Jérome, P. Wzietek, P. Metcalf, J.M. Honig, Universality and critical behavior at the mott transition, Science 302 (5642) (2003) 89–92, http://dx.doi.org/10.1126/science.1088386, URL http://science.sciencemag.org/content/302/5642/89.
[137] S.Y. Kim, M.-C. Lee, G. Han, M. Kratochvilova, S. Yun, S.J. Moon, C. Sohn, J.-G. Park, C. Kim, T.W. Noh, Spectroscopic studies on the metal–insulator transition mechanism in correlated materials, Adv. Mater. 30 (42) (2018) 1704777, http://dx.doi.org/10.1002/adma.201704777.
[138] M. Suda, H.M. Yamamoto, Field-, strain- and light-induced superconductivity in organic strongly correlated electron systems, Phys. Chem. Chem. Phys. 20 (2018) 1321–1331, http://dx.doi.org/10.1039/C7CP06716J.
[139] P. Scheiderer, M. Schmitt, J. Gabel, M. Zapf, M. Stübinger, P. Schütz, L. Dudy, C. Schlueter, T.-L. Lee, M. Sing, R. Claessen, Tailoring materials for mottronics: Excess oxygen doping of a prototypical mott insulator, Adv. Mater. 30 (25) (2018) 1706708, http://dx.doi.org/10.1002/adma.201706708.
[140] H. Takagi, H.Y. Hwang, An emergent change of phase for electronics, Science 327 (5973) (2010) 1601–1602, http://dx.doi.org/10.1126/science.1182541, URL http://science.sciencemag.org/content/327/5973/1601.
[141] J. Son, S. Rajan, S. Stemmer, S. James Allen, A heterojunction modulation-doped mott transistor, J. Appl. Phys. 110 (8) (2011) 084503, http://dx.doi.org/10.1063/1.3651612.
[142] K. Kanoda, R. Kato, Mott physics in organic conductors with triangular lattices, Annu. Rev. Condensed Matter Phys. 2 (1) (2011) 167–188, http://dx.doi.org/10.1146/annurev-conmatphys-062910-140521.
[143] H.M. Yamamoto, M. Suda, Y. Kawasugi, Organic phase-transition transistor with strongly correlated electrons, Japan. J. Appl. Phys. 57 (3S2) (2018) 03EA02, URL http://stacks.iop.org/1347-4065/57/i=3S2/a=03EA02.
[144] T. Miyamoto, H. Yamakawa, T. Morimoto, H. Okamoto, Control of electronic states by a nearly monocyclic terahertz electric-field pulse in organic correlated electron materials, J. Phys. B: At. Mol. Opt. Phys. 51 (16) (2018) 162001, URL http://stacks.iop.org/0953-4075/51/i=16/a=162001.

Please cite this article as: P. Salén, M. Basini, S. Bonetti et al., Matter manipulation with extreme terahertz light: Progress in the enabling THz technology, Physics Reports (2019), https://doi.org/10.1016/j.physrep.2019.09.002.

[145] S. Lupi, L. Baldassarre, B. Mansart, A. Perucchi, A. Barinov, P. Dudin, E. Papalazarou, F. Rodolakis, J.P. Rueff, J.P. Itié, S. Ravy, D. Nicoletti, P. Postorino, P. Hansmann, N. Parragh, A. Toschi, T. Saha-Dasgupta, O.K. Andersen, G. Sangiovanni, K. Held, M. Marsi, A microscopic view on the mott transition in chromium-doped V2O3, Nature Commun. 1 (2010) 105, http://dx.doi.org/10.1038/ncomms1109, URL https://www.nature.com/articles/ncomms1109{#}supplementary-information.
[146] Z. Yang, C. Ko, S. Ramanathan, Oxide electronics utilizing ultrafast metal-insulator transitions, Annu. Rev. Mater. Res. 41 (1) (2011) 337–367, http://dx.doi.org/10.1146/annurev-matsci-062910-100347.
[147] A.G. Gavriliuk, I.A. Trojan, V.V. Struzhkin, Insulator-metal transition in highly compressed NiO, Phys. Rev. Lett. 109 (2012) 086402, http://dx.doi.org/10.1103/PhysRevLett.109.086402.
[148] M. Liu, H.Y. Hwang, H. Tao, A.C. Strikwerda, K. Fan, G.R. Keiser, A.J. Sternbach, K.G. West, S. Kittiwatanakul, J. Lu, S.A. Wolf, F.G. Omenetto, X. Zhang, K.A. Nelson, R.D. Averitt, Terahertz-field-induced insulator-to-metal transition in vanadium dioxide metamaterial, Nature 487 (2012) 345, http://dx.doi.org/10.1038/nature11231, URL https://www.nature.com/articles/nature11231{#}supplementary-information.
[149] A.X. Gray, J. Jeong, N.P. Aetukuri, P. Granitzka, Z. Chen, R. Kukreja, D. Higley, T. Chase, A.H. Reid, H. Ohldag, M.A. Marcus, A. Scholl, A.T. Young, A. Doran, C.A. Jenkins, P. Shafer, E. Arenholz, M.G. Samant, S.S.P. Parkin, H.A. Dürr, Correlation-driven insulator-metal transition in near-ideal vanadium dioxide films, Phys. Rev. Lett. 116 (2016) 116403, http://dx.doi.org/10.1103/PhysRevLett.116.116403.
[150] O. Nájera, M. Civelli, V. Dobrosavljević, M.J. Rozenberg, Resolving the VO2 controversy: Mott mechanism dominates the insulator-to-metal transition, Phys. Rev. B 95 (3) (2017) 035113, http://dx.doi.org/10.1103/physrevb.95.035113.
[151] T.V. Slusar, J.-C. Cho, H.-R. Lee, J.-W. Kim, S.J. Yoo, J.-Y. Bigot, K.-J. Yee, H.-T. Kim, Mott transition in chain structure of strained VO2 films revealed by coherent phonons, Sci. Rep. 7 (1) (2017) 16038, http://dx.doi.org/10.1038/s41598-017-16188-6.
[152] A.X. Gray, M.C. Hoffmann, J. Jeong, N.P. Aetukuri, D. Zhu, H.Y. Hwang, N.C. Brandt, H. Wen, A.J. Sternbach, S. Bonetti, A.H. Reid, R. Kukreja, C. Graves, T. Wang, P. Granitzka, Z. Chen, D.J. Higley, T. Chase, E. Jal, E. Abreu, M.K. Liu, T.-C. Weng, D. Sokaras, D. Nordlund, M. Chollet, R. Alonso-Mori, H. Lemke, J.M. Glownia, M. Trigo, Y. Zhu, H. Ohldag, J.W. Freeland, M.G. Samant, J. Berakdar, R.D. Averitt, K.A. Nelson, S.S.P. Parkin, H.A. Dürr, Ultrafast terahertz field control of electronic and structural interactions in vanadium dioxide, Phys. Rev. B 98 (2018) 045104, http://dx.doi.org/10.1103/PhysRevB.98.045104.
[153] N.B. Aetukuri, A.X. Gray, M. Drouard, M. Cossale, L. Gao, A.H. Reid, R. Kukreja, H. Ohldag, C.A. Jenkins, E. Arenholz, K.P. Roche, H.A. Dürr, M.G. Samant, S.S.P. Parkin, Control of the metal–insulator transition in vanadium dioxide by modifying orbital occupancy, Nat. Phys. 9 (10) (2013) 661–666, http://dx.doi.org/10.1038/nphys2733.
[154] D. Lee, B. Chung, Y. Shi, G.-Y. Kim, N. Campbell, F. Xue, K. Song, S.-Y. Choi, J.P. Podkaminer, T.H. Kim, P.J. Ryan, J.-W. Kim, T.R. Paudel, J.-H. Kang, J.W. Spinuzzi, D.A. Tenne, E.Y. Tsymbal, M.S. Rzchowski, L.Q. Chen, J. Lee, C.B. Eom, Isostructural metal-insulator transition in VO2, Science 362 (6418) (2018) 1037–1040, http://dx.doi.org/10.1126/science.aam9189.
[155] F. Xia, H. Wang, D. Xiao, M. Dubey, A. Ramasubramaniam, Two-dimensional material nanophotonics, Nat. Photonics 8 (12) (2014) 899–907, http://dx.doi.org/10.1038/nphoton.2014.271.
[156] A.K. Geim, I.V. Grigorieva, Van der waals heterostructures, Nature 499 (7459) (2013) 419–425, http://dx.doi.org/10.1038/nature12385.
[157] A. Splendiani, L. Sun, Y. Zhang, T. Li, J. Kim, C.-Y. Chim, G. Galli, F. Wang, Emerging photoluminescence in monolayer MoS2, Nano Lett. 10 (4) (2010) 1271–1275, http://dx.doi.org/10.1021/nl903868w.
[158] Y. Zhang, Y.-W. Tan, H.L. Stormer, P. Kim, Experimental observation of the quantum Hall effect and Berry's phase in graphene, Nature 438 (7065) (2005) 201–204, http://dx.doi.org/10.1038/nature04235.
[159] Y. Cao, V. Fatemi, S. Fang, K. Watanabe, T. Taniguchi, E. Kaxiras, P. Jarillo-Herrero, Unconventional superconductivity in magic-angle graphene superlattices, Nature 556 (7699) (2018) 43–50, http://dx.doi.org/10.1038/nature26160.
[160] D.N. Basov, M.M. Fogler, F.J.G. de Abajo, Polaritons in van der Waals materials, Science 354 (6309) (2016) aag1992, http://dx.doi.org/10.1126/science.aag1992.
[161] T. Low, A. Chaves, J.D. Caldwell, A. Kumar, N.X. Fang, P. Avouris, T.F. Heinz, F. Guinea, L. Martin-Moreno, F. Koppens, Polaritons in layered two-dimensional materials, Nature Mater. 16 (2) (2016) 182–194, http://dx.doi.org/10.1038/nmat4792.
[162] A.K. Geim, K.S. Novoselov, The rise of graphene, Nature Mater. 6 (3) (2007) 183–191, http://dx.doi.org/10.1038/nmat1849.
[163] S. Winnerl, M. Orlita, P. Plochocka, P. Kossacki, M. Potemski, T. Winzer, E. Malic, A. Knorr, M. Sprinkle, C. Berger, W.A. de Heer, H. Schneider, M. Helm, Carrier relaxation in epitaxial graphene photoexcited near the dirac point, Phys. Rev. Lett. 107 (23) (2011) http://dx.doi.org/10.1103/physrevlett.107.237401.
[164] P. Bowlan, E. Martinez-Moreno, K. Reimann, T. Elsaesser, M. Woerner, Ultrafast terahertz response of multilayer graphene in the nonperturbative regime, Phys. Rev. B 89 (4) (2014) http://dx.doi.org/10.1103/physrevb.89.041408.
[165] H.A. Hafez, I. Al-Naib, M.M. Dignam, Y. Sekine, K. Oguri, F. Blanchard, D.G. Cooke, S. Tanaka, F. Komori, H. Hibino, T. Ozaki, Nonlinear terahertz field-induced carrier dynamics in photoexcited epitaxial monolayer graphene, Phys. Rev. B 91 (3) (2015) http://dx.doi.org/10.1103/physrevb.91.035422.
[166] H.A. Hafez, P.L. Lévesque, I. Al-Naib, M.M. Dignam, X. Chai, S. Choubak, P. Desjardins, R. Martel, T. Ozaki, Intense terahertz field effects on photoexcited carrier dynamics in gated graphene, Appl. Phys. Lett. 107 (25) (2015) 251903, http://dx.doi.org/10.1063/1.4938081.
[167] J.L. Cheng, J.E. Sipe, N. Vermeulen, C. Guo, Nonlinear optics of graphene and other 2D materials in layered structures, J. Phys.: Photonics 1 (1) (2018) 015002, http://dx.doi.org/10.1088/2515-7647/aaeadb.
[168] A. Autere, H. Jussila, Y. Dai, Y. Wang, H. Lipsanen, Z. Sun, Nonlinear optics with 2d layered materials, Adv. Mater. 30 (24) (2018) 1705963, http://dx.doi.org/10.1002/adma.201705963.
[169] S. Tani, F. Blanchard, K. Tanaka, Ultrafast carrier dynamics in graphene under a high electric field, Phys. Rev. Lett. 109 (16) (2012) http://dx.doi.org/10.1103/physrevlett.109.166603.
[170] H.Y. Hwang, N.C. Brandt, H. Farhat, A.L. Hsu, J. Kong, K.A. Nelson, Nonlinear THz conductivity dynamics in p-type CVD-grown graphene, J. Phys. Chem. B 117 (49) (2013) 15819–15824, http://dx.doi.org/10.1021/jp407548a, https://doi.org/10.1021/jp407548a.
[171] Y.Q. An, F. Nelson, J.U. Lee, A.C. Diebold, Enhanced optical second-harmonic generation from the current-biased graphene/SiO2/Si(001) structure, Nano Lett. 13 (5) (2013) 2104–2109, http://dx.doi.org/10.1021/nl4004514.
[172] J.L. Cheng, N. Vermeulen, J.E. Sipe, Second order optical nonlinearity of graphene due to electric quadrupole and magnetic dipole effects, Sci. Rep. 7 (1) (2017) http://dx.doi.org/10.1038/srep43843.
[173] H.J. Choi, I.H. Baek, B.J. Kang, H.-D. Kim, S.S. Oh, J.M. Hamm, A. Pusch, J. Park, K. Lee, J. Son, Y.U. k. Jeong, O. Hess, F. Rotermund, B. Min, Control of terahertz nonlinear transmission with electrically gated graphene metadevices, Sci. Rep. 7 (1) (2017) http://dx.doi.org/10.1038/srep42833.
[174] R.R. Hartmann, J. Kono, M.E. Portnoi, Terahertz science and technology of carbon nanomaterials, Nanotechnology 25 (32) (2014) 322001, http://dx.doi.org/10.1088/0957-4484/25/32/322001.
[175] M. Glazov, S. Ganichev, High frequency electric field induced nonlinear effects in graphene, Phys. Rep. 535 (3) (2014) 101–138, http://dx.doi.org/10.1016/j.physrep.2013.10.003, URL http://www.sciencedirect.com/science/article/pii/S0370157313003785.
[176] N. Yoshikawa, T. Tamaya, K. Tanaka, High-harmonic generation in graphene enhanced by elliptically polarized light excitation, Science 356 (6339) (2017) 736–738, http://dx.doi.org/10.1126/science.aam8861.

[177] H.A. Hafez, S. Kovalev, J.-C. Deinert, Z. Mics, B. Green, N. Awari, M. Chen, S. Germanskiy, U. Lehnert, J. Teichert, Z. Wang, K.-J. Tielrooij, Z. Liu, Z. Chen, A. Narita, K. Müllen, M. Bonn, M. Gensch, D. Turchinovich, Extremely efficient terahertz high-harmonic generation in graphene by hot Dirac fermions, Nature 561 (7724) (2018) 507–511, http://dx.doi.org/10.1038/s41586-018-0508-1.
[178] J. Karch, P. Olbrich, M. Schmalzbauer, C. Zoth, C. Brinsteiner, M. Fehrenbacher, U. Wurstbauer, M.M. Glazov, S.A. Tarasenko, E.L. Ivchenko, D. Weiss, J. Eroms, R. Yakimova, S. Lara-Avila, S. Kubatkin, S.D. Ganichev, Dynamic hall effect driven by circularly polarized light in a graphene layer, Phys. Rev. Lett. 105 (22) (2010) http://dx.doi.org/10.1103/physrevlett.105.227402.
[179] P. Weis, J.L. Garcia-Pomar, M. Höh, B. Reinhard, A. Brodyanski, M. Rahm, Spectrally wide-band terahertz wave modulator based on optically tuned graphene, ACS Nano 6 (10) (2012) 9118–9124, http://dx.doi.org/10.1021/nn303392s.
[180] J. Maysonnave, S. Huppert, F. Wang, S. Maero, C. Berger, W. de Heer, T.B. Norris, L.A.D. Vaulchier, S. Dhillon, J. Tignon, R. Ferreira, J. Mangeney, Terahertz generation by dynamical photon drag effect in graphene excited by femtosecond optical pulses, Nano Lett. 14 (10) (2014) 5797–5802, http://dx.doi.org/10.1021/nl502684j.
[181] P.A. Obraztsov, N. Kanda, K. Konishi, M. Kuwata-Gonokami, S.V. Garnov, A.N. Obraztsov, Y.P. Svirko, Photon-drag-induced terahertz emission from graphene, Phys. Rev. B 90 (24) (2014) http://dx.doi.org/10.1103/physrevb.90.241416.
[182] B. Yao, Y. Liu, S.-W. Huang, C. Choi, Z. Xie, J.F. Flores, Y. Wu, M. Yu, D.-L. Kwong, Y. Huang, Y. Rao, X. Duan, C.W. Wong, Broadband gate-tunable terahertz plasmons in graphene heterostructures, Nat. Photonics 12 (1) (2017) 22–28, http://dx.doi.org/10.1038/s41566-017-0054-7.
[183] J.J. Dean, H.M. van Driel, Graphene and few-layer graphite probed by second-harmonic generation: theory and experiment, Phys. Rev. B 82 (12) (2010) http://dx.doi.org/10.1103/physrevb.82.125411.
[184] J.D. Cox, F.J.G. de Abajo, Electrically tunable nonlinear plasmonics in graphene nanoislands, Nature Commun. 5 (1) (2014) http://dx.doi.org/10.1038/ncomms6725.
[185] J.D. Cox, A. Marini, F.J.G. de Abajo, Plasmon-assisted high-harmonic generation in graphene, Nature Commun. 8 (1) (2017) http://dx.doi.org/10.1038/ncomms14380.
[186] M.M. Glazov, Second harmonic generation in graphene, JETP Lett. 93 (7) (2011) 366–371, http://dx.doi.org/10.1134/s0021364011070046.
[187] S.A. Mikhailov, Theory of the giant plasmon-enhanced second-harmonic generation in graphene and semiconductor two-dimensional electron systems, Phys. Rev. B 84 (4) (2011) http://dx.doi.org/10.1103/physrevb.84.045432.
[188] S. Mikhailov, Nonlinear electrodynamic properties of graphene and other two-dimensional materials, Sensors Transducers J. 225 (9) (2018) 25–35, URL http://www.sensorsportal.com/HTML/DIGEST/P_3009.htm.
[189] S.A. Mikhailov, Non-linear electromagnetic response of graphene, Europhys. Lett. 79 (2) (2007) 27002, http://dx.doi.org/10.1209/0295-5075/79/27002.
[190] I. Crassee, J. Levallois, A.L. Walter, M. Ostler, A. Bostwick, E. Rotenberg, T. Seyller, D. van der Marel, A.B. Kuzmenko, Giant faraday rotation in single- and multilayer graphene, Nat. Phys. 7 (1) (2010) 48–51, http://dx.doi.org/10.1038/nphys1816.
[191] J.-M. Poumirol, P.Q. Liu, T.M. Slipchenko, A.Y. Nikitin, L. Martin-Moreno, J. Faist, A.B. Kuzmenko, Electrically controlled terahertz magneto-optical phenomena in continuous and patterned graphene, Nature Commun. 8 (2017) 14626, http://dx.doi.org/10.1038/ncomms14626.
[192] H. Yan, Z. Li, X. Li, W. Zhu, P. Avouris, F. Xia, Infrared spectroscopy of tunable Dirac terahertz magneto-plasmons in graphene, Nano Lett. 12 (7) (2012) 3766–3771, http://dx.doi.org/10.1021/nl3016335.
[193] M. Lakshmanan, The fascinating world of the Landau–Lifshitz–Gilbert equation: an overview, Phil. Trans. R. Soc. A 369 (1939) (2011) 1280–1300.
[194] A. Aharoni, Introduction to the theory of ferromagnetism, in: International Series of Monographs on Physics, Clarendon Press, 2000, URL https://books.google.se/books?id=Ru-z9b3WcfMC.
[195] K. Grishunin, T. Huisman, G. Li, E. Mishina, T. Rasing, A.V. Kimel, K. Zhang, Z. Jin, S. Cao, W. Ren, et al., Terahertz magnon-polaritons in TmFeO3, ACS Photonics 5 (4) (2018) 1375–1380.
[196] S. Gamble, M.H. Burkhardt, A. Kashuba, R. Allenspach, S.S. Parkin, H. Siegmann, J. Stöhr, Electric field induced magnetic anisotropy in a ferromagnet, Phys. Rev. Lett. 102 (21) (2009) 217201.
[197] J.D. Jackson, Classical Electrodynamics, John Wiley & Sons, 2007.
[198] Z. Wang, S. Kovalev, N. Awari, M. Chen, S. Germanskiy, B. Green, J.-C. Deinert, T. Kampfrath, J. Milano, M. Gensch, Magnetic field dependence of antiferromagnetic resonance in NiO, Appl. Phys. Lett. 112 (25) (2018) 252404.
[199] S. Kovalev, Z. Wang, J. Deinert, N. Awari, M. Chen, B. Green, S. Germanskiy, T. de Oliveira, J. Lee, A. Deac, et al., Selective THz control of magnetic order: new opportunities from superradiant undulator sources, J. Phys. D: Appl. Phys. 51 (11) (2018) 114007.
[200] S. Baierl, J.H. Mentink, M. Hohenleutner, L. Braun, T.-M. Do, C. Lange, A. Sell, M. Fiebig, G. Woltersdorf, T. Kampfrath, et al., Terahertz-driven nonlinear spin response of antiferromagnetic nickel oxide, Phys. Rev. Lett. 117 (19) (2016) 197201.
[201] A. Reid, T. Rasing, R. Pisarev, H. Dürr, M. Hoffmann, Terahertz-driven magnetism dynamics in the orthoferrite DyFeO3, Appl. Phys. Lett. 106 (8) (2015) 082403.
[202] J. Lu, X. Li, H.Y. Hwang, B.K. Ofori-Okai, T. Kurihara, T. Suemoto, K.A. Nelson, Coherent two-dimensional terahertz magnetic resonance spectroscopy of collective spin waves, Phys. Rev. Lett. 118 (20) (2017) 207204.
[203] K. Olejník, T. Seifert, Z. Kašpar, V. Novák, P. Wadley, R.P. Campion, M. Baumgartner, P. Gambardella, P. Němec, J. Wunderlich, et al., Terahertz electrical writing speed in an antiferromagnetic memory, Sci. Adv. 4 (3) (2018) eaar3566.
[204] T. Jungwirth, X. Marti, P. Wadley, J. Wunderlich, Antiferromagnetic spintronics, Nature Nanotechnol. 11 (3) (2016) 231.
[205] V. Baltz, A. Manchon, M. Tsoi, T. Moriyama, T. Ono, Y. Tserkovnyak, Antiferromagnetic spintronics, Rev. Modern Phys. 90 (1) (2018) 015005.
[206] S. Baierl, M. Hohenleutner, T. Kampfrath, A. Zvezdin, A. Kimel, R. Huber, R. Mikhaylovskiy, Nonlinear spin control by terahertz-driven anisotropy fields, Nat. Photonics 10 (11) (2016) 715.
[207] S. Schlauderer, C. Lange, S. Baierl, T. Ebnet, C. Schmid, D. Valovcin, A. Zvezdin, A. Kimel, R. Mikhaylovskiy, R. Huber, Temporal and spectral fingerprints of ultrafast all-coherent spin switching, Nature 569 (7756) (2019) 383.
[208] T. Kubacka, J.A. Johnson, M.C. Hoffmann, C. Vicario, S. De Jong, P. Beaud, S. Grübel, S.-W. Huang, L. Huber, L. Patthey, et al., Large-amplitude spin dynamics driven by a THz pulse in resonance with an electromagnon, Science (2014) 1242862.
[209] S.F. Maehrlein, I. Radu, P. Maldonado, A. Paarmann, M. Gensch, A.M. Kalashnikova, R.V. Pisarev, M. Wolf, P.M. Oppeneer, J. Barker, et al., Dissecting spin-phonon equilibration in ferrimagnetic insulators by ultrafast lattice excitation, Sci. Adv. 4 (7) (2018) eaar5164.
[210] C. Vicario, C. Ruchert, F. Ardana-Lamas, P.M. Derlet, B. Tudu, J. Luning, C.P. Hauri, Off-resonant magnetization dynamics phase-locked to an intense phase-stable terahertz transient, Nat. Photonics 7 (9) (2013) 720.
[211] S. Bonetti, M. Hoffmann, M.-J. Sher, Z. Chen, S.-H. Yang, M. Samant, S. Parkin, H. Dürr, THz-driven ultrafast spin-lattice scattering in amorphous metallic ferromagnets, Phys. Rev. Lett. 117 (8) (2016) 087205.
[212] M. Shalaby, C. Vicario, C.P. Hauri, Low frequency terahertz-induced demagnetization in ferromagnetic nickel, Appl. Phys. Lett. 108 (18) (2016) 182903.
[213] D. Polley, M. Pancaldi, M. Hudl, P. Vavassori, S. Urazhdin, S. Bonetti, THz-driven demagnetization with perpendicular magnetic anisotropy: towards ultrafast ballistic switching, J. Phys. D: Appl. Phys. 51 (8) (2018) 084001.
[214] M. Shalaby, A. Donges, K. Carva, R. Allenspach, P.M. Oppeneer, U. Nowak, C.P. Hauri, Coherent and incoherent ultrafast magnetization dynamics in 3 d ferromagnets driven by extreme terahertz fields, Phys. Rev. B 98 (1) (2018) 014405.

Please cite this article as: P. Salén, M. Basini, S. Bonetti et al., Matter manipulation with extreme terahertz light: Progress in the enabling THz technology, Physics Reports (2019), https://doi.org/10.1016/j.physrep.2019.09.002.

[215] C. Back, D. Weller, J. Heidmann, D. Mauri, D. Guarisco, E. Garwin, H. Siegmann, Magnetization reversal in ultrashort magnetic field pulses, Phys. Rev. Lett. 81 (15) (1998) 3251.
[216] I. Tudosa, C. Stamm, A. Kashuba, F. King, H. Siegmann, J. Stöhr, G. Ju, B. Lu, D. Weller, The ultimate speed of magnetic switching in granular recording media, Nature 428 (6985) (2004) 831.
[217] Z. Wang, M. Pietz, J. Walowski, A. Förster, M.I. Lepsa, M. Münzenberg, Spin dynamics triggered by subterahertz magnetic field pulses, J. Appl. Phys. 103 (12) (2008) 123905.
[218] D. Polley, N.Z. Hagström, C. von Korff Schmising, S. Eisebitt, S. Bonetti, Terahertz magnetic field enhancement in an asymmetric spiral metamaterial, J. Phys. B: At. Mol. Opt. Phys. 51 (22) (2018) 224001.
[219] S. Fleischer, Y. Zhou, R.W. Field, K.A. Nelson, Molecular orientation and alignment by intense single-cycle THz pulses, Phys. Rev. Lett. 107 (2011) 163603, http://dx.doi.org/10.1103/PhysRevLett.107.163603.
[220] S. Fleischer, R.W. Field, K.A. Nelson, Commensurate two-quantum coherences induced by time-delayed THz fields, Phys. Rev. Lett. 109 (2012) 123603, http://dx.doi.org/10.1103/PhysRevLett.109.123603.
[221] W. Chin, F. Piuzzi, I. Dimicoli, M. Mons, Probing the competition between secondary structures and local preferences in gas phase isolated peptide backbones, Phys. Chem. Chem. Phys. 8 (2006) 1033–1048, http://dx.doi.org/10.1039/B516245A.
[222] P. Weightman, Investigation of the frohlich hypothesis with high intensity terahertz radiation, Proc. PIE 8941 (2014) http://dx.doi.org/10.1117/12.2057397.
[223] H. Fröhlich, Long-range coherence and energy storage in biological systems, Int. J. Quantum Chem. 2 (5) (1968) 641–649, http://dx.doi.org/10.1002/qua.560020505.
[224] I.V. Lundholm, H. Rodilla, W.Y. Wahlgren, A. Duelli, G. Bourenkov, J. Vukusic, R. Friedman, J. Stake, T. Schneider, G. Katona, Terahertz radiation induces non-thermal structural changes associated with Fröhlich condensation in a protein crystal, Struct. Dyn. 2 (5) (2015) 054702, http://dx.doi.org/10.1063/1.4931825.
[225] M.C. Hoffmann, N.C. Brandt, H.Y. Hwang, K.-L. Yeh, K.A. Nelson, Terahertz Kerr effect, Appl. Phys. Lett. 95 (23) (2009) 231105, http://dx.doi.org/10.1063/1.3271520.
[226] M. Sajadi, M. Wolf, T. Kampfrath, Transient birefringence of liquids induced by terahertz electric-field torque on permanent molecular dipoles, Nature Commun. 8 (1) (2017) http://dx.doi.org/10.1038/ncomms14963.
[227] P. Zalden, L. Song, X. Wu, H. Huang, F. Ahr, O.D. Mücke, J. Reichert, M. Thorwart, P.K. Mishra, R. Welsch, R. Santra, F.X. Kärtner, C. Bressler, Molecular polarizability anisotropy of liquid water revealed by terahertz-induced transient orientation, Nature Commun. 9 (1) (2018) http://dx.doi.org/10.1038/s41467-018-04481-5.
[228] T. Kampfrath, M. Wolf, M. Sajadi, The sign of the polarizability anisotropy of polar molecules is obtained from the terahertz Kerr effect, Chem. Phys. Lett. 692 (2018) 319–323, http://dx.doi.org/10.1016/j.cplett.2017.12.061.
[229] R. Velotta, N. Hay, M.B. Mason, M. Castillejo, J.P. Marangos, High-order harmonic generation in aligned molecules, Phys. Rev. Lett. 87 (2001) 183901, http://dx.doi.org/10.1103/PhysRevLett.87.183901.
[230] J. Itatani, J. Levesque, D. Zeidler, H. Niikura, H. Pépin, J.C. Kieffer, P.B. Corkum, D.M. Villeneuve, Tomographic imaging of molecular orbitals, Nature 432 (7019) (2004) 867–871, http://dx.doi.org/10.1038/nature03183.
[231] H. Soifer, P. Botheron, D. Shafir, A. Diner, O. Raz, B.D. Bruner, Y. Mairesse, B. Pons, N. Dudovich, Near-threshold high-order harmonic spectroscopy with aligned molecules, Phys. Rev. Lett. 105 (2010) 143904, http://dx.doi.org/10.1103/PhysRevLett.105.143904.
[232] B.K. McFarland, J.P. Farrell, P.H. Bucksbaum, M. Gühr, High harmonic generation from multiple orbitals in N2, Science 322 (5905) (2008) 1232–1235, http://dx.doi.org/10.1126/science.1162780, URL http://science.sciencemag.org/content/322/5905/1232.
[233] M. Meckel, D. Comtois, D. Zeidler, A. Staudte, D. Pavičić, H.C. Bandulet, H. Pépin, J.C. Kieffer, R. Dörner, D.M. Villeneuve, P.B. Corkum, Laser-induced electron tunneling and diffraction, Science 320 (5882) (2008) 1478–1482, http://dx.doi.org/10.1126/science.1157980, URL http://science.sciencemag.org/content/320/5882/1478.
[234] L. Holmegaard, J.L. Hansen, L. Kalhøj, S.L. Kragh, H. Stapelfeldt, F. Filsinger, J. Küpper, G. Meijer, D. Dimitrovski, M. Abu-samha, C.P.J. Martiny, L.B. Madsen, Photoelectron angular distributions from strong-field ionization of oriented molecules, Nat. Phys. 6 (6) (2010) 428–432, http://dx.doi.org/10.1038/nphys1666.
[235] J. Hajdu, Single-molecule x-ray diffraction, Curr. Opin. Struct. Biol. 10 (5) (2000) 569–573, http://dx.doi.org/10.1016/S0959-440X(00)00133-0, URL http://www.sciencedirect.com/science/article/pii/S0959440X00001330.
[236] R. Neutze, R. Wouts, D. van der Spoel, E. Weckert, J. Hajdu, Potential for biomolecular imaging with femtosecond x-ray pulses, Nature 406 (6797) (2000) 752–757, http://dx.doi.org/10.1038/35021099.
[237] D. Pavičić, K.F. Lee, D.M. Rayner, P.B. Corkum, D.M. Villeneuve, Direct measurement of the angular dependence of ionization for N_2, O_2, and CO_2 in intense laser fields, Phys. Rev. Lett. 98 (2007) 243001, http://dx.doi.org/10.1103/PhysRevLett.98.243001.
[238] K. Nelson, The keith nelson group webpage, 2019, URL https://nelson.mit.edu/blog/nonlinear-terahertz-spectroscopy.
[239] F. Rosca-Pruna, M.J.J. Vrakking, Experimental observation of revival structures in picosecond laser-induced alignment of I_2, Phys. Rev. Lett. 87 (2001) 153902, http://dx.doi.org/10.1103/PhysRevLett.87.153902.
[240] H. Stapelfeldt, T. Seideman, Colloquium: Aligning molecules with strong laser pulses, Rev. Modern Phys. 75 (2003) 543–557, http://dx.doi.org/10.1103/RevModPhys.75.543.
[241] T. Suzuki, Y. Sugawara, S. Minemoto, H. Sakai, Optimal control of nonadiabatic alignment of rotationally cold N_2 molecules with the feedback of degree of alignment, Phys. Rev. Lett. 100 (2008) 033603, http://dx.doi.org/10.1103/PhysRevLett.100.033603.
[242] O. Ghafur, A. Rouzée, A. Gijsbertsen, W.K. Siu, S. Stolte, M.J.J. Vrakking, Impulsive orientation and alignment of quantum-state-selected NO molecules, Nat. Phys. 5 (4) (2009) 289–293, http://dx.doi.org/10.1038/nphys1225.
[243] M. Machholm, N.E. Henriksen, Field-free orientation of molecules, Phys. Rev. Lett. 87 (2001) 193001, http://dx.doi.org/10.1103/PhysRevLett.87.193001.
[244] C.-C. Shu, K.-J. Yuan, W.-H. Hu, S.-L. Cong, Field-free molecular orientation with terahertz few-cycle pulses, J. Chem. Phys. 132 (24) (2010) 244311, http://dx.doi.org/10.1063/1.3458913.
[245] D. Daems, S. Guérin, D. Sugny, H.R. Jauslin, Efficient and long-lived field-free orientation of molecules by a single hybrid short pulse, Phys. Rev. Lett. 94 (2005) 153003, http://dx.doi.org/10.1103/PhysRevLett.94.153003.
[246] E. Gershnabel, I.S. Averbukh, R.J. Gordon, Enhanced molecular orientation induced by molecular antialignment, Phys. Rev. A 74 (2006) 053414, http://dx.doi.org/10.1103/PhysRevA.74.053414.
[247] D. Sugny, A. Keller, O. Atabek, D. Daems, C.M. Dion, S. Guérin, H.R. Jauslin, Reaching optimally oriented molecular states by laser kicks, Phys. Rev. A 69 (2004) 033402, http://dx.doi.org/10.1103/PhysRevA.69.033402.
[248] C.-C. Shu, N.E. Henriksen, Field-free molecular orientation induced by single-cycle THz pulses: the role of resonance and quantum interference, Phys. Rev. A 87 (1) (2013) 013408, http://dx.doi.org/10.1103/physreva.87.013408.
[249] G. Karras, E. Hertz, F. Billard, B. Lavorel, J.-M. Hartmann, O. Faucher, E. Gershnabel, Y. Prior, I.S. Averbukh, Orientation and alignment echoes, Phys. Rev. Lett. 114 (2015) 153601, http://dx.doi.org/10.1103/PhysRevLett.114.153601.

[250] J. Lu, Y. Zhang, H.Y. Hwang, B.K. Ofori-Okai, S. Fleischer, K.A. Nelson, Nonlinear two-dimensional terahertz photon echo and rotational spectroscopy in the gas phase, Proc. Natl. Acad. Sci. 113 (42) (2016) 11800–11805, http://dx.doi.org/10.1073/pnas.1609558113, URL https://www.pnas.org/content/113/42/11800.
[251] C.T. Kuhs, B.M. Luther, A.T. Krummel, Recent advances in 2d IR spectroscopy driven by advances in ultrafast technology, IEEE J. Sel. Top. Quantum Electron. 25 (4) (2019) 1–13, http://dx.doi.org/10.1109/jstqe.2019.2900597.
[252] A. Ghosh, J.S. Ostrander, M.T. Zanni, Watching proteins wiggle: Mapping structures with two-dimensional infrared spectroscopy, Chem. Rev. 117 (16) (2017) 10726–10759, http://dx.doi.org/10.1021/acs.chemrev.6b00582.
[253] C. Somma, G. Folpini, K. Reimann, M. Woerner, T. Elsaesser, Two-phonon quantum coherences in indium antimonide studied by nonlinear two-dimensional terahertz spectroscopy, Phys. Rev. Lett. 116 (17) (2016) http://dx.doi.org/10.1103/physrevlett.116.177401.
[254] I.A. Finneran, R. Welsch, M.A. Allodi, T.F. Miller, G.A. Blake, Coherent two-dimensional terahertz-terahertz-Raman spectroscopy, Proc. Natl. Acad. Sci. 113 (25) (2016) 6857–6861, http://dx.doi.org/10.1073/pnas.1605631113.
[255] T.L. Cocker, D. Peller, P. Yu, J. Repp, R. Huber, Tracking the ultrafast motion of a single molecule by femtosecond orbital imaging, Nature 539 (7628) (2016) 263–267, http://dx.doi.org/10.1038/nature19816.
[256] S. Du, K. Yoshida, Y. Zhang, I. Hamada, K. Hirakawa, Terahertz dynamics of electron–vibron coupling in single molecules with tunable electrostatic potential, Nat. Photonics 12 (10) (2018) 608–612, http://dx.doi.org/10.1038/s41566-018-0241-1.
[257] M.A. Allodi, I.A. Finneran, G.A. Blake, Nonlinear terahertz coherent excitation of vibrational modes of liquids, J. Chem. Phys. 143 (23) (2015) 234204, http://dx.doi.org/10.1063/1.4938165.
[258] I.A. Finneran, R. Welsch, M.A. Allodi, T.F. Miller, G.A. Blake, 2d THz-THz-Raman photon-echo spectroscopy of molecular vibrations in liquid bromoform, J. Phys. Chem. Lett. 8 (18) (2017) 4640–4644, http://dx.doi.org/10.1021/acs.jpclett.7b02106.
[259] P. Hamm, A. Shalit, Perspective: Echoes in 2d-Raman-THz spectroscopy, J. Chem. Phys. 146 (13) (2017) 130901, http://dx.doi.org/10.1063/1.4979288.
[260] A. Huzayyin, J.H. Chang, K. Lian, F. Dawson, Interaction of water molecule with Au(111) and Au(110) surfaces under the influence of an external electric field, J. Phys. Chem. C 118 (7) (2014) 3459–3470, http://dx.doi.org/10.1021/jp408001t.
[261] H. Ogasawara, A. Nilsson, D. Nordlund, Ultrafast coherent control and characterization of surface reactions using FELs, in: Proceedings of the 27th Free Electron Lasers, Palo Alto, CA, USA, TUPP054, 2005.
[262] T.P. Wangler, RF Linear Accelerators, John Wiley & Sons, 2008.
[263] R.J. England, R.J. Noble, K. Bane, D.H. Dowell, C.-K. Ng, J.E. Spencer, S. Tantawi, Z. Wu, R.L. Byer, E. Peralta, K. Soong, C.-M. Chang, B. Montazeri, S.J. Wolf, B. Cowan, J. Dawson, W. Gai, P. Hommelhoff, Y.-C. Huang, C. Jing, C. McGuinness, R.B. Palmer, B. Naranjo, J. Rosenzweig, G. Travish, A. Mizrahi, L. Schachter, C. Sears, G.R. Werner, R.B. Yoder, Dielectric laser accelerators, Rev. Modern Phys. 86 (2014) 1337–1389, http://dx.doi.org/10.1103/RevModPhys.86.1337.
[264] C. Limborg-Deprey, C. Adolphsen, D. McCormick, M. Dunning, K. Jobe, H. Li, T. Raubenheimer, A. Vrielink, T. Vecchione, F. Wang, S. Weathersby, Performance of a first generation x-band photoelectron rf gun, Phys. Rev. Accel. Beams 19 (2016) 053401, http://dx.doi.org/10.1103/PhysRevAccelBeams.19.053401.
[265] R.A. Marsh, G.G. Anderson, S.G. Anderson, D.J. Gibson, C.P.J. Barty, Y. Hwang, Performance of a second generation *X*-band rf photoinjector, Phys. Rev. Accel. Beams 21 (2018) 073401, http://dx.doi.org/10.1103/PhysRevAccelBeams.21.073401.
[266] E.A. Nanni, W.R. Huang, K.-H. Hong, K. Ravi, A. Fallahi, G. Moriena, R.J.D. Miller, F.X. Kärtner, Terahertz-driven linear electron acceleration, Nature Commun. 6 (1) (2015) 8486, http://dx.doi.org/10.1038/ncomms9486.
[267] D. Zhang, A. Fallahi, M. Hemmer, X. Wu, M. Fakhari, Y. Hua, H. Cankaya, A.-L. Calendron, L.E. Zapata, N.H. Matlis, F.X. Kärtner, Segmented terahertz electron accelerator and manipulator (STEAM), Nat. Photonics 12 (6) (2018) 336–342, http://dx.doi.org/10.1038/s41566-018-0138-z.
[268] E. Curry, S. Fabbri, J. Maxson, P. Musumeci, A. Gover, Meter-scale terahertz-driven acceleration of a relativistic beam, Phys. Rev. Lett. 120 (9) (2018) 094801, http://dx.doi.org/10.1103/physrevlett.120.094801.
[269] D.A. Walsh, D.S. Lake, E.W. Snedden, M.J. Cliffe, D.M. Graham, S.P. Jamison, Demonstration of sub-luminal propagation of single-cycle terahertz pulses for particle acceleration, Nature Commun. 8 (1) (2017) http://dx.doi.org/10.1038/s41467-017-00490-y.
[270] E. Curry, S. Fabbri, P. Musumeci, A. Gover, THZ-driven zero-slippage IFEL scheme for phase space manipulation, New J. Phys. 18 (11) (2016) 113045, http://dx.doi.org/10.1088/1367-2630/18/11/113045.
[271] W.R. Huang, A. Fallahi, X. Wu, H. Cankaya, A.-L. Calendron, K. Ravi, D. Zhang, E.A. Nanni, K.-H. Hong, F.X. Kärtner, Terahertz-driven, all-optical electron gun, Optica 3 (11) (2016) 1209, http://dx.doi.org/10.1364/optica.3.001209.
[272] G. Sciaini, R. Miller, Femtosecond electron diffraction: heralding the era of atomically resolved dynamics, Rep. Progr. Phys. 74 (9) (2011) 096101, http://dx.doi.org/10.1088/0034-4885/74/9/096101.
[273] P. Baum, On the physics of ultrashort single-electron pulses for time-resolved microscopy and diffraction, Chem. Phys. 423 (2013) 55–61, http://dx.doi.org/10.1016/j.chemphys.2013.06.012.
[274] R. Miller, Mapping atomic motions with ultrabright electrons: The chemists' gedanken experiment enters the lab frame, Annu. Rev. Phys. Chem. 65 (1) (2014) 583–604, http://dx.doi.org/10.1146/annurev-physchem-040412-110117.
[275] K. Wynne, J.J. Carey, An integrated description of terahertz generation through optical rectification, charge transfer, and current surge, Opt. Commun. 256 (4–6) (2005) 400–413, http://dx.doi.org/10.1016/j.optcom.2005.06.065.
[276] A. Nahata, A.S. Weling, T.F. Heinz, A wideband coherent terahertz spectroscopy system using optical rectification and electro-optic sampling, Appl. Phys. Lett. 69 (16) (1996) 2321–2323, http://dx.doi.org/10.1063/1.117511.
[277] J. Hebling, K.-L. Yeh, M.C. Hoffmann, B. Bartal, K.A. Nelson, Generation of high-power terahertz pulses by tilted-pulse-front excitation and their application possibilities, J. Opt. Soc. Amer. B 25 (7) (2008) B6, http://dx.doi.org/10.1364/josab.25.0000b6.
[278] R.W. Boyd, Nonlinear optics, third ed., Academic Press, Inc., Orlando, FL, USA, 2008.
[279] W.D. Johnston, I.P. Kaminow, Contributions to optical nonlinearity in GaAs as determined from Raman scattering efficiencies, Phys. Rev. 188 (3) (1969) 1209–1211, http://dx.doi.org/10.1103/physrev.188.1209.
[280] J.A. Fülöp, Z. Ollmann, C. Lombosi, C. Skrobol, S. Klingebiel, L. Pálfalvi, F. Krausz, S. Karsch, J. Hebling, Efficient generation of THz pulses with 04 mj energy, Opt. Express 22 (17) (2014) 20155, http://dx.doi.org/10.1364/oe.22.020155.
[281] S.-W. Huang, E. Granados, W.R. Huang, K.-H. Hong, L.E. Zapata, F.X. Kärtner, High conversion efficiency, high energy terahertz pulses by optical rectification in cryogenically cooled lithium niobate, Opt. Lett. 38 (5) (2013) 796, http://dx.doi.org/10.1364/ol.38.000796.
[282] X. jun Wu, J. long Ma, B. long Zhang, S. su Chai, Z. ji Fang, C.-Y. Xia, D. yin Kong, J. guang Wang, H. Liu, C.-Q. Zhu, X. Wang, C.-J. Ruan, Y.-T. Li, Highly efficient generation of 02 mj terahertz pulses in lithium niobate at room temperature with sub-50 fs chirped Ti:sapphire laser pulses, Opt. Express 26 (6) (2018) 7107, http://dx.doi.org/10.1364/oe.26.007107.
[283] J. Hebling, Derivation of the pulse front tilt caused by angular dispersion, Opt. Quantum Electron. 28 (12) (1996) 1759–1763, http://dx.doi.org/10.1007/bf00698541.
[284] J.A. Fülöp, L. Pálfalvi, G. Almási, J. Hebling, Design of high-energy terahertz sources based on optical rectification, Opt. Express 18 (12) (2010) 12311, http://dx.doi.org/10.1364/oe.18.012311.

[285] G. Polónyi, B. Monoszlai, G. Gäumann, E.J. Rohwer, G. Andriukaitis, T. Balciunas, A. Pugzlys, A. Baltuska, T. Feurer, J. Hebling, J.A. Fülöp, High-energy terahertz pulses from semiconductors pumped beyond the three-photon absorption edge, Opt. Express 24 (21) (2016) 23872, http://dx.doi.org/10.1364/oe.24.023872.
[286] J.A. Fülöp, G. Polónyi, B. Monoszlai, G. Andriukaitis, T. Balciunas, A. Pugzlys, G. Arthur, A. Baltuska, J. Hebling, Highly efficient scalable monolithic semiconductor terahertz pulse source, Optica 3 (10) (2016) 1075, http://dx.doi.org/10.1364/optica.3.001075.
[287] L. Pálfalvi, J.A. Fülöp, G. Almási, J. Hebling, Novel setups for extremely high power single-cycle terahertz pulse generation by optical rectification, Appl. Phys. Lett. 92 (17) (2008) 171107, http://dx.doi.org/10.1063/1.2907494.
[288] Z. Ollmann, J. Hebling, G. Almási, Design of a contact grating setup for mj-energy THz pulse generation by optical rectification, Appl. Phys. B 108 (4) (2012) 821–826, http://dx.doi.org/10.1007/s00340-012-5201-8.
[289] M. Tsubouchi, K. Nagashima, F. Yoshida, Y. Ochi, M. Maruyama, Contact grating device with Fabry–Perot resonator for effective terahertz light generation, Opt. Lett. 39 (18) (2014) 5439, http://dx.doi.org/10.1364/ol.39.005439.
[290] L. Pálfalvi, Z. Ollmann, L. Tokodi, J. Hebling, Hybrid tilted-pulse-front excitation scheme for efficient generation of high-energy terahertz pulses, Opt. Express 24 (8) (2016) 8156, http://dx.doi.org/10.1364/oe.24.008156.
[291] L. Pálfalvi, G. Tóth, L. Tokodi, Z. Márton, J.A. Fülöp, G. Almási, J. Hebling, Numerical investigation of a scalable setup for efficient terahertz generation using a segmented tilted-pulse-front excitation, Opt. Express 25 (24) (2017) 29560, http://dx.doi.org/10.1364/oe.25.029560.
[292] B.K. Ofori-Okai, P. Sivarajah, W.R. Huang, K.A. Nelson, THZ generation using a reflective stair-step echelon, Opt. Express 24 (5) (2016) 5057, http://dx.doi.org/10.1364/oe.24.005057.
[293] G. Tóth, L. Pálfalvi, J.A. Fülöp, G. Krizsán, N. Matlis, G. Almási, J. Hebling, Numerical investigation of imaging-free terahertz generation setup using segmented tilted-pulse-front excitation, Opt. Express 27 (5) (2019) 7762–7775, http://dx.doi.org/10.1364/OE.27.007762.
[294] P. Nugraha, G. Krizsán, C. Lombosi, L. Pálfalvi, G. Tóth, G. Almási, J.A. Fülöp, J. Hebling, Demonstration of a tilted-pulse-front pumped plane-parallel slab terahertz source, 44, (4) 2019, pp. 1023–1026, http://dx.doi.org/10.1364/OL.44.001023.
[295] X.-C. Zhang, Y. Jin, X.F. Ma, Coherent measurement of THz optical rectification from electro-optic crystals, Appl. Phys. Lett. 61 (23) (1992) 2764–2766, http://dx.doi.org/10.1063/1.108083.
[296] T. Löffler, T. Hahn, M. Thomson, F. Jacob, H.G. Roskos, Large-area electro-optic ZnTe terahertz emitters, Opt. Express 13 (14) (2005) 5353, http://dx.doi.org/10.1364/opex.13.005353.
[297] F. Blanchard, L. Razzari, H. Bandulet, G. Sharma, R. Morandotti, J.C. Kieffer, T. Ozaki, M. Reid, H.F. Tiedje, H.K. Haugen, F.A. Hegmann, Generation of 1.5 μj single-cycle terahertz pulses by optical rectification from a large aperture znte crystal, Opt. Express 15 (20) (2007) 13212, http://dx.doi.org/10.1364/oe.15.013212.
[298] G. Chang, C.J. Divin, C.-H. Liu, S.L. Williamson, A. Galvanauskas, T.B. Norris, Power scalable compact THz system based on an ultrafast Yb-doped fiber amplifier, Opt. Express 14 (17) (2006) 7909, http://dx.doi.org/10.1364/oe.14.007909.
[299] F. Blanchard, B.E. Schmidt, X. Ropagnol, N. Thiré, T. Ozaki, R. Morandotti, D.G. Cooke, F. Légaré, Terahertz pulse generation from bulk GaAs by a tilted-pulse-front excitation at 1.8 um, Appl. Phys. Lett. 105 (24) (2014) 241106, http://dx.doi.org/10.1063/1.4904005.
[300] M.C. Hoffmann, K.-L. Yeh, J. Hebling, K.A. Nelson, Efficient terahertz generation by optical rectification at 1035 nm, Opt. Express 15 (18) (2007) 11706, http://dx.doi.org/10.1364/oe.15.011706.
[301] M.I. Bakunov, S.B. Bodrov, Terahertz generation with tilted-front laser pulses in a contact-grating scheme, J. Opt. Soc. Amer. B 31 (11) (2014) 2549, http://dx.doi.org/10.1364/josab.31.002549.
[302] G. Polonyi, M.I. Mechler, J. Hebling, J.A. Fulop, Prospects of semiconductor terahertz pulse sources, IEEE J. Sel. Top. Quantum Electron. 23 (4) (2017) 1–8, http://dx.doi.org/10.1109/jstqe.2017.2662661.
[303] X.-C. Zhang, X.F. Ma, Y. Jin, T.-M. Lu, E.P. Boden, P.D. Phelps, K.R. Stewart, C.P. Yakymyshyn, Terahertz optical rectification from a nonlinear organic crystal, Appl. Phys. Lett. 61 (26) (1992) 3080–3082, http://dx.doi.org/10.1063/1.107968.
[304] A. Schneider, M. Neis, M. Stillhart, B. Ruiz, R.U.A. Khan, P. Günter, Generation of terahertz pulses through optical rectification in organic DAST crystals: theory and experiment, J. Opt. Soc. Amer. B 23 (9) (2006) 1822, http://dx.doi.org/10.1364/josab.23.001822.
[305] C. Ruchert, C. Vicario, C.P. Hauri, Scaling submillimeter single-cycle transients toward megavolts per centimeter field strength via optical rectification in the organic crystal OH1, Opt. Lett. 37 (5) (2012) 899, http://dx.doi.org/10.1364/ol.37.000899.
[306] C. Vicario, A.V. Ovchinnikov, S.I. Ashitkov, M.B. Agranat, V.E. Fortov, C.P. Hauri, Generation of 09-mj THz pulses in DSTMS pumped by a cr:mg_2sio_4 laser, Opt. Lett. 39 (23) (2014) 6632, http://dx.doi.org/10.1364/ol.39.006632.
[307] H. Hamster, A. Sullivan, S. Gordon, W. White, R.W. Falcone, Subpicosecond, electromagnetic pulses from intense laser-plasma interaction, Phys. Rev. Lett. 71 (17) (1993) 2725–2728, http://dx.doi.org/10.1103/physrevlett.71.2725.
[308] T. Löffler, F. Jacob, H.G. Roskos, Generation of terahertz pulses by photoionization of electrically biased air, Appl. Phys. Lett. 77 (3) (2000) 453–455, http://dx.doi.org/10.1063/1.127007.
[309] D.J. Cook, R.M. Hochstrasser, Intense terahertz pulses by four-wave rectification in air, Opt. Lett. 25 (16) (2000) 1210, http://dx.doi.org/10.1364/ol.25.001210.
[310] T. Bartel, P. Gaal, K. Reimann, M. Woerner, T. Elsaesser, Generation of single-cycle THz transients with high electric-field amplitudes, Opt. Lett. 30 (20) (2005) 2805, http://dx.doi.org/10.1364/ol.30.002805.
[311] K.-Y. Kim, J.H. Glownia, A.J. Taylor, G. Rodriguez, Terahertz emission from ultrafast ionizing air in symmetry-broken laser fields, Opt. Express 15 (8) (2007) 4577, http://dx.doi.org/10.1364/oe.15.004577.
[312] K.Y. Kim, A.J. Taylor, J.H. Glownia, G. Rodriguez, Coherent control of terahertz supercontinuum generation in ultrafast laser–gas interactions, Nat. Photonics 2 (10) (2008) 605–609, http://dx.doi.org/10.1038/nphoton.2008.153.
[313] C. D'Amico, A. Houard, M. Franco, B. Prade, A. Mysyrowicz, A. Couairon, V.T. Tikhonchuk, Conical forward THz emission from femtosecond-laser-beam filamentation in air, Phys. Rev. Lett. 98 (23) (2007) 235002, http://dx.doi.org/10.1103/physrevlett.98.235002.
[314] Y.S. You, T.I. Oh, K.Y. Kim, Off-axis phase-matched terahertz emission from two-color laser-induced plasma filaments, Phys. Rev. Lett. 109 (18) (2012) 183902, http://dx.doi.org/10.1103/physrevlett.109.183902.
[315] T.I. Oh, Y.S. You, N. Jhajj, E.W. Rosenthal, H.M. Milchberg, K. Kim, Intense terahertz generation in two-color laser filamentation: energy scaling with terawatt laser systems, New J. Phys. 15 (7) (2013) 075002, URL http://stacks.iop.org/1367-2630/15/i=7/a=075002.
[316] G. Rodriguez, G.L. Dakovski, Scaling behavior of ultrafast two-color terahertz generation in plasma gas targets: energy and pressure dependence, Opt. Express 18 (14) (2010) 15130, http://dx.doi.org/10.1364/oe.18.015130.
[317] A. Gorodetsky, A.D. Koulouklidis, M. Massaouti, S. Tzortzakis, Physics of the conical broadband terahertz emission from two-color laser-induced plasma filaments, Phys. Rev. A 89 (3) (2014) 033838, http://dx.doi.org/10.1103/physreva.89.033838.
[318] M. Clerici, M. Peccianti, B.E. Schmidt, L. Caspani, M. Shalaby, M. Giguère, A. Lotti, A. Couairon, F. Légaré, T. Ozaki, D. Faccio, R. Morandotti, Wavelength scaling of terahertz generation by gas ionization, Phys. Rev. Lett. 110 (25) (2013) 253901, http://dx.doi.org/10.1103/physrevlett.110.253901.
[319] V.Y. Fedorov, S. Tzortzakis, Extreme THz fields from two-color filamentation of midinfrared laser pulses, Phys. Rev. A 97 (6) (2018) 063842, http://dx.doi.org/10.1103/physreva.97.063842.
[320] A. Nguyen, P.G. de Alaiza Martínez, I. Thiele, S. Skupin, L. Bergé, Broadband terahertz radiation from two-color mid- and far-infrared laser filaments in air, Phys. Rev. A 97 (6) (2018) 063839, http://dx.doi.org/10.1103/physreva.97.063839.

[321] A. Sagisaka, H. Daido, S. Nashima, S. Orimo, K. Ogura, M. Mori, A. Yogo, J. Ma, I. Daito, A. Pirozhkov, S. Bulanov, T. Esirkepov, K. Shimizu, M. Hosoda, Simultaneous generation of a proton beam and terahertz radiation in high-intensity laser and thin-foil interaction, Appl. Phys. B 90 (3–4) (2008) 373–377, http://dx.doi.org/10.1007/s00340-008-2931-8.
[322] C. Li, M.-L. Zhou, W.-J. Ding, F. Du, F. Liu, Y.-T. Li, W.-M. Wang, Z.-M. Sheng, J.-L. Ma, L.-M. Chen, X. Lu, Q.-L. Dong, Z.-H. Wang, Z. Lou, S.-C. Shi, Z.-Y. Wei, J. Zhang, Effects of laser-plasma interactions on terahertz radiation from solid targets irradiated by ultrashort intense laser pulses, Phys. Rev. E 84 (3) (2011) 036405, http://dx.doi.org/10.1103/physreve.84.036405.
[323] A. Gopal, S. Herzer, A. Schmidt, P. Singh, A. Reinhard, W. Ziegler, D. Brömmel, A. Karmakar, P. Gibbon, U. Dillner, T. May, H.-G. Meyer, G.G. Paulus, Observation of gigawatt-class THz pulses from a compact laser-driven particle accelerator, Phys. Rev. Lett. 111 (7) (2013) 074802, http://dx.doi.org/10.1103/physrevlett.111.074802.
[324] A. Gopal, P. Singh, S. Herzer, A. Reinhard, A. Schmidt, U. Dillner, T. May, H.-G. Meyer, W. Ziegler, G.G. Paulus, Characterization of 700 t rays generated during high-power laser solid interaction, Opt. Lett. 38 (22) (2013) 4705, http://dx.doi.org/10.1364/ol.38.004705.
[325] S. Herzer, A. Woldegeorgis, J. Polz, A. Reinhard, M. Almassarani, B. Beleites, F. Ronneberger, R. Grosse, G.G. Paulus, U. Hübner, T. May, A. Gopal, An investigation on THz yield from laser-produced solid density plasmas at relativistic laser intensities, New J. Phys. 20 (6) (2018) 063019, URL http://stacks.iop.org/1367-2630/20/i=6/a=063019.
[326] V. Ginzburg, V. Tsytovich, Several problems of the theory of transition radiation and transition scattering, Phys. Rep. 49 (1) (1979) 1–89, http://dx.doi.org/10.1016/0370-1573(79)90052-8.
[327] B.M. Bolotovskii, A.V. Serov, Features of the transition radiation field, Usp. Fiz. Nauk 179 (5) (2009) 517, http://dx.doi.org/10.3367/ufnr.0179.200905c.0517.
[328] J. Jackson, Classical Electrodynamics, John Wiley & Sons, 2012, URL https://books.google.se/books?id=2hZ0CgAAQBAJ.
[329] S. Casalbuoni, B. Schmidt, P. Schmüser, V. Arsov, S. Wesch, Ultrabroadband terahertz source and beamline based on coherent transition radiation, Phys. Rev. ST Accel. Beams 12 (2009) 030705, http://dx.doi.org/10.1103/PhysRevSTAB.12.030705.
[330] W. op't Root, Generation of High-Field, Single-Cycle Terahertz Pulses Using Relativistic Electron Bunches (Ph.D. thesis), Eindhoven University, 2009.
[331] Y. Shen, X. Yang, G.L. Carr, Y. Hidaka, J.B. Murphy, X. Wang, Tunable few-cycle and multicycle coherent terahertz radiation from relativistic electrons, Phys. Rev. Lett. 107 (20) (2011) 204801, http://dx.doi.org/10.1103/physrevlett.107.204801.
[332] S. Feng, H.G. Winful, R.W. Hellwarth, Gouy shift and temporal reshaping of focused single-cycle electromagnetic pulses, Opt. Lett. 23 (5) (1998) 385, http://dx.doi.org/10.1364/ol.23.000385.
[333] G. Shamuilov, A. Mak, P. Salén, V. Goryashko, Analytical model of waveform-controlled single-cycle light pulses from an undulator, Opt. Lett. 43 (4) (2018) 819–822, http://dx.doi.org/10.1364/ol.43.000819.
[334] M.C. Hoffmann, S. Schulz, S. Wesch, S. Wunderlich, A. Cavalleri, B. Schmidt, Coherent single-cycle pulses with MV/cm field strengths from a relativistic transition radiation light source, Opt. Lett. 36 (23) (2011) 4473, http://dx.doi.org/10.1364/ol.36.004473.
[335] B.M. Bolotovski, G.V. Voskresenski, Diffraction radiation, Sov. Phys. Usp. 9 (1) (1966) 73, URL http://stacks.iop.org/0038-5670/9/i=1/a=R04.
[336] M.L. Ter-Mikaelian, High Energy Electromagnetic Processes in Condensed Media, Wiley, 1972.
[337] A.P. Potylitsyn, M.I. Ryazanov, M.N. Strikhanov, A.A. Tishchenko, Diffraction radiation from relativistic particles, Springer Berlin Heidelberg, 2010, http://dx.doi.org/10.1007/978-3-642-12513-3_1.
[338] J. Jo, S. Miginsky, N. Vinokurov, K.N. Kim, B. Gudkov, S.H. Park, Y.U. Jeong, W.J. Ryu, K. Lee, H.N. Kim, High-power ultrashort terahertz pulses generated by a multi-foil radiator with laser-accelerated electron pulses, in: Proceedings of the Free-ELectron Laser Conference, Daejeon, Korea, 2015.
[339] S. Setiniyaz, S.H. Park, H.W. Kim, N.A. Vinokurov, K.-H. Jang, K. Lee, I.H. Baek, Y.U. Jeong, THZ-pump and x-ray-probe sources based on an electron linac, Rev. Sci. Instrum. 88 (11) (2017) 113306, http://dx.doi.org/10.1063/1.5006550.
[340] P.D. Pietro, N. Adhlakha, F. Piccirilli, L. Capasso, C. Svetina, S.D. Mitri, M. Veronese, F. Giorgianni, S. Lupi, A. Perucchi, TeraFERMI: A superradiant beamline for THz nonlinear studies at the FERMI free electron laser facility, Synchrotron Radiat. News 30 (4) (2017) 36–39, http://dx.doi.org/10.1080/08940886.2017.1338423.
[341] R. Pan, E. Zapolnova, T. Golz, A.J. Krmpot, M.D. Rabasovic, J. Petrovic, V. Asgekar, B. Faatz, F. Tavella, A. Perucchi, S. Kovalev, B. Green, G. Geloni, T. Tanikawa, M. Yurkov, E. Schneidmiller, M. Gensch, N. Stojanovic, Photon diagnostics at the FLASH THz beamline, J. Synchrotron Radiat. 26 (3) (2019) 700–707, http://dx.doi.org/10.1107/s1600577519003412.
[342] A.L. Robinson, History of synchrotron radiation, Synchrotron Radiat. News 28 (4) (2015) 4–9, http://dx.doi.org/10.1080/08940886.2015.1059228.
[343] B.J. Burn, A synchrotron model for the continuum spectrum of the crab nebula, Mon. Not. R. Astron. Soc. 165 (4) (1973) 421–429, https://doi.org/10.1093/mnras/165.4.421.
[344] H. Bruck, Accélérateurs circulaires de particules: introduction à la théorie, in: Bibliothèque des sciences et techniques nucléaires, Presses Universitaires de France, 1966, URL https://books.google.se/books?id=_JTFNAEACAAJ.
[345] H. Winick, Synchrotron radiation sources: A primer, Series on Synchrotron Radiation Techniques and Applications, World Scientific, 1995, URL https://books.google.se/books?id=z439h1_oYukC.
[346] J. Ullrich, A. Rudenko, R. Moshammer, Free-electron lasers: New avenues in molecular physics and photochemistry, Annu. Rev. Phys. Chem. 63 (1) (2012) 635–660, http://dx.doi.org/10.1146/annurev-physchem-032511-143720.
[347] A.B. Temnykh, Delta undulator for Cornell energy recovery linac, Phys. Rev. Spec. Top. Accel. Beams 11 (12) (2008) 120702, http://dx.doi.org/10.1103/physrevstab.11.120702.
[348] S. Sasaki, K. Kakuno, T. Takada, T. Shimada, K. Yanagida, Y. Miyahara, Design of a new type of planar undulator for generating variably polarized radiation, Nucl. Instrum. Methods Phys. Res. A 331 (1–3) (1993) 763–767, http://dx.doi.org/10.1016/0168-9002(93)90153-9.
[349] T. Schmidt, A. Anghel, P. Böhler, M. Brügger, M. Calvi, S. Danner, P. Huber, A. Keller, M. Locher, Magnetic design of an APPLE III undulator for SwissFEL, in: Proceedings of FEL 2014, JACoW, 2014, pp. 116–120, URL http://accelconf.web.cern.ch/AccelConf/FEL2014/papers/mop043.pdf.
[350] T. Nakazato, M. Oyamada, N. Niimura, S. Urasawa, O. Konno, A. Kagaya, R. Kato, T. Kamiyama, Y. Torizuka, T. Nanba, Y. Kondo, Y. Shibata, K. Ishi, T. Ohsaka, M. Ikezawa, Observation of coherent synchrotron radiation, Phys. Rev. Lett. 63 (1989) 1245–1248, http://dx.doi.org/10.1103/PhysRevLett.63.1245.
[351] G.L. Carr, M.C. Martin, W.R. McKinney, K. Jordan, G.R. Neil, G.P. Williams, High-power terahertz radiation from relativistic electrons, Nature 420 (6912) (2002) 153–156, http://dx.doi.org/10.1038/nature01175.
[352] M. Abo-Bakr, J. Feikes, K. Holldack, G. Wüstefeld, H.-W. Hübers, Steady-state far-infrared coherent synchrotron radiation detected at BESSY II, Phys. Rev. Lett. 88 (25) (2002) 254801, http://dx.doi.org/10.1103/physrevlett.88.254801.
[353] M. Abo-Bakr, J. Feikes, K. Holldack, P. Kuske, W.B. Peatman, U. Schade, G. Wüstefeld, H.-W. Hübers, Brilliant, coherent far-infrared (THz) synchrotron radiation, Phys. Rev. Lett. 90 (9) (2003) 094801, http://dx.doi.org/10.1103/physrevlett.90.094801.
[354] K. Holldack, S. Khan, R. Mitzner, T. Quast, Femtosecond terahertz radiation from femtoslicing at BESSY, Phys. Rev. Lett. 96 (5) (2006) http://dx.doi.org/10.1103/physrevlett.96.054801.
[355] J.-B. Brubach, L. Manceron, M. Rouzieŕes, O. Pirali, D. Balcon, F.K. Tchana, V. Boudon, M. Tudorie, T. Huet, A. Cuisset, P. Roy, A. Predoi-Cross, B.E. Billinghurst, Performance of the AILES THz-infrared beamline at SOLEIL for high resolution spectroscopy, AIP, 2010, http://dx.doi.org/10.1063/1.3326356, https://doi.org/10.1063/1.3326356.

[356] R. Plathe, D. Martin, M.J. Tobin, L. Puskar, D. Appadoo, The far-infrared/THz beamline at the Australian synchrotron: Performance and applications, in: 2011 International Conference on Infrared, Millimeter, and Terahertz Waves, IEEE, 2011, http://dx.doi.org/10.1109/irmmw-thz.2011.6105080.
[357] K.-J. Kim, K.T. McDonald, G.V. Stupakov, M.S. Zolotorev, A bounded source cannot emit a unipolar electromagnetic wave, 2000, arXiv preprint arXiv:physics/0003064.
[358] B.W.J. McNeil, N.R. Thompson, X-ray free-electron lasers, Nat. Photonics 4 (12) (2010) 814–821, http://dx.doi.org/10.1038/nphoton.2010.239.
[359] P. Tan, J. Huang, K. Liu, Y. Xiong, M. Fan, Terahertz radiation sources based on free electron lasers and their applications, Sci. China Inf. Sci. 55 (1) (2011) 1–15, http://dx.doi.org/10.1007/s11432-011-4515-1.
[360] W.J. van der Zande, R.T. Jongma, L. van der Meer, B. Redlich, FELIX facility: Free electron laser light sources from 0.2 to 75 THz, in: 2013 38th International Conference on Infrared, Millimeter, and Terahertz Waves (IRMMW-THz), IEEE, 2013, http://dx.doi.org/10.1109/irmmw-thz.2013.6665600.
[361] J.-M. Ortega, J.-P. Berthet, F. Glotin, R. Prazeres, Evidence for competition modes in a partially guided far-infrared free-electron laser, Phys. Rev. Spec. Top. Accel. Beams 17 (10) (2014) http://dx.doi.org/10.1103/physrevstab.17.100701.
[362] J. Schmidt, S. Winnerl, W. Seidel, C. Bauer, M. Gensch, H. Schneider, M. Helm, Single-pulse picking at kHz repetition rates using a Ge plasma switch at the free-electron laser FELBE, Rev. Sci. Instrum. 86 (6) (2015) 063103, http://dx.doi.org/10.1063/1.4921864.
[363] Z. Tibai, G. Tóth, M.I. Mechler, J.A. Fülöp, G. Almási, J. Hebling, Proposal for Carrier-envelope-phase stable single-cycle attosecond pulse generation in the extreme-ultraviolet range, Phys. Rev. Lett. 113 (10) (2014) 104801, http://dx.doi.org/10.1103/physrevlett.113.104801.
[364] D. Strickland, G. Mourou, Compression of amplified chirped optical pulses, Opt. Commun. 56 (3) (1985) 219–221, http://dx.doi.org/10.1016/0030-4018(85)90120-8.
[365] I.V. Bazarov, B.M. Dunham, C.K. Sinclair, Maximum achievable beam brightness from photoinjectors, Phys. Rev. Lett. 102 (10) (2009) 104801, http://dx.doi.org/10.1103/physrevlett.102.104801.
[366] E.J. Jaeschke, S. Khan, J.R. Schneider, J.B. Hastings (Eds.), Synchrotron light sources and free-electron lasers, Springer International Publishing, 2016, p. 88, http://dx.doi.org/10.1007/978-3-319-14394-1, https://doi.org/10.1007/978-3-319-14394-1.
[367] E. Hemsing, A. Marinelli, G. Marcus, D. Xiang, Correlated energy-spread removal with space charge for high-harmonic generation, Phys. Rev. Lett. 113 (13) (2014) 134802, http://dx.doi.org/10.1103/physrevlett.113.134802.
[368] A. Buck, M. Nicolai, K. Schmid, C.M.S. Sears, A. Sävert, J.M. Mikhailova, F. Krausz, M.C. Kaluza, L. Veisz, Real-time observation of laser-driven electron acceleration, Nat. Phys. 7 (7) (2011) 543–548, http://dx.doi.org/10.1038/nphys1942.
[369] D. Dowell, I. Bazarov, B. Dunham, K. Harkay, C. Hernandez-Garcia, R. Legg, H. Padmore, T. Rao, J. Smedley, W. Wan, Cathode R&D for future light sources, Nucl. Instrum. Methods Phys. Res. A 622 (3) (2010) 685–697, http://dx.doi.org/10.1016/j.nima.2010.03.104.
[370] P. Musumeci, R.K. Li, A. Marinelli, Nonlinear longitudinal space charge oscillations in relativistic electron beams, Phys. Rev. Lett. 106 (18) (2011) 184801, http://dx.doi.org/10.1103/physrevlett.106.184801.
[371] F. Giorgianni, M. Anania, M. Bellaveglia, A. Biagioni, E. Chiadroni, A. Cianchi, M. Daniele, M.D. Franco, D.D. Giovenale, G.D. Pirro, M. Ferrario, S. Lupi, A. Mostacci, M. Petrarca, S. Pioli, R. Pompili, V. Shpakov, C. Vaccarezza, F. Villa, Tailoring of highly intense THz radiation through high brightness electron beams longitudinal manipulation, Appl. Sci. 6 (2) (2016) 56, http://dx.doi.org/10.3390/app6020056.
[372] B. Marchetti, A. Bacci, E. Chiadroni, A. Cianchi, M. Ferrario, A. Mostacci, R. Pompili, C. Ronsivalle, B. Spataro, I. Zagorodnov, Novel schemes for the optimization of the SPARC narrow band THz source, Rev. Sci. Instrum. 86 (7) (2015) 073301, http://dx.doi.org/10.1063/1.4922882.
[373] Y. Lurie, A. Friedman, Y. Pinhasi, Single pass, THz spectral range free-electron laser driven by a photocathode hybrid rf linear accelerator, Phys. Rev. Spec. Top. Accel. Beams 18 (7) (2015) 070701, http://dx.doi.org/10.1103/physrevstab.18.070701.
[374] Z. Ma, Z. Wang, F. Fu, R. Wang, D. Xiang, Generating quasi-single-cycle THz pulse from frequency-chirped electron bunch train and a tapered undulator, High Power Laser Sci. Eng. 4 (2016) e1, http://dx.doi.org/10.1017/hpl.2015.35.
[375] S.G. Anderson, P. Musumeci, J.B. Rosenzweig, W.J. Brown, R.J. England, M. Ferrario, J.S. Jacob, M.C. Thompson, G. Travish, A.M. Tremaine, R. Yoder, Velocity bunching of high-brightness electron beams, Phys. Rev. Spec. Top. Accel. Beams 8 (1) (2005) 014401, http://dx.doi.org/10.1103/physrevstab.8.014401.
[376] S. Khan, Free-electron lasers, J. Modern Opt. 55 (21) (2008) 3469–3512, http://dx.doi.org/10.1080/09500340802521175.
[377] B. Zeitler, K. Floettmann, F. Grüner, Linearization of the longitudinal phase space without higher harmonic field, Phys. Rev. Spec. Top. Accel. Beams 18 (12) (2015) 120102, http://dx.doi.org/10.1103/physrevstab.18.120102.
[378] L. Zhao, Z. Wang, C. Lu, R. Wang, C. Hu, P. Wang, J. Qi, T. Jiang, S. Liu, Z. Ma, F. Qi, P. Zhu, Y. Cheng, Z. Shi, Y. Shi, W. Song, X. Zhu, J. Shi, Y. Wang, L. Yan, L. Zhu, D. Xiang, J. Zhang, Terahertz streaking of few-femtosecond relativistic electron beams, Phys. Rev. X 8 (2) (2018) 021061, http://dx.doi.org/10.1103/physrevx.8.021061.
[379] L. Zhao, Z. Wang, H. Tang, R. Wang, Y. Cheng, C. Lu, T. Jiang, P. Zhu, L. Hu, W. Song, H. Wang, J. Qiu, R. Kostin, C. Jing, S. Antipov, P. Wang, J. Qi, Y. Cheng, D. Xiang, J. Zhang, Terahertz oscilloscope for recording time information of ultrashort electron beams, Phys. Rev. Lett. 122 (14) (2019) 144801, http://dx.doi.org/10.1103/physrevlett.122.144801.
[380] G. Berden, W.A. Gillespie, S.P. Jamison, E.-A. Knabbe, A.M. MacLeod, A.F.G. van der Meer, P.J. Phillips, H. Schlarb, B. Schmidt, P. Schmüser, B. Steffen, Benchmarking of electro-optic monitors for femtosecond electron bunches, Phys. Rev. Lett. 99 (16) (2007) 164801, http://dx.doi.org/10.1103/physrevlett.99.164801.
[381] C. Behrens, F.-J. Decker, Y. Ding, V.A. Dolgashev, J. Frisch, Z. Huang, P. Krejcik, H. Loos, A. Lutman, T.J. Maxwell, J. Turner, J. Wang, M.-H. Wang, J. Welch, J. Wu, Few-femtosecond time-resolved measurements of x-ray free-electron lasers, Nature Commun. 5 (1) (2014) 3762, http://dx.doi.org/10.1038/ncomms4762.
[382] J.B. Hastings, F.M. Rudakov, D.H. Dowell, J.F. Schmerge, J.D. Cardoza, J.M. Castro, S.M. Gierman, H. Loos, P.M. Weber, Ultrafast time-resolved electron diffraction with megavolt electron beams, Appl. Phys. Lett. 89 (18) (2006) 184109, http://dx.doi.org/10.1063/1.2372697.
[383] R. Li, C. Tang, Y. Du, W. Huang, Q. Du, J. Shi, L. Yan, X. Wang, Experimental demonstration of high quality MeV ultrafast electron diffraction, Rev. Sci. Instrum. 80 (8) (2009) 083303, http://dx.doi.org/10.1063/1.3194047.
[384] R.P. Chatelain, V.R. Morrison, C. Godbout, B.J. Siwick, Ultrafast electron diffraction with radio-frequency compressed electron pulses, Appl. Phys. Lett. 101 (8) (2012) 081901, http://dx.doi.org/10.1063/1.4747155.
[385] S.P. Weathersby, G. Brown, M. Centurion, T.F. Chase, R. Coffee, J. Corbett, J.P. Eichner, J.C. Frisch, A.R. Fry, M. Gühr, N. Hartmann, C. Hast, R. Hettel, R.K. Jobe, E.N. Jongewaard, J.R. Lewandowski, R.K. Li, A.M. Lindenberg, I. Makasyuk, J.E. May, D. McCormick, M.N. Nguyen, A.H. Reid, X. Shen, K. Sokolowski-Tinten, T. Vecchione, S.L. Vetter, J. Wu, J. Yang, H.A. Dürr, X.J. Wang, Mega-electron-volt ultrafast electron diffraction at SLAC national accelerator laboratory, Rev. Sci. Instrum. 86 (7) (2015) 073702, http://dx.doi.org/10.1063/1.4926994.
[386] T. van Oudheusden, P.L.E.M. Pasmans, S.B. van der Geer, M.J. de Loos, M.J. van der Wiel, O.J. Luiten, Compression of subrelativistic space-charge-dominated electron bunches for single-shot femtosecond electron diffraction, Phys. Rev. Lett. 105 (26) (2010) 264801, http://dx.doi.org/10.1103/physrevlett.105.264801.
[387] C. Kealhofer, W. Schneider, D. Ehberger, A. Ryabov, F. Krausz, P. Baum, All-optical control and metrology of electron pulses, Science 352 (6284) (2016) 429–433, http://dx.doi.org/10.1126/science.aae0003.

[388] R.K. Li, M.C. Hoffmann, E.A. Nanni, S.H. Glenzer, M.E. Kozina, A.M. Lindenberg, B.K. Ofori-Okai, A.H. Reid, X. Shen, S.P. Weathersby, J. Yang, M. Zajac, X.J. Wang, Terahertz-based subfemtosecond metrology of relativistic electron beams, Phys. Rev. Accel. Beams 22 (1) (2019) 012803, http://dx.doi.org/10.1103/physrevaccelbeams.22.012803.
[389] D. Bradley, B. Liddy, W. Sleat, Direct linear measurement of ultrashort light pulses with a picosecond streak camera, Opt. Commun. 2 (8) (1971) 391–395, http://dx.doi.org/10.1016/0030-4018(71)90252-5.
[390] J. Itatani, F. Quéré, G.L. Yudin, M.Y. Ivanov, F. Krausz, P.B. Corkum, Attosecond streak Camera, Phys. Rev. Lett. 88 (17) (2002) 173903, http://dx.doi.org/10.1103/physrevlett.88.173903.
[391] F. Quéré, Y. Mairesse, J. Itatani, Temporal characterization of attosecond XUV fields, J. Modern Opt. 52 (2–3) (2005) 339–360, http://dx.doi.org/10.1080/09500340412331307942.
[392] U. Frühling, Light-field streaking for FELs, J. Phys. B: At. Mol. Opt. Phys. 44 (24) (2011) 243001, http://dx.doi.org/10.1088/0953-4075/44/24/243001.
[393] I. Grguraš, A.R. Maier, C. Behrens, T. Mazza, T.J. Kelly, P. Radcliffe, S. Düsterer, A.K. Kazansky, N.M. Kabachnik, T. Tschentscher, J.T. Costello, M. Meyer, M.C. Hoffmann, H. Schlarb, A.L. Cavalieri, Ultrafast x-ray pulse characterization at free-electron lasers, Nat. Photonics 6 (12) (2012) 852–857, http://dx.doi.org/10.1038/nphoton.2012.276.
[394] E. Allaria, L. Badano, S. Bassanese, F. Capotondi, D. Castronovo, P. Cinquegrana, M.B. Danailov, G. D'Auria, A. Demidovich, R.D. Monte, G.D. Ninno, S.D. Mitri, B. Diviacco, W.M. Fawley, M. Ferianis, E. Ferrari, G. Gaio, D. Gauthier, L. Giannessi, F. Iazzourene, G. Kurdi, N. Mahne, I. Nikolov, F. Parmigiani, G. Penco, L. Raimondi, P. Rebernik, F. Rossi, E. Roussel, C. Scafuri, C. Serpico, P. Sigalotti, C. Spezzani, M. Svandrlik, C. Svetina, M. Trovó, M. Veronese, D. Zangrando, M. Zangrando, The FERMI free-electron lasers, J. Synch. Rad. 22 (3) (2015) 485–491, http://dx.doi.org/10.1107/s1600577515005366.
[395] S. Schreiber, B. Faatz, The free-electron laser FLASH, High Power Laser Sci. Eng. 3 (2015) http://dx.doi.org/10.1017/hpl.2015.16.
[396] P. Emma, R. Akre, J. Arthur, R. Bionta, C. Bostedt, J. Bozek, A. Brachmann, P. Bucksbaum, R. Coffee, F.-J. Decker, Y. Ding, D. Dowell, S. Edstrom, A. Fisher, J. Frisch, S. Gilevich, J. Hastings, G. Hays, P. Hering, Z. Huang, R. Iverson, H. Loos, M. Messerschmidt, A. Miahnahri, S. Moeller, H.-D. Nuhn, G. Pile, D. Ratner, J. Rzepiela, D. Schultz, T. Smith, P. Stefan, H. Tompkins, J. Turner, J. Welch, W. White, J. Wu, G. Yocky, J. Galayda, First lasing and operation of an ångstrom-wavelength free-electron laser, Nat. Photonics 4 (9) (2010) 641–647, http://dx.doi.org/10.1038/nphoton.2010.176.
[397] E. Cartlidge, European XFEL to shine as brightest, fastest x-ray source, Science 354 (6308) (2016) 22–23, http://dx.doi.org/10.1126/science.354.6308.22.
[398] T. Ishikawa, H. Aoyagi, T. Asaka, Y. Asano, N. Azumi, T. Bizen, H. Ego, K. Fukami, T. Fukui, Y. Furukawa, S. Goto, H. Hanaki, T. Hara, T. Hasegawa, T. Hatsui, A. Higashiya, T. Hirono, N. Hosoda, M. Ishii, T. Inagaki, Y. Inubushi, T. Itoga, Y. Joti, M. Kago, T. Kameshima, H. Kimura, Y. Kirihara, A. Kiyomichi, T. Kobayashi, C. Kondo, T. Kudo, H. Maesaka, X.M. Maréchal, T. Masuda, S. Matsubara, T. Matsumoto, T. Matsushita, S. Matsui, M. Nagasono, N. Nariyama, H. Ohashi, T. Ohata, T. Ohshima, S. Ono, Y. Otake, C. Saji, T. Sakurai, T. Sato, K. Sawada, T. Seike, K. Shirasawa, T. Sugimoto, S. Suzuki, S. Takahashi, H. Takebe, K. Takeshita, K. Tamasaku, H. Tanaka, R. Tanaka, T. Tanaka, T. Togashi, K. Togawa, A. Tokuhisa, H. Tomizawa, K. Tono, S. Wu, M. Yabashi, M. Yamaga, A. Yamashita, K. Yanagida, C. Zhang, T. Shintake, H. Kitamura, N. Kumagai, A compact X-ray free-electron laser emitting in the sub-ångström region, Nat. Photonics 6 (8) (2012) 540–544, http://dx.doi.org/10.1038/nphoton.2012.141.
[399] S.V. Milton, Exponential gain and saturation of a self-amplified spontaneous emission free-electron laser, Science 292 (5524) (2001) 2037–2041, http://dx.doi.org/10.1126/science.1059955.
[400] U. Frühling, M. Wieland, M. Gensch, T. Gebert, B. Schütte, M. Krikunova, R. Kalms, F. Budzyn, O. Grimm, J. Rossbach, E. Plönjes, M. Drescher, Single-shot terahertz-field-driven x-ray streak camera, Nat. Photonics 3 (9) (2009) 523–528, http://dx.doi.org/10.1038/nphoton.2009.160.
[401] I. Gorgisyan, R. Ischebeck, C. Erny, A. Dax, L. Patthey, C. Pradervand, L. Sala, C. Milne, H.T. Lemke, C.P. Hauri, T. Katayama, S. Owada, M. Yabashi, T. Togashi, R. Abela, L. Rivkin, P. Juranić, THZ streak camera method for synchronous arrival time measurement of two-color hard x-ray FEL pulses, Opt. Express 25 (3) (2017) 2080, http://dx.doi.org/10.1364/oe.25.002080.
[402] C. Gahl, A. Azima, M. Beye, M. Deppe, K. Döbrich, U. Hasslinger, F. Hennies, A. Melnikov, M. Nagasono, A. Pietzsch, M. Wolf, W. Wurth, A. Föhlisch, A femtosecond x-ray/optical cross-correlator, Nat. Photonics 2 (3) (2008) 165–169, http://dx.doi.org/10.1038/nphoton.2007.298.
[403] T. Maltezopoulos, S. Cunovic, M. Wieland, M. Beye, A. Azima, H. Redlin, M. Krikunova, R. Kalms, U. Frühling, F. Budzyn, W. Wurth, A. Föhlisch, M. Drescher, Single-shot timing measurement of extreme-ultraviolet free-electron laser pulses, New J. Phys. 10 (3) (2008) 033026, http://dx.doi.org/10.1088/1367-2630/10/3/033026.
[404] M.R. Bionta, H.T. Lemke, J.P. Cryan, J.M. Glownia, C. Bostedt, M. Cammarata, J.-C. Castagna, Y. Ding, D.M. Fritz, A.R. Fry, J. Krzywinski, M. Messerschmidt, S. Schorb, M.L. Swiggers, R.N. Coffee, Spectral encoding of x-ray/optical relative delay, Opt. Express 19 (22) (2011) 21855, http://dx.doi.org/10.1364/oe.19.021855.
[405] M. Harmand, R. Coffee, M.R. Bionta, M. Chollet, D. French, D. Zhu, D.M. Fritz, H.T. Lemke, N. Medvedev, B. Ziaja, S. Toleikis, M. Cammarata, Achieving few-femtosecond time-sorting at hard x-ray free-electron lasers, Nat. Photonics 7 (3) (2013) 215–218, http://dx.doi.org/10.1038/nphoton.2013.11.
[406] T. Sato, T. Togashi, K. Ogawa, T. Katayama, Y. Inubushi, K. Tono, M. Yabashi, Highly efficient arrival timing diagnostics for femtosecond x-ray and optical laser pulses, Appl. Phys. Express 8 (1) (2014) 012702, http://dx.doi.org/10.7567/apex.8.012702.
[407] H. Timmers, N. Shivaram, A. Sandhu, Ultrafast dynamics of neutral superexcited oxygen: A direct measurement of the competition between autoionization and predissociation, Phys. Rev. Lett. 109 (17) (2012) 173001, http://dx.doi.org/10.1103/physrevlett.109.173001.
[408] A.S. Sandhu, E. Gagnon, R. Santra, V. Sharma, W. Li, P. Ho, P. Ranitovic, C.L. Cocke, M.M. Murnane, H.C. Kapteyn, Observing the creation of electronic Feshbach resonances in soft x-ray-induced o2 dissociation, Science 322 (5904) (2008) 1081–1085, http://dx.doi.org/10.1126/science.1164498.
[409] Y. Liu, K. Schnorr, G. Schmid, S. Augustin, S. Meister, H. Lindenblatt, A. Rudenko, M. Kübel, C. Burger, N. Stojanovic, R. Treusch, S. Düsterer, T. Jahnke, M. Kling, C. Schröter, T. Pfeifer, R. Moshammer, THZ streaking of the autoionization dynamics of o2 at the free-electron-laser FLASH, J. Phys. Conf. Ser. 875 (2017) 032031, http://dx.doi.org/10.1088/1742-6596/875/4/032031.
[410] T. Kampfrath, M. Battiato, P. Maldonado, G. Eilers, J. Nötzold, S. Mährlein, V. Zbarsky, F. Freimuth, Y. Mokrousov, S. Blügel, M. Wolf, I. Radu, P.M. Oppeneer, M. Münzenberg, Terahertz spin current pulses controlled by magnetic heterostructures, Nature Nanotechnol. 8 (2013) 256, http://dx.doi.org/10.1038/nnano.2013.43, URL https://www.nature.com/articles/nnano.2013.43{#}supplementary-information.
[411] T. Seifert, S. Jaiswal, U. Martens, J. Hannegan, L. Braun, P. Maldonado, F. Freimuth, A. Kronenberg, J. Henrizi, I. Radu, E. Beaurepaire, Y. Mokrousov, P.M. Oppeneer, M. Jourdan, G. Jakob, D. Turchinovich, L.M. Hayden, M. Wolf, M. Münzenberg, M. Kläui, T. Kampfrath, Efficient metallic spintronic emitters of ultrabroadband terahertz radiation, Nat. Photonics 10 (2016) 483, http://dx.doi.org/10.1038/nphoton.2016.91, URL https://www.nature.com/articles/nphoton.2016.91{#}supplementary-information.
[412] T.J. Huisman, R.V. Mikhaylovskiy, J.D. Costa, F. Freimuth, E. Paz, J. Ventura, P.P. Freitas, S. Blügel, Y. Mokrousov, T. Rasing, A.V. Kimel, Femtosecond control of electric currents in metallic ferromagnetic heterostructures, Nature Nanotechnol. 11 (2016) 455, http://dx.doi.org/10.1038/nnano.2015.331, https://www.nature.com/articles/nnano.2015.331{#}supplementary-information.
[413] L. Cheng, X. Wang, W. Yang, J. Chai, M. Yang, M. Chen, Y. Wu, X. Chen, D. Chi, K.E.J. Goh, J.-X. Zhu, H. Sun, S. Wang, J.C.W. Song, M. Battiato, H. Yang, E.E.M. Chia, Far out-of-equilibrium spin populations trigger giant spin injection into atomically thin MoS2, Nat. Phys. 15 (4) (2019) 347–351, http://dx.doi.org/10.1038/s41567-018-0406-3, https://doi.org/10.1038/s41567-018-0406-3.

Please cite this article as: P. Salén, M. Basini, S. Bonetti et al., Matter manipulation with extreme terahertz light: Progress in the enabling THz technology, Physics Reports (2019), https://doi.org/10.1016/j.physrep.2019.09.002.

[414] T. Seifert, S. Jaiswal, M. Sajadi, G. Jakob, S. Winnerl, M. Wolf, M. Kläui, T. Kampfrath, Ultrabroadband single-cycle terahertz pulses with peak fields of 300 kV cm1 from a metallic spintronic emitter, Appl. Phys. Lett. 110 (25) (2017) 252402, http://dx.doi.org/10.1063/1.4986755.
[415] M.T. Hibberd, D.S. Lake, N.A.B. Johansson, T. Thomson, S.P. Jamison, D.M. Graham, Magnetic-field tailoring of the terahertz polarization emitted from a spintronic source, Appl. Phys. Lett. 114 (3) (2019) 031101, http://dx.doi.org/10.1063/1.5055736.
[416] J. Park, C. Kim, J. Lee, C. Yim, C.H. Kim, J. Lee, S. Jung, J. Ryu, H.-S. Kang, T. Joo, Generation, transport, and detection of linear accelerator based femtosecond-terahertz pulses, Rev. Sci. Instrum. 82 (1) (2011) 013305, http://dx.doi.org/10.1063/1.3529921.
[417] P.U. Jepsen, R.H. Jacobsen, S.R. Keiding, Generation and detection of terahertz pulses from biased semiconductor antennas, J. Opt. Soc. Amer. B 13 (11) (1996) 2424, http://dx.doi.org/10.1364/josab.13.002424.
[418] Q. Wu, X.-C. Zhang, Ultrafast electro-optic field sensors, Appl. Phys. Lett. 68 (12) (1996) 1604–1606, http://dx.doi.org/10.1063/1.115665.
[419] J. Dai, X. Xie, X.-C. Zhang, Detection of broadband terahertz waves with a laser-induced plasma in gases, Phys. Rev. Lett. 97 (10) (2006) 103903, http://dx.doi.org/10.1103/physrevlett.97.103903.
[420] P.C.M. Planken, H.-K. Nienhuys, H.J. Bakker, T. Wenckebach, Measurement and calculation of the orientation dependence of terahertz pulse detection in ZnTe, J. Opt. Soc. Amer. B 18 (3) (2001) 313, http://dx.doi.org/10.1364/josab.18.000313.
[421] Q. Wu, X.-C. Zhang, 7 terahertz broadband GaP electro-optic sensor, Appl. Phys. Lett. 70 (14) (1997) 1784–1786, http://dx.doi.org/10.1063/1.118691.
[422] A. Leitenstorfer, S. Hunsche, J. Shah, M.C. Nuss, W.H. Knox, Detectors and sources for ultrabroadband electro-optic sampling: Experiment and theory, Appl. Phys. Lett. 74 (11) (1999) 1516–1518, http://dx.doi.org/10.1063/1.123601.
[423] C. Riek, D.V. Seletskiy, A.S. Moskalenko, J.F. Schmidt, P. Krauspe, S. Eckart, S. Eggert, G. Burkard, A. Leitenstorfer, Direct sampling of electric-field vacuum fluctuations, Science 350 (6259) (2015) 420–423, http://dx.doi.org/10.1126/science.aac9788.
[424] M. Usami, M. Yamashita, K. Fukushima, C. Otani, K. Kawase, Terahertz wideband spectroscopic imaging based on two-dimensional electro-optic sampling technique, Appl. Phys. Lett. 86 (14) (2005) 141109, http://dx.doi.org/10.1063/1.1899259.
[425] Z. Jiang, X.-C. Zhang, Single-shot spatiotemporal terahertz field imaging, Opt. Lett. 23 (14) (1998) 1114, http://dx.doi.org/10.1364/ol.23.001114.
[426] K.Y. Kim, B. Yellampalle, A.J. Taylor, G. Rodriguez, J.H. Glownia, Single-shot terahertz pulse characterization via two-dimensional electro-optic imaging with dual echelons, Opt. Lett. 32 (14) (2007) 1968, http://dx.doi.org/10.1364/ol.32.001968.
[427] Y. Kawada, T. Yasuda, A. Nakanishi, K. Akiyama, H. Takahashi, Single-shot terahertz spectroscopy using pulse-front tilting of an ultra-short probe pulse, Opt. Express 19 (12) (2011) 11228, http://dx.doi.org/10.1364/oe.19.011228.
[428] F. Bonaccorso, Z. Sun, T. Hasan, A.C. Ferrari, Graphene photonics and optoelectronics, Nat. Photonics 4 (9) (2010) 611–622, http://dx.doi.org/10.1038/nphoton.2010.186.
[429] F.H.L. Koppens, T. Mueller, P. Avouris, A.C. Ferrari, M.S. Vitiello, M. Polini, Photodetectors based on graphene, other two-dimensional materials and hybrid systems, Nature Nanotechnol. 9 (10) (2014) 780–793, http://dx.doi.org/10.1038/nnano.2014.215.
[430] A.N. Grigorenko, M. Polini, K.S. Novoselov, Graphene plasmonics, Nat. Photonics 6 (11) (2012) 749–758, http://dx.doi.org/10.1038/nphoton.2012.262.
[431] T. Low, P. Avouris, Graphene plasmonics for terahertz to mid-infrared applications, ACS Nano 8 (2) (2014) 1086–1101, http://dx.doi.org/10.1021/nn406627u.
[432] G.X. Ni, L. Wang, M.D. Goldflam, M. Wagner, Z. Fei, A.S. McLeod, M.K. Liu, F. Keilmann, B. Özyilmaz, A.H.C. Neto, J. Hone, M.M. Fogler, D.N. Basov, Ultrafast optical switching of infrared plasmon polaritons in high-mobility graphene, Nat. Photonics 10 (4) (2016) 244–247, http://dx.doi.org/10.1038/nphoton.2016.45.
[433] M.B. Lundeberg, Y. Gao, R. Asgari, C. Tan, B.V. Duppen, M. Autore, P. Alonso-González, A. Woessner, K. Watanabe, T. Taniguchi, R. Hillenbrand, J. Hone, M. Polini, F.H.L. Koppens, Tuning quantum nonlocal effects in graphene plasmonics, Science 357 (6347) (2017) 187–191, http://dx.doi.org/10.1126/science.aan2735.
[434] D.N. Basov, M.M. Fogler, A. Lanzara, F. Wang, Y. Zhang, Colloquium: Graphene spectroscopy, Rev. Modern Phys. 86 (3) (2014) 959–994, http://dx.doi.org/10.1103/revmodphys.86.959.
[435] M. Jablan, H. Buljan, M. Soljačić, Plasmonics in graphene at infrared frequencies, Phys. Rev. B 80 (24) (2009) 245435, http://dx.doi.org/10.1103/physrevb.80.245435.
[436] M. Romagnoli, V. Sorianello, M. Midrio, F.H.L. Koppens, C. Huyghebaert, D. Neumaier, P. Galli, W. Templ, A. D'Errico, A.C. Ferrari, Graphene-based integrated photonics for next-generation datacom and telecom, Nat. Rev. Mater. 3 (10) (2018) 392–414, http://dx.doi.org/10.1038/s41578-018-0040-9.
[437] H. Rostami, M.I. Katsnelson, M. Polini, Theory of plasmonic effects in nonlinear optics: The case of graphene, Phys. Rev. B 95 (3) (2017) 035416, http://dx.doi.org/10.1103/physrevb.95.035416.
[438] K.J.A. Ooi, D.T.H. Tan, Nonlinear graphene plasmonics, Proc. R. Soc. Lond. Ser. A Math. Phys. Eng. Sci. 473 (2206) (2017) 20170433, http://dx.doi.org/10.1098/rspa.2017.0433.
[439] A. Woessner, M.B. Lundeberg, Y. Gao, A. Principi, P. Alonso-González, M. Carrega, K. Watanabe, T. Taniguchi, G. Vignale, M. Polini, J. Hone, R. Hillenbrand, F.H.L. Koppens, Highly confined low-loss plasmons in graphene–boron nitride heterostructures, Nature Mater. 14 (4) (2014) 421–425, http://dx.doi.org/10.1038/nmat4169.
[440] P. Alonso-González, A.Y. Nikitin, Y. Gao, A. Woessner, M.B. Lundeberg, A. Principi, N. Forcellini, W. Yan, S. Vélez, A.J. Huber, K. Watanabe, T. Taniguchi, F. Casanova, L.E. Hueso, M. Polini, J. Hone, F.H.L. Koppens, R. Hillenbrand, Acoustic terahertz graphene plasmons revealed by photocurrent nanoscopy, Nature Nanotechnol. 12 (1) (2016) 31–35, http://dx.doi.org/10.1038/nnano.2016.185.
[441] J. Christensen, A. Manjavacas, S. Thongrattanasiri, F.H.L. Koppens, F.J.G. de Abajo, Graphene plasmon waveguiding and hybridization in individual and paired nanoribbons, ACS Nano 6 (1) (2011) 431–440, http://dx.doi.org/10.1021/nn2037626.
[442] R.E.V. Profumo, R. Asgari, M. Polini, A.H. MacDonald, Double-layer graphene and topological insulator thin-film plasmons, Phys. Rev. B 85 (8) (2012) 085443, http://dx.doi.org/10.1103/physrevb.85.085443.
[443] D.A. Iranzo, S. Nanot, E.J.C. Dias, I. Epstein, C. Peng, D.K. Efetov, M.B. Lundeberg, R. Parret, J. Osmond, J.-Y. Hong, J. Kong, D.R. Englund, N.M.R. Peres, F.H.L. Koppens, Probing the ultimate plasmon confinement limits with a van der Waals heterostructure, Science 360 (6386) (2018) 291–295, http://dx.doi.org/10.1126/science.aar8438.
[444] P. Alonso-Gonzalez, A.Y. Nikitin, F. Golmar, A. Centeno, A. Pesquera, S. Velez, J. Chen, G. Navickaite, F. Koppens, A. Zurutuza, F. Casanova, L.E. Hueso, R. Hillenbrand, Controlling graphene plasmons with resonant metal antennas and spatial conductivity patterns, Science 344 (6190) (2014) 1369–1373, http://dx.doi.org/10.1126/science.1253202.
[445] T.M. Slipchenko, M.L. Nesterov, L. Martin-Moreno, A.Y. Nikitin, Analytical solution for the diffraction of an electromagnetic wave by a graphene grating, J. Opt. 15 (11) (2013) 114008, http://dx.doi.org/10.1088/2040-8978/15/11/114008.
[446] L. Ju, B. Geng, J. Horng, C. Girit, M. Martin, Z. Hao, H.A. Bechtel, X. Liang, A. Zettl, Y.R. Shen, F. Wang, Graphene plasmonics for tunable terahertz metamaterials, Nature Nanotechnol. 6 (10) (2011) 630–634, http://dx.doi.org/10.1038/nnano.2011.146.
[447] F.J.G. de Abajo, Multiple excitation of confined graphene plasmons by single free electrons, ACS Nano 7 (12) (2013) 11409–11419, http://dx.doi.org/10.1021/nn405367e.
[448] B. Liu, H. Bromberger, A. Cartella, T. Gebert, M. Först, A. Cavalleri, Generation of narrowband, high-intensity, carrier-envelope phase-stable pulses tunable between 4 and 18 THz, Opt. Lett. 42 (1) (2016) 129, http://dx.doi.org/10.1364/ol.42.000129.

[449] S. Castilla, B. Terrés, M. Autore, L. Viti, J. Li, A.Y. Nikitin, I. Vangelidis, K. Watanabe, T. Taniguchi, E. Lidorikis, M.S. Vitiello, R. Hillenbrand, K.-J. Tielrooij, F.H. Koppens, Fast and sensitive terahertz detection using an antenna-integrated graphene pn junction, Nano Lett. 19 (5) (2019) 2765–2773, http://dx.doi.org/10.1021/acs.nanolett.8b04171.
[450] D.A. Bandurin, D. Svintsov, I. Gayduchenko, S.G. Xu, A. Principi, M. Moskotin, I. Tretyakov, D. Yagodkin, S. Zhukov, T. Taniguchi, K. Watanabe, I.V. Grigorieva, M. Polini, G.N. Goltsman, A.K. Geim, G. Fedorov, Resonant terahertz detection using graphene plasmons, Nature Commun. 9 (1) (2018) http://dx.doi.org/10.1038/s41467-018-07848-w.